Studies into the mis-identification probability of tau leptons and a measurement of the cross section $\sigma(pp \to W) \times \mathbf{BR}(W \to \tau\nu_\tau)$ at a center-of-mass energy of $\sqrt{s} = 7$ TeV with the ATLAS detector

Dissertation
zur
Erlangung des Doktorgrades (Dr. rer. nat.)
der
Mathematisch-Naturwissenschaftlichen Fakultät
der
Rheinischen Friedrich-Wilhelms-Universität Bonn

vorgelegt von

Mathias Uhlenbrock

aus
Gummersbach

Bonn 2015

Dieser Forschungsbericht wurde als Dissertation von der Mathematisch-Naturwissenschaftlichen Fakultät der Universität Bonn angenommen und ist 2015 auf dem Hochschulschriftenserver der ULB Bonn http://hss.ulb.uni-bonn.de/diss_online elektronisch publiziert.

1. Gutachter:	Prof. Dr. Klaus Desch
2. Gutachter:	Prof. Dr. Jochen Dingfelder
Tag der Promotion:	25.02.2015
Erscheinungsjahr:	2016

Abstract

Since the start of data taking in the year 2009 the Large Hadron Collider has been operated very successfully. Next to the ongoing efforts to fully determine the properties of the newly found Higgs-like boson, precision measurements of the Standard Model and the search for New Physics are the most important topics on the LHC's scientific agenda. For all that, a good understanding of the detectors and the performance of the experimental techniques is absolutely necessary. This work contributes to this task with a measurement of the mis-identification probability of tau leptons, which play an important role i.a. in the understanding of the Higgs mechanism and the search for supersymmetric particles.

Before New Physics can be discovered, the various backgrounds have to be thoroughly determined. An important Standard Model process is the electro-weak production of tau leptons via the decay of a W boson. In this work a measurement of the total cross section $\sigma(pp \rightarrow W) \times \mathrm{BR}(W \rightarrow \tau\nu_\tau)$ at a center-of-mass energy of $\sqrt{s} = 7$ TeV with the ATLAS detector is presented. The treatment is extended by the development of an alternative measurement method aiming for higher precision, which in turn has the potential to reveal signs of New Physics in a possible deviation from the Standard Model.

Contents

Preface

The long lasting efforts of mankind to systematically order the phenomena in its environment have proved tremendously successful in the past and led to a deeper understanding of the underlying principles. According to today's conception, all natural processes can be ultimately understood as the interplay between two kinds of elementary particles. In the Standard Model, matter is composed of combinations of 12 fermions which interact by four fundamental forces mediated by the interchange of bosons. Furthermore, recent findings strongly suggest that particle masses are generated by spontaneous symmetry breaking of a Higgs field.

The predictions of the Standard Model, together with the theory of relativity have shown impressive agreement with experiments. Despite this, a number of questions concerning the energy content of the universe, the relationship between matter and anti-matter, the structure of fermion generations or the continued unification of the fundamental forces remain unanswered. In addition, some precision measurements show but marginal compliance with the expectations such as the anomalous magnetic moment of the muon.

The Large Hadron Collider (LHC) has been built with mind to further develop the current understanding and to search for hints for New Physics, which might solve many of the Standard Model's difficulties. Within the performed experiments, an important role is played by the tau lepton, which is shown to couple to the newly found Higgs-like particle, an essential prerequisite for the mass generation mechanism to work also for fermions. Furthermore, the tau appears in the decays of many heavy particles postulated by theories expanding the Standard Model. One likewise prominent and attractive example is the connection between bosons and fermions via a so-called Supersymmetry.

At the early stages of data taking, one of the most important goals is to obtain a good understanding of the detector and the performance of the applied object reconstruction and identification methods. This work contributes to this task with a measurement of the tau mis-identification probability for various identification algorithms used in the ATLAS experiment.

Before new discoveries can be made, however, a thorough investigation of the various backgrounds is absolutely necessary. An important Standard Model process is the electro-weak production of tau leptons via the decay of a W boson. In this work, a measurement of the production cross section $\sigma(pp \rightarrow W) \times \mathrm{BR}(W \rightarrow \tau\nu_\tau)$ is presented, which is e.g. about a factor 10^4 higher than the cross section $\sigma(pp \rightarrow H) \times \mathrm{BR}(H \rightarrow \tau\tau)$ of a Standard Model Higgs boson H decaying into two taus at an assumed mass of $m_H = 126$ GeV. The treatment is extended by the development of an alternative measurement method aiming for higher precision, which in turn has the potential to reveal signs of New Physics in a possible deviation from the Standard Model. Here, the direct measurement is replaced by the measurement of a ratio, where many systematic uncertainties cancel out. In addition, the method does not rely on the experimentally challenging identification of hadronically decaying tau leptons.

The organization is as follows. In chapter 1 a brief introduction to the most important underlying theoretical concepts is given. Chapter 2 provides a sketch of the experimental setup and in chapter 3 the applied methods of object reconstruction and identification are described. Chapter 4 is dedicated in some detail to the estimation of the mis-identification probability of tau leptons. In chapter 5 the measurement of the cross section $\sigma(pp \rightarrow W) \times \mathrm{BR}(W \rightarrow \tau\nu_\tau)$ is presented before chapter 6 concludes with the exploration of a novel measurement method aiming for higher precision.

Chapter 1

Theoretical background

This chapter is meant to serve as a brief overview on the most important theoretical concepts of elementary particle physics often referred to in this work. The properties and interactions of elementary particles are described by the so-called Standard Model, a collection of renormalizable quantum field theories [1–4]. Starting with free fields representing free particles, interactions are added by requiring certain gauge symmetries. Some emphasis is placed on the emergence of particle masses via spontaneous symmetry breaking, a mechanism whose realization is strongly supported by the recent discovery of a Higgs-like boson [5–8], [9].

Because of their importance for this thesis, dedicated sections address the properties of tau leptons and QCD jets in somewhat more detail and introduce the concept of a cross section in a scattering process.

The chapter concludes with a short compilation of some of the most important open questions which cannot be answered by the Standard Model but call for a suitable modification or extension of the theory.

1.1 The Standard Model of particle physics

The Standard Model of particle physics (SM) can be expressed in terms of so-called Lagrange densities $\mathcal{L}$ [10]. These are functions of quantum fields φ_i ($i = 1, \ldots, N$), which describe the particles in the theory (with N being the number of different particle fields), and their derivatives

$$\mathcal{L} = \mathcal{L}(\varphi_i, \partial_\mu \varphi_i). \tag{1.1}$$

The equations of motion can be obtained from the the Lagrange densities via the Euler-Lagrange relation

$$\frac{\partial \mathcal{L}}{\partial \varphi_i} - \frac{\partial}{\partial x^\mu} \frac{\partial \mathcal{L}}{\partial_\mu \varphi_i} = 0, \tag{1.2}$$

where the x^μ ($\mu = 0, 1, 2, 3$) are the four-dimensional space-time coordinates of the quantum fields.

According to Hamilton's principle, the solutions of the equations of motion minimize the action S, defined as

$$S(\Omega) = \int_\Omega d^4x \mathcal{L}(\varphi_i, \partial_\mu \varphi_i). \tag{1.3}$$

1.1.1 Free fields

The fields can be classified according to their spin, a particle property with similarities to angular momentum. Particles with integer spin are called bosons and particles with half-integer spin are called fermions. In the Standard Model, particles exist only with spin 0, 1 or 1/2.

The free Lagrange density for massless charged bosons ϕ_i with spin 0 is

$$\mathcal{L} = \partial_\mu \phi_i^* \partial^\mu \phi_i, \tag{1.4}$$

where the index i loops over the number of different spin-0 fields. On the other hand, the free Lagrange density for massless fermions ψ_j is

$$\mathcal{L} = \overline{\psi}_j \mathrm{i} \gamma^\mu \partial_\mu \psi_j, \tag{1.5}$$

where the index j loops over the number of different fermion fields and where

$$\overline{\psi} = \psi^\dagger \gamma^0 \tag{1.6}$$

with the gamma matrices γ^μ, defined as

$$\gamma^0 = \begin{pmatrix} 1 & 0 \\ 0 & -1 \end{pmatrix}, \quad \gamma^i = \begin{pmatrix} 0 & \sigma^i \\ -\sigma^i & 0 \end{pmatrix} \tag{1.7}$$

and the Pauli matrices

$$\sigma^1 = \begin{pmatrix} 0 & 1 \\ -1 & 0 \end{pmatrix}, \quad \sigma^2 = \begin{pmatrix} 0 & -\mathrm{i} \\ \mathrm{i} & 0 \end{pmatrix}, \quad \sigma^3 = \begin{pmatrix} 1 & 0 \\ 0 & -1 \end{pmatrix}. \tag{1.8}$$

The free Lagrange density for massless vector bosons (spin 1) is

$$\mathcal{L} = -\frac{1}{4} F^a_{\mu\nu} F^{\mu\nu a} \tag{1.9}$$

with the field strength tensor

$$F^a_{\mu\nu} = \partial_\mu A^a_\nu - \partial_\nu A^a_\mu - g f^{abc} A^b_\mu A^c_\nu, \tag{1.10}$$

where the A^a_μ are the vector potentials, g is the coupling constant and the f^{abc} are commonly referred to as structure functions. The values of the structure functions as well as the range of the index a depend on the gauge group of the considered vector bosons (see next section).

From the free Lagrange densities the equations of motion for free particles can be derived. These are the Dirac equation for fermions and the Laplace equation for vector bosons. Note that in the case of the massless Dirac equation the left- and right-handed components of the four-spinors decouple and the Lagrange density of the form (1.5) can be specified independently for both parts (leading to the Weyl equations).

The next section shows how interactions between the particles are a consequence of certain symmetry relations.

1.1.2 Gauge symmetries

Transformations of the fields which do not change the form of the equations of motion are called symmetries. In the context of the Standard Model, interactions between the particles are introduced by requiring the invariance of the equations of motion under so-called gauge transformations. These are e.g. elements U of the unitary Lie-groups $U(1)$, $SU(2)$ and $SU(3)$ which are responsible for the electromagnetic, weak and strong force, respectively. The transformed fields φ' are then obtained from the original fields as

$$\varphi' = U\varphi. \tag{1.11}$$

Most generally, such a transformation is of the form

$$U = \exp\left(\mathrm{i}g \sum_i \alpha_i(x^\mu) G_i\right), \tag{1.12}$$

where the α_i are space-time dependent continuous parameters, g is the coupling constant and the G_i are the Hermitian generators of the group.

It is a feature of the Lie groups that in order to study their properties, it suffices to consider the infinitesimal transformation

$$\varphi' = (1 + \delta_\epsilon)\varphi, \ \epsilon \in \mathbb{R}^+ \tag{1.13}$$

with

$$\delta_\epsilon = \mathrm{i}g \sum_i \epsilon_i(x^\mu) G_i. \tag{1.14}$$

It has been found that the electromagnetic and weak forces can be interpreted as two distinct manifestations of one underlying unified electro-weak force (Glashow-Salam-Weinberg (GWS) model) [11–13]. In order to describe this interaction, a symmetry under the combined group $U(1) \otimes SU(2)$ is required.

The free Lagrange densities are not invariant under these gauge transformations. They have to be extended by terms containing products of fields which represent the mutual interactions between the particles. The partial derivatives of the free Lagrange densities have to be replaced by the covariant derivatives

$$\partial_\mu \to D_\mu = \partial_\mu + \mathrm{i}g\frac{\tau}{2}\mathbf{W}_\mu + \mathrm{i}g'\frac{Y}{2}B_\mu \tag{1.15}$$

with the electro-weak coupling constants g and g', the hypercharge Y, the (iso-spin) Pauli matrices τ_i and the electro-weak generators $\mathbf{W}$ and B. In addition, invariance under $SU(3)$ is achieved by making the transition

$$\partial_\mu \to D_\mu = \partial_\mu + \mathrm{i}g_S \sum_a^8 \frac{\lambda^a}{2} A_\mu^a \tag{1.16}$$

with the strong coupling constant g_S, sometimes also denoted as α_S, the generators A^a and the Gell-Mann matrices λ^a. Because the charge of the strong interaction is referred to as color, the underlying theory is called quantum chromodynamics or QCD [14]. The numerical values for the coupling constants are not predicted by the theory and can only be determined experimentally.

The particle content of the Standard Model is summarized in tables 1.1, 1.2 and 1.3. The 12 fermions are further subdivided into quarks and leptons which can be grouped into three families or generations. Only the left-handed fermions form a doublet and participate in the weak interactions. For each generator of the gauge groups exists a corresponding messenger boson. The four generators of the electro-weak force correspond to the photon, the Z and the two W bosons and the 8 generators of the strong force correspond to 8 types of gluons. As messenger particles the Ws, Zs and gluons are special because they are likewise carrier of the charges they couple to. As a consequence the strong and weak forces are self-interacting. The role of the Higgs boson in generating the particle masses is described in the next section.

1.1.3 The Higgs mechanism

Explicit mass terms of the form $M^2\varphi^\dagger\varphi$ violate gauge invariance and the Lagrange density is no longer renormalizable [17]. Via the Higgs mechanism mass terms are created for the electro-weak gauge bosons and also the fermions by spontaneous breaking of the $U(1) \otimes SU(2)$ symmetry.

Scalar bosons					
	Mass [GeV]	Electric charge [e]	Color	Weak isospin	Spin
Higgs boson	126	0	-	-	0

Table 1.1: Properties of the elementary particles, part 1: scalar bosons. According to the Higgs mechanism, the masses of the elementary particles are generated by spontaneous symmetry breaking of a Higgs field. The quantization of this field is the Higgs boson.

Fermions						
	Flavour	Mass [GeV]	Electric charge [e]	Color	Weak isospin	Spin
Quarks	u	$2.3 + 0.7 - 0.5$	2/3	r,g,b	1/2	$\frac{1}{2}$
	d	$4.8 + 0.5 - 0.3$	-1/3		$-1/2$	
	c	1.275 ± 0.025	2/3		1/2	
	s	0.095 ± 0.005	-1/3		$-1/2$	
	t	$173.07 \pm 0.52 \pm 0.72$	2/3		1/2	
	b	4.18 ± 0.03	-1/3		$-1/2$	
	Lepton	Mass [MeV]	Electric Charge [e]	Color	Weak isospin	Spin
Leptons	ν_e	< 3 eV	0	-	1/2	$\frac{1}{2}$
	e	0.510998928(22)	-1		$-1/2$	
	ν_μ	< 0.19	0		1/2	
	μ	105.6583715(35)	-1		$-1/2$	
	ν_τ	< 18.2	0		1/2	
	τ	1776.82 ± 16	-1		$-1/2$	

Table 1.2: Properties of the elementary particles, part 2: fermions. The quoted masses are taken from [15] (2014). The meanings of the used abbreviations are as follows: u(p), d(own), s(trange), c(harm), b(ottom), t(op) for the quark flavours; r(ed), g(reen), b(lue) for the color charges; e electron, ν_e electron-neutrino, μ muon, ν_μ muon-neutrino, τ tau, ν_τ tau-neutrino. The leptons do not carry color charge and therefore do not participate in strong interactions.

Vector bosons				
Interaction	Coupling	Messenger particle	Mass [GeV]	Spin
Strong force	Color	8 gluons	0 (theo. value)	1
Electromagnetic force	Electric charge	photon	$< 1 \cdot 10^{-18}$	
Weak force	Weak isospin	W	80.385 ± 0.015	
		Z	91.1876 ± 0.0021	

Table 1.3: Properties of the elementary particles, part 3: vector bosons. The bosons with spin 1 are the messenger particles of the fundamental interactions. Contrary to photons, the W bosons, the Z boson and the gluons are also carrier of the charge they couple to. For that reason, the weak and strong forces are self-interacting. The quoted masses are taken from [15] (2014). A gluon mass as large as a few MeV may not be precluded [16].

The Higgs mechanism postulates a doublet of complex fields which provide one degree of freedom for each generator of the to-be-broken $U(1) \otimes SU(2)$ symmetry. A Lagrange density of the form

$$\mathcal{L} = \left(\partial_\mu \phi + \mathrm{i}g\frac{\tau}{2}\mathbf{W}_\mu\phi + \mathrm{i}g'\frac{Y}{2}B_\mu\phi\right)^\dagger \left(\partial\phi^\mu + \mathrm{i}g\frac{\tau}{2}\mathbf{W}^\mu\phi + \mathrm{i}g'\frac{Y}{2}B^\mu\phi\right) \tag{1.17}$$

$$- V(\phi) - \frac{1}{4}\mathbf{W}_{\mu\nu}\mathbf{W}^{\mu\nu} - \frac{1}{4}B_{\mu\nu}B^{\mu\nu} \tag{1.18}$$

with

$$\phi \equiv \sqrt{\frac{1}{2}}\begin{pmatrix}\phi_1 + \mathrm{i}\phi_2\\ \phi_3 + \mathrm{i}\phi_4\end{pmatrix} \equiv \begin{pmatrix}\phi^+\\ \phi^0\end{pmatrix} \tag{1.19}$$

and particularly the Higgs potential

$$V(\phi) = \mu^2\phi^\dagger\phi + \lambda(\phi^\dagger\phi)^2 \tag{1.20}$$

with $\mu^2 < 0$, $\lambda > 0$ is invariant under $U(1) \otimes SU(2)$ transformations. The Higgs potential has its minimum at

$$\phi^\dagger\phi \equiv \frac{1}{2}(\phi_1^2 + \phi_2^2 + \phi_3^2 + \phi_4^2) = -\frac{\mu^2}{2\lambda}. \tag{1.21}$$

For simplicity, among all possible ground states choose

$$\phi_1 = \phi_2 = \phi_4 = 0, \quad \phi_3^2 = -\frac{\mu^2}{\lambda} \equiv v^2 \tag{1.22}$$

and therefore

$$\phi_0 \equiv \sqrt{\frac{1}{2}}\begin{pmatrix}0\\ v\end{pmatrix}. \tag{1.23}$$

The expansion of the Higgs field to first order is

$$\phi(x) \equiv \sqrt{\frac{1}{2}}\begin{pmatrix}0\\ v + h(x)\end{pmatrix} \tag{1.24}$$

with the vacuum expectation value v. If one inserts this expression into the Lagrange density, it is no longer symmetric under $U(1) \otimes SU(2)$ or, with other words, the symmetry is broken. The terms

$$\begin{aligned}\left|\left(-\mathrm{i}g\frac{\tau}{2}\mathbf{W}_\mu - \mathrm{i}g'\frac{1}{2}B_\mu\right)\phi\right|^2 &= \frac{1}{8}\left|\begin{pmatrix} gW_\mu^3 + g'B_\mu & g\left(W_\mu^1 - \mathrm{i}W_\mu^2\right)\\ g\left(W_\mu^1 + \mathrm{i}W_\mu^2\right) & -gW_\mu^3 + g'B_\mu\end{pmatrix}\begin{pmatrix}0\\ v\end{pmatrix}\right|^2\\ &= \left(\frac{1}{2}gv\right)^2 W_\mu^+ W^{-\mu}\\ &\quad + \frac{1}{8}v^2\left(W_\mu^3, B_\mu\right)\begin{pmatrix} g^2 & -gg'\\ -gg' & g'^2\end{pmatrix}\begin{pmatrix}W_\mu^3\\ B^\mu\end{pmatrix}\end{aligned}$$

with

$$W_\mu^\pm = W_\mu^1 \mp W_\mu^2 \tag{1.25}$$

now have the form of mass terms for the two W bosons with mass

$$M_W = \frac{1}{2}vg. \tag{1.26}$$

Diagonalization of the matrix in $W^{(3)}$ and B leads to the correct mass states with

$$M_Z = \frac{1}{2} v \sqrt{g^2 + g'^2}, \tag{1.27}$$

the mass of the Z boson and

$$M_\gamma = 0, \tag{1.28}$$

the mass of the photon. The vacuum expectation value v is connected to the mass of the W bosons and the Fermi constant G_F, respectively, via

$$\frac{1}{2v^2} = \frac{g^2}{8M_W^2} = \frac{G_F}{\sqrt{2}} \tag{1.29}$$

and is obtained to $v = 246$ GeV.

The masses of the fermions are eventually created by adding Yukawa couplings of the form

$$\mathcal{L} = -G_f \left[\overline{L} \begin{pmatrix} \phi^+ \\ \phi^0 \end{pmatrix} R + \overline{R}(\phi^-, \overline{\phi}^0) L \right] \tag{1.30}$$

with fermion coupling constant G_f, L the left-handed iso-doublets and R the right-handed iso-singlets. The coupling of a left-handed particle with its right-handed counterpart is the expected behavior of a fermion mass term. The expansion of the Higgs field leads in the case of the electron ($L = e_L$, $R = e_R$) to

$$\mathcal{L} = -\frac{G_e}{\sqrt{2}} v(\overline{e}_L e_R + \overline{e}_R e_L) - \frac{G_e}{\sqrt{2}} v(\overline{e}_L e_R + \overline{e}_R e_L) h \tag{1.31}$$

and corresponding terms for the other leptons and quarks. With the identification

$$m_e = \frac{G_e v}{\sqrt{2}} \tag{1.32}$$

of the electron mass one obtains

$$\mathcal{L} = m_e \overline{e} e - \frac{m_e}{v} \overline{e} e h, \tag{1.33}$$

where

$$-m_e \overline{e} e = -m_e \overline{e} \left[\frac{1}{2}(1 - \gamma^5) + \frac{1}{2}(1 - \gamma^5) \right] e \tag{1.34}$$

$$= m_e(\overline{e}_L e_R + \overline{e}_R e_L) \tag{1.35}$$

has been used. This way, the Higgs mechanism leads to a mixing of the left and right-handed particle components which would otherwise be independent fields.

1.1.4 The Lagrange density of the Standard Model

After the remarks made in the previous sections, the full Lagrange density of the Standard Model can be assembled. The GWS model consists of the following components:

- Kinematics and self interaction of the $W^\pm$ and the Z bosons, kinematics of the photon

The kinematics of the weak eigenstates are given by the Lagrangian

$$-\frac{1}{4}\mathbf{W}_{\mu\nu}\mathbf{W}^{\mu\nu}-\frac{1}{4}B_{\mu\nu}B^{\mu\nu} \tag{1.36}$$

which mix to the mass eigenstates via

$$\begin{pmatrix}W_\mu^+\\W_\mu^-\end{pmatrix}=\frac{1}{\sqrt{2}}\begin{pmatrix}1&-1\\1&1\end{pmatrix}\begin{pmatrix}W_\mu^1\\W_\mu^2\end{pmatrix} \tag{1.37}$$

and

$$\begin{pmatrix}Z_\mu\\\gamma_\mu\end{pmatrix}=\begin{pmatrix}\cos\theta_\mathrm{W}&-\sin\theta_\mathrm{W}\\\sin\theta_\mathrm{W}&\cos\theta_\mathrm{W}\end{pmatrix}\begin{pmatrix}W_\mu^3\\B_\mu\end{pmatrix} \tag{1.38}$$

The angle θ_W is also called the Weinberg angle, which is related to the weak coupling constants via

$$\cos\theta_\mathrm{W}=\frac{g}{\sqrt{g^2+g'^2}},\quad \sin\theta_\mathrm{W}=\frac{g'}{\sqrt{g^2+g'^2}} \tag{1.39}$$

- Kinematics of the leptons and quarks and their electro-weak gauge interactions

$$\overline{L}\mathrm{i}\gamma^\mu\left(\partial_\mu+\mathrm{i}g\frac{\tau}{2}\mathbf{W}_\mu+\mathrm{i}g'\frac{Y}{2}B_\mu\right)L+\overline{R}\mathrm{i}\gamma^\mu\left(\partial_\mu+\mathrm{i}g'\frac{Y}{2}B_\mu\right)R \tag{1.40}$$

- Couplings of the $W^\pm$ and the Z to the Higgs (mass terms), self interactions of the Higgs

$$-\left|\left(\partial_\mu+\mathrm{i}g\frac{\tau}{2}\mathbf{W}_\mu+\mathrm{i}g'\frac{Y}{2}B_\mu\right)\phi\right|^2-V(\phi) \tag{1.41}$$

- Yukawa couplings of the leptons and the quarks to the Higgs

$$-\left(G_1\overline{L}\phi R+G_2\overline{L}\phi_c R+\mathrm{h.c.}\right) \tag{1.42}$$

and the QCD Lagrange density consists of the following terms:

- Kinematics and self interactions of the gluons

$$-\frac{1}{4}F^a_{\mu\nu}F^{\mu\nu a} \tag{1.43}$$

- Kinematics of (massless) quarks and their strong interactions

$$\mathrm{i}\sum_q\overline{\psi}_q^i(\gamma^\mu D_\mu)_{ij}\psi_q^j \tag{1.44}$$

with

$$(D_\mu)_{ij}=\delta_{ij}\partial_\mu+\mathrm{i}g_S\sum_a\frac{\lambda_{ij}^a}{2}A_\mu^a. \tag{1.45}$$

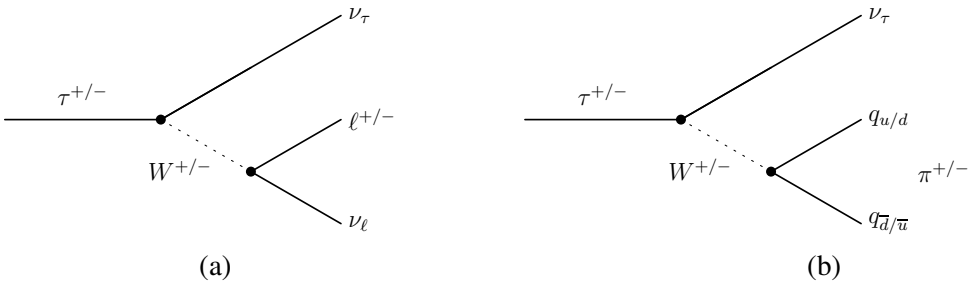

Figure 1.1: Feynman diagrams of the leptonic (a) and hadronic 1-prong (b) decays of the tau lepton.

In addition, the electro-weak states mix via the 3×3 Cabibbo-Kobayashi-Maskawa (CKM) matrix, defined as

$$\begin{pmatrix} d' \\ s' \\ b' \end{pmatrix} = \begin{pmatrix} V_{ud} & V_{us} & V_{ub} \\ V_{cd} & V_{cs} & V_{cb} \\ V_{td} & V_{ts} & V_{tb} \end{pmatrix} \begin{pmatrix} d \\ s \\ b \end{pmatrix}. \tag{1.46}$$

to the mass states [18]. The CKM matrix is unitary and can be parametrized by three mixing angles and one complex phase. The phase is the only source of CP-violation in the Standard Model which is, however, not sufficient to explain the asymmetry between the amount of matter and antimatter observed today [19].

Neutrinos are considered massless in the Standard Model. It has been established experimentally, however, that neutrinos possess a small but finite mass [20]. For that reason, a corresponding mixing matrix exists also for leptons (P-MNS matrix, named after Pontecorvo, Maki, Nakagawa and Sakata) [21].

1.2 The tau lepton

The tau was discovered in 1975 at the Stanford Linear Accelerator Center (SLAC, now SLAC National Accelerator Laboratory) [22]. Events produced in e^+e^- collisions at the Stanford Positron Electron Asymmetric Rings (SPEAR) operated at 4.8 GeV containing a muon and an opposite sign electron with no additional photons or hadrons were interpreted as the leptonic decays

$$\begin{aligned} \tau &\to \mu \overline{\nu}_\mu \nu_\tau \\ \tau &\to e \overline{\nu}_e \nu_\tau \end{aligned} \tag{1.47}$$

of a pair of a new kind of lepton. Ever since, its mass has been determined to be

$$m_\tau = 1776.82 \pm 0.16 \text{ MeV} \tag{1.48}$$

and therefore, the tau is almost 17 times heavier than the muon. The tau lifetime has been measured to be

$$t_\tau = 290.6 \pm 1.0 \cdot 10^{-15} \text{ s}. \tag{1.49}$$

As a consequence, the tau travels on average a distance

$$\beta\gamma c t_\tau = \beta\gamma \cdot 87 \ \mu\text{m} \tag{1.50}$$

Decay modes of the tau lepton		
Decay modes with one charged particle		
	Decay mode	Branching fraction
leptonic	$\nu_\tau \mu^- \overline{\nu}_\mu$	(17.41 ± 0.04) %
	$\nu_\tau e^- \overline{\nu}_e$	(17.83 ± 0.04) %
hadronic (1-prong)	$h^- + \geq 0$ neutrals $+ \geq 0\ K^0 + \nu_\tau$	(50.11 ± 0.04) %
all	1 charged particle + ≥ 0 neutrals + ≥ 0 $K^0 + \nu_\tau$	(85.35 ± 0.07) %
Decay modes with three charged particles		
	Decay mode	Branching fraction
hadronic (3-prong)	$h^- h^- h^+ + \geq 0$ neutrals $+ \nu_\tau$	(14.57 ± 0.07) %
all	3 charged particles ≥ 0 neutrals + ≥ 0 $K^0 + \nu_\tau$	(15.20 ± 0.08) %

Table 1.4: Tau decay modes of particular interest for this work. The hadronic 1-prong and 3-prong decays play an important role in chapters 4 and 5, whereas the leptonic decay into a muon is exploited in chapter 6 [15] (2014).

before it decays, where c is the speed of light in vacuum, $\beta = v/c$ is the velocity and γ is the Lorentz factor

$$\gamma = \frac{1}{\sqrt{1 - \frac{v^2}{c^2}}} \tag{1.51}$$

(all values taken from [15]). Due to its high mass the tau is the only lepton which decays not only leptonically but also hadronically. That means that next to the decays listed in (1.47), it can decay into one or more hadrons which are essentially pions. The most frequent hadronic tau decays are the so-called 1-prong decay, where one charged pion is produced and the 3-prong decay, where three charged pions are produced, respectively.

Figure 1.1 shows the Feynman diagrams of the leptonic and hadronic 1-prong tau decay and table 1.4 summarizes again the decays which are of particular importance for this work.

If one wants to identify tau leptons, one usually looks for the hadronic decays (τ_h) because the leptonic decays are difficult to distinguish from other electro-weak processes where muons or electrons are produced directly. The hadronic decays, on the other hand, exhibit a similar signature in the detector as QCD jets, which are described in the next section. Since at a hadron collider like the LHC QCD jets are produced at very high rates, tau identification is experimentally challenging. Some of the methods used for discrimination are described in more detail in section 3.2.

The hadronic decays make the taus unique among all leptons and therefore allow for measurements which would not be possible otherwise. One example is the determination of the tau polarization which makes use of the fact that the kinematics of the decay products are dependent on the spin orientation of the tau.

As already mentioned in the introduction, taus are thought to be utterly important in searches for new physics like e.g. Supersymmetry because some of the most favored models imply abundant production. In order to answer the question if the Higgs mechanism is also responsible for the fermion masses, the Higgs must, among other things, couple to leptons. In this context, the Higgs is expected to couple the strongest to taus because they have the largest lepton mass.

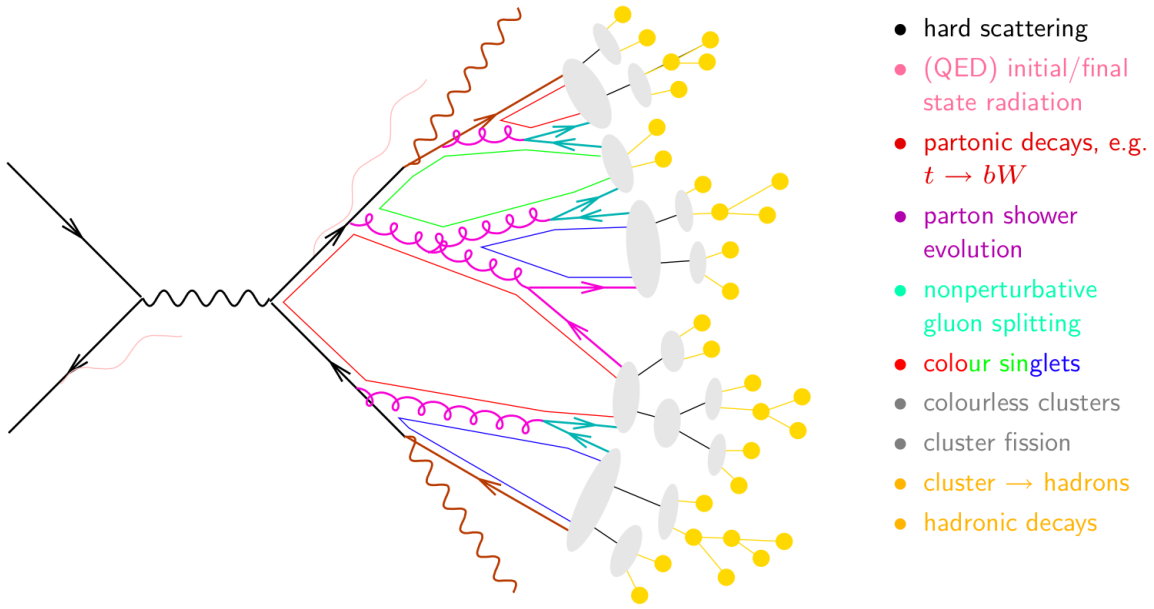

Figure 1.2: Schematic view of the hadronization process [23]. Solid lines represent quarks, curled lines represent gluons and wiggled lies represent photons. The initially created pair of quarks radiates a spectrum of gluons which themselves split into quark-antiquark pairs. At a certain point of this parton shower, marked by the gray spots, the quarks and gluons are converted into hadrons, a process which as of today can only be described phenomenologically.

1.3 QCD jets

Free quarks and gluons cannot exist because the strong force between two color-charged particles does not diminish in strength with increasing distance. Instead, they are forced to form color-neutral objects like pions or kaons after they are created. Therefore, quarks and gluons appear in the detector as streams of hadrons collimated in a cone around the direction of the outgoing parton, the so-called (QCD) jets. It is easily conceivable that if the jet cones are very narrow and the hadron multiplicity is low, they look very similar to hadronically decaying tau leptons. As a consequence, QCD jets form an important background to taus.

Because of the non-perturbative nature of the formation process which turns quarks and gluons into jets of hadrons, it cannot be calculated from first principles. The next section outlines some of the physics models describing the hadronization which are also used for the simulation of jets.

1.3.1 Hadronization/Fragmentation

An illustrative picture of a modeling of the hadronization process is given in figure 1.2. After a quark or a gluon is created, it can radiate further gluons. In addition, a gluon can split into a quark-antiquark pair. In this manner, more and more quarks and gluons are created which is often referred to as the parton shower. The parton shower can still be calculated (to very low order) in perturbation theory. At some point, however, α_S gets large and the perturbation calculations no longer apply. In figure 1.2, gray spots mark the point of conversion into hadrons indicating that from here on the hadronization process can be merely described phenomenologically. For that purpose a set of dimensionless fragmentation functions are defined which describe the distribution of the final state particles in hard scattering processes. The

total fragmentation function for hadrons of type h at a center-of-mass energy of $\sqrt{s}$ is

$$F^h(x,s) = \frac{1}{\sigma_{\text{tot}}}\frac{\mathrm{d}\sigma}{\mathrm{d}x}(pp \to hX) = \sum_i \int_x^1 \frac{\mathrm{d}z}{z} C_i(s;z,\alpha_S) D_i^h(x/z,s) \tag{1.52}$$

where $x = 2E_h/\sqrt{s} \leq 1$ is the scaled hadron energy and σ_{tot} denotes the total cross section. The fragmentation function sums over the contributions of all partons $i = u, \overline{u}, d, \overline{d}, ..., g$, where the D_i^h are the parton fragmentation functions and z is the fraction of the original parton momentum that is carried by the parton that produces the hadron. The C_i functions are called coefficient functions. In lowest order, they are given by $C_g = 0$ for gluons and $C_i = g_i\delta(1-z)$ for quarks, with $g_i(s)$ being the respective electro-weak coupling. For the case where $s \ll M_Z^2$, $g_i(s)$ is proportional to the squared charge of the parton i. The integral of the $F^h(x,s)$ over x gives the average multiplicity of the hadrons, whereas the integral of the $D_i^h(z,t)$ over z gives the average multiplicity of the hadrons of type h. The rise in the hadron multiplicity and jet width with s is logarithmic.

The parton fragmentation functions are analogous to the parton distribution functions in deep inelastic scattering which describe the probability that a parton carries a certain fraction of the proton's momentum. As a consequence, the fragmentation functions show a similar scaling violation behavior when QCD corrections are taken into account. This means, that with higher resolution, the fragmentation functions are shifted towards lower x.

A distinction is made between light and heavy quark fragmentation. For light quarks the parametrization of the fragmentation function is

$$D_q^h(z) = \alpha\frac{1}{z}(1-z)^b \tag{1.53}$$

where a and b are free parameters, whereas for heavy quarks the fragmentation function is given by

$$D_Q^H(z) = \frac{N_H}{z}\left[1 - \frac{1}{z} - \frac{\epsilon_Q}{1-z}\right] \tag{1.54}$$

which is also known as the Peterson fragmentation function. Here, ϵ_Q is another free parameter. The free parameters are usually adjusted to bring the fragmentation model in accordance with the data.

Two very successful and therefore popular fragmentation models are string fragmentation and cluster fragmentation. In the cluster fragmentation model it is assumed that at the end of the parton shower evolution the remaining gluons initially split non-perturbatively into quark-antiquark pairs. This way, one is left exclusively with quarks and antiquarks which subsequently regroup to form color-neutral clusters. These clusters then directly decay into one or more hadrons. The cluster fragmentation model is e.g. implemented in the HERWIG Monte Carlo event generator.

In the string fragmentation model, on the other hand, the fragmenting entity is the color force field between the partons rather than the partons themselves. Two partons moving apart are considered to be connected by a flux tube, the string, formed by the self-interacting gluons. As the energy stored in the string increases with the distance between the two partons, at some point, the energy is sufficient to form a quark-antiquark pair. Thus, the string breaks up repeatedly into color-neutral systems as long as the invariant mass of the string exceeds the mass of a hadron. The string fragmentation model is e.g. implemented in the JETSET Monte Carlo event generator.

1.4 Cross sections in particle interactions

In high energy physics, the fundamental method of gaining insight into the properties of (subatomic) objects is the scattering experiment, where information is shared between probing particles, target particles and the forces between them. Normally two of these items are known beforehand, whereas one tries to learn about the third. If e.g. the probing particles are electrons and the target particles are atomic nuclei, one can learn about the form of the electromagnetic force field and hence the (electric) charge distribution of the nuclei.

Usually, a distinction is made between elastic and inelastic scattering. In contrast to elastic scattering, where the kinetic energy of the incident and outgoing particles is identical, in inelastic scattering part of the energy of the incident particles is converted into e.g. heat or a change of form, like a breakup of one or more particles.

The proton-proton collisions at the LHC are inelastic since the proton is destroyed in the course of the scattering process. However, the relevant reaction can be interpreted as the elastic scattering of the proton's gluon and quark constituents.

In all scattering experiments an important quantity is the so-called (total) cross section, which is a measure of the probability of a certain interaction to take place. Even more information is obtained by considering the differential cross section which subdivides the probability with respect to another quantity as e.g the scattering angle (scattering means exchange of momentum, which may alter the direction of the the scattered particles). With the help of the differential cross section deeper insight can be gained into target properties like the spacial distribution of charges or the particle spin.

By starting with a particle beam with its particles being equally distributed within an area F perpendicular to the beam direction and which interacts with a number of target particles N_T per unit time t, the total cross section σ is defined as

$$\sigma = W\frac{F}{N_\mathrm{T}t}. \tag{1.55}$$

The cross section has the dimension of an area and is measured in barns. The probability that an interaction takes place is given by

$$W = \frac{N^\mathrm{scattered}}{N_\mathrm{P}} \tag{1.56}$$

which is the fraction of scattered particles $N^\mathrm{scattered}$ w.r.t the number of all projectile particles N_P. Together this yields

$$\sigma = \frac{N^\mathrm{scattered}F}{N_\mathrm{P}N_\mathrm{T}t} = \frac{N^\mathrm{scattered}}{jN_\mathrm{T}t} = \frac{N^\mathrm{scattered}}{Lt} \tag{1.57}$$

with $j = N_\mathrm{P}/Ft$ being the particle flux density and

$$L = N_\mathrm{T}j \tag{1.58}$$

being the (instantaneous) luminosity (compare also with equation 5.2 in section 5.1).

1.4.1 Fermi's golden rule

The theoretical calculation of the cross section of a certain physical process can be done with the help of perturbation theory. For that, one assumes that a particle in some initial eigenstate $|i^0\rangle$ of the unperturbed Hamiltonian H^0 makes the transition to another (final) eigenstate $|f^0\rangle$ under the influence of a time-

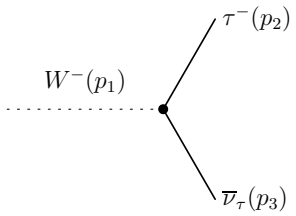

Figure 1.3: Feynman diagram of the decay of a W^- boson into a τ lepton and a tau-antineutrino.

dependent perturbing potential $V(t)$. The Hamiltonian of the perturbed system is then given by

$$H(t) = H^0 + V(t). \tag{1.59}$$

It is further assumed that the solution of the perturbed system can be expanded in a series of eigenstates of the unperturbed system with time-dependent coefficients. One is mostly interested in the evolution of the coefficient $c_f(t)$ belonging to the final state $|f^0\rangle$. If the system is in the state $|i^0\rangle$ at the time $t = 0$, it is found that

$$c_f(t) = \delta_{fi} - \frac{i}{\hbar}\int_0^t \langle f^0|V(t')|i^0\rangle e^{i\frac{E_f^0 - E_i^0}{\hbar}t'}\,\mathrm{d}t' \tag{1.60}$$

with E_f^0 and E_i^0 being the eigenvalues of $|i^0\rangle$ and $|f^0\rangle$, respectively.

The transition probability is now obtained by integrating $c_f(t)$ over all times and by calculating the scalar product. If for the average transition rate one additionally divides by a time unit T one obtains

$$R_{i\to f} = \frac{P_{i\to f}}{T} = \frac{|c_f|^2}{T} = \frac{2\pi}{\hbar}|\langle f^0|V|i^0\rangle|^2\rho(E_f^0, E_i^0) \tag{1.61}$$

where $|\langle f^0|V|i^0\rangle| = M_{fi}$ is called the matrix element and $\rho(E_f^0, E_i^0)$ is the phase space. This relationship is known as Fermi's golden rule [24]. By identifying the transition probability $P_{i\to f}$ with W specified above, the cross section of physical interactions described by the perturbing potential V can be calculated.

As an example, the evaluation of the matrix element of the decay $W \to \tau\nu_\tau$, which enters the theoretical calculation of the cross section measured in chapter 5, is sketched in the following [25]. The Feynman diagram of the process can be seen in figure 1.3. According to the Feynman rules, the graphical representation corresponds to the following terms:

- Incoming W boson with momentum p_1: $\epsilon_W^\mu(p_1)$
- Outgoing tau lepton with momentum p_2: $\overline{u}_\tau(p_2)$
- Outgoing tau-antineutrino with momentum p_3: $v_{\overline{\nu}_\tau}(p_3)$
- Charged current interaction: $i\frac{g}{\sqrt{2}}\gamma_\mu\frac{1-\gamma^5}{2}$

By applying these rules the matrix element can be calculated as

$$M = -i\frac{g}{2\sqrt{2}}\overline{u}_\tau(p_2)\gamma_\mu(1-\gamma^5)v_{\overline{\nu}_\tau}(p_3)\epsilon_W^\mu(p_1) \tag{1.62}$$

After taking the sum over all lepton spins, the absolute squared matrix element is

$$\begin{aligned}\overline{|M|^2} &= \frac{g^2}{8}\,\mathrm{Tr}(\not\epsilon(1-\gamma^5)\not p_2\not\epsilon^*(1-\gamma^5)\not p_1)\\ &= \frac{g^2}{4}\,\mathrm{Tr}((1+\gamma^5)\not\epsilon\not p_2\not\epsilon^*\not p_1)\\ &= g^2[(\epsilon\cdot p_2)(\epsilon^*\cdot p_1)+(\epsilon\cdot p_1)(\epsilon^*\cdot p_2)-(\epsilon\cdot\epsilon^*)(p_1\cdot p_2)+i\epsilon_{\mu\nu\rho\sigma}\epsilon^\mu p_2^\nu\epsilon^{*\rho}p_1^\sigma],\end{aligned}$$

where $\not p = \gamma^\mu p_\mu$ has been used and the asterisk denotes the complex conjugate. With a longitudinally polarized W (helicity = 0) the term containing the total antisymmetric tensor $\epsilon_{\mu\nu\rho\sigma}$ vanishes. By neglecting the τ mass the following relations hold in the rest system of the W:

$$p_1^\mu = \frac{M_W}{2}(1,\sin\theta,0,\cos\theta),\quad p_2^\mu = \frac{M_W}{2}(1,-\sin\theta,0,-\cos\theta), \tag{1.63}$$

where θ is the angle between the momentum of the τ and the z-axis. The matrix element averaged over all spins is then

$$|M|^2 = \frac{g^2}{M_W^2}2\sin^2\theta \tag{1.64}$$

and the decay width is

$$\frac{\mathrm{d}\Gamma}{\mathrm{d}\Omega} = \frac{\overline{|M|^2}}{64\pi^2 M_W} = \frac{G_F M_W^3}{16\pi^2\sqrt{2}\sin^2\theta}. \tag{1.65}$$

Integration over the solid angle gives a factor $8\pi/3$ and one eventually obtains for the decay width

$$\Gamma(W\to\tau\nu_\tau) = \frac{G_F M_W^3}{6\pi\sqrt{2}}. \tag{1.66}$$

The calculation has been performed for longitudinally polarized W bosons. However, since in the rest system of the W there is no preferred direction, the decay probability is independent of the polarization. After inserting the W mass one obtains

$$\Gamma(W\to\tau\nu_\tau) = 227\ \mathrm{MeV}. \tag{1.67}$$

and further (neglecting lepton masses)

$$\Gamma(W\to e\nu_e) = \Gamma(W\to\mu\nu_\mu) = \Gamma(W\to\tau\nu_\tau), \tag{1.68}$$

a fact which is made use of in chapter 6.

1.5 The need for expanding the Standard Model

Despite the fact that the majority of the theoretical predictions of the Standard Model (with added neutrino masses) has been impressively verified by experiment, a number of open questions still remains, some of which should be outlined in the following section. Interestingly, all of these problems can be solved by introducing only one single further principle, which is Supersymmetry.

One of the fundamental driving forces behind every physical theory is the search for connections

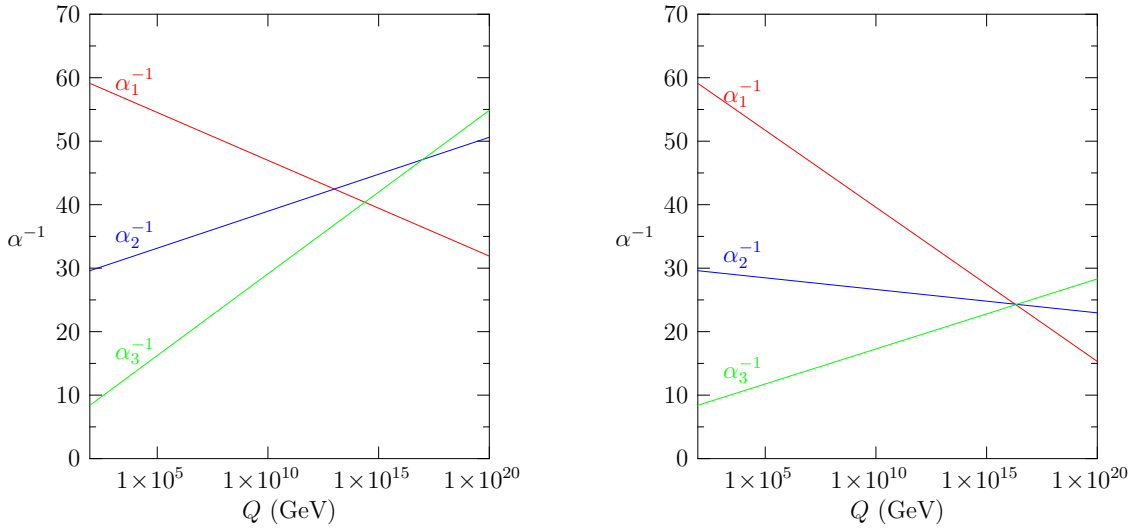

Figure 1.4: Dependence of the coupling constants α_1^{-1}, α_2^{-1} and α_3^{-1} from the considered energy scale Q (at which e.g. particle interactions take place) in the Standard Model (a) and its minimal supersymmetric expansion (MSSM) (b). The evolution is, among other things, a function of the particle content of the respective theory. A unification is only approximately fulfilled in the Standard Model and is realized not until expanded by Supersymmetry. The plot shows only the analytic solutions of the equations of renormalization to first order (see e.g. [26]).

between seemingly independent phenomena. In the same manner as e.g. electromagnetism and the weak force have been successfully reduced to a single unified electro-weak force, one tries to unify the GWS model and quantum chromodynamics. The dependence of the coupling constants of the energy scale at which the interactions take place suggests that at energies of order $O(10^{16})$ GeV they take on a single value. In figure 1.4 the evolution of the coupling constants, which depends among other things on the particle content of a theory, is shown for the Standard Model and its minimal supersymmetric expansion (MSSM). One can see that convergence is only approximately fulfilled in the case of the Standard Model, whereas the MSSM with its extended particle content convincingly predicts unification [27].

Higher order calculations in perturbation theory lead to huge numerical correction factors to the Higgs boson mass [26]. In figure 1.5 some examples of these processes are displayed. A diagram which contains a fermion loop modifies the Higgs mass by

$$\Delta m_H^2 = -\frac{|\lambda_f|^2}{8\pi^2}\Lambda_{UV}^2 + \dots . \tag{1.69}$$

Here, λ_f denotes the coupling strength of the Higgs to the fermion f and Λ_{UV} is a so-called cut-off-term, which is of order of the Planck mass and is introduced to handle quadratic divergences. Consequently, such a diagram contributes $O(10^{38})$ GeV to the Higgs mass. On the other hand, a loop containing a scalar particle S leads to a correction

$$\Delta m_H^2 = \frac{|\lambda_S|^2}{16\pi^2}\Lambda_{UV}^2 + \dots , \tag{1.70}$$

where λ_S is the coupling of the Higgs to the corresponding scalar particle. The huge respective contri-

Figure 1.5: Fermionic (left) and bosonic (or scalar) loop corrections (right) contribute terms of order $O(10^{38})$ GeV to the Higgs mass with opposite sign. If, however, a bosonic partner particle exists for every fermion as predicted by Supersymmetry, these terms exactly cancel each other out.

butions require a rather fine tuning to yield a finite Higgs mass of order $O(10^2)$ GeV. Supersymmetry predicts for every fermion a corresponding boson which couple with identical strength to the Higgs ($\lambda_f = \lambda_S$), so that the remaining expression

$$(|\lambda_S|^2 - |\lambda_f|^2)\Lambda_{UV}^2 \tag{1.71}$$

simply vanishes.

Numerous observations in recent years have established the fact that the universe consists only partly of visible, that is electromagnetic interacting, baryonic matter which forms stars, planets and interstellar gas. It seems that there exists an additional form of matter which, on cosmic scales, takes only part in gravitational interaction, and is hence considered "dark" [28, 29].

The rotational velocities, for instance, of objects circulating around the galactic center of the milky way do not match the predictions made by Newtonian mechanics, hereby considering only estimations of the existent matter based on visible stars and gas. Similar observations are made for the dynamics of galaxy clusters and the so-called gravity lens effect, which is the deflection of light in the presence of a gravitational field, as predicted by general relativity.

Under the assumption, that the laws of gravity are valid also on cosmic scales, an explanation of the phenomena would be the existence of one or more stable massive particles that do not participate in electromagnetic interactions (so-called WIMPs: weakly interacting massive particles). The neutrinos in the Standard Model are examples of such particles but due to their very small masses large contributions to the energy density could only be created dynamically (hot dark matter (HDM)).

Models of galaxy creation, however, suggest that there has to be another form of dark matter with a relatively high rest mass (cold dark matter (CDM)). Under certain circumstances, however, Supersymmetry predicts additional particles with properties which make them suitable dark matter candidates.

Chapter 2

The ATLAS detector at the LHC

The purpose of this chapter is to give an overview on the experimental setup providing the data which is analyzed in this thesis. It mainly consists of two parts: in section 2.1 the Large Hadron Collider (LHC) is described which delivers high-energetic particle beams and brings them to collision. Section 2.2 covers the ATLAS detector and its subsystems which are responsible for recording the collision event information.

2.1 The Large Hadron Collider

The Large Hadron Collider (LHC) [30, 31] is a particle accelerator built and maintained by the European Organization for Nuclear Research (CERN) which is located near the city of Geneva, Switzerland, with parts of its site on both French and Swiss territory. It reuses the tunnel originally constructed for its predecessor, the Large Electron-Positron Collider (LEP) [32], which has a circumference of nearly 27 km and resides 50 to 170 meters below ground. The LHC is designed to accelerate protons up to 7 TeV (Teraelectronvolts, 1TeV = 10^{12} eV) and lead ions up to 2.76 TeV per nucleon, which makes it the current (2014) most powerful particle accelerator in the world. It hereby surpasses the energy reached by the formerly leading Tevatron [33] at Fermilab by roughly one order of magnitude. Strictly speaking, the accelerated particles are not available as a continuous beam but rather form sequences of separated particle packages, the so-called bunches. This is due to the applied acceleration method which makes use of high frequency elements. Each bunch contains ~100 billion protons. The particles counter-rotate in the accelerator ring and are brought to collision at four dedicated points surrounded by particle detectors.

To characterize the power of a particle collider one often quotes the center-of-mass energy of such collisions in terms of the so-called Mandelstam variable

$$\sqrt{s} = \sqrt{(p_1 + p_2)^2},$$

where p_1 and p_2 are the four-momenta of the colliding particles, respectively. At colliders, the center-of-mass energy is simply twice the energy of the particles, that is e.g. up to 14 TeV for protons.

Next to collision energy, the second important quantity which defines the power of an accelerator machine is the (instantaneous) luminosity. The luminosity is a measure for the beam intensity and hence the average number of particle interactions per given time interval and unit area. It is defined as

$$L = f \frac{n_1 n_2}{4\pi\sigma_1\sigma_2},$$

where f is the circulation frequency n_1, n_2 are the numbers of particles per bunch, and σ_1, σ_2 are the two beam widths in the directions perpendicular to the beam axis. In figure 2.2 the total amount of data

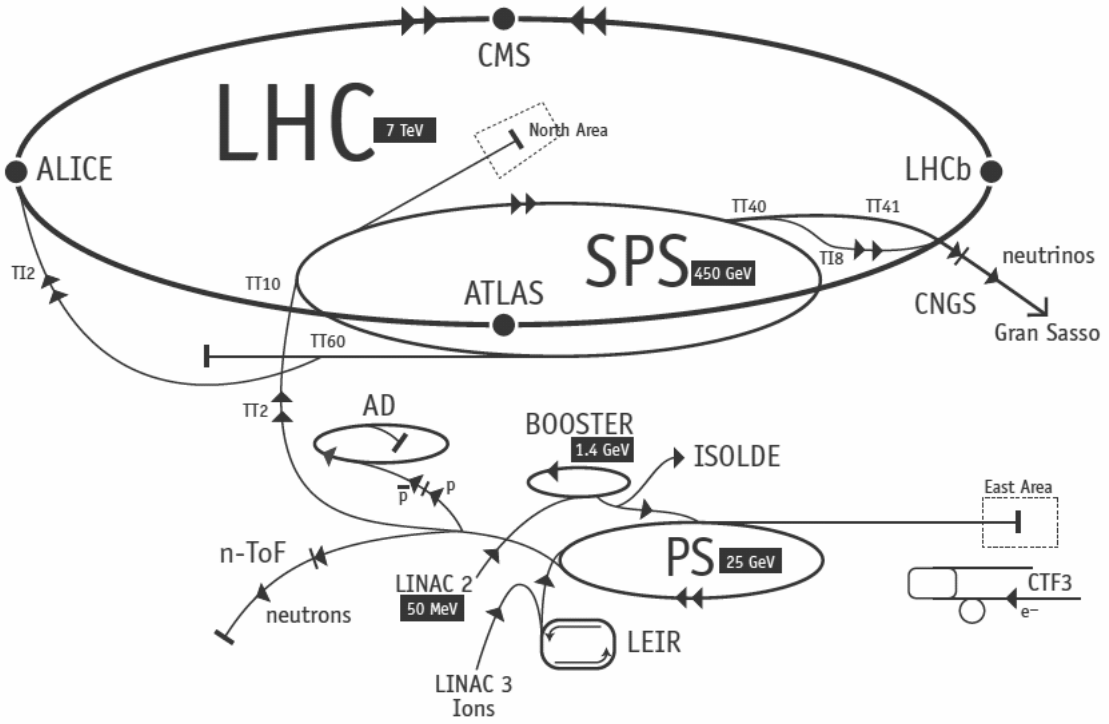

Figure 2.1: Schematic view of the LHC together with its system of pre-accelerators. The protons are obtained by stripping off electrons from hydrogen atoms which come from a bottle stored near the LINAC2 linear accelerator. The protons are subsequently accelerated to 50 MeV before they are injected in the booster synchrotron. After that, they are injected in the Proton Synchrotron (PS) and the Super Proton Synchrotron (SPS) where they are further accelerated to 25 GeV and 450 GeV, respectively. In the last step the protons enter the LHC ring where they are stored and accelerated to maximal energy. Eventually, the proton beams are brought to collision at four dedicated points where the detectors ATLAS, CMS, ALICE, and LHCb are installed. The sketch also shows the acceleration sequence for lead ions and the extraction point of the neutrino beam which is sent to a detector residing in a cave at Gran Sasso in Italy [34].

collected with the ATLAS detector in the years 2010 and 2011 is quoted in terms of the recorded (time) integrated luminosity, corresponding to 45.0 pb^{-1} and 5.08 fb^{-1}, respectively.

To obtain high luminosities, however, is crucial in order to detect rare events. At full luminosity the time between two passing bunches amounts to 25 ns which results in a maximal crossing rate of 40 MHz. Since at every bunch crossing up to 20 protons happen to interact, the achievable collision rate is 800 million per second.

In conclusion, the high energies together with an unprecedented (instantaneous) luminosity of 10^{34} cm^{-2} s^{-1} put the LHC in a position to explore for the first time the yet unmapped energy regime of the Terascale.

The design parameters of the LHC are characteristic for a typical discovery machine prioritizing collision energy over measurement precision. The applied ring geometry, for instance, is better suited to reach high energies than e.g. a linear accelerator, having the big advantage that the circulating particles can be accelerated multiple times by the same elements. In addition, the beam can be reused after the collision, which helps keeping up a high luminosity.

This means, however, that in addition considerable effort has to be put in the bending of the particle

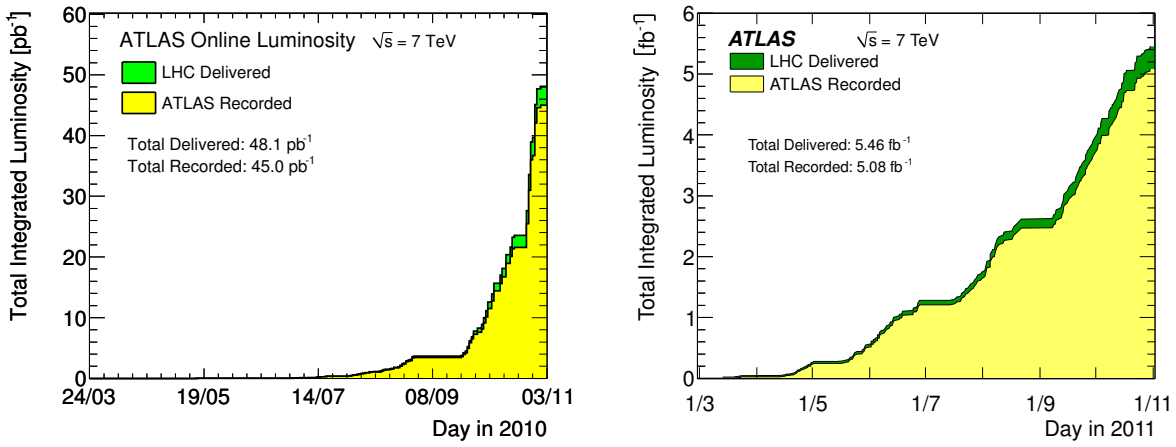

(a) (b)

Figure 2.2: Total amount of data delivered by the LHC in the years 2010 (a) and 2011 (b) at a center-of-mass energy of $\sqrt{s} = 7$ TeV. A large fraction of the data has actually been recorded by the ATLAS detector corresponding to an integrated luminosity of 45.0 pb^{-1} and 5.08 fb^{-1}, respectively. The amount of data available for analyses, however, may be somewhat smaller, due to high quality requirements [35].

beams. For that purpose, powerful magnets based on superconducting technology provide a magnetic field of 8.33 T. The relationship between the strength of the magnetic field B, the particle momentum p and the curvature radius r of the accelerator ring is given by

$$B = \frac{p}{0.3r},$$

where the field strength is measured in Tesla, the momentum is measured in GeV and the curvature radius is measured in meters (the factor 0.3 is introduced to convert between SI and natural units).

Protons are used in collider experiments because with them it is easier to reach high center-of-mass energies than e.g. with electrons. The reason for that is that protons do not suffer as much from energy losses due to synchrotron radiation which always occurs if charges are deflected from linear motion which naturally is a necessity with ring accelerators.

Another advantage of protons is that they can be produced straightforwardly in large amounts. Although e.g. proton-antiproton reactions have higher cross sections, the production rate of antiprotons severely limits the obtainable luminosities.

The big disadvantage of protons, however, is the fact that they are not elementary particles but composed of quarks and gluons. This means that the proton collisions are in reality collisions of the composing partons which carry only a fraction of the proton energy according to a certain probability distribution. Since the initial energy of such a parton collision is unknown a priori, the final state of an event cannot be reconstructed unambiguously. However, the transverse component of the total momentum is known to be zero before the collision, so it has to be zero afterwards. For this reason, at colliders, one is often restricted to measure but the transverse part of a quantity, as will be seen later when the data analyses are discussed.

Before the particle beams enter the LHC, they pass a sequence of pre-accelerators as can be seen in figure 2.1, which shows a schematic view of the accelerator array. The protons are obtained by stripping off electrons from hydrogen atoms which come from a bottle stored near the LINAC2 linear accelerator. The protons are subsequently accelerated to 50 MeV before they are injected in the booster

synchrotron (PBS). After that, they are injected in the Proton Synchrotron (PS) and the Super Proton Synchrotron (SPS) where they are further accelerated to 25 GeV and 450 GeV, respectively. In the last step the protons enter the LHC ring where they are stored and accelerated to maximal energy. Eventually, the proton beams are the brought to collision at four dedicated points where the detectors ATLAS (A Toroidal LHC Apparatus), CMS (Compact Muon Solenoid) [36], ALICE (A Large Ion Collider Experiment) [37], and LHCb (Large Hadron Collider beauty) [38] are situated.

While ATLAS and CMS are multi-purpose detectors, ALICE and LHCb are designed to meet special objectives. The goal of ALICE is to measure the quark-gluon-plasma created by colliding lead ions, a state of matter thought to be existent a millionth second after the Big Bang. LHCb on the other side looks for the decays of hadrons containing heavy quarks, in order to investigate CP-violating processes and thereby shed some more light on the relationship between matter and anti-matter.

In this thesis, only data from proton-proton collisions recorded by the ATLAS detector has been analyzed. During all of the considered data taking periods, the LHC has been operated at a center-of-mass energy of $\sqrt{s} = 7$ TeV.

2.2 The ATLAS detector

ATLAS (A Toroidal LHC Apparatus) [39] is one of two multi-purpose detectors at the Large Hadron Collider. It consists of a set of subdetectors which are arranged around the interaction point similar to the shells of an onion. From inside to outside it consists of the inner detector, the calorimetry system and the muon spectrometer. Additionally, the ATLAS detector features a sophisticated magnet system providing a magnetic field strong enough to bend the tracks of even the highest-energetic particles. A schematic view of the ATLAS detector can be seen in figure 2.3. In the following sections each individual subsystem is discussed in more detail.

2.2.1 The ATLAS coordinate system

Within ATLAS, a right-handed orthonormal Cartesian coordinate system is used with its origin chosen to be at the nominal interaction point. The x-axis points to the center of the LHC's circle, the y-axis points upwards and the z-axis points in the direction of the beam pipe. A common alternative are the spherical coordinates r, ϕ, and θ which are obtained from the Cartesian coordinates via the usual transformations

$$r = \sqrt{x^2 + y^2 + z^2}; \quad \phi = \arctan\frac{y}{x}; \quad \theta = \arccos\frac{z}{\sqrt{x^2 + y^2 + z^2}}$$

with $x, y, z \in [-\infty, \infty]$, $r \in [0, \infty]$, $\phi \in [0, 2\pi]$ and $\theta \in [0, \pi]$. Another alternative frequently used are the cylindrical coordinates r, ϕ and z (with r pointing in the direction perpendicular to z).

One issue with hadron colliders is that the colliding particles are not elementary but composite objects. As a consequence, the longitudinal momenta of the interacting particles are not known a-priori. Since in addition the longitudinal momenta differ from each other with high probability, the center-of-mass system is likely to be boosted along the z-axis. Therefore, a coordinate system which transforms independently of the boost has been introduced.

Coordinates perpendicular to the the z-axis are clearly invariant under boost transformations. The rapidity of a particle with four-momentum (E, p_x, p_y, p_z) and mass m is given by

$$y = \frac{1}{2}\ln\frac{E + p_z}{E - p_z} = \ln\frac{E + p_z}{m_\mathrm{T}} = \coth\frac{p_z}{E}, \tag{2.1}$$

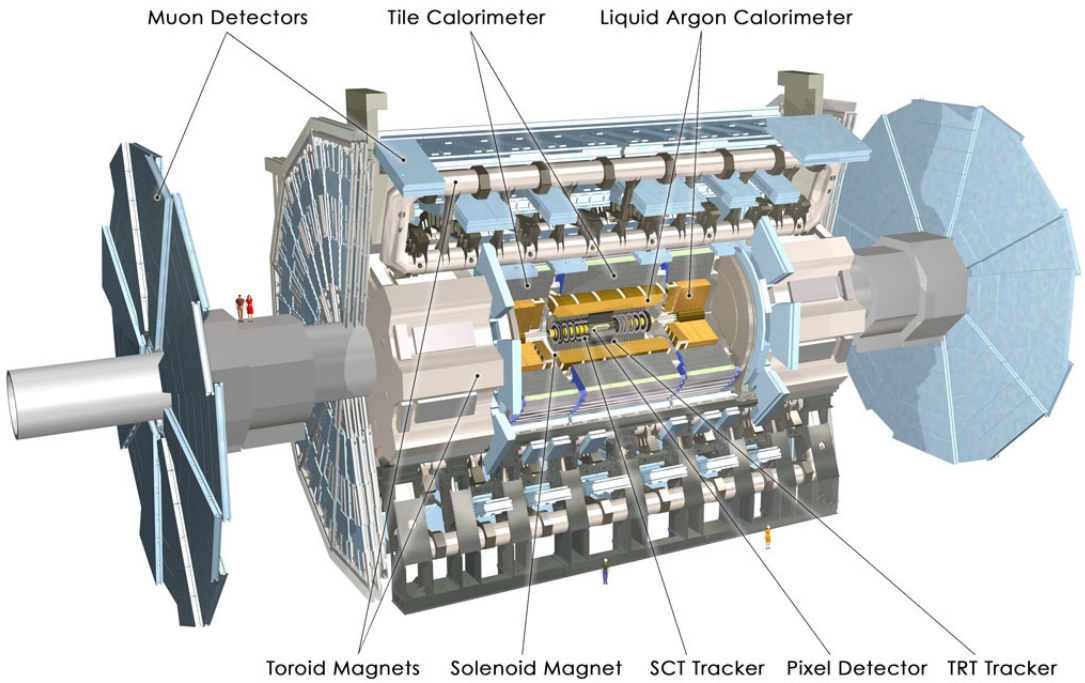

Figure 2.3: Schematic view of the ATLAS detector and its most important subsystems. The inner detector, consisting of the pixel detector, the SCT tracker and the TRT tracker is responsible for the reconstruction of particle tracks. The magnet system, consisting of the solenoid and toroid magnets, bends the particle tracks which enables the measurement of the particle momenta. The calorimetry system measures the particle's energies and consists of the electromagnetic calorimeter and the hadron calorimeter. Eventually, the outermost layer of the detector is made up by the muon spectrometer [39].

where m_{T} is the transverse mass defined as $m_{\mathrm{T}} = \sqrt{m^2 + p_{\mathrm{T}}^2}$, and p_{T} is the transverse momentum defined as $p_{\mathrm{T}} = \sqrt{p_x^2 + p_y^2}$. The rapidity transforms under boost with velocity β in the z-direction as

$$y \to y' = y - \coth\beta, \tag{2.2}$$

which means that the shape of the rapidity distribution is invariant against longitudinal boost. The disadvantage of the rapidity is, that the particle masses are often unknown. At the energies reached at the LHC, however, one can assume $m \ll E$, so that the momenta can be used instead of the energies. The quantity

$$\eta = \frac{1}{2} \ln \frac{|\mathbf{p}| + p_z}{|\mathbf{p}| - p_z} = -\ln\left(\tan\frac{\theta}{2}\right) \tag{2.3}$$

with $\eta \in [0, \infty]$ is called the pseudorapidity.

Particle and jet coordinates are thus given in terms of the polar angle ϕ and the pseudorapidity η. The Euclidean distance in the ϕ-η plane is usually denoted as $\Delta R = \sqrt{\Delta\phi^2 + \Delta\eta^2}$. For example, the distance between two objects flying in opposite directions in the center-of-mass system are separated by $\Delta R \approx 3$.

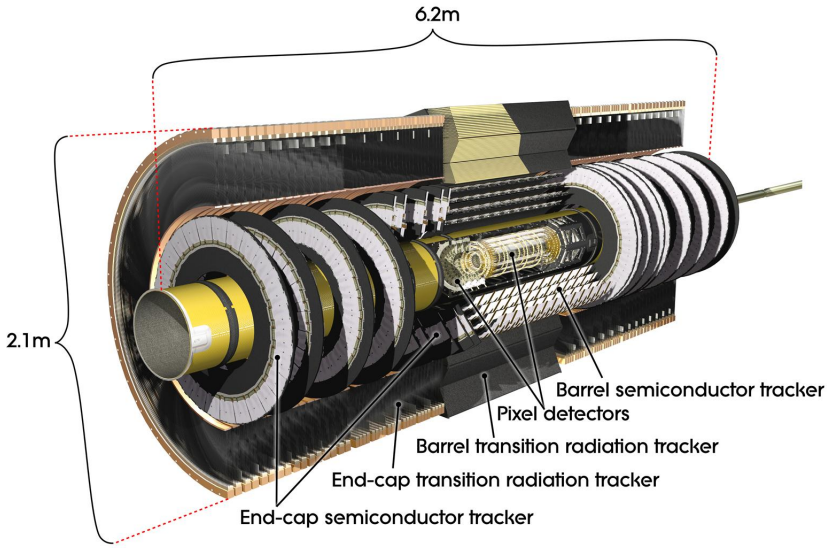

Figure 2.4: Sketch of the ATLAS inner detector system consisting of the pixel detector, the semiconductor (silicon) tracker and the transition radiation tracker. The main purpose of the inner detector is a high-resolution track measurement to enable the reconstruction of interaction vertices and the determination of particle momenta [40].

2.2.2 The inner detector

A schematic view of the layout of the inner detector can be seen in figure 2.4. It consists of the pixel detector, the silicon tracker and the transition radiation tracker, which are described in more detail in the following, and is contained in the central solenoid which provides a magnetic field of 2 T. The inner detector hereby combines high resolution tracking components at inner radii with continuous tracking on the outside. In the barrel region the high-precision detectors are arranged in concentric cylinders around the beam axis, while the end-cap detectors are mounted on disks perpendicular to the beam axis. The acceptance of the inner detector in pseudorapidity is $|\eta| < 2.5$ for particles coming from the center of the detector and full coverage in the azimuthal angle ϕ. The design transverse momentum resolution in the plane perpendicular to the beam axis is $\sigma_{p_T}/p_T = 0.5\% p_T \oplus 1\%$ GeV and the design impact parameter resolution is 10 μm for high momentum particles in the central η region [39, 41]. The relative precisions of the individual subsystems are such that no single measurement dominates the momentum resolution.

The pixel detector

The main task of the pixel detector is vertex reconstruction [42]. For that, it contributes three highly resolved track points as close to the interaction point as possible. The performance of the pixel detector determines the impact parameter resolution and the ability of the inner detector to find short lived particles such as B-hadrons. The system consists of three barrels at average radii of ~5 cm, 9 cm, and 12 cm, and three disks on each side, between radii of 9 and 15 cm. The sensitive elements are organized in 1744 silicon pixel modules which are 62.4 mm long and 21.4 mm wide. Each module consists of 46080 pixel elements read out by 16 chips, each serving an array of 18 by 160 pixels. There is a total number of ~80.4 million pixels and the size of a single pixel is 50 μm $\times$ 400 μm, with the shorter pitch pointing in the x-direction and the longer pitch pointing along the beam axis, respectively. The modules are overlapped on the support structure to give hermetic coverage. Hits in a pixel are read out if the

signal exceeds a tunable threshold. The pulse height is measured using the Time-over-Threshold (ToT) technique.

The silicon tracker

The silicon (semiconductor) tracker (SCT) contributes four space track points to the measurement of particle momenta and (secondary) vertex positions [43]. It hereby plays an essential role for the reconstruction of tau secondary vertices as well as the identification of jets coming from a b-quark (b-tagging). The silicon tracker consists of four barrels with radii of 30.0, 37.3, 44.7 and 52.0 cm and two end-caps with nine disks each. Overall, there are 4088 modules silicon microstrip detectors and each strip covers an area of 6.36×6.40 cm^2. On each module two identical sensors are glued back-to-back allowing for the determination of the z-coordinate by exploiting small angle stereo. The number of sensors is two times 768 which results in a number of readout channels of ~6.3 million. A hit is registered if the pulse height in a channel exceeds a preset threshold, normally corresponding to a charge of 1 fC.

The transition radiation tracker

The transition radiation tracker (TRT) adds up to 36 space track points to the measurement of particle momenta [44]. The detector consists of 298,304 proportional drift tubes (straws), which are combined in the barrel region into three cylindrical layers covering a radial range from 56 to 107 cm and into two end-caps consisting of 18 wheels each. The barrel straws are arranged parallel to the beam direction and the straws in the end-cap wheels are radially oriented. Each straw is 4 mm in diameter with a maximum length of 144 cm. In order to reduce the occupancy, the straws are divided in two at the center and read out at both ends. Each readout channel provides a drift time measurement, giving a spatial resolution of 170 μm per straw.

Electron identification capability via transition radiation is added by employing a Xenon-CO_2-Oxygen gas mixture to detect photons created in a radiator between the straws. The transition radiation photons have energies in the keV region and can therefore be easily distinguished from the energies deposited by ionizing particles in the tracker.

2.2.3 The calorimetry system

Particle energies are measured with the ATLAS calorimetry system. Next to a good energy resolution over a large range, a fast detector response is mandatory as well as radiation hardness in the face of the high collision rates achieved at the LHC. Both requirements can be met using a detector design based on liquid argon technology. In addition, a fine granularity of the active elements is needed in order to exploit information on the location and shape of the energy depositions for the reconstruction and discrimination between physical objects. The calorimetry system consists of the electromagnetic calorimeter which mostly measures the energy depositions of electrons and photons and the hadronic calorimeter which measures the energy depositions of neutrons. Pions on the other hand deposit energy in both parts of the calorimeter. Common to all calorimeters is a typical sandwich structure consisting of alternating absorber and sensing elements. Incoming particles react with the absorber material where showers of secondary particles (mostly electrons) are created. The energy of the secondary particle shower is subsequently measured in the sensing material.

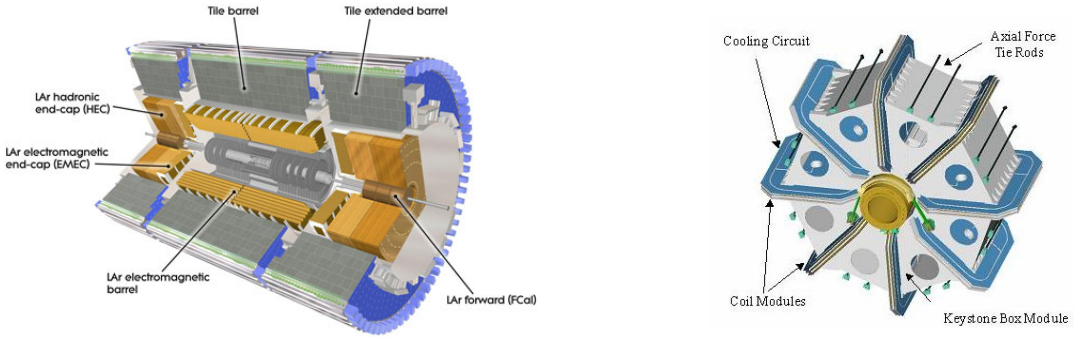

(a) (b)

Figure 2.5: Schematic view of the ATLAS calorimetry system (a) [39]. It consists of the electromagnetic calorimeter based on liquid argon (LAr) technology and the hadronic calorimeter which uses scintillating tiles. Schematic view of the end-cap toroid coils of the ATLAS magnet system (b) [45].

The electromagnetic calorimeter

The electromagnetic calorimeter consists of the electromagnetic barrel, the electromagnetic end-caps (EMEC) and the forward calorimeters (FCAL) providing coverage up to $|\eta| \leq 4.9$ and full coverage in ϕ (see figure 2.5 (a)) [46]. The electromagnetic barrel and end-caps ($|\eta| \leq 3.2$) feature accordion-shaped anodes and are segmented into cells with increasing granularity from outside to inside. The absorber material is lead and the sensing material is liquid argon (LAr). Passing charged particles produce ionization electrons which drift to the electrodes and hereby cause electrical currents proportional to the energy deposited.

In the forward direction ($3.1 \leq |\eta| \leq 4.9$), the calorimeter makes use of a more compact design. Whereas the sensing material is still liquid argon, the absorber consists of copper rods arranged parallel to the beam axis and tungsten alloy.

Each calorimeter cell is calibrated by comparing a test pulse of known shape and amplitude with the output signal. Corrections of order a few percents are applied. During operation, the noise level typically ranges from 10 to 50 MeV. The energy resolutions that can be achieved are $\frac{\sigma_E}{E} = \frac{10\%}{E} \oplus 0.7\%$ for the electromagnetic barrel and for the electromagnetic end-cap and $\frac{\sigma_E}{E} = \frac{100\%}{E} \oplus 10\%$ for the forward calorimeter.

The hadronic calorimeter

The hadronic calorimeter (HCAL) consists of the tile barrel (and tile extended barrel) and the hadronic end-caps (HEC) [47]. The tile and tile extended barrel provide coverage within pseudorapidity $|\eta| \leq 1.7$ and the hadronic end-caps are located in the forward direction between $1.5 \leq |\eta| \leq 3.2$. In the iron absorber of the tile calorimeter showers of electrons are produced. Subsequently, the shower electrons cause the scintillating plastic elements to emit light which is detected and recorded. The hadronic end-caps make again use of liquid argon technology because of its intrinsic radiation hardness. The energy resolutions that can be achieved are $\frac{\sigma_E}{E} = \frac{40\%}{E}$ for the tile calorimeters and $\frac{\sigma_E}{E} = \frac{50\%}{E} \oplus 3\%$ for the hadronic end-caps.

2.2.4 The muon spectrometer

The muon spectrometer (MS) constitutes the outermost shell of the ATLAS detector since muons are the only particles which are able to traverse the calorimeters without being stopped [48]. The main purposes of the muon spectrometer are to measure the muon momenta and to provide a muon trigger. Muon track points are recorded with Monitored Drift Tubes (MDT) which are drift chambers made from aluminium with lengths ranging from 0.9 to 6.2 m and a diameter of 3 cm. The working principle is very similar to that of the TRT straw tubes discussed earlier. The altogether 1174 drift tubes are stacked into tracking chambers which are arranged in three consecutive cylindrical layers in the barrel region ($|\eta| \leq 1$) and mounted on wheels perpendicular to the beam axis in the forward direction ($|\eta| \leq 2.7$). The spacial resolution of a single tube is below 100 μm for most of the range in drift distance and approximately 50 μm for the multi-layer. Additionally, Cathode Strip Chambers (CSC) are placed in the forward region ($2 < |\eta| < 2.7$) since the background rate demands for a detector with higher granularity. In order to fully profit from the intrinsic momentum resolution of the drift tubes, considerable effort has to be put into detector alignment and the monitoring of the operating conditions.

The muon triggers look for muons with high transverse momenta. The extrapolated track of the muon is required to traverse the interaction point in order to discriminate photons, neutrons or cosmic muons. For that, two fast response detectors, the Resistive Plate Chambers (RPC) and the Thin Gap Chambers (TGC) are installed, which are optimized for the differing rates in the barrel and forward region, respectively.

2.2.5 The magnet system

The magnet system in ATLAS consists of a central solenoid and a toroid magnet [45, 49–51]. Its main purpose is to provide a strong magnetic field in order to bend the particle trajectories. By reconstructing the particle tracks and by measuring the track curvature radius the particle momenta can be determined.

The solenoid magnet

The central ATLAS solenoid has a length of 5.3 m with a bore of 2.4 m and weighs 5.7 tons. It encloses the inner detector and is designed to provide a magnetic field of 2 T with a peak field of 2.6 T. For that, the superconducting cable needs to be cooled down to 4.8 Kelvin using liquid helium.

The toroid magnet

The toroid Magnet system consists of eight barrel and end-cap coils, respectively, assembled radially and symmetrically around the beam axis. The torus shaped barrel coils are each 25 meters long with a diameter of 5 meters and weigh 830 tons. The peak field provided by the barrel toroid coils is 3.9 T, providing 2 to 6 Tm of bending power in the pseudorapidity range from 0 to 1.3. The end-cap coils are positioned at both ends of the inner detector. Each end-cap coil has an axial length of 5 m and extends radially from 1.65 m to 10.7 m. The total assembly weight is 249 tons. The peak field provided by the barrel toroid coils is 4.1 T, providing 4 to 8 Tm of bending power in the pseudorapidity range from 1.6 to 2.7. A detailed view of the end-cap coils can be seen in figure 2.5.

2.2.6 The trigger system

The recording of every event occurring during the collisions at the LHC is yet impossible and furthermore unnecessary, because the majority consists of (low-energetic) QCD reactions. In order to select

only the most interesting event signatures, a fast and efficient trigger system is required [52, 53]. For that, usually a multi-level trigger is employed which achieves fast decisions by only reading out part of the detector at lower levels and allows for a more and more refined selection at higher levels by eventually including the full detector information.

The ATLAS trigger system reduces the event rate by a factor 10^7 and comprises three stages. A so-called trigger menu can be defined which allows to select very specific event signatures (online as well as in the course of an offline analysis). Trigger signatures have typical identifiers such as e.g. L1_J10 or EF_tau12_loose_xe20 where the individual items indicate the trigger level, the physical object and energy threshold (in GeV), respectively. Triggers with very high rates as e.g. pure jet triggers are often prescaled by a certain factor n which means that only every nth triggered event is recorded.

Level-1 trigger

The first-level (L1) trigger is implemented purely in electronics and its decision is based on a subset of the information from the calorimeter and muon detectors. In order to cause the Level-1 trigger to fire, a certain degree of activity has to be measured in regions of size $\Delta\phi \times \Delta\eta = 0.1 \times 0.1$ in the calorimeter, the so-called trigger towers, or in the trigger elements of the muon spectrometer. It takes the trigger about 2 μs to deliver its judgment, including the propagation delays on cables between the detector and the underground counting room where the trigger logic is housed. All of the information from the detector must be stored in pipeline memories until the Level-1 trigger decision is available.

Level-2 trigger

For events selected by the Level-1 trigger, the information from the detector must be retained for further analysis. The data for such events are transferred to readout buffers where they remain until the Level-2 decision is available. The data can be accessed selectively by the Level-2 trigger which uses regions of interest (RoI) defined by the Level-1 trigger.

The Level-2 trigger refines the selection of candidate objects compared to Level-1, using full-granularity information from all detectors, including the inner tracker which is not used at Level-1. In this way, the rate can be reduced to ~1 kHz. Many events are analyzed concurrently by the Level-2 trigger system using processor farms where an average latency of up to ~10 ms is considered reasonable.

Event filter trigger

At event filter (EF) level, eventually the full detector information is available including detector calibration and alignment.

Although the event rate is already massively reduced by the ATLAS trigger system, a globally operating computer network is needed in order to cope with the enormous amount of data created at the LHC.

The (hadronic) tau trigger

Due to its importance for this work, the (hadronic) tau trigger is discussed in more detail in the following. Its main goal is to efficiently filter events with hadronically decaying tau leptons from an overwhelming background of QCD events already at the earliest possible chance [54]. Events with taus decaying into an electron or a muon are triggered with an electron or muon trigger, respectively. Since time is limited, only a subset of the available discrimination information can be used at the lowest trigger levels in order to make a decision.

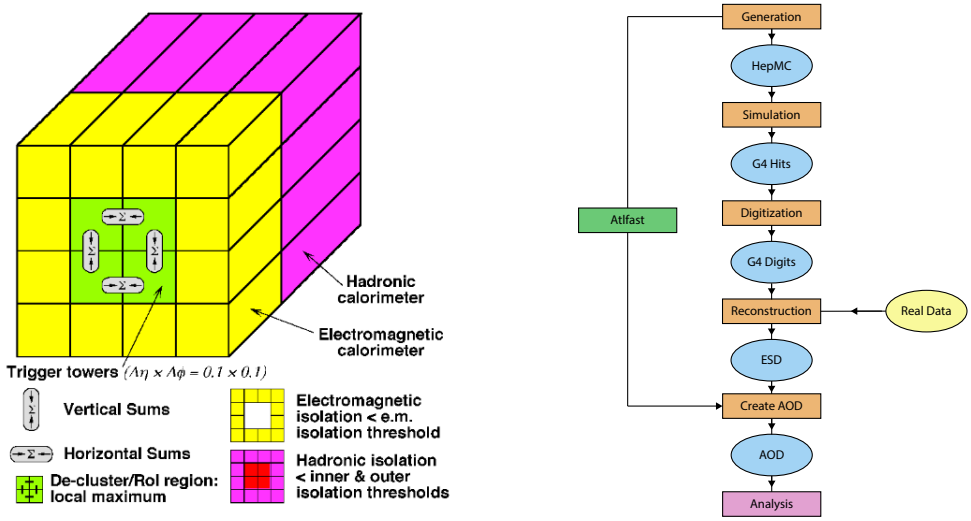

(a) (b)

Figure 2.6: Schematic view of the tau trigger decision process at Level-1. A region of interest is seeded by activity measured in a 2×2 tower cluster in the electromagnetic and hadronic calorimeter (green, red). In order to cause the trigger to fire, the sum of energies deposited in at least one of a 2×1 or 1×2 tower cluster in the electromagnetic calorimeter and the 2×2 tower cluster in the hadronic calorimeter is required to be above the desired object energy threshold. The towers surrounding the core region (yellow, magenta) can be used to apply isolation criteria (a) [54]. Sketch of the simulation and reconstruction chain of data within the analysis software framework Athena. Alternatively, a less complex but fast detector simulation (ATLFAST) is available (b).

At Level-1 a tau region of interest is identified by measuring activity in a 2×2 tower cluster in the electromagnetic and hadronic calorimeter. Within this core region, the sum of energies deposited in at least one of a 2×1 or 1×2 tower cluster in the electromagnetic calorimeter and in the 2×2 tower cluster in the hadronic calorimeter is required to be above the desired object energy threshold. The highest energy measured in one of the four possible cluster combinations in the core of the RoI is then taken as the energy of the tau candidate. The towers surrounding the core region can be used to apply isolation criteria. A schematic view of the Level-1 tau trigger decision process can be seen in figure 2.6 (a).

At Level-2, tracking and even more calorimetry information within the RoI seeded by Level-1 can be exploited in addition to look for refined tau candidates. These include the narrowness of the decay cone, the low multiplicity of charged tracks and the isolation from other activity in the detector (for more details on the discriminating variables see section 3.2.2). Also, the energy of the tau candidate can be estimated more accurately than at Level-1.

Eventually at event filter level, the full tau reconstruction and calibration algorithms can be applied in order to maximize the rejection power against QCD events. Despite this, the ultimate goal to obtain high efficiencies while keeping the trigger rate as low as possible remains experimentally challenging.

2.3 Data formats

The data coming from the detector deemed suitable for recording is organized into various streams designed to meet dedicated purposes. The so-called express stream for instance contains only a subset of the events and is optimized for early access in order to obtain insight into the quality of the data as quickly as possible. Calibration streams on the other hand provide selected information on the

performance of individual subsystems which is used for detector calibration. For data analyses, the most important streams are the physics streams which are further subdivided according to the contained physics objects. The data analyzed in this thesis comes from the JetTauETMiss stream (formerly L1Calo stream) and the Muon stream. There might be a small but significant overlap between streams which has to be taken into account if streams are combined. In addition, the data collected in the course of one year is divided into run periods denoted with capital letters reflecting differing run conditions.

In order to be usable for physics analyses, the raw data has to be processed and the physics objects have to be reconstructed. This is done with the help of the data analysis software framework Athena [55]. The most common data formats available are the Event Summary Data (ESD) containing rather detailed event information needed for detector and reconstruction studies and the Analysis Object Data (AOD) which provides the basis for the majority of physics studies. In practice, the object data stored in the AODs are often further converted into a flat n-tuple format (also known as D3PD format) which comes with reduced overhead and usually contains highly customized information.

An indispensable tool for the interpretation of the data is the simulation of both physics processes and the experimental setup. For that purpose, a number of event generators as well as detailed detector simulations are available. The generation of a typical event starts with the determination of the four-vectors of the interacting partons at Born-level. Subsequently, the event is refined by adding the decay of short-lived particles, initial and final state radiation or the fragmentation of quarks and gluons into jets of hadrons. The event generator output is eventually provided in the form of HecMC files. After that, the interactions of the generated particles with the detector material is simulated with the GEometry ANd Tracking package GEANT [56]. The position of every interaction is stored as a so-called hit. In the last step of the event generation the hit information is translated into actual output of the individual subsystems, hereby modelling the detector response. The simulated data can then be submitted to the same reconstruction and identification algorithms which are used for real data.

A sketch of the full reconstruction and simulation chain of real and simulated data can be seen in figure 2.6 (b). Alternatively a less complex but fast detector simulation (ATLFAST) is available which is used in case an overly detailed representation of the detector is not needed [57].

Chapter 3

Object reconstruction and identification

Before the events recorded with the detector can be analyzed, the physical objects have to be reconstructed from the vast amount of individual subdetector measurements. In this chapter, the most important experimental techniques used to reconstruct the objects which are of particular interest for this work are described in more detail. Sections 3.1 and 3.2 deal with the reconstruction and identification of QCD jets and tau leptons, whereas section 3.3 covers the reconstruction of muons. The calculation of the missing transverse energy is presented in section 3.4. Each section concludes with an overview on the performance level of the used reconstruction and identification procedures.

3.1 QCD jet reconstruction

The purpose of jet reconstruction is to correctly assign the measured individual hadrons to the original quarks or gluons in order to determine the parton properties such as the energy or the flight direction. For good results, the particle detector needs a finely segmented calorimeter and a tracking system with high track resolution. Since reconstruction is particularly difficult for wide-spread low-energetic jets which are not well separated, one often considers only jets which surpass a lower energy threshold.

The process of jet reconstruction can be divided into three distinct steps which are described in the following. First, the energy depositions in the calorimeter are grouped to obtain so-called topological clusters. Subsequently, starting from these topoclusters, a jet algorithm is applied in order to build the actual jets. Finally, the jet energies have to be corrected in an additional calibration step.

3.1.1 Topological clustering

In the first step of the jet reconstruction the particle energy depositions in the calorimeter are grouped and discriminated against noise [58]. The procedure is seeded by calorimeter cells with a large signal-to-noise ratio, typically $|E_{\text{cell}}|/\sigma_{\text{noise}} > 4$. The noise level σ_{noise} is determined for each cell by measuring the root mean square (RMS) of the energy depositions in random events. Now all neighboring cells with a signal-to-noise ratio of 2 are added to the seed. Then all neighbouring cells to this cluster are added with no further requirement on their part. In an additional step, the obtained topoclusters are split if they contain local energy maxima.

Before the topoclusters can be used by the jet algorithms, they have to be converted into four-vectors. For that it is assumed that the topoclusters are massless and have an energy equal to the sum of the energy deposited in the cluster cells. The cluster direction is defined as the vector pointing from the origin of the ATLAS coordinate system to its energy-weighted barycenter.

3.1.2 Jet algorithms

The main task of any jet algorithm is to decide which outgoing particles should be grouped together to build a jet [59]. Since there is more than one way to define a jet, it is necessary to decide on a definition which suits best the needs of the analysis. Ideally, a jet algorithm should meet the following requirements

- It should be well defined an easy to calculate from the hadronic final state
- It should be easy to calculate order by order in perturbation theory
- It should have a close correspondence with the distributions of the final state quarks and gluons that one is really interested in

Two additional requirements are especially worthwhile at hadron colliders

- The jet algorithm should be invariant under longitudinal boosts along the beam direction
- The hadron remnant (and the underlying event) should not affect the jet algorithm

The last item is of particular importance since it may be difficult to separate the scattered parton from the hadron remnant.

Several jet algorithms exist. Within the ATLAS experiment the so-called anti-k_T algorithm is widely used. It begins by calculating the distance parameter

$$d_{ij} = \min\left\{k_{\mathrm{T},i}^{2p}, k_{\mathrm{T},j}^{2p}\right\} \frac{\Delta_{ij}^2}{R^2} \tag{3.1}$$

between each pair of particles, with $\Delta_{ij}^2 = (y_i - y_j)^2 + (\phi_i - \phi_j^2)$, where y is the rapidity, k_T is the transverse momentum of the ith particle and R is an adjustable parameter which is typically chosen to be 0.4 or 0.6. Here, a particle is usually a (charged) track with an associated calorimetry entry and all calorimetry entries without assigned track. The parameter p governs the relative power of the energy versus geometrical scale. The anti-k_T algorithm is defined by the choice $p = -1$ (in contrast to the k_T algorithm where p is set to 1). This way, the anti-k_T algorithm is resilient against collinear splitting and soft radiation and produces regular jet shapes at the same time.

The further steps of the algorithm are then as follows

1. Calculate the distance parameter for each particle pair
2. For every particle define a closeness to the beam particle

$$d_{ib} = k_{\mathrm{T},i}^{p2} \tag{3.2}$$

3. If $\min\left\{d_{ij}\right\} < \min\{d_{ib}\}$, merge particle i and j
4. If $\min\left\{d_{ij}\right\} < \min\{d_{ib}\}$, the jet i is complete

The steps are iterated until a given stopping condition is satisfied. One possible criterion is a separation of all jets larger than R^2, where $R = 1$ is preferred if one wants to be compatible with alternative algorithms such as the cone algorithm. The advantage of the anti-k_T algorithm over the cone algorithm is that it performs better if one is interested in physical quantities like the invariant mass of a jet system. The usage of a suitable jet algorithm has been crucial in finding the Higgs boson in certain channels and is still very important in searches for supersymmetric particles.

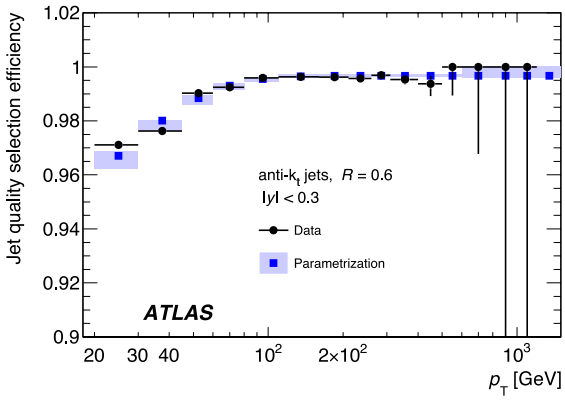

Figure 3.1: Jet reconstruction efficiency as a function of transverse momentum measured in QCD di-jet events using a tag-and-probe method. The obtained efficiencies are ranging from (97 - 99)% which is in agreement with the expectations from Monte Carlo simulations [60].

3.1.3 Jet energy calibration

The purpose of the jet calibration is to correct the assignment of energies to the measured calorimeter jets [61–65]. Various (detector) effects are known to have an influence on the energy measurement

- Only part of the energy deposited in the calorimeter is measured
- Energy is lost in dead detector material
- Leakage of the calorimeter
- Signal loss in the course of topological clustering and jet reconstruction

The energies deposited in the calorimeter are measured at the so-called electromagnetic scale (EMS) which has been determined by calibrated test beam measurements. In order to correct for hadronic objects a calibration scheme based on the jet energies measured at the electromagnetic scale and the jet pseudorapidity has been applied.

In the first step of the calibration the average additional energy due to pile-up is subtracted. This correction is applied at the electromagnetic scale and is determined from minimum bias events as a function of pseudorapidity and the number of primary vertices. Subsequently the cluster and hence jet positions are recalculated w.r.t the primary vertex instead of the origin of the ATLAS coordinate system. Finally the jet energies are corrected by comparing the kinematics with simulated jets. The uncertainties that come with this so-called jet energy scale (JES) calibration ranges between 2% and 8% depending on the jet momentum and pseudorapidity [66].

3.1.4 Performance

The jet reconstruction and identification efficiency is studied on events containing QCD di-jets with a so-called tag-and-probe method which is largely identical to the one described in detail in section 4.1. A clean sample of probe jets is selected which are back-to-back and p_{T}-balanced to a well identified QCD jet. The efficiency is then defined as the fraction of reconstructed and identified probe jets w.r.t all probe jets. The measurement result can be inspected in figure 3.1 where the jet efficiency is shown as a function of the transverse momentum of the jet, ranging from (97 - 99)% in agreement with the expectations from Monte Carlo simulations [60].

3.2 Tau lepton reconstruction and identification

In the following section the reconstruction from basic building blocks (tracks, calorimeter clusters) and the subsequent identification of tau leptons to discriminate against other physics objects is described (following [67, 68]). The procedure is implemented in the `tauRec` package which runs within Athena.

3.2.1 Tau lepton reconstruction

The goal of tau lepton reconstruction is to derive the properties of a tau candidate from the combination of measurements done in the inner detector and the calorimeter. Strictly speaking only the visible part of the tau can be reconstructed since the neutrinos escape undetected. Due to this fact, however, events containing tau leptons can be enriched by additionally requiring missing transverse energy.

Every jet reconstructed by the anti-k_T-algorithm (see also section 3.1) using a distance parameter $R = 0.4$ with transverse momentum $p_T \geq 10$ GeV and within pseudorapidity $|\eta| \leq 2.5$ serves as a so-called seed for the tau candidates. The mass of the tau candidate is defined to be zero. The η- and ϕ-coordinates of the tau are taken directly from the corresponding coordinates of the jet which are calculated by the sum of the four-vectors of the zero-mass constituent topological clusters. The energies of the jet candidates being calibrated by Local Hadron Calibration (LC), however, have to be recalculated when interpreted as the energies of a tau candidate. This is mostly due to differences between the compositions of charged and neutral components for jets and tau leptons. For that, a tau calibration scheme based on Monte Carlo has been established which assigns a correction factor in order to obtain the tau energy scale. The calibration curves are binned in tau prongs and pseudorapidity.

After the four-vector of the taus have been reconstructed as described above, tracks are associated to the candidates in the following manner.

Track association criteria

Tracks within a cone of $\Delta R < 0.2$ around the seed jet axis are associated to the tau candidate if the following quality criteria are met

- $p_T > 1$ GeV
- # pixel hits ≥ 2
- # pixel hits + # SCT hits ≥ 7
- $|d_0| < 1$ mm
- $|z_0 \sin\theta| < 1.5$ mm

where d_0 is the distance of closest approach of the track to the reconstructed primary vertex in the transverse plane, while z_0 is the longitudinal distance of closest approach.

The number of hits per track in the pixel and semiconductor tracker are particularly sensitive to how well the simulation describes the data, convoluting factors such as module efficiencies, the description of disabled modules, the measured beam spot position, alignment and the material description. The (weighted) longitudinal impact parameter $|z_0|$ is used to reject tracks which were not produced in the primary collision, beam background and tracks coming from pile-up.

The tau candidates are classified as n-prong depending on the number n of tracks counted in the core cone. The tau charge is directly calculated from the sum of track charges. Tracks within the isolation annulus, defined by $0.4 < \Delta R < 0.2$ of the axis of the seed jet, are also counted for variable calculations and are required to satisfy the same track quality criteria.

3.2.2 Tau lepton identification

The reconstruction of tau candidates alone provides very little rejection against backgrounds especially coming from QCD jets. This rejection is provided in a separate identification step, using a set of discriminating variables that are calculated during the reconstruction. The list of variables used is defined in section 3.2.2.

In the following, the three identification methods for which the tau-jet mis-identification probability is measured in the next chapter are described in more detail. Ever since, the individual methods have been updated in order to reduce the dependency on the increasing amount of pile-up. Other methods exist as well, making sophisticated use of the particle flow concept.

Cut based identification

For early ATLAS data (10 - 200 pb^{-1}) tau identification is done by introducing rectangular cuts on sets of well understood (safe) discriminating variables [69]. Two sets of variables are usually distinguished: one set uses calorimetry information (energy deposits) only (calorimeter identification method) and the other uses calorimetry plus tracking information (calorimeter+track identification method). The applied cuts are independent of each other only if the considered discriminating variables are uncorrelated.

Log-likelihood tau identification

For the tau identification using the log-likelihood method (LLH) a likelihood function $L_{S(B)}$ is defined for signal and background as the product of the probability density functions $p_i^{S(B)}$ of each identification variable x_i

$$L_{S(B)} = \prod_i^N p_i^{S(B)}(x_i). \tag{3.3}$$

The discriminant used by the likelihood based tau identification method is then defined as the log-likelihood ratio between signal and background

$$d = \ln\left(\frac{L_S}{L_B}\right) = \sum_{i=1}^{N} \ln\left(\frac{p_i^S(x_i)}{p_i^B(x_i)}\right). \tag{3.4}$$

The $p_i^{S(B)}$ are calculated as the fraction of events per bin in a histogram of the ith distribution produced from simulated signal and background samples. The samples are split into bins of transverse momentum, number of prongs and number of reconstructed vertices in order to maximize the discrimination power. To avoid discontinuities in the transverse momentum, interpolations are applied in the vicinity of the bin edges. The likelihood discriminant is then trained separately for each combination of these categories. Loose, medium and tight selections have been defined on the log-likelihood score which yield signal efficiencies of 60%, 45% and 30%, respectively, approximately independent of the tau transverse momentum.

Boosted decision tree tau identification

Decision trees are diagrams where classification rules are represented by so-called "branches" (sprouting from "nodes") and a certain classification is represented by so-called "leaves". In the simplest case a decision tree consists of one root node, two branches representing a binary decision and two adjacent

leaves representing the outcome of this decision. Principally, every decision tree can be converted in a binary decision tree.

In the context of tau lepton identification one is interested in classifying a certain object as signal or background. A decision is made based on cuts on a set of discriminating variables. The tree is initially trained with the help of a data sample containing a known mixture of signal and background events. Now, the root node represents the distribution of the best discriminating variable. By cutting at the optimal value two samples are obtained and the procedure is repeated for the second-best variable and so on. It is possible to stop the iteration prematurely if a certain classification purity is reached or too few events are left for testing. The test statistic being optimized is the so called Gini criterion g, defined as

$$g = P(1 - P) \sum_i W_i, \tag{3.5}$$

where the W_i are the event weights and P is the classification purity defined as the weight of signal events divided by the total event weight. Leaves with $P \geq 0.5$ are defined as signal leaves and the rest are background leaves.

As it is, decision trees tend to be unstable since a small change in the training data can produce large changes in the tree. This is remedied by the use of boosting. For boosting, the training events which were misclassified have their weights increased (boosted), and a new tree is built. The score from the mth tree is taken as +1 if the event is classified as signal and -1 if the event is classified as background. The final score is then taken as the weighted sum of the scores of the individual leaves. This way, a cut-based procedure is transformed into a multivariate technique with a continuous discriminant output.

Identification variables

The tau identification uses eight variables, which are described in the following. They exploit the fact that taus are relatively heavy objects and have smaller cone sizes and lower track multiplicity than QCD jets of the same energy. In addition, 3-prong taus feature a displaced secondary vertex, a feature which is shared only by b-quark-initiated jets.

Cluster mass : the invariant mass computed from associated topoclusters (m_{clusters}).

Track mass : the invariant mass of the track system (m_{tracks}), where the tracks used for the invariant mass calculation use both core and isolation tracks.

Track radius : the p_{T} weighted track width:

$$\text{R}_{\text{track}} = \frac{\sum_i^{\Delta\text{R}_i<0.4} p_{\text{T},i}\Delta\text{R}_i}{\sum_i^{\Delta\text{R}_i<0.4} p_{\text{T},i}}, \tag{3.6}$$

where i runs over the core and isolation tracks associated to the τ_{h} candidate, ΔR_i is defined relative to the τ_{h} jet seed axis and $p_{T,i}$ is the track transverse momentum.

Leading track momentum fraction : defined as:

$$f_{\text{trk},1} = \frac{p_{\text{T},1}^{\text{track}}}{p_{\text{T}}^{\tau}}, \tag{3.7}$$

where $p_{\text{T},1}^{\text{track}}$ is the transverse momentum of the leading core track of the τ_{h} candidate and p_{T}^{τ} is the transverse momentum of the τ_{h} candidate.

	R_{EM}	R_{track}	$f_{trk,1}$	f_{core}	f_{EM}	$m_{clusters}$	m_{tracks}	S_T^{flight}
Cuts	•	•	•					
Likelihood single-prong	•	•				•		
Likelihood multi-prong	•		•		•		•	•
Jet BDT single-prong	•	•	•	•	•	•		
Jet BDT multi-prong	•	•	•	•	•	•	•	•
Electron BDT single-prong	•	•	•	•	•	•		
Electron BDT multi-prong	•	•	•	•	•	•	•	•

Table 3.1: Overview on the variables used by the different discrimination methods.

Electromagnetic radius : the transverse energy weighted shower width in the electromagnetic (EM) calorimeter:

$$R_{EM} = \frac{\sum_i^{\Delta R_i<0.4} E_{T,i}^{EM} \Delta R_i}{\sum_i^{\Delta R_i<0.4} E_{T,i}^{EM}}, \tag{3.8}$$

where i runs over cells in the first three layers of the EM calorimeter associated to the τ_h candidate, ΔR_i is defined relative to the τ_h jet seed axis and $E_{T,i}^{EM}$ is the cell transverse energy.

Core energy fraction : (also called centrality fraction) the fraction of transverse energy in the core ($\Delta R < 0.1$) of the τ_h candidate:

$$f_{core} = \frac{\sum_i^{\Delta R<0.1} E_{T,i}}{\sum_i^{\Delta R<0.4} E_{T,i}}, \tag{3.9}$$

where i runs over all cells associated to the τ_h candidate within ΔR_i of the τ_h jet seed axis.

Isolation energy fraction : the fraction of transverse energy in a ring ($0.1 < \Delta R < 0.2$) of the τ_h candidate:

$$f_{ring} = \frac{\sum_i^{0.1<\Delta R<0.2} E_{T,i}}{\sum_i^{\Delta R<0.4} E_{T,i}}, \tag{3.10}$$

where i runs over all cells associated to the τ_h candidate within ΔR_i of the τ_h jet seed axis.

Electromagnetic fraction : the fraction of transverse energy of the τ_h candidate deposited in the EM calorimeter:

$$f_{EM} = \frac{\sum_i^{\Delta R_i<0.4} E_{T,i}^{EM}}{\sum_j^{\Delta R_i<0.4} E_{T,j}^{EM}}, \tag{3.11}$$

where $E_{T,i}$ ($E_{T,j}$) is the transverse energy, calibrated at the EM scale, deposited in cell i (j) at EM scale, and i runs over the cells in the three layers of the EM calorimeter, while j runs over the cells in all layers of the calorimeter.

Transverse flight path significance : the decay length significance of the secondary vertex for multitrack tau candidates in the transverse plane:

$$S_T^{flight} = \frac{L_T^{flight}}{\delta L_T^{flight}}, \tag{3.12}$$

where $L_{\mathrm{T}}^{\mathrm{flight}}$ is the reconstructed signed decay length, and $\delta L_{\mathrm{T}}^{\mathrm{flight}}$ is its estimated uncertainty.

3.2.3 Tau energy calibration

Similar to the calibration procedure applied to QCD jets, the calorimeter response has to be corrected in order to make the transition from the electromagnetic scale (EM) to the tau energy scale (TES) [70]. In this manner, the transverse tau momentum is corrected by

$$p_{\mathrm{T}}^{\mathrm{TES}} = \frac{1}{R\left(p_{\mathrm{T}}^{\mathrm{EM}}\right)} p_{\mathrm{T}}^{\mathrm{EM}}, \tag{3.13}$$

where R is called the response function defined as

$$R\left(p_{\mathrm{T}}^{\mathrm{EM}}\right) = \frac{p_{\mathrm{T}}^{\mathrm{EM}}}{p_{\mathrm{T}}^{\mathrm{gen}}}, \tag{3.14}$$

the ratio between the momentum at the electromagnetic scale and the true momentum of simulated hadronically decaying tau leptons. As usual, the reliability of the Monte Carlo has been checked and validated by test-beam measurements.

Response functions are constructed separately for single-prong and multi-prong taus and various pseudorapidity regions. Single-prong taus are further divided by electromagnetic energy fraction at the EM scale in order to classify these tau candidates based on the π^0 content.

Systematic uncertainties on the tau energy scale are also evaluated using Monte Carlo studies. The TES uncertainty is found to range from (4 - 2)% for single-prong taus and from (10 - 5)% for multi-prong taus.

3.2.4 Performance

The performance of the tau reconstruction and identification has been studied with the help of $W \rightarrow \tau\nu_\tau$ and $Z \rightarrow \tau\tau$ signal samples. For the investigation of the background rejection power a QCD di-jet sample has been used. The results can be observed in figure 3.2 where the the inverse background efficiency is shown as a function of the signal efficiency. One can see that the multivariate discrimination methods usually outperform the simple cut-based approach. This can be understood since the cut-based approach uses only three discrimination variables. In addition, with multivariate techniques an event is not simply discarded if it does not pass a cut but further investigated by determining cuts on other variables to save signal. An overview on the variables used by the various identification methods is shown in table 3.1.

One can see that the cut based method is evaluated at three distinct so-called working points (commonly referred to as loose, medium and tight, where the tight working point provides the highest background rejection power) which define various trade-offs between signal efficiency and background rejection. A measurement of the probability that a jet is falsely reconstructed as a tau is presented in chapter 4.

3.3 Muon reconstruction

The properties of a muon are determined by reconstructing its track through the inner detector and the muon spectrometer. The characteristics of the track translate straightforwardly to those of the muon

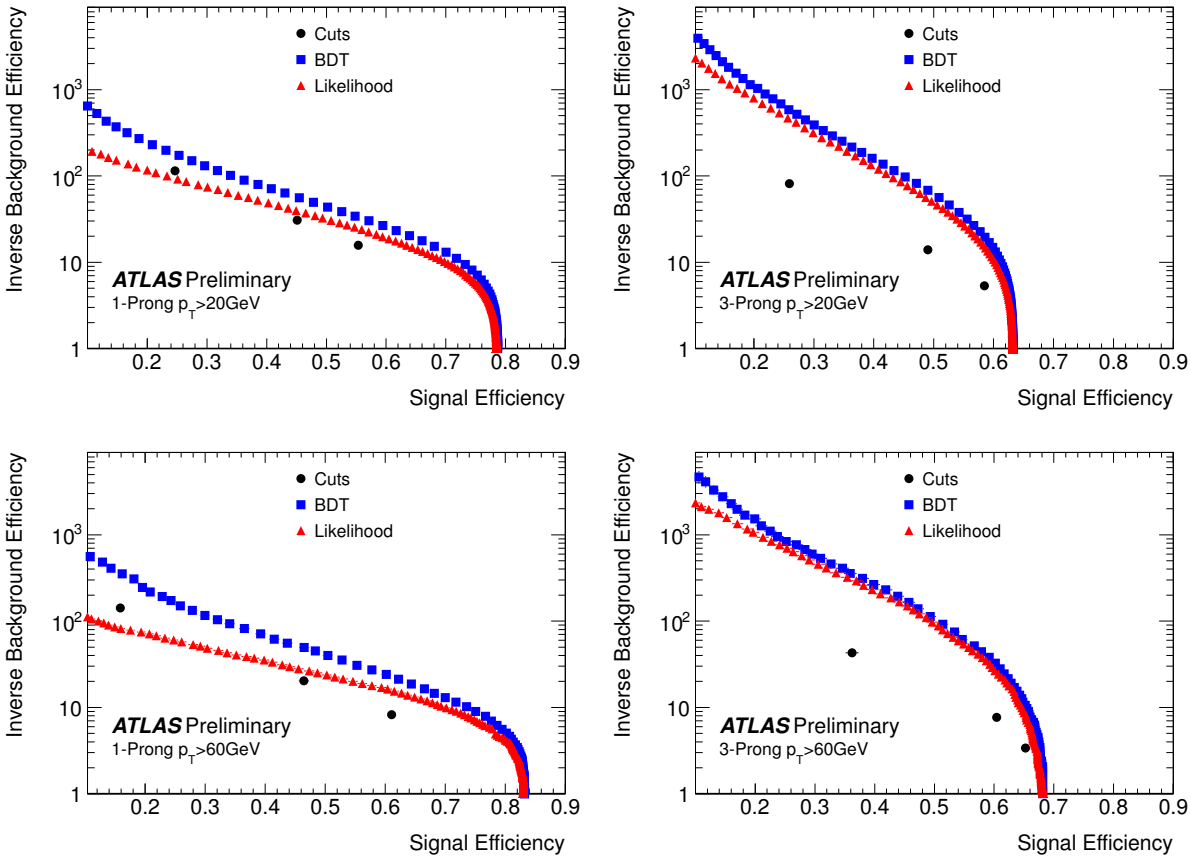

Figure 3.2: Inverse background efficiency as a function of signal efficiency for 1-prong (left) and 3-prong (right) candidates, in low (top) and high (bottom) p_{T} ranges, for all jet discriminants. The cut-based method is evaluated at three distinct working points [70].

or can easily be calculated. The muon energy, for example, is derived from the track curvature. A distinction is made between three reconstruction classes

- Stand-alone muons (SA): The muons are reconstructed by the measurements in the muon spectrometer only. The impact parameter of the muon track is derived by extrapolating the muon track to the beam line

- Combined muons (CB): The muons are reconstructed by the combination of a measured muon track in the muon spectrometer and a matching track in the inner detector

- Segment tagged muons (ST): The muons are reconstructed by extrapolating and associating a good track measured by the inner detector to a track segment measured in the muon spectrometer

The best track resolutions are obtained by combining the measurements in the muon spectrometer and the inner detector. Segment tagged muons show a slightly higher efficiency when compared to combined muons since there is a chance for them to be recovered even if a signal in the tracking chambers of the muon spectrometer is missed out. From the existing muon reconstruction algorithms the so-called Staco algorithm (or Chain 1) have been used for the analyses presented in this thesis.

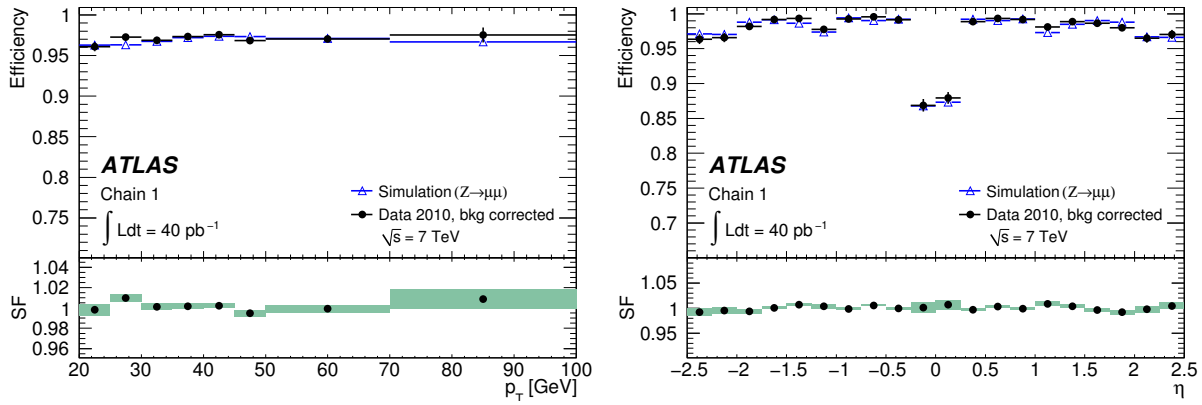

(a) (b)

Figure 3.3: Reconstruction efficiency of combined muons reconstructed with the Staco algorithm (Chain 1) w.r.t segment tagged muons as a function of transverse momentum p_{T} (a) and pseudorapidity η (b). The plot shows the efficiencies measured in 2010 data compared to simulations [71].

3.3.1 Performance

The efficiency for the combined muon reconstruction is a product of the inner detector reconstruction efficiency, the muon spectrometer efficiency and the efficiency of successfully matching the tracks measured in both subsystems. The muon spectrometer reconstruction efficiency and the matching efficiency are measured with the help of a selection of $Z \rightarrow \mu\mu$ events [71]. One of two oppositely charged muons with an invariant mass consistent with the Z mass is checked to be reconstructed as a combined muon. A matching is successful if both tracks are equally charged and maximally separated by a distance parameter which typically ranges from $\Delta R \leq 0.05 - 0.01$. The inner detector reconstruction efficiency on the other hand is defined as the fraction of SA muons which can be associated to an inner detector track. An example of the measurement results can be seen in figure 3.3, where the reconstruction efficiency of combined muons reconstructed with the Staco algorithm (Chain 1) w.r.t segment tagged muons as a function of transverse momentum and pseudorapidity can be seen. The efficiencies are found to be of order 97% which is in excellent agreement with the expectations from simulated events.

The muon momentum resolution is also determined using $Z \rightarrow \mu\mu$ events. For that, the distribution of the measured invariant masses of the two muons is fitted with a convolution of the Z line shape with one Gaussian for each independent contribution to the overall resolution. From the fitted standard deviations of the Gaussians the resolutions are extracted which are found to be of order $\sigma_{p_{\mathrm{T}}}/p_{\mathrm{T}} = (3 - 10)\% p_{\mathrm{T}}$, which is a bit worse than the design resolution due to still preliminary alignment and calibration settings.

3.4 Missing transverse energy reconstruction

The missing transverse energy $E_{\mathrm{T}}^{\mathrm{miss}}$ is defined as the momentum (energy) imbalance in the plane perpendicular to the beam axis. The vectorial sum of the transverse momenta of the particles created in the course of a collision is expected to be zero due to momentum conversation. However, particles which are exclusively weakly-interacting such as neutrinos cannot be detected and therefore appear as $E_{\mathrm{T}}^{\mathrm{miss}}$.

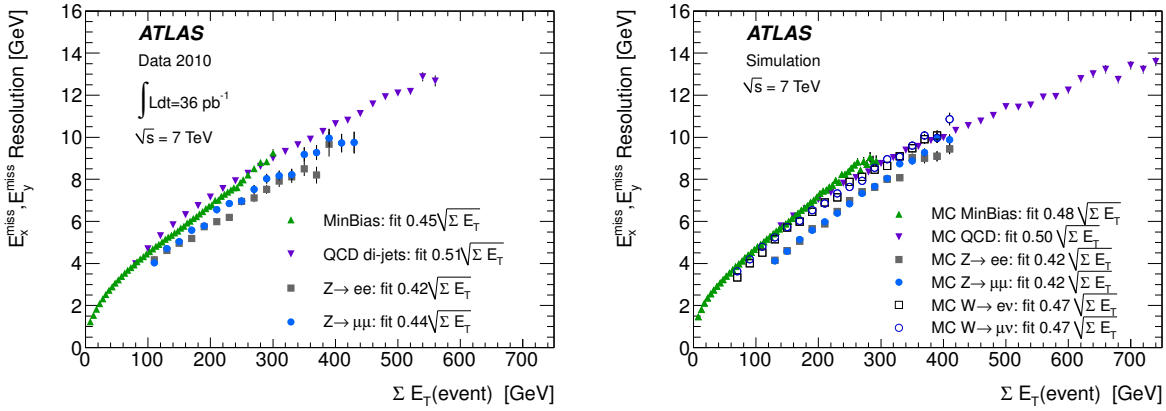

(a) (b)

Figure 3.4: Resolution of the x and y components of $E_{\mathrm{T}}^{\mathrm{miss}}$ as a function of the total sum of transverse energy in 2010 data (a) and in simulated events (b). The measured resolutions obtained from various processes are consistent, ranging from $0.42\sqrt{\sum E_{\mathrm{T}}}$ to $0.51\sqrt{\sum E_{\mathrm{T}}}$, and agree well with the predictions [72].

The missing transverse energy is calculated as

$$E_{\mathrm{T}}^{\mathrm{miss}} = \sqrt{\left(E_x^{\mathrm{miss}}\right)^2 + \left(E_y^{\mathrm{miss}}\right)^2}, \tag{3.15}$$

where for each component the energy depositions in the calorimeter and the contribution from the muon spectrometer measurement are considered separately

$$E_{x(y)}^{\mathrm{miss}} = E_{x(y)}^{\mathrm{miss,\,calo}} + E_{x(y)}^{\mathrm{miss,}\,\mu}. \tag{3.16}$$

For the determination of $E_{x(y)}^{\mathrm{miss,\,calo}}$ the sum of the energy deposits in all calorimeter cells is calculated as

$$E_x^{\mathrm{miss}} = -\sum_i^{N^{\mathrm{cells}}} E_i \sin\theta_i \cos\phi_i, \quad E_y^{\mathrm{miss}} = -\sum_i^{N^{\mathrm{cells}}} E_i \sin\theta_i \sin\phi_i \tag{3.17}$$

where ϕ_i and θ_i are the azimuthal and polar angle of the ith cell, respectively. The E_is are calibrated individually according to the physical object whose energy has been deposited. Cells which are associated to clusters but not assigned to any physics object are grouped in the so-called cell out term. All cells belonging to an object with pseudorapidity $|\eta| < 4.5$ are considered.

The $E_{x(y)}^{\mathrm{miss},\mu}$ term is calculated from the momentum of reconstructed muons within $|\eta| < 2.7$. In the pseudorapidity range $|\eta| < 2.5$ only combined muons are considered. The muon term is calculated differently for isolated and non-isolated muons. A muon is defined as isolated if it is separated by $\Delta R > 0.3$ from the closest reconstructed jet. If the muon is not isolated the energy loss in the calorimeter is added to $E_{\mathrm{T}}^{\mathrm{miss,\,calo}}$.

3.4.1 Performance

The missing transverse energy resolution σ is measured in minimum bias, QCD di-jet and $Z \rightarrow \ell\ell$ events in 2010 data [72]. The result can be seen in figure 3.4 (d). A function

$$\sigma = k \cdot \sqrt{\sum E_{\mathrm{T}}} \tag{3.18}$$

is fitted to the data with k being a factor characterizing the quality of the resolution. It can be stated that the resolutions obtained are consistent among the various processes, ranging from $0.42\sqrt{\sum E_{\mathrm{T}}}$ to $0.51\sqrt{\sum E_{\mathrm{T}}}$. Further, the measured resolutions are in excellent agreement with the expectations as can be seen from simulated events which are depicted in figure 3.4 (e).

Chapter 4

Determination of the jet-tau mis-identification probability from di-jet events

As already described in section 1.2, the unique property of the tau among all leptons is to decay rapidly into a number of lighter particles in many different ways. Consequently, the tau does not show a distinctive signature of its own in the detector but can only be identified indirectly by the analysis of the various decay products, which is experimentally challenging. One usually considers exclusively the hadronic decay modes, which come for the most part in two flavors depending on the number of charged particles produced. In the case of the so-called 1-prong mode, however, where the tau decays among other things into one charged pion, the signature in the detector of one track and associated calorimetry entries is very similar to that of an electron. In the case of the 3-prong mode, where 3 charged pions are produced, the resulting signature of diverging tracks and associated calorimetry entries is shared with that of jets coming from fragmenting colored particles as quarks and gluons (QCD jets). In other words, by exhibiting a signature which is in between that of electrons and jets, taus are likely to be mismatched in the course of object reconstruction.

One is interested in knowing the tau mis-identification probability or fake rate, i.e. the relative number of objects mis-identified as hadronically decaying tau leptons. Since at a hadron collider like the LHC quarks and gluons are created copiously and exceed the number of real taus by far, especially the tau fake rate from QCD jets is a crucial number for all analyses relying on tau reconstruction.

The following chapter introduces a tag-and-probe method that is used to determine the tau fake rate coming from QCD jets by an analysis of ATLAS data taken in the course of the year 2010. Following up on some preparatory work, the results of this study provided one of the very first looks at properties relevant for tau physics at the ATLAS detector. The presentation starts with a general description of tag-and-probe methods and a short overview of available analyses determining tau fake rates in section 4.1. In sections 4.2 and 4.3 the used datasets and event selection is described in more detail. Sources of systematic uncertainties are discussed in section 4.4 before measurement results are summarized in section 4.6.

4.1 Tag-and-probe methods

For the determination of the tau fake rate so-called tag-and-probe methods are applied. The goal of these methods is to obtain a clean, that is a mostly background-free sample of physics objects, in this case ideally representing a full spectrum of tau fake sources of a certain kind (i.e. QCD jets, electrons, etc.). This is achieved by selecting suitable “tag” objects which are kinematically connected to “probe” objects with the desired properties. In this manner, the probe objects are not directly subjected to the selection and therefore the sample is not biased by the applied selection criteria. Since the physical nature of the probe objects is controlled by the selection of the tag object it is possible to directly extract them from data. Consequently, compared to the approaches taken by other studies [68], tag-and-probe

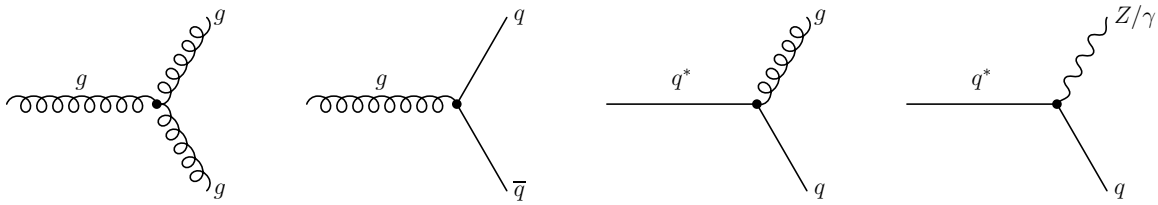

(a) (b) (c) (d)

Figure 4.1: Leading order Feynman diagrams of QCD processes resulting in a back-to-back di-jet final state from the fragmentation of (a) two gluons, (b) a quark-antiquark pair or (c) a combination of a gluon and a quark. Leading order diagram resulting in a photon+jet or Z+jet event (d).

methods rely to a much lesser extent on the use of Monte Carlo simulations. Also, much more emphasis is placed on the actual physical objects which are responsible for the mis-identification.
The sample of probe objects can then be used to test the performance of the existing tau identification algorithms. A probe object which is mis-identified as tau from now on is referred to as a "fake" tau.

To conclude, in this context the tau fake rate f is defined as the number of probe objects which are identified as hadronically decaying tau leptons divided by the number of all probe objects:

$$f = \frac{\text{number of probe objects identified as } \tau}{\text{number of all probe objects}}. \tag{4.1}$$

As mentioned before, the sample of tau fake sources can be influenced by the choice of the tag object. This work is focused on QCD jets as the most abundant source for tau fakes. The method is based on selecting so-called di-jet events, meaning events with at least two jets. Pairs of jets are constructed, where one of the jets is randomly chosen and considered to be the tag jet if it qualifies as a good QCD jet. If the second jet is balanced in transverse momentum p_{T} and back-to-back in the azimuthal plane with respect to the first jet, it is considered to be the probe jet. These criteria ensure that the two jets are coming from the decay of a gluon into two gluons or two quarks, or from a quark decaying into a gluon and a quark with high probability which makes the probe jet another QCD jet. The reason for that is momentum conservation in the strong interaction: the momentum of the interacting partons is zero in the plane perpendicular to the beam axis before the collision, hence the sum of the transverse momenta of the decay products has to be zero afterwards. A graphical depiction of the relevant physics processes can be found in figure 4.1.

However, as described in more detail later, it turns out that the resulting fake rates can depend heavily on the choice of a certain event topology. This is interpreted as a dependence on the intrinsic ratio of quark-to-gluon-initiated jets in the selected events. Since quarks and gluons are thought to behave differently in the process of hadronization, jet properties and hence tau fake rates are likewise expected to vary.

Given the fact that it cannot be directly disentangled experimentally if a jet is quark- or gluon-initiated, the effect is studied by considering event topologies with different quark-to-gluon ratios independently of each other. The available topologies apart from the di-jet analysis presented in this thesis are (in increasing order of the quark-to-gluon jet ratio (see also figure 4.3 (b)) [73]:

- Three-jet topology: the tag object is a jet balancing a pair of QCD jets and the probe object is one of the balanced jets [74]

- $Z(\rightarrow \ell\ell)$+jets topology: events are selected by requiring a pair of same-flavor light leptons with an invariant mass compatible with the Z boson mass. The probe object is an additional jet in the

Event generator: PYTHIA				
Dataset ID	Simulation tag	Events	Cross section [pb]	Description
105010	e574_s934_s946_r1833_r1700	1.4 M	6.78×10^8	MC10 J1
105011	e574_s934_s946_r1833_r1700	2.8 M	4.10×10^7	MC10 J2
105012	e574_s934_s946_r1833_r1700	2.5 M	2.20×10^6	MC10 J3
105013	e574_s934_s946_r1833_r1700	2.8 M	8.78×10^4	MC10 J4
106052	e574_s934_s946_r1833_r1700	10 k	0.99×10^3	MC10 $Z \to \tau\tau$
107054	e574_s934_s946_r1833_r1700	10 k	10.46×10^3	MC10 $W \to \tau\nu$ (incl.)

Table 4.1: Overview on the Monte Carlo datasets used in the analysis. The main part comprises di-jet QCD events generated by the PYTHIA event generator. Tau signal samples as $Z \to \tau\tau$ and $W \to \tau\nu$ are used to study the degree of true tau pollution in the selected events.

events [73]

- Photon+jet topology: the tag object is a well-identified photon, and the probe object is a jet, which is back-to-back with the tag photon [74]

A clean sample of electrons as tau fake sources is obtained by selecting $Z \to ee$ events as described in [75]. Here, the tag object is a well-identified electron and the probe object is a second electron with minimal requirements on its properties. The pair of electrons is furthermore required to have an invariant mass which is compatible with the Z boson mass.

For completeness, the physics processes which can lead to the event topologies mentioned above can also be found in figure 4.1.

4.2 Data and simulation samples

This analysis uses basically the full dataset recorded by ATLAS in the year 2010, corresponding approximately to an integrated luminosity of $\int L\,\mathrm{dt} = 36.5\,\mathrm{pb}^{-1}$, which is calculated using official tools [76] with the `OflLumi-7TeV-003` luminosity calibration [77].

4.2.1 Data samples

The data samples used for analysis come from the L1Calo stream for run periods A-D, and from the JetTauETMiss stream for periods E-I. D3PD ntuples are produced from the recorded AOD data files using `TauD3PDMaker` version 01-00-01-01. The integrated luminosity recorded in each run period is shown in table 4.2.

4.2.2 Simulation samples

The measured data is compared with simulated Monte Carlo events of proton-proton collisions at a center-of-mass energy of $\sqrt{s} = 7$ TeV generated by PYTHIA [78] with the ATLAS AMBT1 tune [79]. The simulation of the detector response is done with the ATLAS simulation framework [80] which is based on `Geant4` [56]. All samples are generated with an average number of vertices of $\langle n \rangle = 2$, including bunch trains with a bunch train spacing of 150 ns, followed by a 225 ns gap, and a second bunch train with again 150 ns bunch train spacing [81]. An overview on the used sample types, their corresponding cross sections and the generated statistics can be found in table 4.1.

Data stream	Period	Subperiod	Run range	Integrated luminosity $\int L\,dt$ [nb^{-1}]
L1Calo	MayGRL	MayGRL	152166 - 155160	9
	C	C1 C2	155228 - 156682	8
	D	D1 D2 D3 D4 D5 D6	158045 - 159224	299
Data stream	Period	Subperiod	Run range	Integrated luminosity $\int L\,dt$ [nb^{-1}]
JetTauETMiss	E	E1 E2 E3 E4 E5 E6 E7	160387 - 161948	1004
	F	F1 F2	162347 - 162882	1816
	G	G1 G2 G3 G4 G5 G6	165591 - 166383	6963
	H	H1 H2	166466 - 166964	7346
	I	I1 I2	167575 - 167844	19099
Total				36454

Table 4.2: Overview on the ATLAS run periods used in the analysis. The numbers shown correspond to the integrated luminosities in the list of good quality runs. The total integrated luminosity is $\int L\,dt = 36.45\,pb^{-1}$. This luminosity represents the total available luminosity, before any selection or trigger criteria (as described in section 4.3) are applied.

Trigger signature	Prescale factor	Prescale corrected integrated luminosity $\int L\,dt$ [nb^{-1}]
L1_J5	97	32.49
L1_J10	26	121.43
L1_J15	6	557.09
L1_J30	2	2016.39
L1_J55	1	3135.97
L1_J75	1	3135.97
EF_j20_jetNoEF	14486	2.31
EF_j30_jetNoEF	1341	24.91
EF_j35_jetNoEF	657	50.86
EF_j50_jetNoEF	134	249.98
EF_j75_jetNoEF	5	6530.51
EF_j95_jetNoEF	5	6121.33

Table 4.3: Prescale weighted integrated luminosities from periods A-F for the L1 triggers, and from periods G-I for the EF triggers. These integrated luminosities are calculated independently, and do not account for overlaps between different triggers.

4.3 Event selection

In the following section the selection procedure for the analysis and the process for extracting the fake rate will be described. To begin with, each event must pass a number of preselection cuts in order to be considered. The preselection criteria are:

- The event must be present in the Good Runs List (GRL), indicating that it is within a luminosity block which was deemed suitable for physics analysis following Data Quality assessment outlined in [82]. The GRL files used are GRL_Tau_ICHEP_7TeV2010Colls_v10.xml

- The event must satisfy the following trigger conditions; For periods A-F: The event must be accepted by one or more of the L1 triggers: “L1_J5” OR “L1_J10” OR “L1_J15” OR “L1_J30” OR “L1_J55” OR “L1_J75”. For periods G-I: The event must be accepted by one or more of the event filter (EF) conditions: “EF_j20_jetNoEF” OR “EF_j30_jetNoEF” OR “EF_j35_jetNoEF” OR “EF_j50_jetNoEF” OR “EF_j75_jetNoEF” OR “EF_j95_jetNoEF”. The relative contributions of these triggers following prescaling are shown in table 4.3

- All jets in the event are required to originate from proton-proton collisions. Whether this is the case is determined by a set of jet cleaning cuts, designed to remove spurious jet candidates (‘bad jets’) arising from three main sources: single cell spikes in the HEC, coherent noise in the ECAL, and out-of-time jets from cosmic rays and beam background [82]. ‘Tight’ cleaning as defined in figure A.1 in appendix A is used. Furthermore, the jet cleaning is not applied to simulated events since some of the cleaning variables are found to be not very well described

- The event must contain at least one reconstructed vertex, with 4 or more associated tracks

Cut	# events
GRL	240,456,965
Trigger	40,723,856
Only good jets	40,068,292
Vertex	39,992,428
$\|\eta\| \leq 2.5$	35,175,892
$p_{\mathrm{T}} \geq 15$ GeV	23,662,782
back to back criterion	14,808,037
p_{T}-balance	11,687,422
# tag tracks	7,767,489
tag triggered	3,978,967

Table 4.4: Number of events after the application of selection cuts.

4.3.1 Tag object selection

In the first stage of the analysis, every combination of two jets in the event is built into a pair of jets. The jets are chosen to be reconstructed by an anti-k_{T} algorithm [83] working on topological clusters [84] and calibrated according to the Global Cell Weighting (GCW) scheme, because these kinds of jets serve as seeds for the calorimetry based tau reconstruction algorithm [85]. While the GCW calibration scheme is used in jet finding, the jet p_{T} used in the rest of the analysis is calibrated to the tau energy scale (see section 3.2.3). In addition, the following topological criteria are applied:

- Each jet in the pair must be reconstructed within the pseudorapidity range $|\eta| \leq 2.5$. This standard cut reflects the fact that in ATLAS, regions with higher absolute pseudorapidities are uncovered by the inner detector system which is responsible for the measurement of tracks
- Each jet in the pair must have a transverse momentum $p_{\mathrm{T}} \geq 15$ GeV

The kinematic connection between the two jets in the pair is achieved by requiring them to be back-to-back in the azimuthal plane (the plane transverse to the beam axis) and to have similar transverse momenta. This enriches the sample with jets originating from the same vertex, and is achieved by applying the following conditions:

- The difference between the azimuthal angles of the jets in the pair must be $|\Delta\phi| = \pi \pm 0.30$ radians
- The jets in the pair must be balanced in p_{T}. The difference between the transverse momenta of the two jets is required to be $|\Delta p_{\mathrm{T}}| \leq \frac{p_{\mathrm{T}}^{\mathrm{max}}}{2}$, where $p_{\mathrm{T}}^{\mathrm{max}}$ is the transverse momentum of the leading jet

For the jets pairs satisfying all of the criteria, one jet is randomly chosen to be the tag jet, whereas the opposing jet is then called the probe jet. If the tag jet is a QCD jet, the probe jet is very likely to be another QCD jet. To select for QCD jets and discriminate against real taus, the tag jet is required to have a minimum number of associated tracks:

- The number of associated tracks must be ≥ 4. The tracks have to meet certain quality criteria which are summarized in [86]. This should remove most of the true taus from the selected sample, because taus are expected to have at most three tracks in the majority of cases. This is discussed further in section 4.4.2

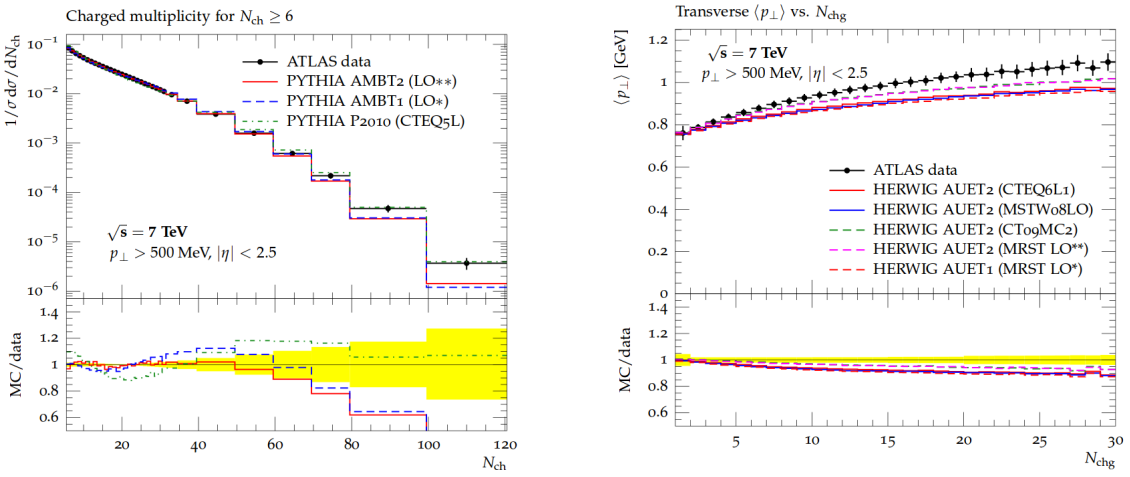

(a) (b)

Figure 4.2: Comparison between different Monte Carlo tunes for the PYTHIA (a) and HERWIG (b) event generators. The distributions produced with the AMBT1 tune still show slight inaccuracies in the description of the data [87].

The tag jet must be matched to a trigger region of interest (RoI) for the relevant L1 trigger:

- This is done in order to minimize a possible bias of the trigger decision on the properties of the probe jet. In this manner, pairs with RoIs not pointing in the direction of the tag jet are removed. For the data from periods G-I, the relevant L1 trigger to which the tag jet is matched is the one which initiates the trigger chain of the EF trigger

No further cuts are applied to the probe jets, allowing a comprehensive and unbiased spectrum of test objects to be obtained and subjected to the tau identification.

A summary of the applied cuts and the associated cut flow can be found in table 4.4. A comparison between data and the Monte Carlo prediction for the distributions of some basic kinematic variables of the probe jets are shown in figures 4.4 and 4.6 for periods A-D and G-I respectively. Comparisons of identification variables for these periods are shown in figures 4.5 and 4.7. The data and MC show overall good agreement within statistical uncertainties, indicating that the data is well understood up to this point in the selection. However, discrepancies can be observed in the distribution of the number of tracks associated to the tau candidate, which show a clear shift to fewer tracks in data. This might be explained by remaining inaccuracies of the used Monte Carlo tune (see figure 4.2) which are still present at this early stage of data taking. Deviations are also found in the extreme tails of the distributions of the track and cluster masses. In the regions relevant for the discrimination between tau and jet, which is typically below 10 GeV, however, the agreement is reasonable. Nevertheless, it should be stated again that the measurement method does not rely on the quality of the Monte Carlo description at this point.

To produce these comparisons, an extra constraint was placed on both the data and MC, limiting the number of primary vertices per event to exactly one. This is due to the fact that the data and MC do not have the same number of pileup interactions per event on average. Single triggers (L1_J10 and EF_j95_jetNoEF) were used for these comparisons, to avoid complications due to prescale weighting.

One can see that the spectrum of the tag jets is shifted to slightly higher transverse momenta with respect to the probe jets. This is due to the matching of the tag jets to the objects which caused the trigger to fire, which are usually amongst the highest energetic objects in the event. For the same

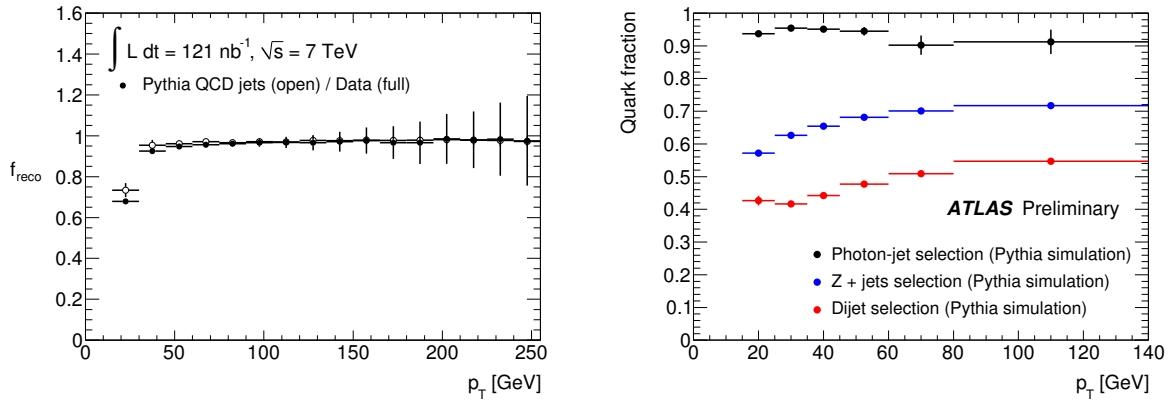

(a) (b)

Figure 4.3: Reconstruction fake rate f_{reco} of the tau candidates matched to a probe jet in dependence of the probe jet transverse momentum p_{T} as defined in equation 4.2. For the most part in the considered range nearly every probe jet is also reconstructed as a tau candidate (a). Fraction of quark initiated jets as a function of the p_{T} of the probe τ candidates as determined from Monte Carlo simulation for the photon+jet, the Z+jets and the di-jet selection (b). The errors shown are statistical only.

reason, the η spectrum of the tag jets shows characteristic inefficiencies since the jet energy is often not fully reconstructed in the transition region. The distributions of the transverse momenta also show the reduced trigger efficiency for objects which energies are close to the trigger threshold.

4.3.2 Fake rate definitions

The final step is to determine whether a reconstructed and identified tau candidate can be matched to the probe jet. The matching criterion requires the direction of the tau candidate to lie within a cone of $\Delta R < 0.2$ around the jet direction. We restrict ourselves to tau candidates which are reconstructed by both the calorimetry-based and track-based algorithm or the calorimetry-based algorithm only. In addition, every tau candidate must have a transverse energy $E_{\text{T}} \geq 15$ GeV and at least one associated track, in agreement with [68]. The reconstruction fake rate, f_{reco}, for tau candidates is defined as

$$f_{\text{reco}} = \frac{\text{\# probe jets reconstructed as } \tau}{\text{\# probe jets}}. \tag{4.2}$$

There are three different tau identification methods available: cut-based [85], likelihood [88], and boosted decision tree [89]. The cut-based ID method uses optimized cuts on a set of discriminating variables which are already well understood at an early stage of data taking. The likelihood and BDT methods are multivariate approaches, offering better discrimination, which can be applied once the data is better understood. In this context, the full tau fake rate, f, is then defined for each ID method as (see also [85]).

$$f = \frac{\text{\# probe jets identified as } \tau}{\text{\# probe jets}}. \tag{4.3}$$

One can see in Figure 4.3, that for most of the considered p_{T} range, almost every probe jet is reconstructed as a tau candidate.

Consequently, we define an identification fake rate, f_{ID}, which is independent of the reconstruction

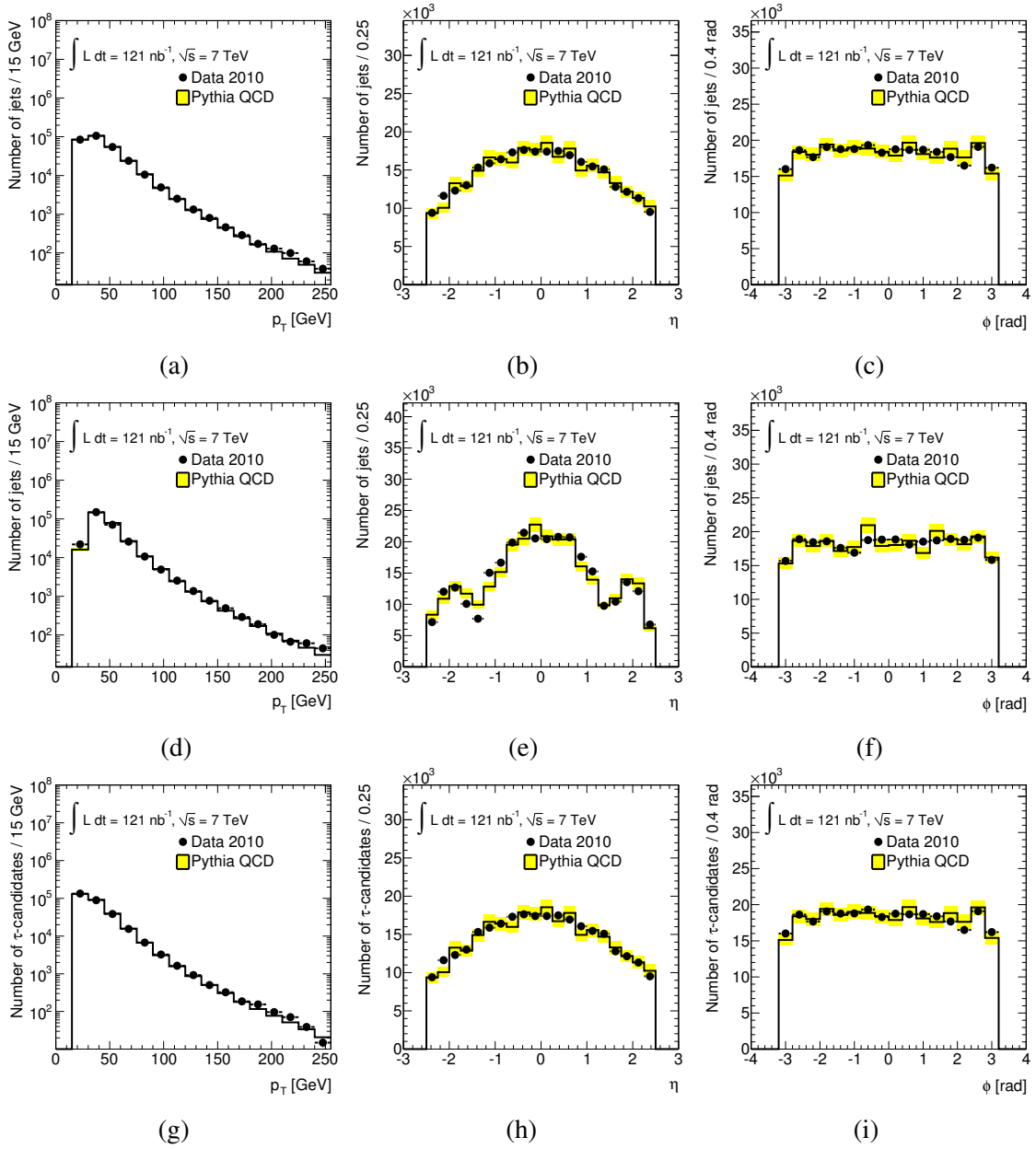

Figure 4.4: For L1_J10: top row: basic kinematic quantities of the probe jets: transverse momentum p_{T} (a), pseudorapidity η (b) and azimuthal angle ϕ (c), middle row: basic kinematic quantities of the tag jets: transverse momentum p_{T} (d), pseudorapidity η (e) and azimuthal angle ϕ (f), bottom row: basic kinematic quantities of the reconstructed tau candidates matched to the probe jets: transverse energy E_{T} (g), pseudorapidity η (h) and azimuthal angle ϕ (i).

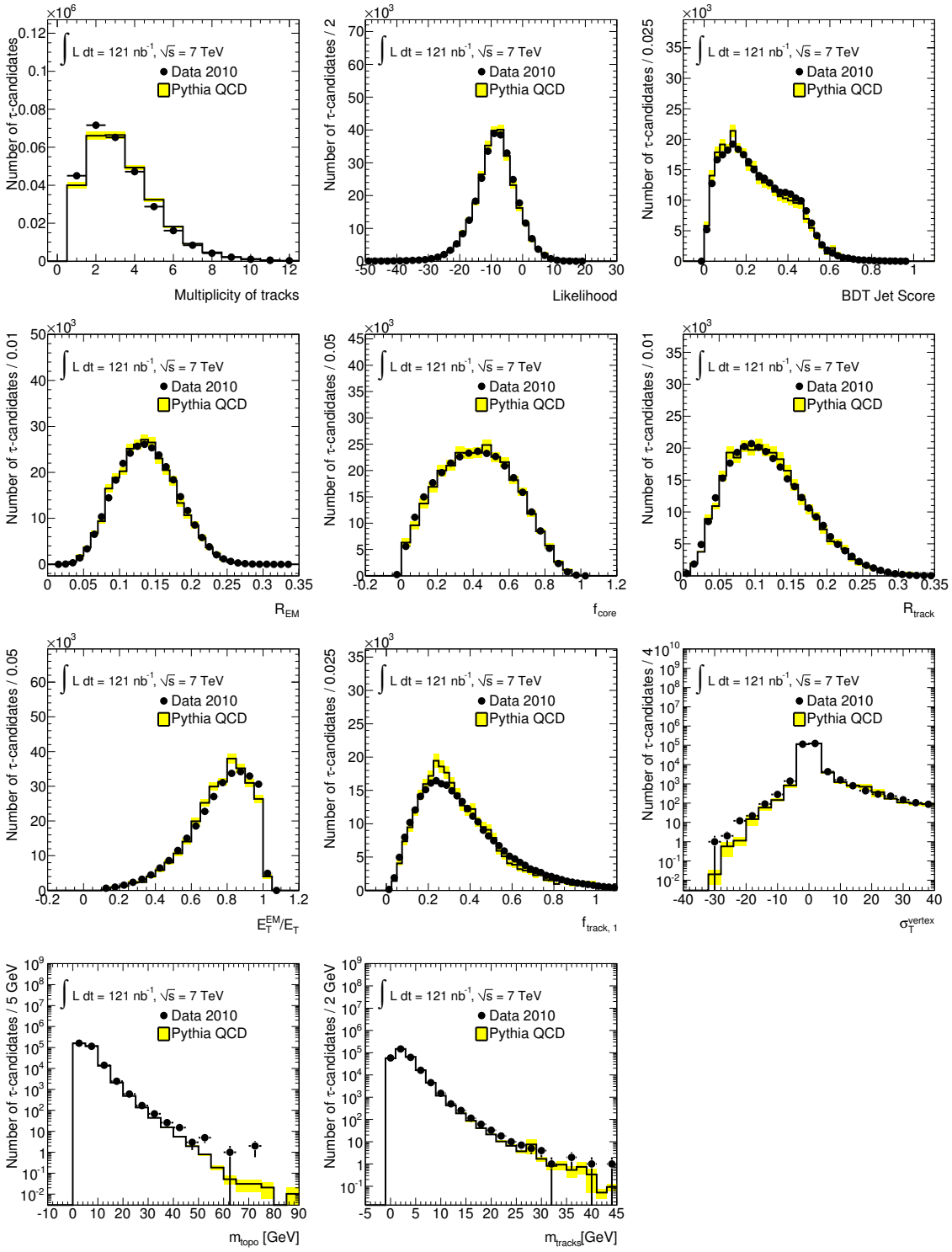

Figure 4.5: For periods A-D: identification variables for the reconstructed tau candidates matched to the probe jet. From top to bottom: number of associated tracks, likelihood, BDT jet score, electromagnetic radius R_{EM}, centrality fraction f_{core}, track average distance R_{track}, longitudinal fraction of the electromagnetic energy $E_{\mathrm{T}}^{\mathrm{EM}}/E_{\mathrm{T}}$, fraction of the leading track p_{T} to E_{T}, $f_{\mathrm{track,1}}$, flight path significance of the tracks $\sigma_{\mathrm{T}}^{\mathrm{vertex}}$, invariant cluster mass m_{topo} and invariant track mass m_{tracks}.

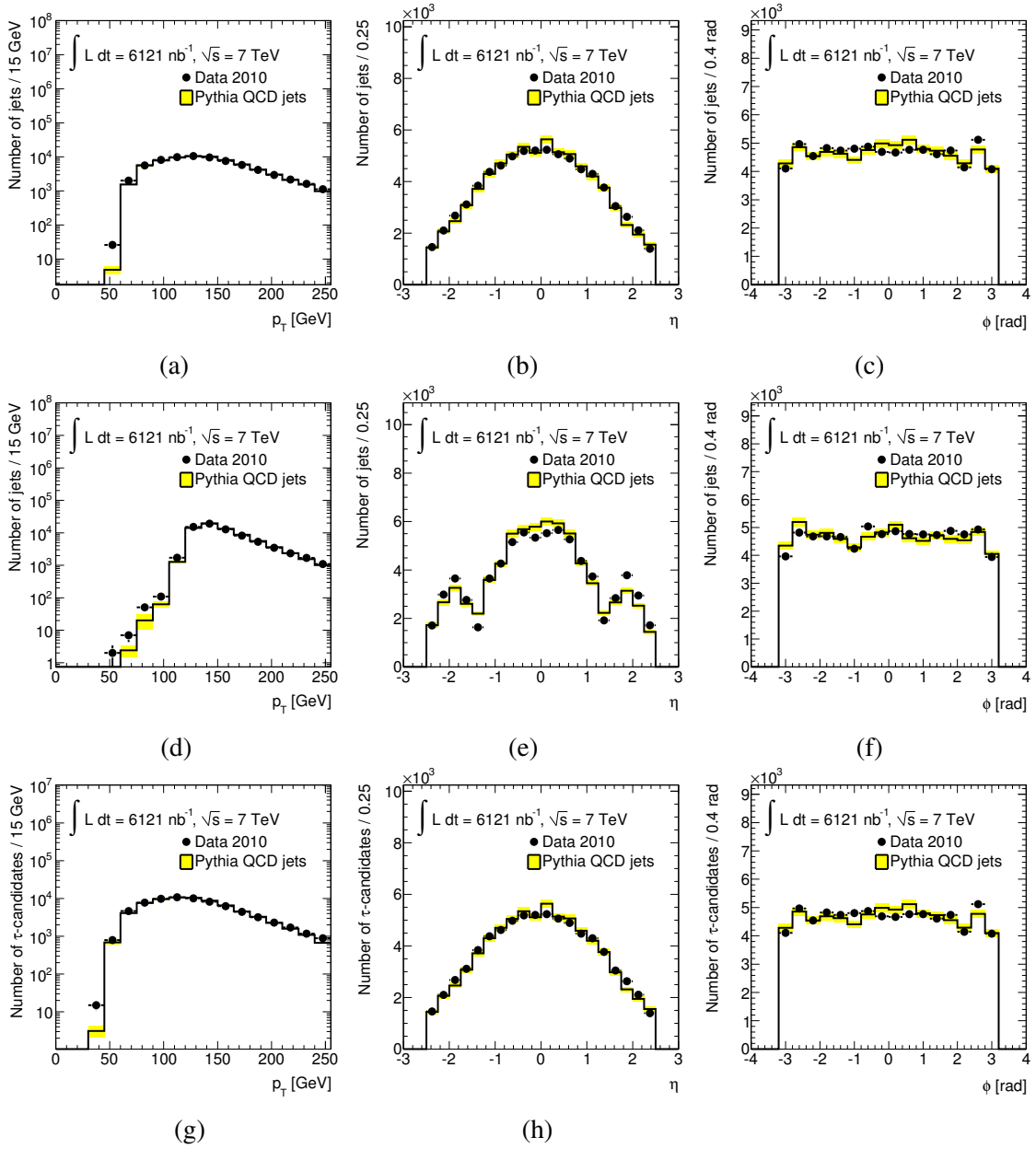

Figure 4.6: For periods G-I, EF_j95_jetNoEF: top row: basic kinematic quantities of the probe jets: transverse momentum p_{T} (a), pseudorapidity η (b) and azimuthal angle ϕ (c), middle row: basic kinematic quantities of the tag jets: transverse momentum p_{T} (d), pseudorapidity η (e) and azimuthal angle ϕ (f), bottom row: basic kinematic quantities of the reconstructed tau candidates matched to the probe jets: transverse momentum p_{T} (g), pseudorapidity η (h) and azimuthal angle ϕ (i).

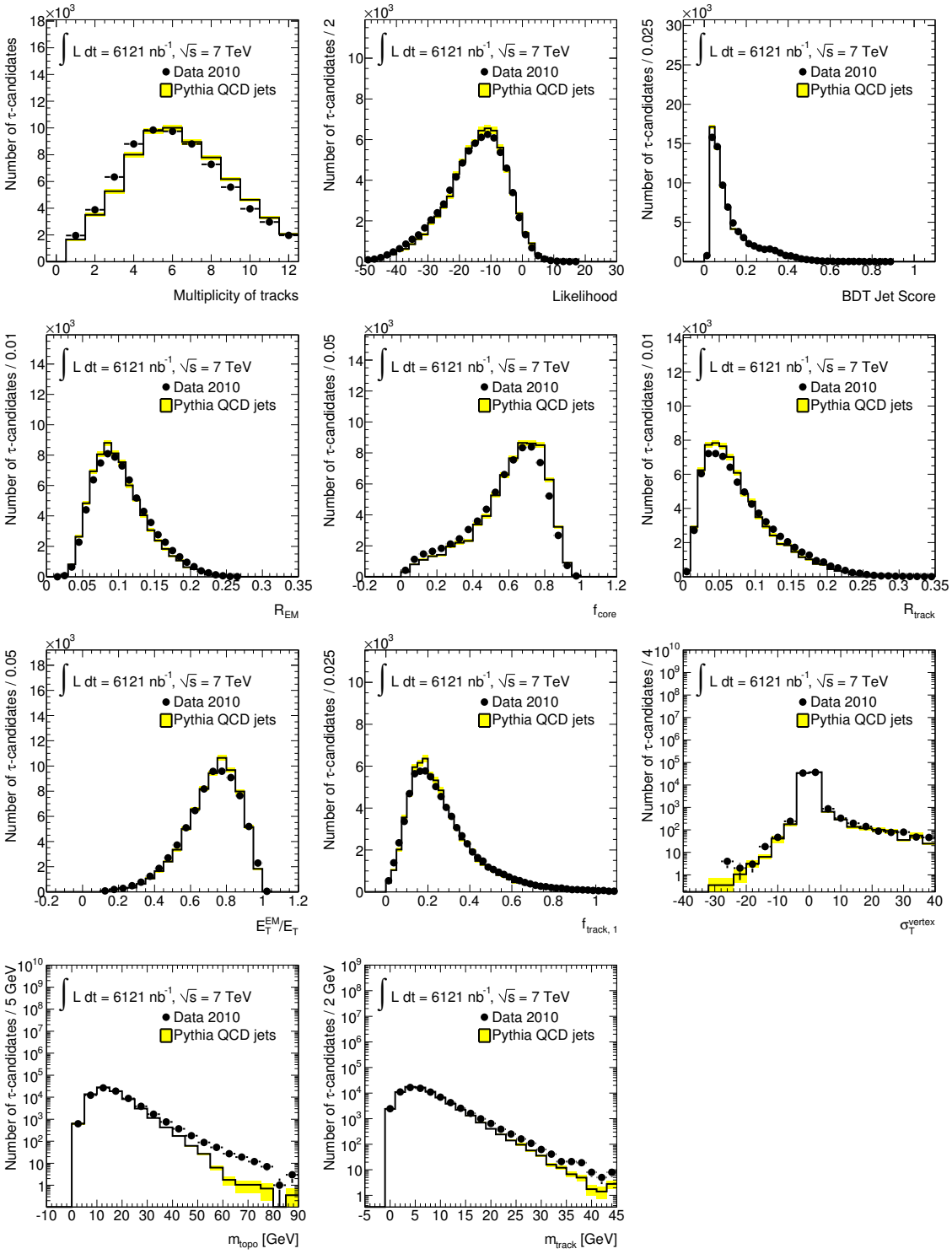

Figure 4.7: For periods G-I, EF_j95_jetNoEF: identification variables for the reconstructed tau candidates matched to the probe jet. From top to bottom: number of associated tracks, likelihood, BDT jet score, electromagnetic radius R_{EM}, centrality fraction f_{core}, track average distance R_{track}, longitudinal fraction of the electromagnetic energy $E_{\mathrm{T}}^{\mathrm{EM}}/E_{\mathrm{T}}$, fraction of the leading track p_{T} to E_{T}, $f_{\mathrm{track,1}}$, flight path significance of the tracks $\sigma_{\mathrm{T}}^{\mathrm{vertex}}$, invariant cluster mass m_{topo} and invariant track mass m_{tracks}.

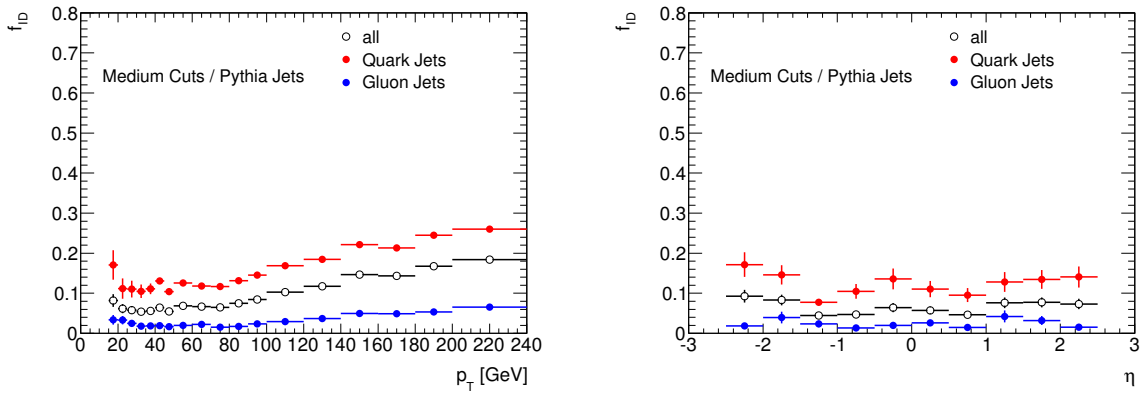

(a) (b)

Figure 4.8: Comparison of the identification fake rate from MC between jets whose leading parton has been identified via truth information as a quark, and those whose leading parton has been identified as a gluon, as a function of jet p_{T} (a) and η (b). The L1_J10 trigger was used, with 1 vertex per event.

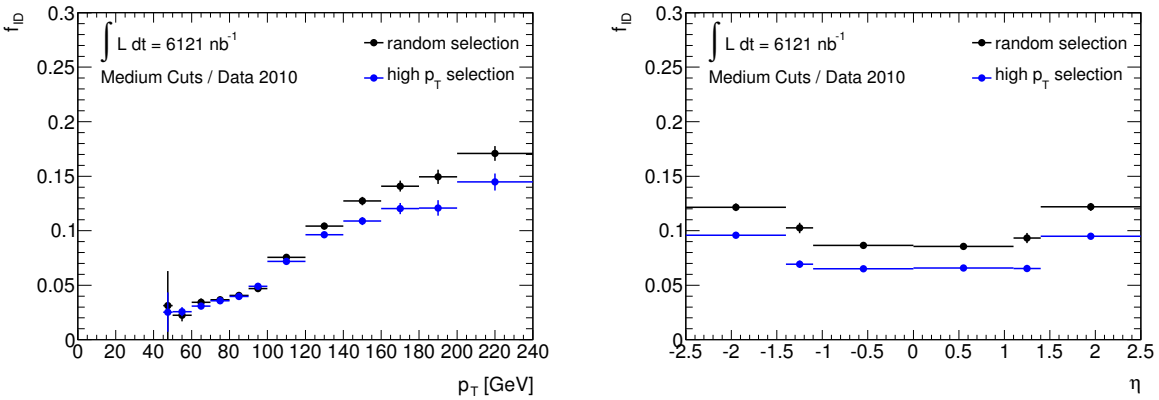

(a) (b)

Figure 4.9: Influence of the selection of the tag jet on the identification fake rate for the simple cuts method with a medium selection as a function of p_{T} (a) and as a function of η (b) of the tau candidates matching to the probe jets. Period G-I data, with EF_j95_jetNoEF trigger and 1 vertex per event.

fake rate, and consistent with other studies [68]:

$$f_{\mathrm{ID}} = \frac{\#\text{ probe jets identified as } \tau}{\#\text{ probe jets reconstructed as } \tau}. \tag{4.4}$$

4.3.3 Quark-to-gluon ratio

Following the di-jet selection applied, the probe jet sample consists of a mixture of quark and gluon jets. Due to their different properties, quark and gluon jets will have very different fake rates, as shown exemplary for MC in figure 4.8. Jets originating from gluons are less likely to fake a tau, since they are usually wider and have a higher track multiplicity which results in overall lower fake rates. Factors affecting the fraction of these two types of jet have been investigated.

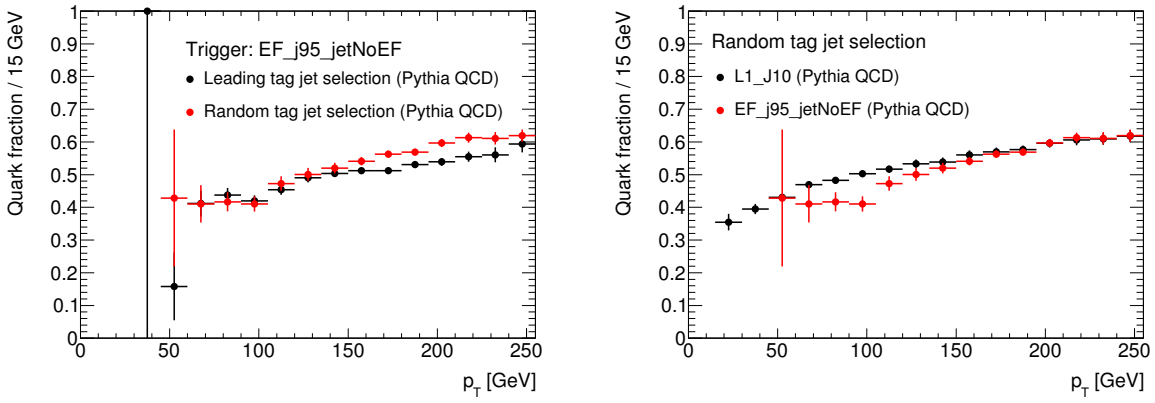

(a) (b)

Figure 4.10: Quark jet fraction from MC truth information in dependence of the probe jet transverse momentum p_{T}, comparing the high p_{T} and random tag jet selection for EF_j95_jetNoEF trigger and 1 vertex per event (a), and comparing L1_J10 and EF_j95_jetNoEF with 1 vertex per event (b).

Tag jet selection effects

As described previously, one of the jets in the pair is chosen randomly to be the tag jet. By instead choosing the higher p_{T} jet as the tag, additional statistics can be gained due to the fact that a higher p_{T} jet is more likely to pass the trigger matching cut. Figures 4.9 (a) & (b) show the effect on the fake rate as a function of tau E_{T} and η if the higher p_{T} jet in the pair is selected as the tag jet. It can be seen that this results in a lower fake rate than for the case where the tag jet is chosen randomly. The reason for this can be understood by looking at the truth information for the MC jets shown in figure 4.10 (a). For the case where the higher p_{T} jet is used as the tag, the fraction of quark jets is reduced compared to using a random tag jet. Consequently, in order to avoid biasing the quark jet fraction in the probe jet sample unnecessarily, the random tag jet selection was used.

4.3.4 Trigger effects

The use of high-threshold triggers can affect the probe jet sample in p_{T} bins below the trigger threshold. This is due to an increase in events where the tag p_{T} significantly exceeds that of the probe, which can affect the quark-gluon fraction and the reconstruction quality of the probe jets. Differences can be observed in figures 4.11 (a), (c) and (e) between the L1_J10 and EF_j95_jetNoEF in the low p_{T} region below the EF_j95_jetNoEF threshold region. The figures show the fake rates for the three ID methods (Safe Cuts, Likelihood, and BDT) respectively. Good agreement between the data and MC can also be observed. As in figures 4.4 - 4.7, both data and MC are limited to exactly one vertex per event to simplify the comparison. Figure 4.10 (b) shows the fraction of quark jets obtained from the MC truth information as a function of jet p_{T} for the L1_J10 and EF_j95_jetNoEF triggers, which also exhibits a difference below the EF_j95_jetNoEF threshold region. While these effects could in principle be reduced by introducing a tighter p_{T} balance cut, this would limit the applicability of the results. A reasonably wide p_{T} balance range is deliberately chosen in order to not constrain the probe sample to a specific jet composition. A p_{T} balance systematic, discussed in section 4.4.3, is included in the overall systematic uncertainties, in order that these effects are accounted for in our final results.

By using the two trigger OR conditions described in section 4.3, we ensure that data both from the L1 periods (A-E, early) and EF periods (G-I, late) contain probe jets both above and below trigger threshold

Cut	$W \rightarrow \tau\nu$	$Z \rightarrow \tau\tau$
No cut on num. tracks	9.45%	24.93%
$\geq$ 4 tracks	4.86%	7.87%
$\geq$ 4 tracks + 1/50 GeV	4.83%	7.80%
$\geq$ 4 tracks + 1/10 GeV	4.79%	7.68%
$\geq$ 5 tracks	3.51%	5.03%
$\geq$ 6 tracks	2.16%	2.90%
$\geq$ 7 tracks	1.11%	1.71%
$\geq$ 8 tracks	0.60%	1.00%

Table 4.5: Percentage of events surviving various requirements on the number of tracks of the tag jet starting with a simulated sample of $W \rightarrow \tau\nu$ and $Z \rightarrow \tau\tau$ events, respectively. Requiring four or more tracks significantly improves the rejection of true tau events. However, starting with a higher minimal number of tracks would cut away many of the QCD jets while not contributing as much in addition to the true tau rejection.

regions. Figures 4.11 (a), (c) and (e) show the good agreement in fake rates between the early and late periods for the three ID methods using these trigger configurations. Using only a single trigger with the same threshold for both the L1 and EF (such as L1_J30 and EF_30_jetNoEF) periods is statistically prohibitive, and so this approach is not feasible.

4.4 Systematics

This section covers the estimation of the systematic error on the fake rate measurement. For once, the fake rates are altered systematically if the probe sample is polluted by objects other than jets. Secondly, since the properties of the tag jets directly influence the composition of the probe jets, the variation of the fake rates for various choices of tag jet selection cuts is investigated. The effect of pile-up is taken into account by providing fake rate results dependent on the number of vertices, rather than adding to the systematic uncertainty.

4.4.1 Overlap between probe jet and tau candidate

As discussed in section 4.3.2, a reconstructed tau is matched to a probe jet, if the direction of the tau candidate lies within a cone of $\Delta R < 0.2$ around the jet direction. In the current reconstruction, the tau direction is defined by the direction of its calorimeter seed and thus is equal to the direction of the corresponding jet. Variations in ΔR therefore have no influence on this analysis.

4.4.2 True tau pollution of the probe jet sample

One of the most obvious systematic errors would be the presence of true taus in the selected sample. In order to estimate the number of true taus passing the selection, the analysis was run over samples of simulated $W \rightarrow \tau\nu$ and $Z \rightarrow \tau\tau$ events. As discussed in section 4.3, the number of associated tracks can be used to discriminate between QCD jets and true taus. The effect of varying the number of required tracks can be seen in table 4.4.

Requiring the tag jet to have at least 4 tracks associated significantly improves the rejection of true taus. Given these results, and the cross section ratio of $\sim 1/10^3$ between QCD jets and true taus, the pollution of the selected sample by true taus is expected to be negligible.

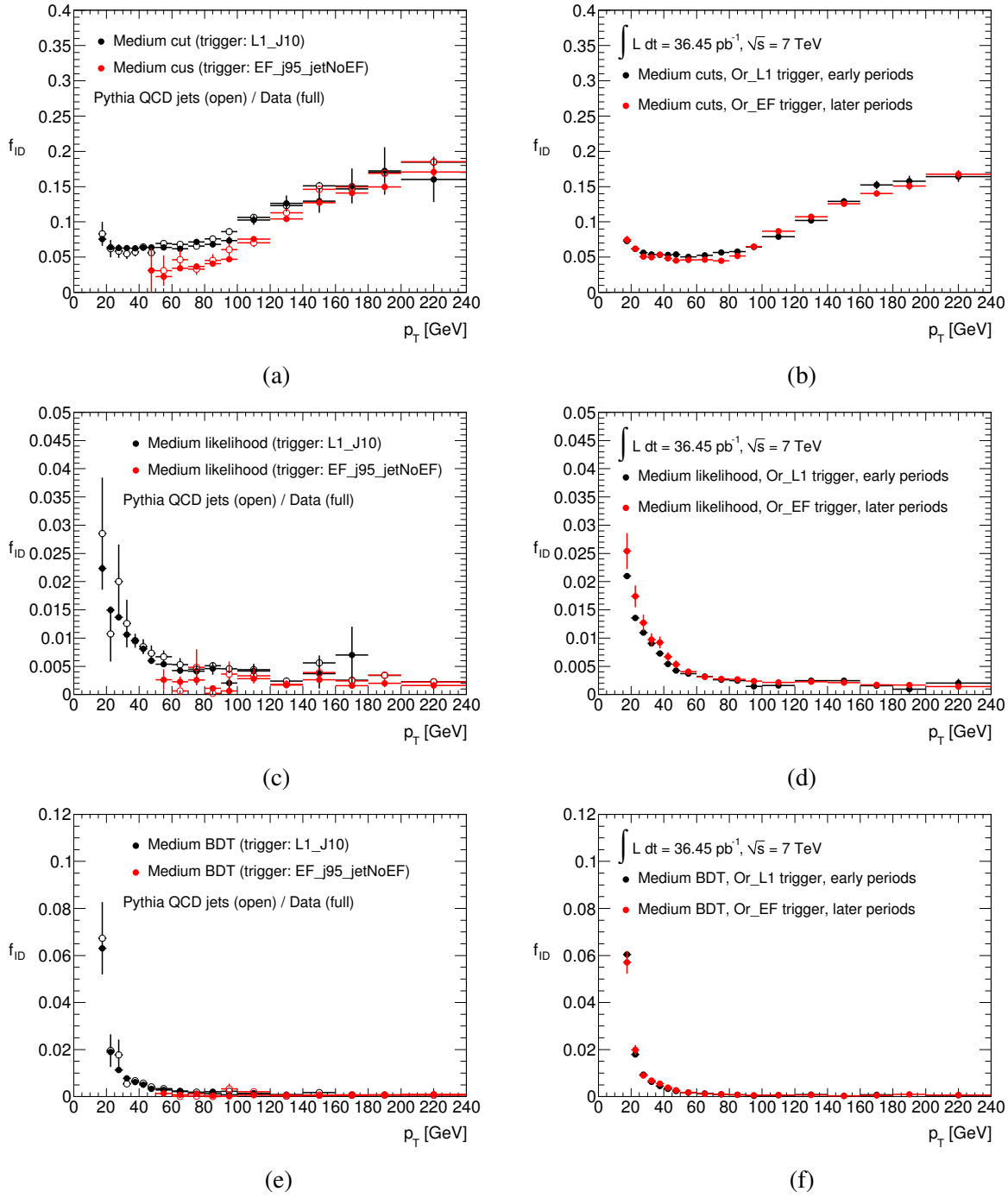

Figure 4.11: ID fake rates f_{ID} for periods A-F and for periods G-I as a function of the transverse momentum p_{T} of the tau candidates matched to the probe jets for the simple cut method (top row), the likelihood method (middle row) and the BDT method (bottom row). Differences between the fake rates occur if the events were selected with separate individual triggers for the early and later periods (left column). These trigger effects can be reduced by requiring a combined L1 trigger for periods A-F and a combined EF trigger for periods G-I. Good agreement between the fake rates for the two trigger setups can be observed (right column). The clean trigger structure, however, simplifies the comparison between data and the Monte Carlo prediction which turns out to be good within the uncertainties in both cases.

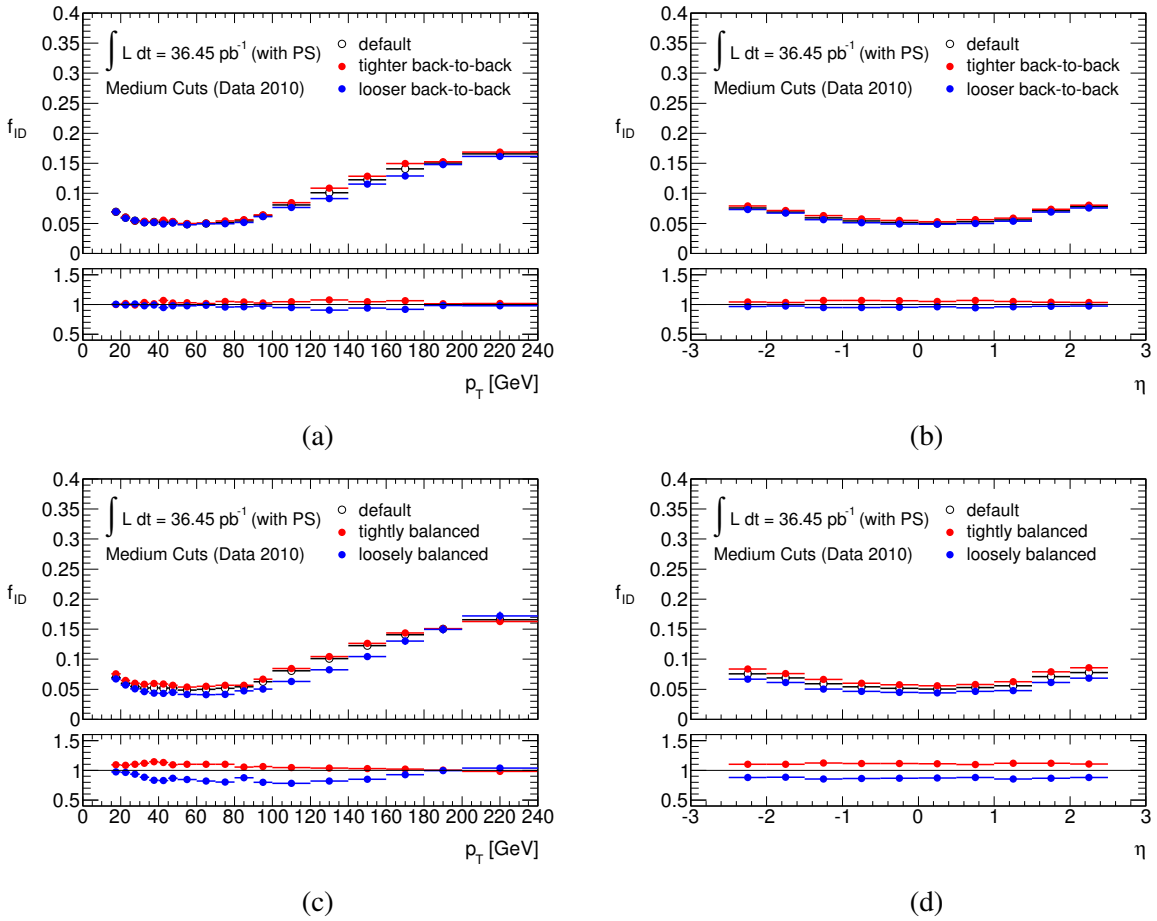

Figure 4.12: Comparison between the default sample, the sample which fulfills the looser cut requirement and the sample which fulfills the tighter cut requirement for the simple cuts method with a medium selection in the di-jet method. Identification fake rate and relative variance as a function of tau p_{T} and η for the back-to-back cut ((a) and (b)) and for the p_{T} balance cut ((c) and (d)).

4.4.3 Uncertainties from tag jet selection cuts

As discussed in section 4.3, the di-jet selection requires that the two jets are back-to-back and balanced in p_{T}. These cuts are allowed to vary within a tolerance of 10% for the back-to-back criterion and 50% for the transverse momentum requirement, respectively. The variation of the fake rates resulting from a variation of the cuts within their tolerances is taken as a systematic uncertainty. For its determination, two subsamples are created; one containing events which fulfill a tighter requirement on the variable in question, and one containing events which fulfill a looser requirement up to the maximal allowed value. The thresholds are chosen such that the subsamples contain similar numbers of events and are defined as follows:

- Back-to-back criterion:
  Looser cut: $\Delta\phi < \pi - \frac{1}{3} \cdot 0.3$
  Tighter cut: $\Delta\phi \geq \pi - \frac{1}{3} \cdot 0.3$

- Transverse momentum balance criterion:

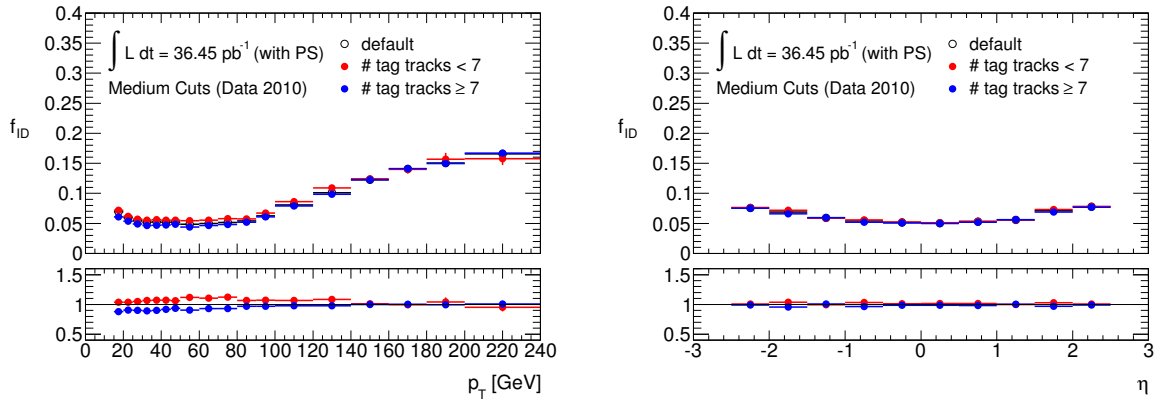

(a) (b)

Figure 4.13: Comparison between the samples with a different number of tracks for the tag jet for the simple cuts method with a medium selection in the di-jet method. Identification fake rate and relative variance as a function of tau p_{T} (a) and η (b).

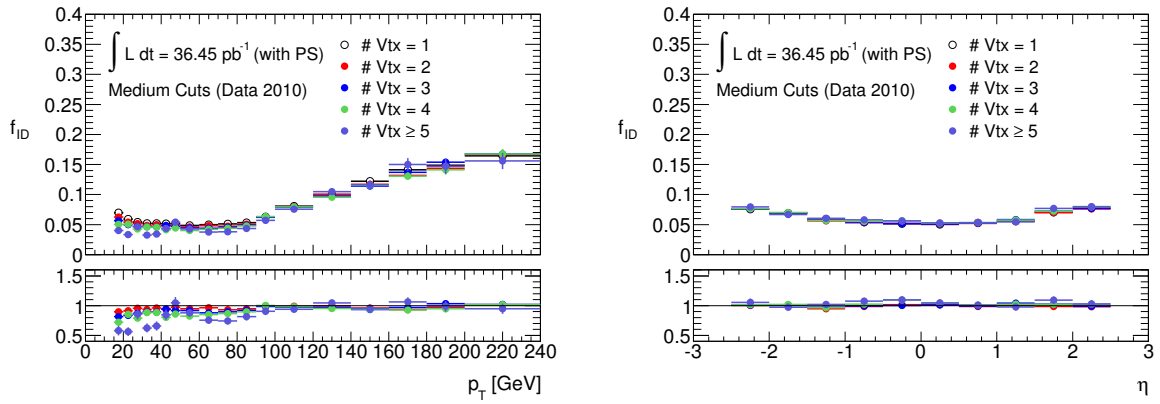

(a) (b)

Figure 4.14: Comparison between events with different numbers of pp-collisions for the simple cuts method with a medium selection. Identification fake rate and relative variance as a function of tau p_{T} (a) and η (b).

$$\text{Looser cut: } |\Delta p_{\mathrm{T}}| \geq 0.44 \cdot \frac{p_{\mathrm{T}}^{\mathrm{max}}}{2}$$
$$\text{Tighter cut: } |\Delta p_{\mathrm{T}}| < 0.44 \cdot \frac{p_{\mathrm{T}}^{\mathrm{max}}}{2}$$

The results for the di-jet study for the medium cuts identification algorithm can be seen in figure 4.12. In both cases, the fake rate for the sample with the tighter requirement is slightly higher than for the sample with the looser requirement. This can be understood, given the effects described in section 4.3.4. This suggests that well-balanced, back-to-back jets are more likely to be mis-identified as taus. Both effects are taken into account for the estimation of the total systematic uncertainty.

The required number of associated tracks for the tag jet can influence the probe jet. To study the effect of this correlation, the fake rates are compared for two subsamples, one with the tag jets to have at most 6 associated tracks and one with the tag jets to have at least 7 tracks. Again, the threshold value was chosen such that the two subsamples have comparable statistics. The results can be seen in figure

4.13. It can be observed that the fake rates are slightly higher for the sample with fewer tracks per jet, as expected. This variation is included in the estimation of the total systematic uncertainty.

4.4.4 Pile-up

Pile-up events occur when there is more than one proton-proton interaction per bunch crossing, which results in a more crowded environment with a higher jet multiplicity. The effects of pile-up will become increasingly important, as it rises with the instantaneous luminosity delivered by the LHC. To study these effects, the fake rate was calculated for events with different amounts of pile-up, by separating the events into five subsamples according the the number of reconstructed vertices with at least 4 tracks (1, 2, 3, 4 & $\geq$5 vertices). The results are shown in figure 4.14. It is clearly visible that the fake rate decreases with more proton-proton collisions per bunch crossing. This result is expected, as a more crowded environment leads to a lower fake rate due to fewer tau candidates meeting the isolation criteria of the identification algorithms. Due to this dependence, it was decided to bin the fake rate results by the number of vertices. The bins chosen are events with 1-2 vertices, and events with $\geq$3 vertices. Consequently, pile-up effects are not included in the estimate of the total systematics.

4.5 Comparison with other methods

As mentioned already in the introduction, a number of analyses applying tag-and-probe methods in order to study the jet-tau mis-identification probability exist. The topologies investigated include di-jet/three-jet events, γ+jets events, and those with additional jets in $Z \rightarrow \ell\ell$ events. When comparing the fake rate results obtained by these analyses, however, differences are found. The fake rates obtained from photon+jets events, for instance, are significantly higher than the ones obtained from di-jet events [81].

According to the remarks made in section 4.3.3, these differences are expected and attributed to the different fraction of quark-initiated jets (as opposed to gluon-initiated jets) in the topologies studied, ranging from roughly 50% for the di-jet/three-jet topology to above 90% in γ+jet topologies, based on Monte Carlo truth-level studies, as can be seen in figure 4.10.

When separating quark-initiated and gluon-initiated jets on truth-level, Monte Carlo studies indicate that good agreement of the mis-identification probabilities is observed across the different topologies studied. This is shown in figure 4.15 for quark initiated jets on the left-hand side and for gluon-initiated jets on the right-hand side. The analyses presented here suffered from the limited statistics available in the data taken in 2010, which is in part due to the large trigger prescales applied to low-E_{T} triggers during data taking. By including more data, it could be possible to parametrize the mis-identification probability of jets as tau leptons as a function of variables sensitive to the differences between quark-initiated and gluon-initiated jets in the event. More data could also allow a construction of pure quark-initiated and gluon-initiated jet mis-identification probabilities from the different channels involved.

In addition, differences between the obtained fake rates from di-jet and three-jet events occur due to different kinematics and jet isolation. Figures 4.17 (a) and (b) show for instance that the p_{T} spectra of the probe jets are shifted towards lower values for the three-jet selection. This is due to the fact that in the tree-jet selection the probe jet has a chance to originate from a radiated gluon which is less energetic than the jets of the primary pair.

The isolation of a jet can be quantified as the angular distance to its nearest neighbor. On average, the jet isolation is lower for three-jet events (see figures 4.17 (c) and (d)), indicating a more crowded environment.

Working point	Identification method	1-prong taus	3-prong taus	Electron veto
1	Safe cuts	medium	tight	tight
2	BDT	medium	tight	tight
3	Likelihood	medium	tight	tight
4	Safe cuts	loose	medium	medium
5	BDT	loose	medium	medium
6	Likelihood	loose	medium	medium
7	BDT	Jet score > 0.5	Jet score > 0.6	Electron score > 0.5
8	Safe cuts	medium	tight	Electron score > 0.5
9	Likelihood	loose	loose	medium

Table 4.6: Working points.

Eventually, the different quark-gluon composition in di-jet and three-jet events is also expressed in terms of different jet widths. As can be seen from figure 4.17 (e) and (f), the jets in the gluon enriched three-jet sample are usually wider than in the di-jet sample.

In order to check if the observed differences in the jet kinematics and isolation are indeed responsible for the differences in the fake rates, a two-dimensional reweighting in p_{T} and $\Delta R_{\text{closest jet}}$ is applied. As shown in figure 4.16, the reweighting significantly reduces the discrepancies between the ID fake rates obtained via the two methods. The remaining differences between the di-jet and three-jet results are attributed to the different quark-gluon ratio and are not considered as a systematic error on the final results.

4.6 Fake rate results

As shown in previous sections, the fake rate is dependent on p_{T}, η and the number of pile-up vertices. When using the cut-based or likelihood identification, it is found that the fake rate tends to get larger with increasing transverse momenta. This can be explained by the increasing collimation of the jet with higher energy. On the other hand, the slight rise of the fake rate for large $|\eta|$ can be explained by jets being only partly reconstructed in this region and are hence looking more like taus.

In addition, the fake rate depends on the tau decay channel. In contrast to 1-prong tau candidates, 3-prong tau candidates are less likely to be faked by a jet since these these objects provide more information that can be exploited to discriminate between tau and jet.

As a consequence, the fake rate provided for physics analyses is binned simultaneously in these variables. Results for various working points as defined in table 4.6 can be seen in figures 4.18. The systematic bands shown on the plots represent the quadratic sum of the contributions from the Δp_{T}, $\Delta\phi$ and number of tag tracks systematics.

4.7 Summary

In this analysis, estimates for the jet-tau mis-identification probability in 2010 ATLAS data have been obtained. For that, pairs of jets have been selected, which are kinematically connected by the requirement to point in opposite directions and to be balanced in p_{T}. In addition, the randomly assigned tag jet is required to have triggered the event and is ensured to be a good QCD jet by demanding at least four

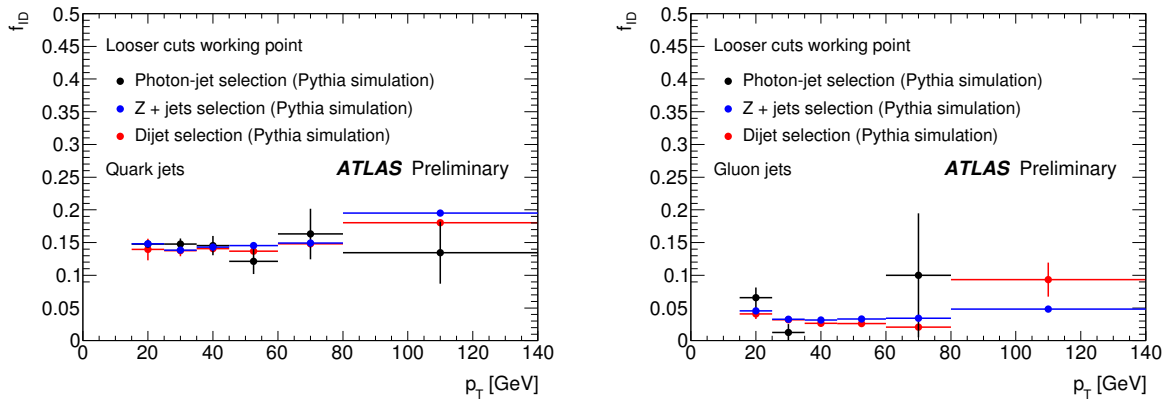

(a) (b)

Figure 4.15: Mis-identification probability, as a function of τ-lepton pt, for quark-initiated (left) and gluon-initiated (right) probe τ candidates for the looser cut-based working point, as determined from Monte Carlo simulation for the three channels presented in Section 4.1. The errors shown are statistical only.

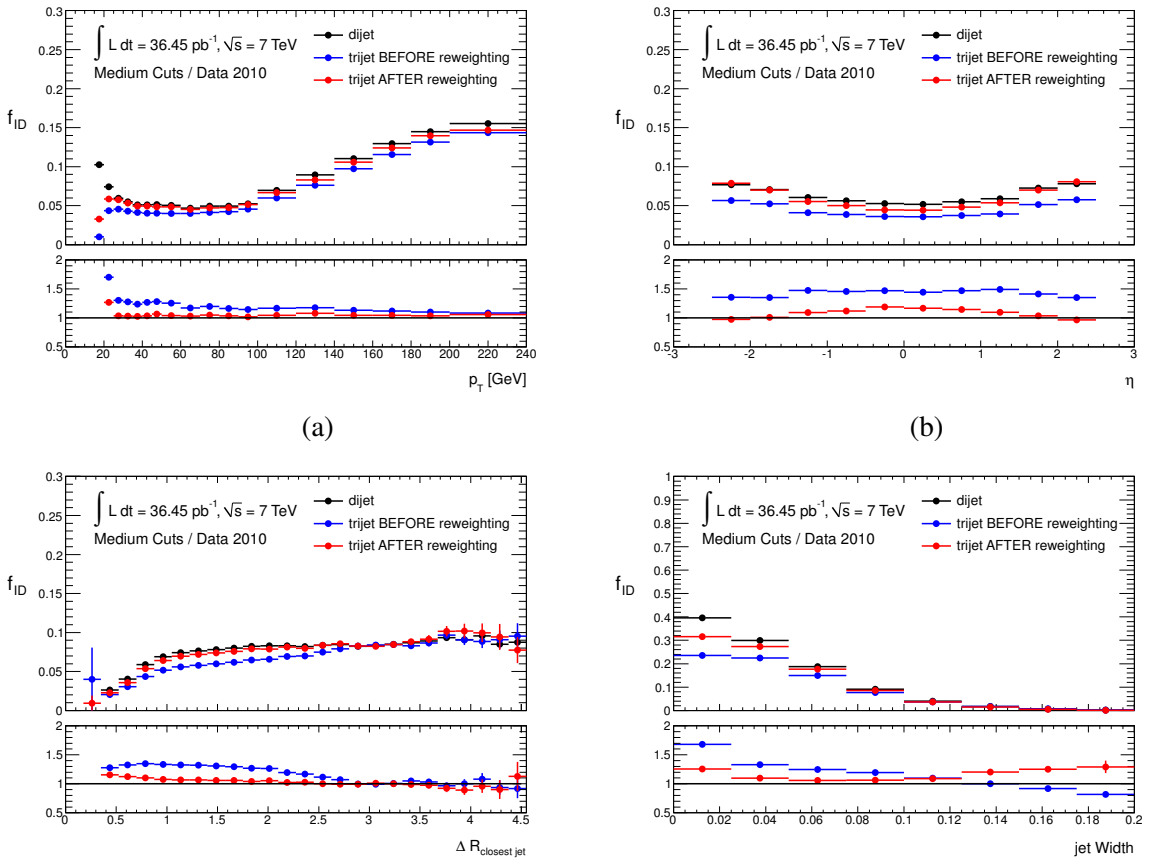

(a) (b)

(c) (d)

Figure 4.16: ID fake rates from all tau candidates for the medium safe cut method in dependence of the probe jet transverse momentum p_{T} (a), the probe jet pseudorapidity η (b), the jet isolation $\Delta R_{\mathrm{Closest\ jet}}$ (c) and the with of the probe jet (d). The result obtained from the di-jet method (black) is compared with the result from the three-jet method before any correction (blue) and p_{T} and $\Delta R_{\mathrm{closestjet}}$ correction (red).

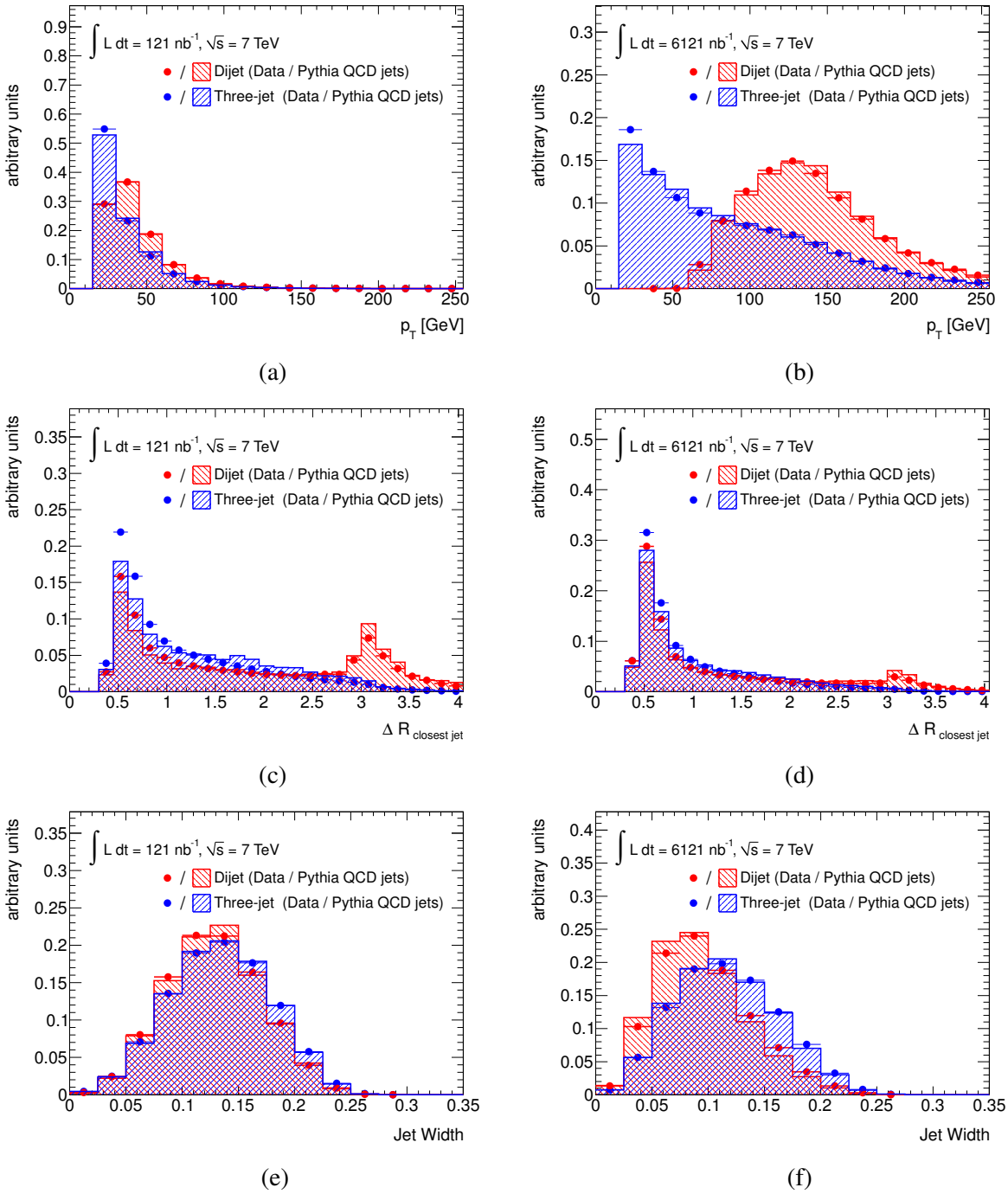

Figure 4.17: Comparison of jet kinematic quantities between the di-jet (red) and three-jet (blue) analysis for early (left) and later data taking periods (right): transverse momentum p_{T} of the probe jet (a), (b), angular distance between the probe jet and the closest jet object (c), (d) and width of the probe jet (e), (f). All distributions are normalized to unity.

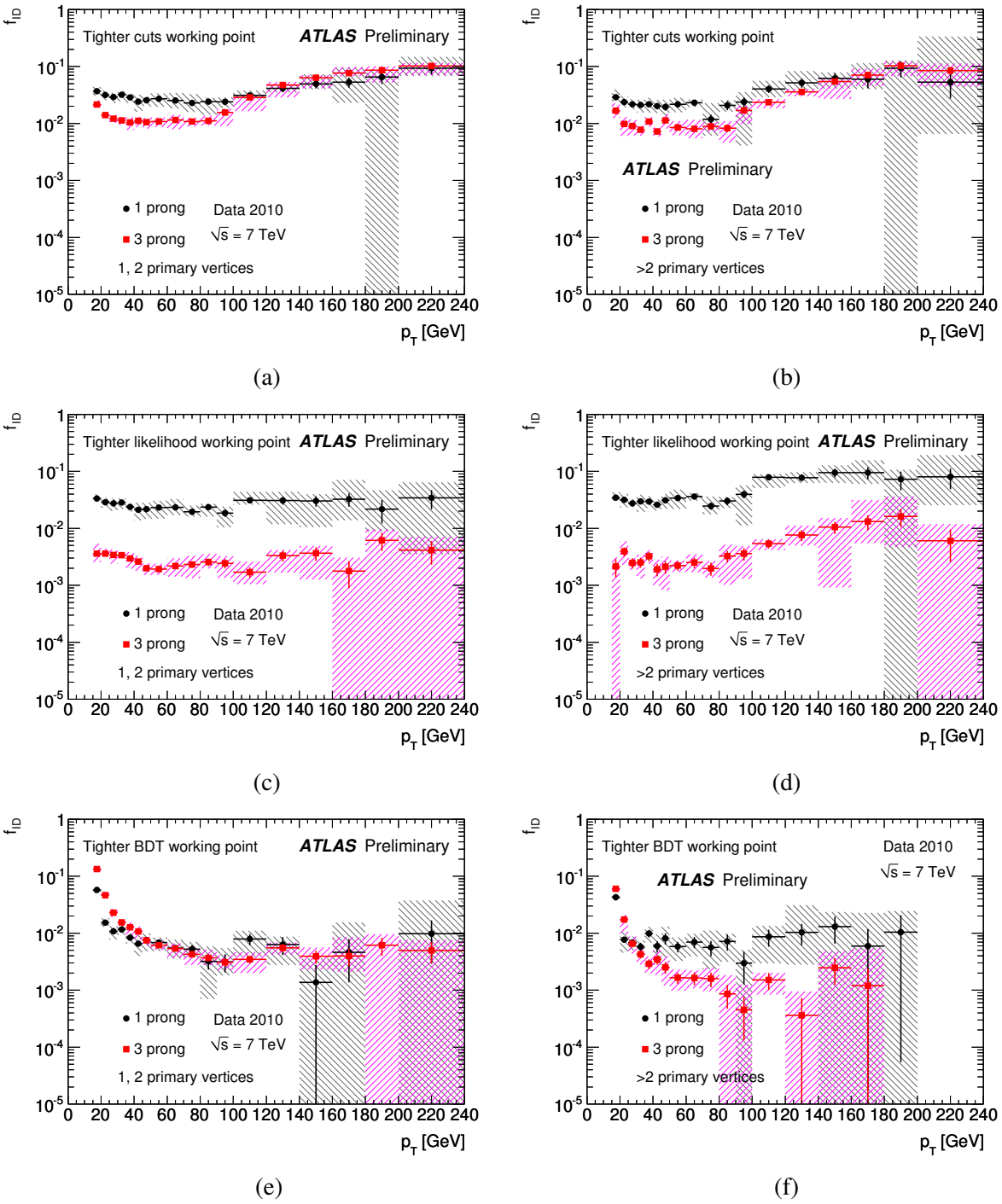

Figure 4.18: The mis-identification probability of hadronic jets from di-jet topologies as τ leptons. These are shown as a function of τ-lepton p_{T} for 1-prong and 3-prong candidates in events with one or two primary vertices (left column) and more than two primary vertices (right column) for the cut-based (top row), likelihood-based (middle row) and BDT-based (bottom row) identification algorithms. The level of the identification algorithms corresponds to the tighter working point. The statistical uncertainties are represented by the vertical bars; the shaded areas correspond to the total uncertainty. For the definition of the working points, see table 4.6.

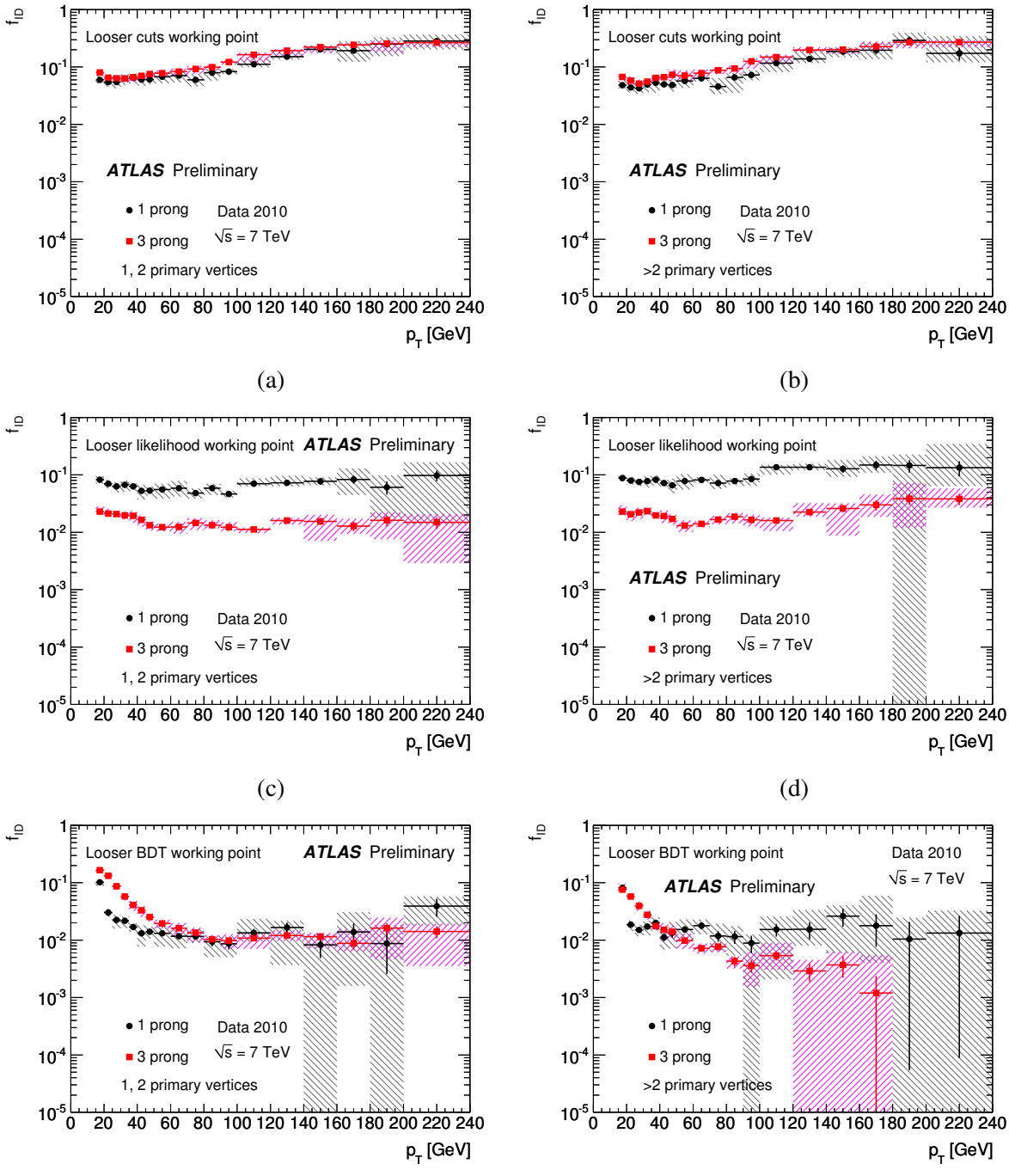

Figure 4.19: The mis-identification probability of hadronic jets from di-jet topologies as τ leptons. These are shown as a function of τ-lepton p_{T} for 1-prong and 3-prong candidates in events with one or two primary vertices (left column) and more than two primary vertices (right column) and for the cut-based (top row), likelihood-based (middle row) and BDT-based (bottom row) identification algorithms. The level of the identification algorithms corresponds to the looser working point. The statistical uncertainties are represented by the vertical bars; the shaded areas correspond to the total uncertainty. For the definition of the working points, see table 4.6.

tracks. The probe jet is then likely another good QCD jet, which is, however, not biased by any further selection. This way a clean sample of good QCD jets is obtained.

The events are triggered by a combination of Level-1 and event filter triggers since single jet triggers are usually heavily prescaled, hereby removing trigger effects at the transition between trigger eras. For individual triggers, reasonable agreement between the selected data and Monte Carlo is observed.

By subsequently subjecting the jets to tau reconstruction and identification algorithms the fake rate can then be calculated according to formula

$$f = \frac{\text{number of probe jets identified as } \tau}{\text{number of all probe jets}}.$$

Fake rates from 0.1%-10% have been obtained with errors dominated by systematics. Through binning these fake rates in appropriate variables, they offer a useful input into various analyses where the identification of taus is required. As expected, the multivariate techniques are found to usually outperform the simple cut based tau identification. No attempt has currently been made to address potential differences between the quark-gluon ratio of the probe jet samples and the expected jet composition of the samples they will be applied to. However, the di-jet fake rates can nevertheless be used where a significant gluon jet contribution is expected.

Chapter 5

A measurement of the cross section $\sigma(pp \to W) \times \mathbf{BR}(W \to \tau\nu_\tau)$

The re-establishment of the Standard Model of particle physics has been one of the most important topics of the scientific program of the LHC and its detectors in the early stages of data taking next to the search for hints of new physics. As far as tau leptons are concerned, the dominating Standard Model production processes are decays of the W and Z bosons. For once, one is interested in fundamental properties of these processes at the unprecedented collision energies reached at the LHC, such as the production cross sections. Secondly, these processes are important backgrounds for the decay of the Higgs boson into taus and decays of yet undetected heavy particles postulated by theories extending the Standard Model.

In the following chapter, a measurement of the total proton-proton production cross section

$$\sigma^{\text{tot}}_{W\to\tau_{\text{h}}\nu_\tau} \equiv \sigma(pp \to W) \times \text{BR}(W \to \tau\nu_\tau) \times \text{BR}(\tau \to \text{hadrons} + \nu) \tag{5.1}$$

at $\sqrt{s} = 7$ TeV with the ATLAS experiment is described. The measurement, however, can be easily extrapolated to the fully inclusive cross section $\sigma(pp \to W) \times \text{BR}(W \to \tau\nu_\tau)$ by dividing by the well measured branching ratio $\text{BR}(\tau \to \text{hadrons} + \nu)$. Section 5.1 briefly outlines the measurement method, followed by an overview on the considered data and simulation samples in section 5.2. Subsequently, the event selection and background estimation techniques are addressed in sections 5.3 - 5.4, before results are presented in sections 5.5 - 5.8. Special emphasis is placed on the determination of the systematic error arising from an imperfectly modelled trigger response.

5.1 Method

Most generally, the cross section of a certain (signal) process is defined as

$$\sigma^{\text{signal}} = \frac{N^{\text{signal}}}{L_{\text{int}}}, \tag{5.2}$$

where N^{signal} is the number of signal events present in an amount of taken data corresponding to an integrated luminosity of $L_{\text{int}} = \int L \, \text{dt}$ (see also section 1.4).

However, a real detector cannot detect the full event information due to coverage and resolution limitations, hence some of the signal events are never recognized. As a consequence, the luminosity has to be corrected by the detector acceptance A, which depends on the detector geometry and the kinematics of the signal process

$$A = \frac{N^{\text{signal}}_{\text{detected}}}{N^{\text{signal}}_{\text{all}}}. \tag{5.3}$$

Data stream	Period	Run range	Integrated luminosity $\int L\,\mathrm{dt}$ [pb^{-1}]
L1Calo/	First period	158632 - 166658	10.7
JetTauETMiss	Second period	166786 - 167844	23.6
Total			34.3

Table 5.1: Overview on the ATLAS data samples used in the analysis. For the computation of the quoted integrated luminosities only runs on the list of good quality runs are considered. The total integrated luminosity is $\int L\,\mathrm{dt}$ = 34.3 pb^{-1}. The two run periods correspond to the usage of two different triggers.

Data stream	Period	Run range	Integrated luminosity $\int L\,\mathrm{dt}$ [pb^{-1}]
L1Calo/	First period	158632 - 166658	10.7
JetTauETMiss	Second period	166786 - 167844	5.6
Total			16.3

Table 5.2: Overview on the ATLAS data samples used for the QCD background determination. The looser of the two tau triggers has been used for both periods resulting in a total integrated luminosity of $\int L\,\mathrm{dt}$ = 16.3 pb^{-1}.

The region of acceptance is also known as the fiducial region. Strictly speaking, the cross section can only be measured in the fiducial region and has to be extrapolated to the full cross section with the help of the acceptance.

The number of signal events is usually defined as the difference between the number of observed events and the number of events resulting from all known background processes $N_{\mathrm{obs}} - N_{\mathrm{bkg}}$. In order not to suffer from large systematic uncertainties, one commonly tries to enhance the signal-to-background ratio by cutting away uninteresting events. Naturally, if in the course of this process signal events are removed as well, the luminosity has to be further corrected by a factor

$$C = \frac{N^{\mathrm{signal}}_{\mathrm{detected,\ after\ cuts}}}{N^{\mathrm{signal}}_{\mathrm{detected,\ before\ cuts}}}, \tag{5.4}$$

corresponding to the signal efficiency, which depends on the actual event selection, the efficiencies of the particle identification algorithms, the used background estimation techniques, etc.

To conclude, the cross section is defined as

$$\sigma^{\mathrm{tot}}_{W\to\tau_{\mathrm{h}}\nu_\tau} = \frac{N_{\mathrm{obs}} - N_{\mathrm{bkg}}}{A_{W\to\tau_{\mathrm{h}}\nu_\tau} C_{W\to\tau_{\mathrm{h}}\nu_\tau} L_{\mathrm{int}}}. \tag{5.5}$$

The measurement strategy now consists of optimizing the signal-to-background ratio with the help of suitable cuts, precisely estimating the amount of remaining background and count the number of observed events. The correction factors A and C can be obtained from simulations of the signal process.

Event generator: PYTHIA6					
Dataset ID	Simulation tag	Events	Underlying event modeling	Cross section [nb]	Sample
106043	e574_s933_s946_r1661_r1700	1.4M	AMBT1	10.46	$W \to e\nu_e$
106044	e574_s933_s946_r1659_r1700	1.4M	AMBT1	10.46	$W \to \mu\nu_\mu$
107054	e574_s934_s946_r1660_r2040	1M	AMBT1	10.46	$W \to \tau\nu_\tau$
106046	e574_s933_s946_r1661_r1700	1M	AMBT1	0.99	$Z \to ee$
106047	e574_s933_s946_r1659_r1700	1M	AMBT1	0.99	$Z \to \mu\mu$
106052	e574_s934_s946_r1660_r2040	1M	AMBT1	0.99	$Z \to \tau\tau$
105010	e574_s934_s946_r1833_r1700	1.4 M	AMBT1	6.78×10^8	J1
105011	e574_s934_s946_r1833_r1700	2.8 M	AMBT1	4.10×10^7	J2
105012	e574_s934_s946_r1833_r1700	2.5 M	AMBT1	2.20×10^6	J3
105013	e574_s934_s946_r1833_r1700	2.8 M	AMBT1	8.78×10^4	J4
107419	e618_s934_s946_r1660_r2040	500k	Perugia2010	10.46	$W \to \tau\nu_\tau$
107418	e618_s934_s946_r1660_r2040	500k	Perugia2010	0.99	$Z \to \tau\tau$

Table 5.3: Overview on the PYTHIA Monte Carlo datasets used in the analysis. Next to the signal process $W \to \tau\nu_\tau$, the list consists of the most important non-QCD background processes such as other W and Z decays. For checks of the systematic uncertainty due to a specific tuning of the event generator, the processes $W \to \tau\nu_\tau$ and $Z \to \tau\tau$ are used with an alternative underlying event modelling (Perugia2010). QCD samples (J1 - J4) are used for preliminary studies only. For the measurement, the QCD background is determined from data as described in section 5.4.2.

5.2 Data and simulation samples

This analysis also uses basically the full dataset recorded by ATLAS in the year 2010. In contrast to the analysis described in the previous chapter, the very first runs of this period (runs 152166 to 158582) are not considered here, since triggers on event filter level (EF) were still not activated. In addition, the data is required to fulfill slightly tighter quality criteria. The total integrated luminosity being considered corresponds to $\int L\,\mathrm{dt} = 34.3\,\mathrm{pb}^{-1}$ calculated with official tools [76] using the `OflLumi-7TeV-003` luminosity calibration [77], [90], [91].

5.2.1 Data samples

An overview on the used data samples can be found in table 5.1. A more detailed list of the various run periods of ATLAS data taking in 2010 is compiled in table 4.2. Again, D3PD ntuples are produced from the recorded AOD data files using `TauD3PDMaker` version 01-00-01-01. The data samples have been divided into two periods corresponding to the usage of two different triggers, which are described in section 5.3. The requirement of a second, tighter trigger has become necessary because the looser trigger was prescaled during later runs.

As will be explained later, the QCD background is estimated directly from data. Here, the looser tau trigger has been used for both periods resulting in a total integrated luminosity of $\int L\,\mathrm{dt} = 16.3\,\mathrm{pb}^{-1}$ (see also table 5.2).

Event generator: MC@NLO					
Dataset ID	Simulation tag	Events	Underlying Event Modelling	Cross section [nb]	Sample
105200	e598_s933_s946_r1659_r1700	200k	AMBT1	0.144×0.556	$t\bar{t}$ leptonic
105204	e598_s933_s946_r1659_r1700	30k	AMBT1	0.144×0.444	$t\bar{t}$ hadronic

Table 5.4: Overview on the MC@NLO Monte Carlo datasets used in the analysis. Leptonic and hadronic decaying $t\bar{t}$ events are added to list of non-QCD backgrounds.

5.2.2 Simulation samples

The measured data is compared with simulated Monte Carlo events of proton-proton collisions at a center-of-mass energy of $\sqrt{s} = 7$ TeV generated using PYTHIA [78] and MC@NLO [92] with the ATLAS AMBT1 tune [79] (see also the remarks made in section 4.3.1). Just as in the analysis described in the previous chapter, the simulation of the detector response is done with the ATLAS simulation framework [80]. In all samples the tau decays are modelled with the TAUOLA [93] package and all generators are interfaced to PHOTOS [94] to simulate the effect of final state QED radiation. Next to the signal process $W \to \tau\nu_\tau$, the samples incorporate the most important non-QCD background processes such as $t\bar{t}$, Z and the other W decays. The QCD background is estimated using a data-driven technique which is described in section 5.4.2. Again, in-time pile-up is added to all samples with an average number of vertices of $\langle n \rangle = 2$. Since the distribution of vertices in the simulated samples is not exactly identical to those found in (good quality) data, the Monte Carlo events are reweighted to exactly match the conditions in the measurements. Weights are computed separately for each Monte Carlo sample for events passing the trigger and cleaning cuts. An overview on the used sample types, their corresponding cross sections and the generated statistics can be found in tables 5.3 and 5.4.

The $W \to \tau\nu_\tau$ sample comprises all tau decays inclusively. Because of the fact that only hadronically decaying taus are considered as signal and the leptonically decaying taus are considered as background the sample has to be split beforehand. For that, the truth information of the simulated events has been used; an event is considered as background if a true tau produced in a W decay has a final state electron or muon in its list of child particles.

5.3 Event selection

In the following section the event selection for the analysis will be described. Similar to the procedure described in the previous chapter a number of cleaning steps are performed in advance in order to ensure good quality of the data.

- The event must be present in the Good Runs List (GRL). The GRL file used is data10_7TeV.pro05.merged_LBSUMM_taumetcalo_7TeV.xml
- The event must contain at least one reconstructed vertex, with 3 or more associated tracks
- In the same manner as already described in section 4.3, events with bad jets are removed. This is especially important since these kind of jets directly affect the accuracy of the determination of the missing transverse energy, a quantity which is crucial for this analysis as will be seen in the next section. Therefore, all jets in the event are required to fulfill the 'loose' definition for good jets according to figure A.2 in appendix A

Again, the jet cleaning is not applied to simulated events. However, since the ratio of affected data events is below 0.1% for the first period and below 0.2% for the second period, this negligible effect has not been corrected for in the course of the calculation of the simulated total integrated luminosity.

- The calorimeter of the ATLAS detector has a lower resolution in the transition region between the barrel and the end-cap calorimeters. If a jet is reconstructed in that region, the energy measurement is assumed to be biased, which affects the measurement of the total deposited energy. Since a reliable energy measurement is crucial for this analysis, events which have at least one jet with $p_{\mathrm{T}} > 20$ GeV reconstructed in the transition region are rejected. For jets, the transition region is defined as pseudorapidity $1.3 < |\eta| < 1.7$

5.3.1 Event signature selection

$W \rightarrow \tau_{\mathrm{h}}\nu_{\tau}$ events are characterized by one hadronically decaying tau lepton and missing transverse energy due to the involved neutrinos (see e.g. figures 1.1, 5.1 and 5.3). To efficiently select events with this kind of signature, a combined $E_{\mathrm{T}}^{\mathrm{miss}}$ and τ_{h} trigger is used. The available triggers are active on event filter level (EF) which include triggers on lower levels (levels L1 and L2):

- Each event has to be selected by the following trigger signatures:
  First period: EF_tau12_loose_xe20_noMu
  Second period: EF_tau16_medium_xe22_noMu

The impact of matching the region of interest (RoI) of the trigger to the direction of the decaying tau has been checked on simulations and was found to reduce the signal selection efficiency by 0.6%. Therefore, the effect of such a matching is deemed negligible for the determination of the trigger efficiency.

The process signature is further selected by the following cuts acting on the fully reconstructed events:

- The event has to contain at least $E_{\mathrm{T}}^{\mathrm{miss}} \geq 30$ GeV
  (the used object definition is MET_LocHadTopo)

An event is required to contain at least one calorimeter-seeded tau candidate which has to be classified as tau by an identification algorithm based on a boosted decision tree (BDT). The individual cuts on the tau candidate objects are listed below:

- The tau candidate has to have at least one track

- The tau candidate has to be reconstructed within $|\eta| < 2.5$. Again, the reason for this cut is the limited coverage of the tracking system

- The taus have to fulfill the "medium" identification criteria for 1-prong candidates and the "tight" criteria for multi-prong candidates

- The highest-p_{T} tau candidate has to satisfy all the conditions noted above and is additionally required to have a visible transverse momentum between 20 and 60 GeV

For an accurate energy measurement the following is still necessary:

- The event is rejected if a tau candidate is reconstructed in the transition region $1.3 < |\eta| < 1.7$

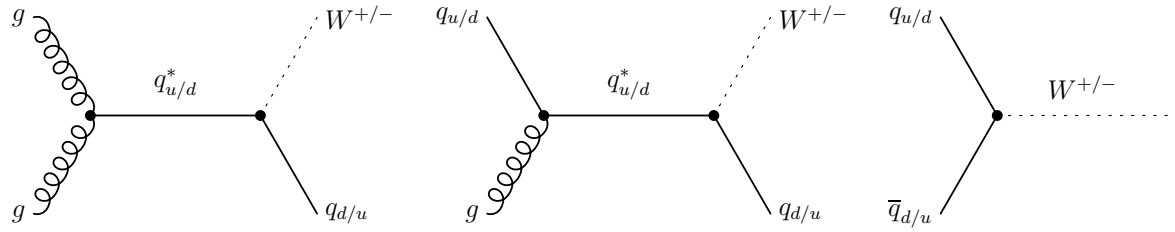

Figure 5.1: Feynman diagrams of W production in proton-proton collisions.

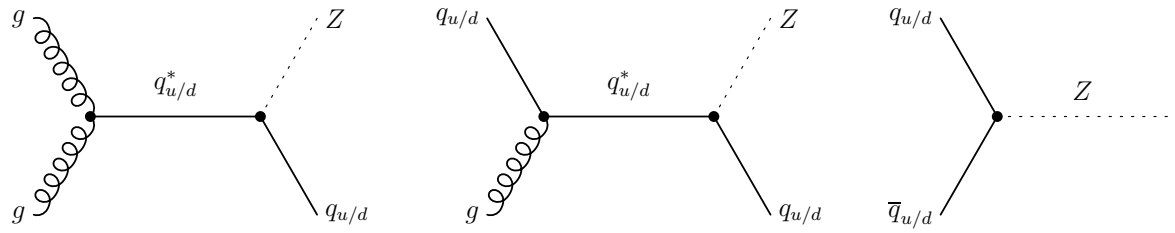

Figure 5.2: Feynman diagrams of Z production in proton-proton collisions.

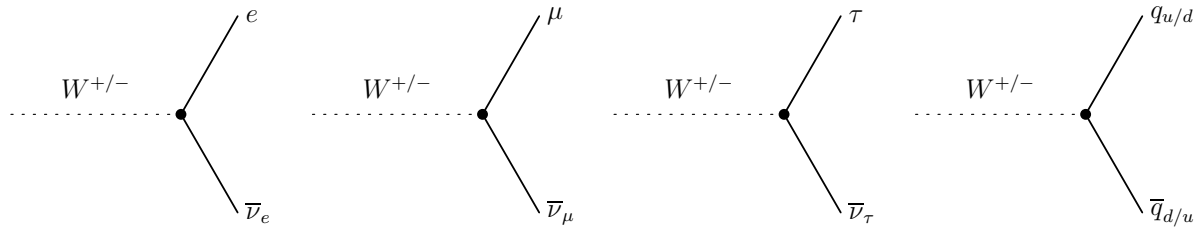

Figure 5.3: Feynman diagrams of W decays.

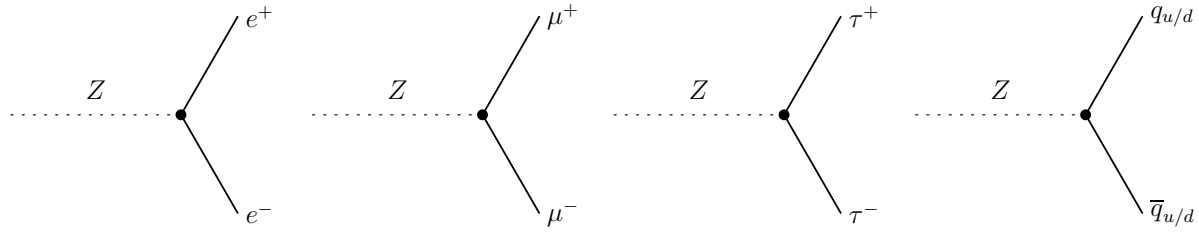

Figure 5.4: Feynman diagrams of Z decays.

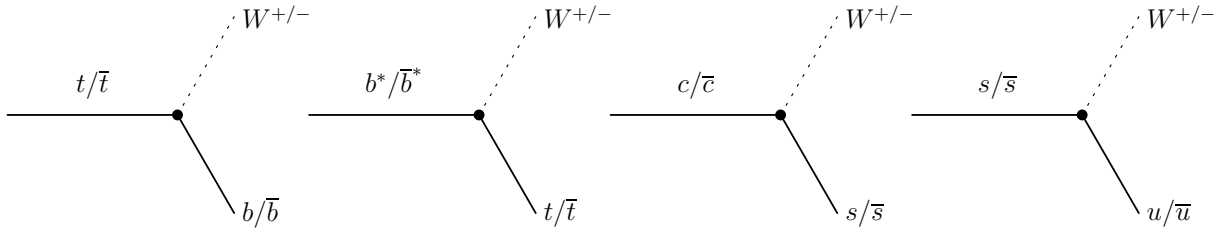

Figure 5.5: Feynman diagrams of top and heavy quark decays.

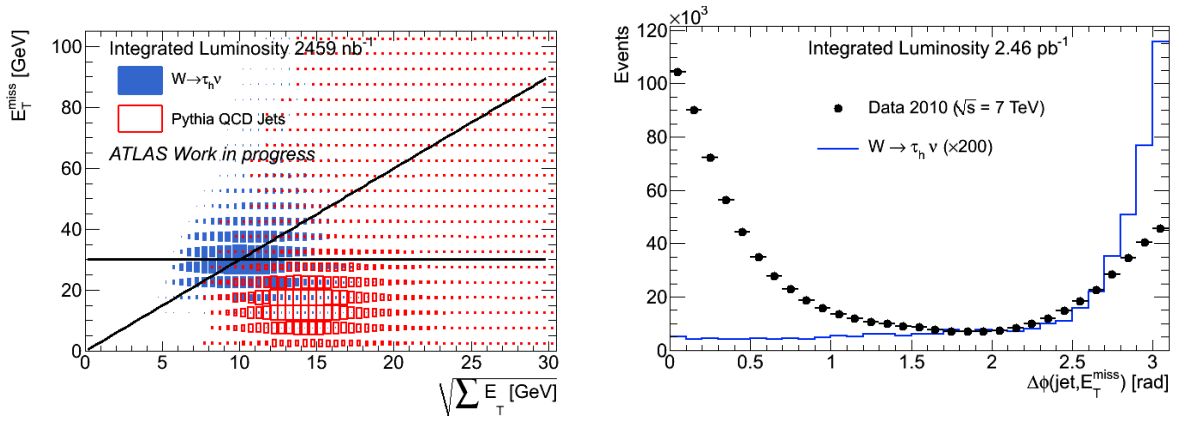

(a) (b)

Figure 5.6: Distribution of events in the $\left(E_{\mathrm{T}}^{\mathrm{miss}},\ \sqrt{\sum E_{\mathrm{T}}}\right)$ plane after the trigger requirement for all QCD background and the $W \rightarrow \tau_{\mathrm{h}}\nu_{\tau}$ signal Monte Carlo samples. Each sample is scaled by its cross section. The applied $E_{\mathrm{T}}^{\mathrm{miss}}$ and $S_{E_{\mathrm{T}}^{\mathrm{miss}}}$ cuts are represented by solid lines (a). Distribution of $\min(\Delta\phi(\mathrm{jet},\ E_{\mathrm{T}}^{\mathrm{miss}}))$ for simulated $W \rightarrow \tau_{\mathrm{h}}\nu_{\tau}$ events and data. The Monte Carlo events have been scaled by a factor of 200 for better visibility (b).

5.3.2 Electro-weak background rejection

Electro-weak background comprises the other leptonic decays of the W and the Z and the leptonic decay modes of the tau in $W \rightarrow \tau\nu_{\tau}$ processes (for a diagrammatic view of these processes see figures 5.2, 5.3, 5.4 and 5.5 for top and heavy quark decays). These kind of events survive the signature selection mainly because either at least one accompanying jet or the light lepton itself is mis-identified as a tau. In the first case, this background can be reduced by vetoing events with reconstructed light leptons.

- An event is rejected if it contains at least one reconstructed electron with $p_{\mathrm{T}} > 15$ GeV, satisfying the medium identification criteria
- An event is rejected if it contains at least one reconstructed combined muon with $p_{\mathrm{T}} > 15$ GeV

The second case can be accounted for by applying a lepton veto on reconstructed τ_{h} candidates. The lepton veto is also based on a BDT identification algorithm.

- An event is rejected if a τ_{h} candidate is vetoed by a BDT based electron veto algorithm (for muons no explicit τ_{h}-ID veto exists, since these events are already sufficiently suppressed)

5.3.3 QCD background rejection

Background due to QCD multi-jet events arises mainly because of two reasons. For once, it can happen that one or more jets in the event are incorrectly identified as hadronically decaying tau leptons. A measurement of the relative frequency of such tau fakes is presented in chapter 4 for various tau identification algorithms. The second reason is a mis-measurement of the transverse energy by a considerable factor. A quantity which is suitable to determine the degree of this mis-measurement is the so-called significance of $E_{\mathrm{T}}^{\mathrm{miss}}$ (abbreviated as $S_{E_{\mathrm{T}}^{\mathrm{miss}}}$), defined as

$$S_{E_{\mathrm{T}}^{\mathrm{miss}}} = \frac{E_{\mathrm{T}}^{\mathrm{miss}}}{0.5\sqrt{\sum E_{\mathrm{T}}}}, \tag{5.6}$$

where $\sqrt{\sum E_\mathrm{T}}$ can be regarded as the uncertainty of the energy measurement. One can easily see that the significance is large if the measurement is precise and small if the error is big, respectively. This means that in $W \to \tau_\mathrm{h}\nu_\tau$ events featuring true missing transverse energy, the significance is expected to be higher than in QCD events, where $E_\mathrm{T}^\mathrm{miss}$ is faked. Therefore, a lower limit on $S_{E_\mathrm{T}^\mathrm{miss}}$ is required for each event in order to be considered

- An event is rejected if $S_{E_\mathrm{T}^\mathrm{miss}} < 6$

A visualization of the cuts on $E_\mathrm{T}^\mathrm{miss}$ and $S_{E_\mathrm{T}^\mathrm{miss}}$ can be found in figure 5.6 (a), where the distributions of signal and QCD background Monte Carlo events in the $\left(E_\mathrm{T}^\mathrm{miss}, \sqrt{\sum E_\mathrm{T}}\right)$ plane are shown. One can see that the cut on $E_\mathrm{T}^\mathrm{miss}$ already removes the bulk of the QCD background while keeping still the larger part of the signal. Eventually, the cut on $S_{E_\mathrm{T}^\mathrm{miss}}$ discards many of the surviving QCD events with high values of $E_\mathrm{T}^\mathrm{miss}$, but where the measurement similarly comes with large uncertainties.

As described in the previous chapter, QCD multi-jets are often found to be pairwise back-to-back in the transverse plane of the detector and balanced in transverse energy. If the transverse energy of one of these jets is mis-measured, in this plane, the $E_\mathrm{T}^\mathrm{miss}$ either points along or in the opposite direction of this jet. In $W \to \tau_\mathrm{h}\nu_\tau$ events, on the other hand, $E_\mathrm{T}^\mathrm{miss}$ is expected to be found only in the direction opposing a jet. In this case the jet is most likely the hadronically decaying tau which is back-to-back with the tau-neutrino which causes the $E_\mathrm{T}^\mathrm{miss}$. This can be seen in figure 5.6 (b), where the minimal angle between a jet and $E_\mathrm{T}^\mathrm{miss}$ in the transverse plane is shown for signal Monte Carlo and data after the trigger cut. The data, at this stage still dominated by QCD, peaks at $\Delta\phi = 0$ and $\Delta\phi = \pi$, corresponding to the $E_\mathrm{T}^\mathrm{miss}$ and the jet being parallel or anti-parallel. For $W \to \tau_\mathrm{h}\nu_\tau$ events the distribution only peaks an $\Delta\phi = \pi$. This is exploited in the following way:

- An event is rejected if $\min\left(\Delta\phi\left(\text{jet}, E_\mathrm{T}^\mathrm{miss}\right)\right) < 0.5$ for jets with $p_\mathrm{T} > 20$ GeV

5.4 Background estimation

In the following section the various methods used to estimate the remaining amount of background are presented. Whereas the electro-weak background is shown to be reliably described by the Monte Carlo simulations, a data-driven technique has been developed to estimate the background from QCD events.

5.4.1 Estimation of the electro-weak background

In this analysis the electro-weak background is estimated from Monte Carlo simulations. Since in particular the $E_\mathrm{T}^\mathrm{miss}$ related quantities used to extract the $W \to \tau_\mathrm{h}\nu_\tau$ signal strongly depend on the underlying event processes, it is important to ensure that these are well modelled and provide a good description of the data. In order to check this, a so-called embedded sample is produced for the signal process and compared to the events generated by PYTHIA. The embedded sample consists of $W \to \mu\nu_\mu$ data events where the signal process is replaced by a simulated $W \to \tau_\mathrm{h}\nu_\tau$ decay. In this manner the underlying event is estimated directly from data. Figure 5.7 shows a comparison of the two samples for the $S_{E_\mathrm{T}^\mathrm{miss}}$ and the τ_h p_T distribution. Good agreement can be observed which leads to the conclusion that the PYTHIA Monte Carlo samples are modelling the underlying event sufficiently well and that they can indeed be used for a reliable electro-weak background estimation and signal efficiency extraction. Instead of simply validating the Monte Carlo prediction, the embedded sample is often produced with the goal to be used as an alternative to full simulations. This, however, was not possible at the time of the analysis due to missing trigger information.

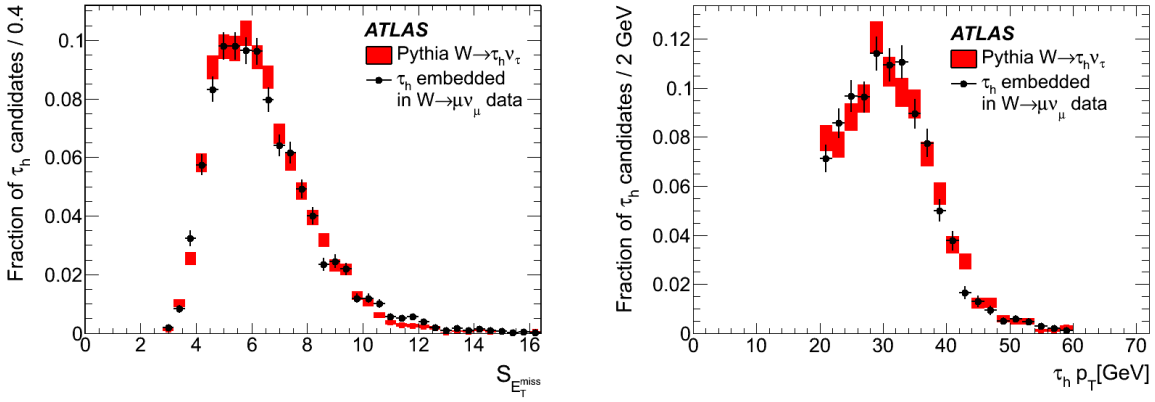

(a) (b)

Figure 5.7: Significance of $E_{\mathrm{T}}^{\mathrm{miss}}$ (a) and τ_{h} p_{T} (b), shown for embedded data and events simulated by PYTHIA after the event selection.

5.4.2 Estimation of the QCD background

The number and distribution of QCD events contributing to the overall background is estimated directly from data. This is necessary because on the one hand at a hadron collider these kind of events have a huge cross section compared to electro-weak processes (see e.g. table 5.3) but on the other hand can often be rejected similarly with high efficiency. This usually leads to a situation where the simulated integrated luminosity is much smaller than the integrated luminosity in data. If the reduced statistical significance of the simulations additionally suffers from discriminating cuts, one is faced with big statistical uncertainties on the few remaining events which results in a poor background description. To make things worse, the total cross section of QCD events comes with rather large theoretical uncertainties. In addition, given a suitable method, an estimation derived from data is considered advantageous because it is not biased by possible imperfections of the Monte Carlo simulation.

For this analysis a two-dimensional side-bin background subtraction technique, also known as the ABCD method, is used. It can be applied if it is possible to separate events with rectangular cuts into four disjunct regions, called A, B, C and D in a way that the following assumptions are fulfilled:

- One region (commonly called region A, or the signal region) is dominated by signal events
- The remaining regions B, C and D (also referred to as control regions) are dominated by background events of the kind one aims to estimate (this means in particular that in the control regions the number of events originating from other sources of background is small)
- The two variables used for the rectangular cuts are independent of each other

The number of background events in the signal region can then be computed from the number of observed events in the control regions as

$$\mathrm{N}^{\mathrm{A}} = \mathrm{N}^{\mathrm{B}}\mathrm{N}^{\mathrm{C}}/\mathrm{N}^{\mathrm{D}}, \tag{5.7}$$

where N^{i} represents the number of events in region i. If in addition the shape of the distributions of the variables are independent of each other, it is possible to also derive the shape of the background distribution in the signal region from those in the control regions by suitable projection.

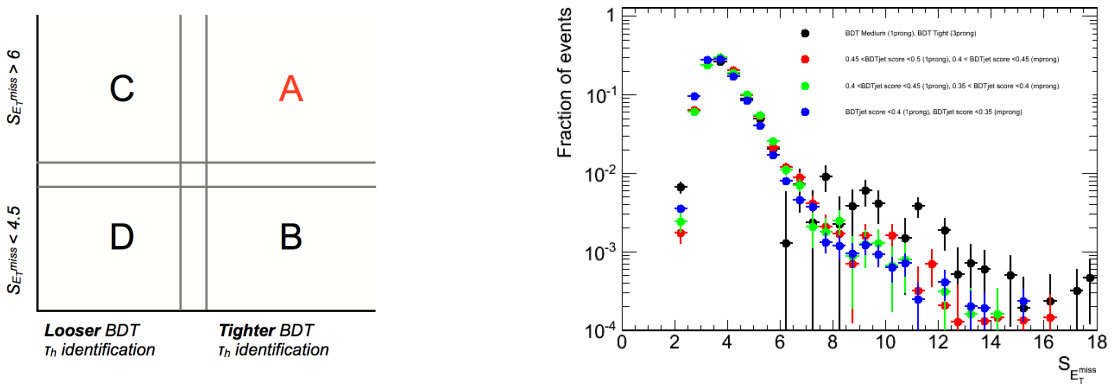

(a) (b)

Figure 5.8: Schematic display of the various regions defined in the course of the determination of the QCD background using the ABCD method. The signal region A is characterized by tighter cuts on the BDT score and the significance of the missing transverse energy, whereas for the control regions B, C and D at least one of the two cuts is inverted (a); $S_{E_T^{miss}}$ distributions for different regions of the BDT τ_h-ID. The signal and EW background contributions have been subtracted (b).

Here, the two separating variables are $S_{E_T^{miss}}$ and τ_h-ID. With these variables, however the requirements specified above are not perfectly fulfilled. The second assumption, demanding the signal and EW background contamination in the control regions to be small, is not fully satisfied, which has been checked using $W \to \tau\nu_\tau$ and EW background Monte Carlo samples, and corrections to account for this contamination have to be applied. For once, the cuts on $S_{E_T^{miss}}$ and on the τ_h-ID variable are further loosened in the definition of the control regions C and D in order to reduce signal and EW background pollution. That being said, the definition of the four regions is as follows:

- Region A: events with $S_{E_T^{miss}} > 6.0$ and τ_h candidates satisfying the medium/tight τ_h-ID as described in section 5.3
- Region B: events with $S_{E_T^{miss}} < 4.5$ and τ_h candidates satisfying the medium/tight τ_h-ID as described in section 5.3
- Region C: events with $S_{E_T^{miss}} > 6.0$ and τ_h candidates satisfying a looser τ_h-ID but failing the medium/tight τ_h-ID
- Region D: events with $S_{E_T^{miss}} < 4.5$ and τ_h candidates satisfying a looser τ_h-ID but failing the medium/tight τ_h-ID

A schematic display of the various regions can be seen in figure 5.8 (a).

To take into account the remaining signal and EW background contamination in the control regions, the number of observed events in the control regions is corrected as follows:

$$N^i \to N^i_{corr} = N^i - c_i(N^A - N^A_{QCD}), \qquad i = B, C, D, \tag{5.8}$$

where the c_i are the ratios of simulated signal and EW background events in the control regions and the

	A	B	C	D
N^i (Data)	2335	4796	1577	27636
N^i_{sig} ($W \to \tau_h \nu_\tau$)	1811 ±25	683 ±16	269 ±8	93 ±5
N^i_{EW}	284 ±7	118 ±4	388 ±9	90 ±4
c_i		0.38 ±0.01	0.31 ±0.01	0.087 ±0.003
N^i_{QCD}	127 ±8	3953 ±75	885 ±45	27444 ±166

Table 5.5: Estimated sample compositions and c_i factors (as defined in equation (5.9)) in the signal region A and control regions B, C, and D as defined in the text.

signal region:

$$c_i = \frac{N^i_{\text{sig}} + N^i_{\text{EW}}}{N^A_{\text{sig}} + N^A_{\text{EW}}}. \qquad i = B, C, D \tag{5.9}$$

Therefore equation (5.7) becomes:

$$N^A_{\text{QCD}} = \frac{[N^B - c_B(N^A - N^A_{\text{QCD}})][N^C - c_C(N^A - N^A_{\text{QCD}})]}{N^D - c_D(N^A - N^A_{\text{QCD}})}.$$

To make it more symmetric, N^A_{QCD} can be substituted with $N^A - c_A(N^A - N^A_{\text{QCD}})$, where clearly c_A is equal to 1 by construction. The previous equation thus becomes:

$$N^A - c_A(N^A - N^A_{\text{QCD}}) = \frac{[N^B - c_B(N^A - N^A_{\text{QCD}})][N^C - c_C(N^A - N^A_{\text{QCD}})]}{N^D - c_D(N^A - N^A_{\text{QCD}})}. \tag{5.10}$$

Equation (5.10) is a second order equation in $(N^A - N^A_{\text{QCD}})$. Calling $x = N^A - N^A_{\text{QCD}}$ leads to

$$(c_A c_D - c_B c_C)x^2 + (N^B c_C + N^C c_B - N^A c_D - N^D c_A)x + (N^A N^D - N^B N^C) = 0.$$

Just one of the two solutions can be accepted, with the requirements that it is positive and smaller than N^A. Finally, the result of the QCD background extraction method is $N^A_{\text{QCD}} = N^A - x$.

For the determination of the number of QCD events a largely independent data sample as described in table 5.2 has been used. The statistical error on N^A_{QCD} has to include both the uncertainty on the calculation of the coefficients c_i due to the limited Monte Carlo statistics and the uncertainty on the amount of data in the four control regions. Therefore, the statistical error on N^A_{QCD} has been evaluated using a toy Monte Carlo in which the number of data events in the four regions and the number of expected signal and EW background events have been varied within their statistical uncertainties. The coefficients c_i are then recalculated and ΔN^A_{QCD} is extracted.

For the successful prediction of the QCD background in the signal region with the data-driven method it has to be verified that the $S_{E_T^{\text{miss}}}$ distribution for the QCD background in the combined regions AB and CD is the same, i.e. that the $S_{E_T^{\text{miss}}}$ distribution is independent of the τ_h-ID selection. This has been done by comparing the $S_{E_T^{\text{miss}}}$ distributions for different BDT τ_h-ID regions. Four different regions are compared:

- The combined region AB with the medium BDT τ_h-ID selection for 1-prong and tight BDT τ_h-ID selection for the multi-prong candidates

- A subsample of control region CD with the looser τ_h-ID selection for candidates with 0.45 < BDT jet score < 0.5 for 1-prong candidates, 0.4 < BDT jet score < 0.45 for multi-prong candidates
- A subsample of control region CD with the looser τ_h-ID selection for candidates with 0.4 < BDT jet score < 0.45 for 1-prong candidates, 0.35 < BDT jet score < 0.4 for multi-prong candidates
- A subsample of control region CD with the looser τ_h-ID selection for candidates with BDT jet score < 0.4 for 1-prong candidates, BDT jet score < 0.35 for multi-prong candidates

In all four regions the contributions from signal and EW background as predicted from Monte Carlo are subtracted. The comparison of the shape of $S_{E_T^{miss}}$ in these four regions is shown in figure 5.8 (b). No major deviations can be seen between the different regions, thus the assumption that $S_{E_T^{miss}}$ is independent of the τ_h-ID is reasonable.

For distributions related to transverse energy, the QCD background is usually extracted from control region C where events share a similar $S_{E_T^{miss}}$ distribution, while for distributions related to τ_h identification and kinematics, the QCD background is extracted from control region B.

5.5 Result

The selection described in the previous sections has been applied to data and Monte Carlo. The absolute and relative cut flows are reported in tables 5.6 and 5.7, respectively. A striking feature are the very different numbers of events after applying the trigger cut for the various W decay samples. One would probably assume the trigger cut efficiency to be highest for signal events and lower (and also rather similar) for $W \to e\nu_e$ and $W \to \mu\nu_\mu$ events. The actual efficiencies become understandable, however, if one considers the following: first of all, it should be noted that the E_T^{miss} definition used for the trigger (and also for the later dedicated cut on E_T^{miss}) only incorporates missing energy calculated from calorimeter topoclusters. This means that in $W \to \mu\nu_\mu$ events there is almost no E_T^{miss} according to this definition, since the extra muon energy is not taken into account. Consequently, this results in a high rejection rate for this kind of process. Secondly, the E_T^{miss} spectrum in $W \to \tau_h\nu_\tau$ events is shifted towards lower values because the involved neutrinos are flying in opposite directions and hence are neutralizing their individual contributions.

It can now be stated that after all selection cuts one is left with 2335 events in data. The number of expected electro-weak background events in the signal region is 284 ± 7 (stat.) and the expected number of QCD background events is 127 ± 8 (stat.). This means that the measured number of signal events is 1924 ± 45 (stat.) which is in good agreement with an expected number of signal events of 1811 ± 25 (stat.). In figures 5.9 - 5.11 the expected signal and background distributions of variables characterizing the event and tau properties are compared to data. Even more control plots are depicted in [95]. Overall good agreement is found, which gives confidence in the validity of the used estimation techniques. Deviations occur mostly in bins with relative large fractions of QCD events, pointing at remaining inaccuracies in the background descriptions. One prominent example is the tau charge distribution where the discrepancies might be explained by an imperfect modelling of the background charge asymmetry.

5.6 Detector acceptance and cut efficiency

The only remaining ingredients needed to determine the total cross section according to equation (5.5) are the detector acceptance $A_{W\to\tau_h\nu_\tau}$ and the cut efficiency $C_{W\to\tau_h\nu_\tau}$. Both quantities depend on the

	Data	$W \to \tau\nu_\tau$	$W \to \tau_\ell\nu_\tau$	$W \to e\nu_e$	$W \to \mu\nu_\mu$	$Z \to \tau\tau$	$Z \to ee$	$Z \to \mu\mu$
Events	191991948	232377	126672	358359	358656	34034	34644	33918
GRL	165757532	232377	126672	358359	358656	34034	34644	33918
Trigger	6879843	20111 ± 81	7507 ± 50	175936 ± 152	5620 ± 37	2664 ± 9	2306 ± 9	707 ± 5
Collision cleaning	6879795	20108 ± 81	7507 ± 50	175882 ± 152	5620 ± 37	2664 ± 9	2306 ± 9	707 ± 5
Jet cleaning	6873901	20108 ± 81	7507 ± 50	175882 ± 152	5620 ± 37	2664 ± 9	2306 ± 9	707 ± 5
Jet in gap veto	4962570	16373 ± 74	6123 ± 45	143338 ± 149	4505 ± 33	2086 ± 8	1459 ± 7	570 ± 4
$\min(\Delta\Phi(jet, E_{\mathrm{T}}^{\mathrm{miss}})) > 0.5$	2421757	15326 ± 71	5771 ± 44	137755 ± 148	4216 ± 32	1659 ± 7	656 ± 5	527 ± 4
$E_{\mathrm{T}}^{\mathrm{miss}} > 30$GeV	350444	11899 ± 64	3718 ± 36	104857 ± 138	3829 ± 31	1145 ± 6	19.3 ± 0.8	459 ± 4
p_{T} (τ_{h})> 20 GeV	321246	11600 ± 63	3545 ± 35	103800 ± 138	3761 ± 31	1123 ± 6	18.7 ± 0.8	451 ± 4
τ_{h} identification	62754	5526 ± 44	1112 ± 20	23919 ± 76	663 ± 13	580 ± 4	5.2 ± 0.4	124 ± 2
p_{T} (τ_{h})< 60GeV	37199	4790 ± 41	767 ± 16	19648 ± 69	280 ± 8	446 ± 4	3.2 ± 0.3	54.5 ± 1.4
τ_{h}-ID ele/mu veto	10199	3976 ± 38	44.0 ± 3.9	453 ± 11	202 ± 7	347 ± 3	0.1 ± 0.0	38.1 ± 1.1
Electron veto	9912	3959 ± 38	35.7 ± 3.5	196 ± 7	198 ± 7	344 ± 3	0.0 ± 0.0	36.7 ± 1.1
Muon veto	9604	3959 ± 38	29.4 ± 3.2	196 ± 7	111 ± 5	259 ± 3	0.0 ± 0.0	2.9 ± 0.3
$S_{E_{\mathrm{T}}^{\mathrm{miss}}} > 6$	2335	1811 ± 25	15.1 ± 2.3	92.5 ± 4.9	56.1 ± 3.8	112 ± 2	0.0 ± 0.0	1.4 ± 0.2
	$t\bar{t}$ Lep	$t\bar{t}$ Had						
Events	2746	2186						
GRL	2746	2186						
Trigger	1305 ± 3	395 ± 5						
Collision cleaning	1305 ± 3	395 ± 5						
Jet cleaning	1305 ± 3	395 ± 5						
Jet in gap veto	674 ± 3	175 ± 4						
$\min(\Delta\Phi(jet, E_{\mathrm{T}}^{\mathrm{miss}})) > 0.5$	376 ± 2	27.2 ± 1.6						
$E_{\mathrm{T}}^{\mathrm{miss}} > 30$GeV	349 ± 2	6.5 ± 0.8						
p_{T} (τ_{h})> 20 GeV	349 ± 2	6.5 ± 0.8						
τ_{h} identification	120 ± 1	1.3 ± 0.4						
p_{T} (τ_{h})< 60GeV	51.9 ± 0.9	0.1 ± 0.1						
τ_{h}-ID ele/mu veto	18.2 ± 0.6	0.1 ± 0.1						
Electron veto	15.0 ± 0.5	0.1 ± 0.1						
Muon veto	10.9 ± 0.4	0.1 ± 0.1						
$S_{E_{\mathrm{T}}^{\mathrm{miss}}} > 6$	6.4 ± 0.3	0.0 ± 0.0						

Table 5.6: Number of events after cuts for data and simulations. The quoted errors are statistical only.

	Data	$W \to \tau_h \nu_\tau$	$W \to e\nu_e$	$W \to \mu\nu_\mu$	$W \to \tau_\ell \nu_\tau$	$Z \to ee$	$Z \to \mu\mu$	$Z \to \tau\tau$	$t\bar{t}$ Lep	$t\bar{t}$ Had
Events	191991948	232377	126672	358359	358656	34033.7	34644.3	33917.5	2746.2	2185.9
GRL	86.3%	100.0%	100.0%	100.0%	100.0%	100.0%	100.0%	100.0%	100.0%	100.0%
Trigger	4.2%	8.7%	49.1%	1.6%	5.9%	6.6%	2.1%	7.8%	47.6%	18.1%
Collision cleaning	100.0%	100.0%	100.0%	100.0%	100.0%	100.0%	100.0%	100.0%	100.0%	100.0%
Jet cleaning	99.9%	100.0%	100.0%	100.0%	100.0%	100.0%	100.0%	100.0%	100.0%	100.0%
Jet in gap veto	72.2%	81.2%	81.5%	80.2%	81.5%	63.3%	80.5%	78.3%	51.7%	44.5%
$\min(\Delta\Phi(jet, E_T^{miss})) > 0.5$	48.8%	93.7%	96.1%	93.6%	94.3%	45.1%	92.5%	79.6%	55.8%	15.5%
$E_T^{miss} > 30$ GeV	14.5%	77.6%	76.1%	90.7%	64.5%	2.9%	86.9%	69.0%	93.0%	23.8%
τ_h identification	12.6%	44.8%	20.4%	9.0%	22.7%	20.2%	14.3%	43.3%	19.7%	2.1%
$20 < p_T(\tau_h) < 60$ GeV	84.6%	89.8%	91.6%	81.9%	91.1%	80.2%	83.5%	89.8%	73.7%	65.6%
τ_h in gap veto	100.0%	100.0%	100.0%	100.0%	100.0%	100.0%	100.0%	100.0%	100.0%	100.0%
τ_h-ID ele/mu veto	27.4%	83.1%	2.3%	72.0%	5.8%	2.4%	69.8%	77.7%	35.5%	100.0%
Electron veto	97.2%	99.6%	43.9%	97.7%	80.1%	0.0%	96.3%	99.1%	82.7%	100.0%
Muon veto	96.9%	100.0%	99.9%	54.3%	84.8%	-	8.1%	75.4%	72.0%	100.0%
$S_{E_T^{miss}} > 6$	24.3%	45.4%	47.1%	51.8%	50.2%	-	49.7%	42.7%	58.7%	0.0%
Overall efficiency	0.00122%	0.77684%	0.02605%	0.01546%	0.01197%	0.00000%	0.00438%	0.32398%	0.22978%	0.00000%

Table 5.7: Cut efficiencies of each cut with respect to the previous.

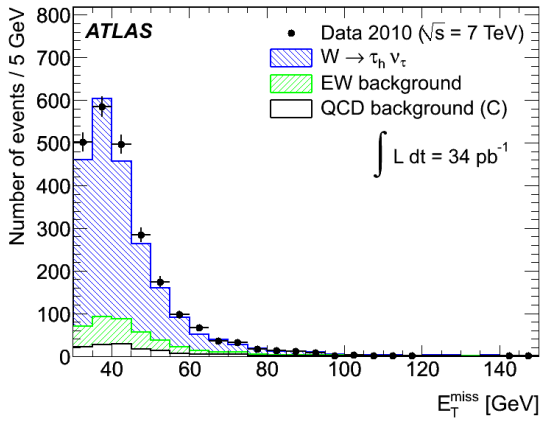

(a)

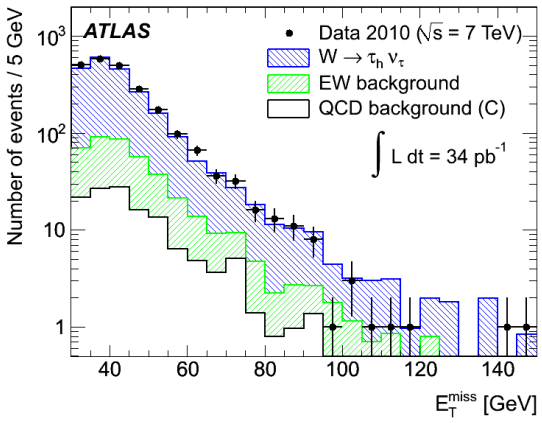

(b)

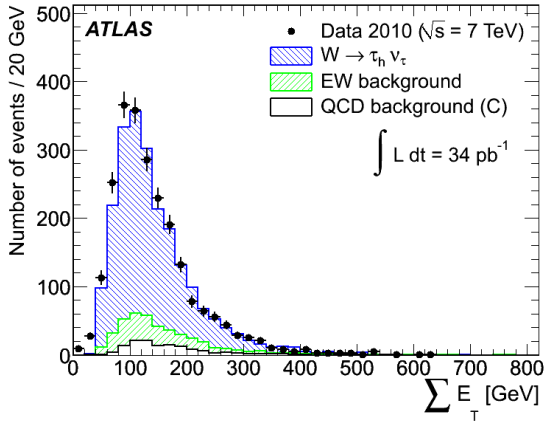

(c)

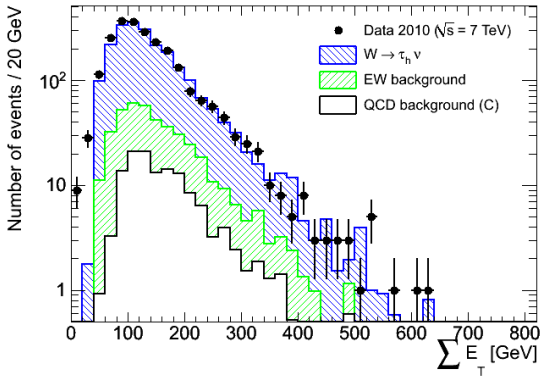

(d)

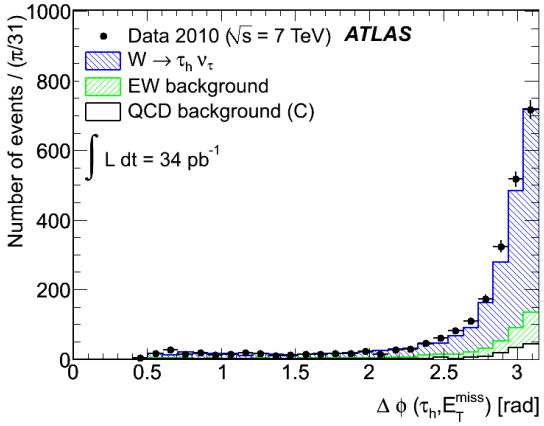

(e)

Figure 5.9: Distributions of selected variables in the signal region, comparing signal and background expectations to data. In all plots, the shape of the QCD background has been extracted from control region C. Missing transverse energy $E_{\mathrm{T}}^{\mathrm{miss}}$ in linear (a) and logarithmic scale (b), $\sum E_{\mathrm{T}}$ in linear (c) and logarithmic scale (d), the minimal angle between a jet and $E_{\mathrm{T}}^{\mathrm{miss}}$ in the transverse plane $\min\left(\Delta\phi\left(\text{jet},\ E_{\mathrm{T}}^{\mathrm{miss}}\right)\right)$ (e).

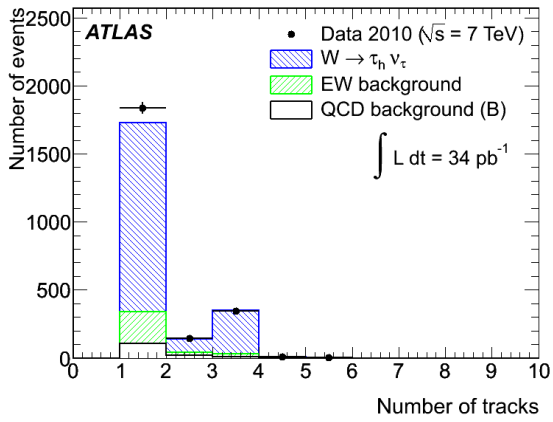

(a)

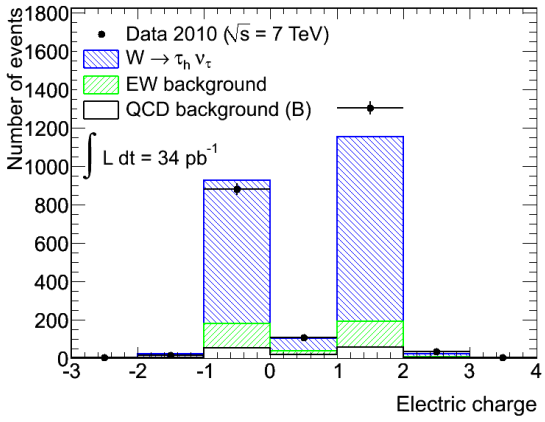

(b)

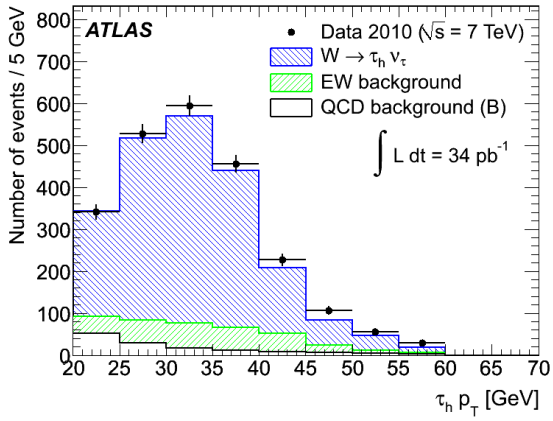

(c)

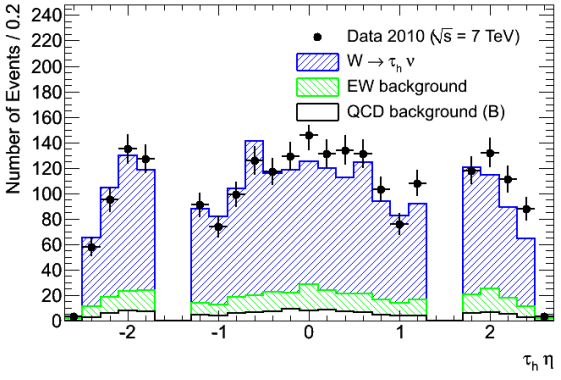

(d)

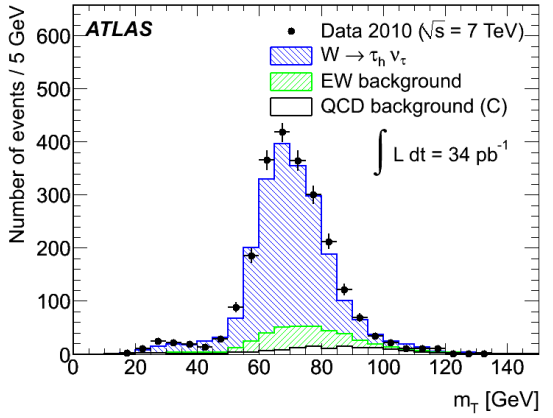

(e)

Figure 5.10: Distributions of selected kinematic variables of the taus in the signal region, comparing signal and background expectations to data. In all plots, the shape of the QCD background has been extracted from control region B, with the exception of (e), where control region C has been used. Number of tracks (a), electric charge (b), transverse momentum p_{T} (c), pseudorapidity η (d), transverse mass m_{T} (e).

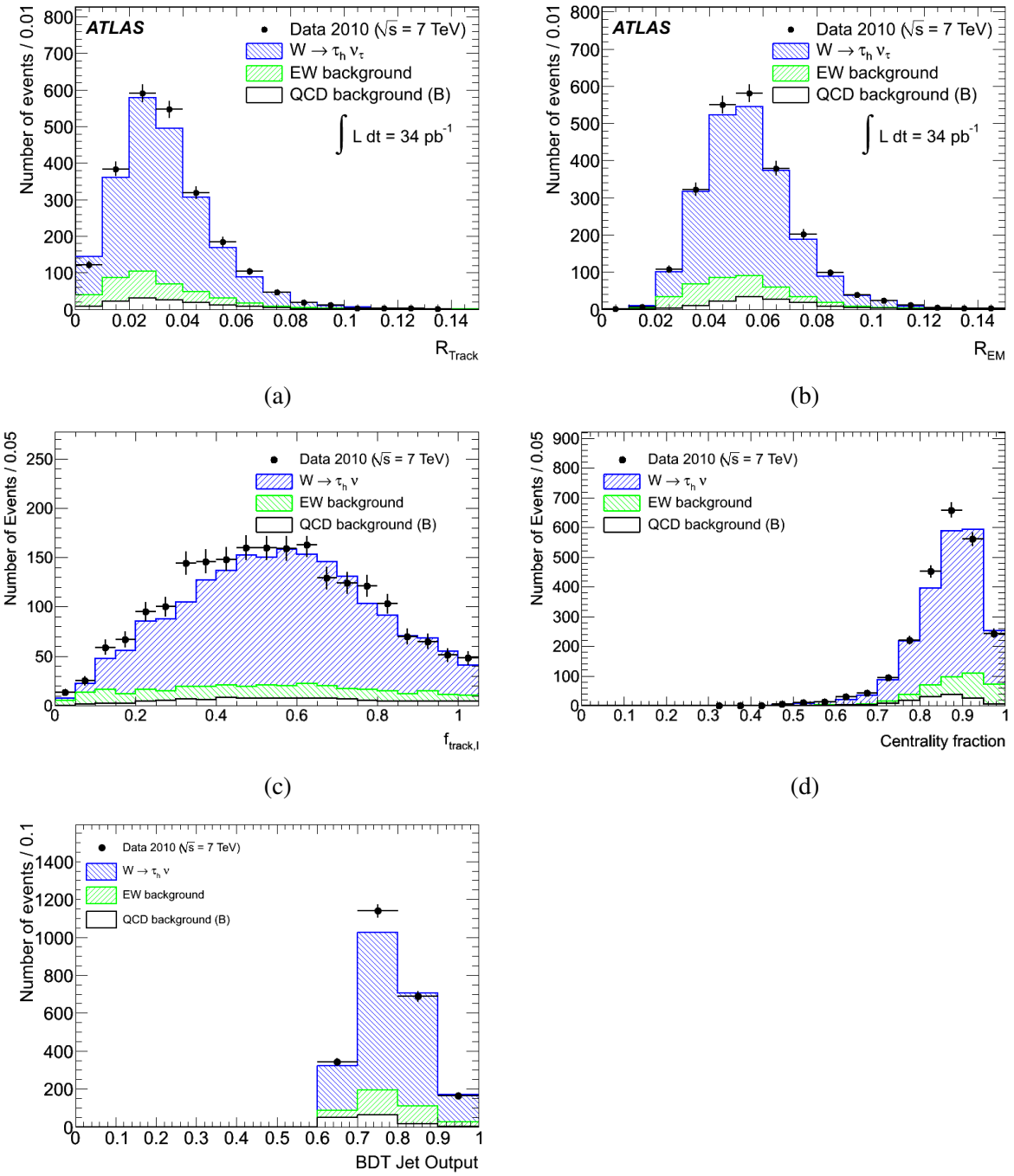

Figure 5.11: Distributions of selected tau identification variables in the signal region, comparing signal and background expectations to data. In all plots, the shape of the QCD background has been extracted from control region B. Track radius R_{Track} (a), electro-magnetic radius R_{EM} (b), track fraction f_{track} (c), centrality fraction (d), BDT score (e).

	W (all)
$A_{W\to\tau_h\nu_\tau}$	0.0975 ± 0.0004 (MC, stat.)
$C_{W\to\tau_h\nu_\tau}$	0.0799 ± 0.0011 (MC, stat.)

Table 5.8: Central values for the detector acceptance $A_{W\to\tau_h\nu_\tau}$ and the cut efficiency $C_{W\to\tau_h\nu_\tau}$. Both are determined from a sample generated by PYTHIA using the MRSTLO* PDF and the ATLAS MC10 tune.

signal process which is indicated by the subscript $W \to \tau_h\nu_\tau$. As a reminder and to be be more specific, the detector acceptance is defined as

$$A_{W\to\tau_h\nu_\tau} = \frac{N_{\text{gen, kin/geom}}}{N_{\text{gen, all}}}, \tag{5.11}$$

where $N_{\text{gen, all}}$ is the total number of generated events while $N_{\text{gen, kin/geom}}$ is the number of events at generator level within the so-called fiducial region defined by the following parameter ranges

- $20\ \text{GeV} < p_T^{\tau^{\text{vis}}} < 60\ \text{GeV}$
- $|\eta^{\tau^{\text{vis}}}| < 2.5$, excluding $1.3 < |\eta^{\tau^{\text{vis}}}| < 1.7$
- $(\sum p^{\nu})_T > 30\ \text{GeV}$
- $|\Delta\phi(\tau^{\text{vis}}, \sum \nu)| > 0.5$

where τ^{vis} denotes the sum of the four-vectors of the decay products of a simulated hadronic tau decay which are not neutrinos.

The central values for $A_{W\to\tau_h\nu_\tau}$ are determined using a sample generated by PYTHIA with the modified leading-order parton distribution function (PDF) MRSTLO* [96] and the corresponding ATLAS MC10 tune [97].

The cut efficiency $C_{W\to\tau_h\nu_\tau}$ is the combined efficiency of the trigger and the τ_h reconstruction and identification algorithms (within the acceptance). It is defined as

$$C_{W\to\tau_h\nu_\tau} = \frac{N_{\text{reco, all cuts}}}{N^{\text{dressed}}_{\text{gen, kin/geom}}}, \tag{5.12}$$

where $N_{\text{reco, all cuts}}$ is the number of signal events passing the selection cuts of the analysis after the full detector simulation. Using the same Monte Carlo sample as defined above the following values for the detector acceptance and cut efficiency are obtained

$$\begin{aligned} A_{W\to\tau_h\nu_\tau} &= 0.0975 \pm 0.0004 \text{ (MC, stat.)} \\ C_{W\to\tau_h\nu_\tau} &= 0.0799 \pm 0.0011 \text{ (MC, stat.).} \end{aligned}$$

These values are also reported in table 5.8. Before the final result is quoted in section 5.8, however, the various sources of systematic uncertainties are discussed in the following sections.

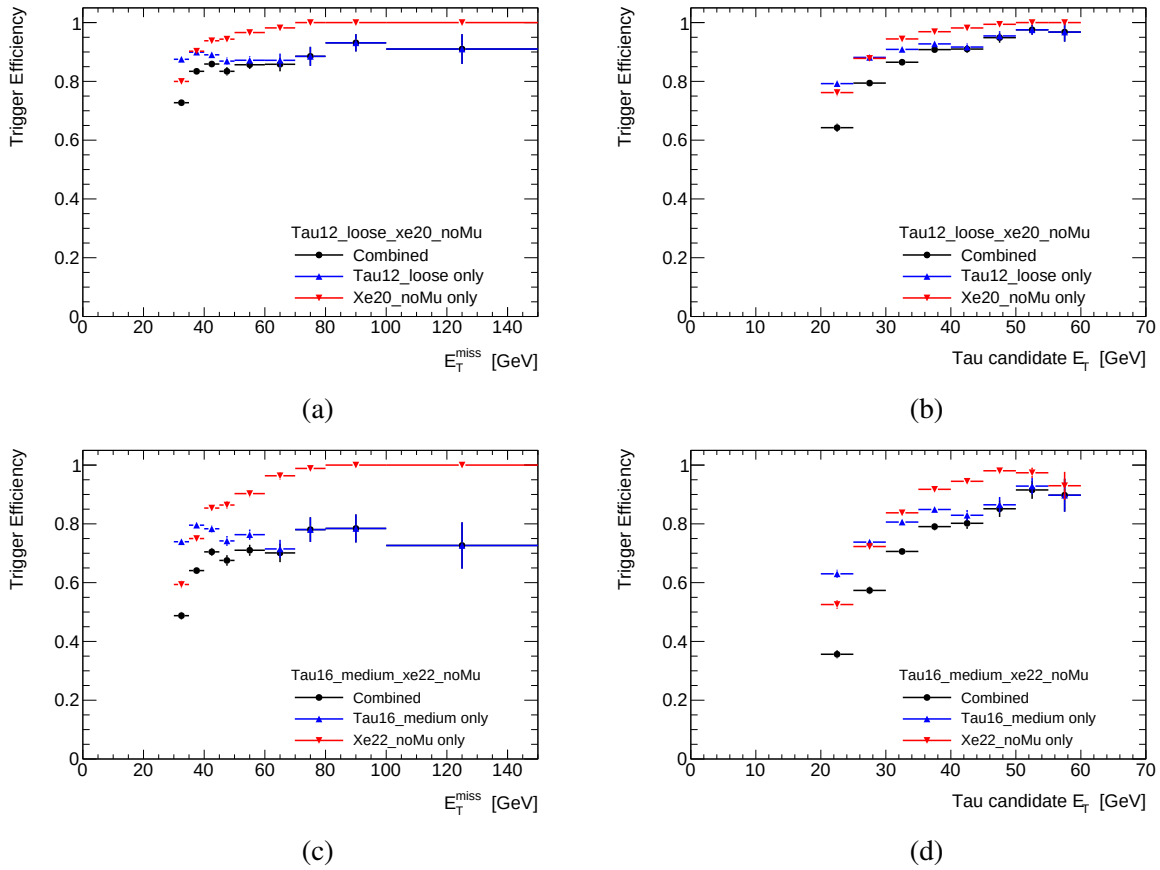

Figure 5.12: Trigger turn-on curves for $W \rightarrow \tau_h \nu_\tau$ Monte Carlo events as a function of the reconstructed E_T^{miss} and τ_h E_T with respect to the offline selection for EF_tau12_loose_xe20_noMu (a), (b) and for EF_tau16_medium_xe22_noMu (c), (d).

5.7 Systematics

This section covers the estimation of the systematic error on the cross section measurement. It includes the errors on the cross sections of the background processes, luminosity measurement errors, errors due to pile-up, trigger efficiency uncertainties, object energy scale and resolution errors as well as the systematic error due to fake objects. An additional source of error are imperfections of the QCD background determination method. Finally, since some components of the cross section measurement depend on Monte Carlo simulations, errors due to the limited accuracy of the event generators are taken into account.

5.7.1 Cross sections of background processes

The cross sections of the background processes $W \rightarrow e\nu_e$, $W \rightarrow \mu\nu_\mu$, $Z \rightarrow ee$, $Z \rightarrow \mu\mu$ and $t\bar{t}$ have been measured independently with ATLAS [98], [99]. The errors on these measurements naturally add to the total systematic uncertainty, except of course for the common error on the integrated luminosity. For the remaining channels with no ATLAS measurement available, the uncertainty on the theoretically predicted NNLO cross section is used. These uncertainties have already been evaluated for the other ATLAS measurements and have been found to be of order 5% [100].

Process	Cross section [pb]	Total error [pb]	Total relative error	Combination
$W \to e\nu_e / W \to \mu\nu_\mu$	10.391	± 0.022 (stat.) ± 0.238 (syst.) ± 0.353 (lumi.) ± 0.312 (acc.)	± 0.2% (stat.) ± 2.3% (syst.) ± 3.4% (lumi.) ± 3.0% (acc.)	3.8%
$W \to \tau_\ell \nu_\tau$	10.46		5%	5%
$Z \to ee / Z \to \mu\mu$	0.945	± 0.006 (stat.) ± 0.011 (syst.) ± 0.032 (lumi.) ± 0.038 (acc.)	± 0.6% (stat.) ± 1.2% (syst.) ± 3.4% (lumi.) ± 4.0% (acc.)	4.2%
$Z \to \tau\tau$	0.99		5%	5%
$t\bar{t}$	180	± 9 (stat.) ± 15 (syst.) ± 6 (lumi.)	± 5.0% (stat.) ± 8.3% (syst.) ± 3.3% (lumi.)	9.7%

Table 5.9: Cross section of electro-weak and $t\bar{t}$ backgrounds as measured by ATLAS. The measurement errors add to the total systematic uncertainty.

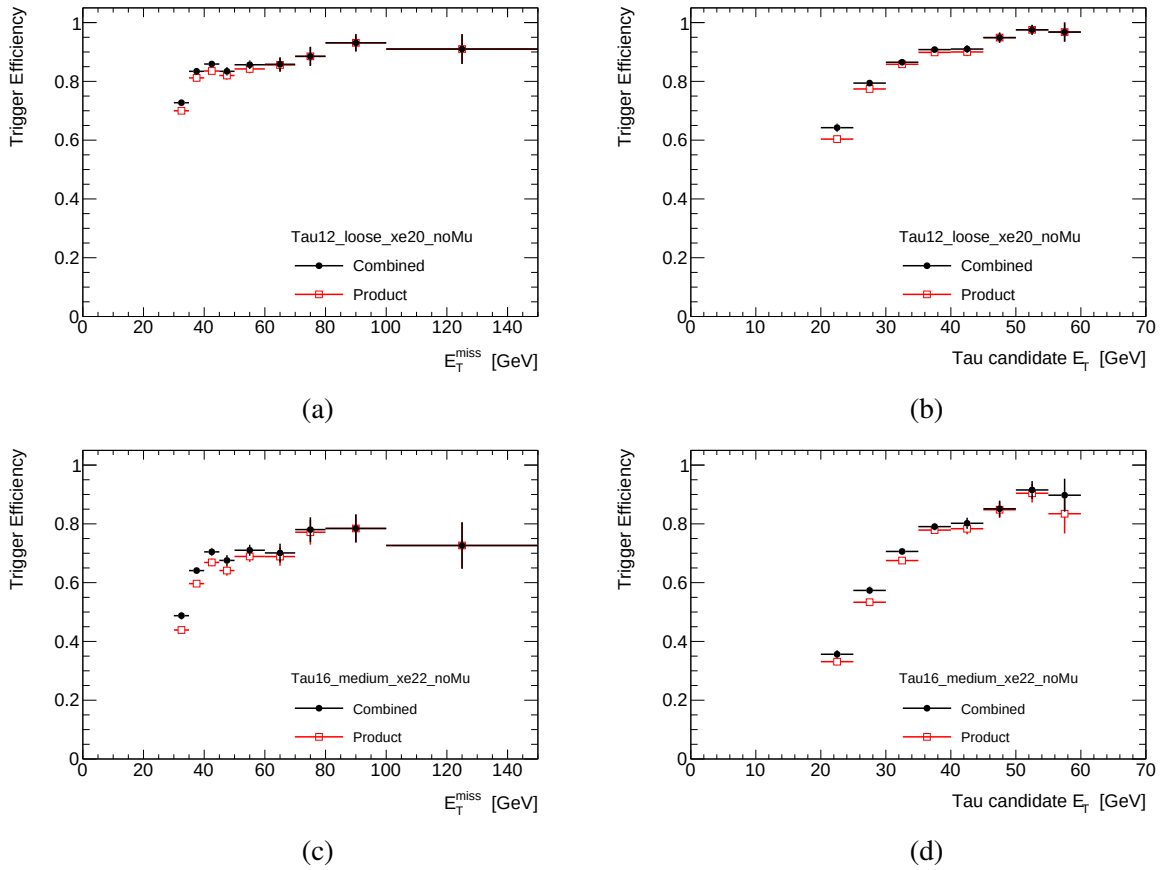

Figure 5.13: Product and combined trigger response for $W \rightarrow \tau_h \nu_\tau$ Monte Carlo events as a function of the reconstructed E_T^{miss} and τ_h E_T with respect to the offline selection for EF_tau12_loose_xe20_noMu (a), (b) and EF_tau16_medium_xe22_noMu (c), (d).

Since the QCD background is extracted directly from data, no assumption on its cross section have been made. The systematic error due to the imperfection of the method of the QCD background extraction is described in section 5.7.13. A summary of the uncertainties on the cross sections of the background processes is reported in table 5.9.

5.7.2 Luminosity

The instantaneous luminosity is monitored online by dedicated luminosity detectors which essentially count the number of interactions per bunch crossing. The absolute luminosity scale is calibrated by van-der-Meer scans (beam separation scans) where the beams are swept transversely across each other in order to obtain the total inelastic proton-proton cross section. According to [101], the relative uncertainty on the total integrated luminosity is 3.4% which is largely dominated by uncertainties on the measurement of the beam intensities.

5.7.3 Pile-up

The simulated events have been reweighted to have the same vertex multiplicity as the data events. The accuracy of the weight factors is limited by the available statistics of the used Monte Carlo samples.

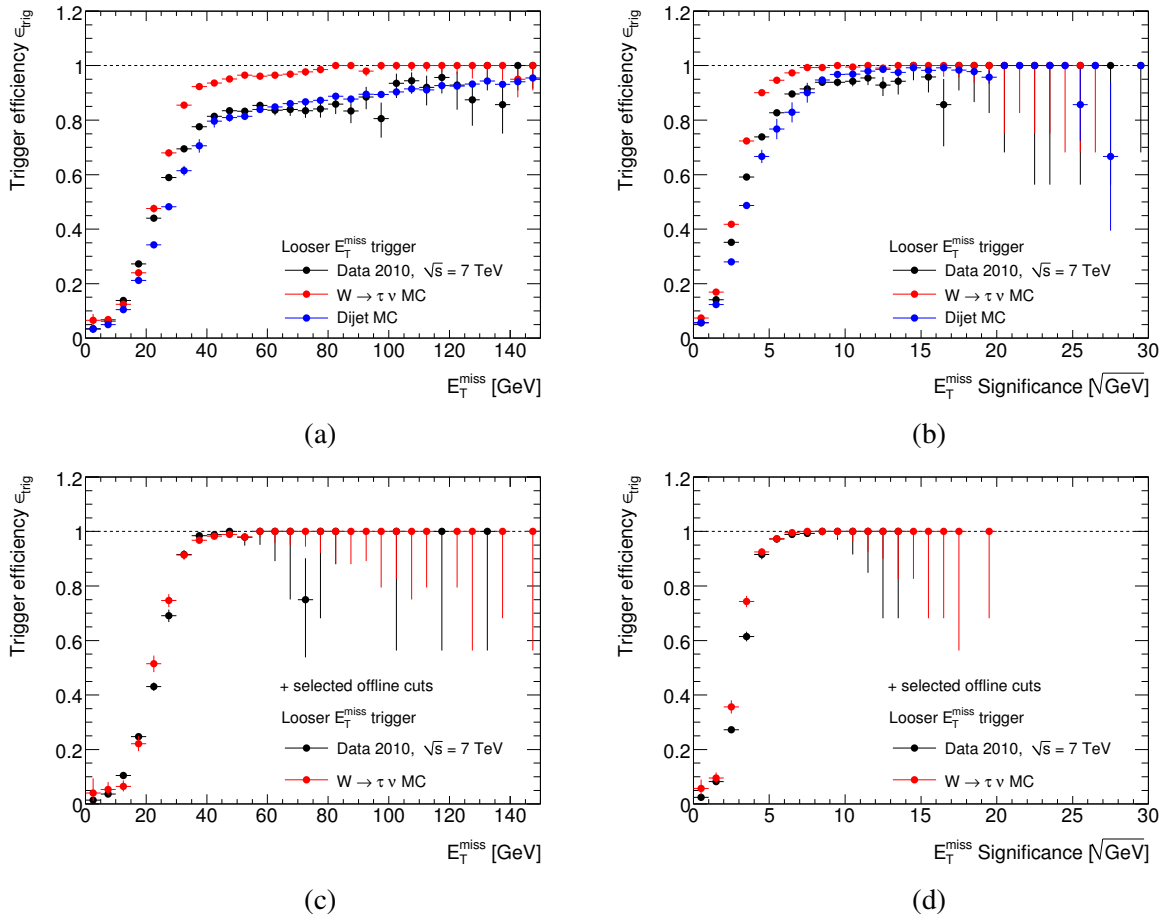

Figure 5.14: Trigger response of EF_xe20_noMu in data compared to signal and QCD background Monte Carlo with respect to EF_tau38_loose as a function of $E_{\mathrm{T}}^{\mathrm{miss}}$ (a) and $S_{E_{\mathrm{T}}^{\mathrm{miss}}}$ (b) without further selection cuts; (c) and (d) show the same distributions after applying the τ_{h}-ID and the $\Delta\phi$ cut.

This systematic uncertainty has been evaluated by varying the weights within their uncertainty and comparing the results after the event selection. The effects on the main background processes are as follows:

- $W \to e\nu_e$: 0.4%
- $W \to \mu\nu_\mu$: 2.3%
- $W \to \tau_\ell\nu_\tau$: 2.6%
- $Z \to \tau\tau$: 1.2%

5.7.4 Trigger systematics

A measurement on data of the combined τ_{h}-$E_{\mathrm{T}}^{\mathrm{miss}}$ trigger efficiency is not possible with 2010 data statistics. Comparisons between data and simulations, however, show good agreement, therefore a measurement based on Monte Carlo is considered reliable and it is not necessary to apply a trigger efficiency

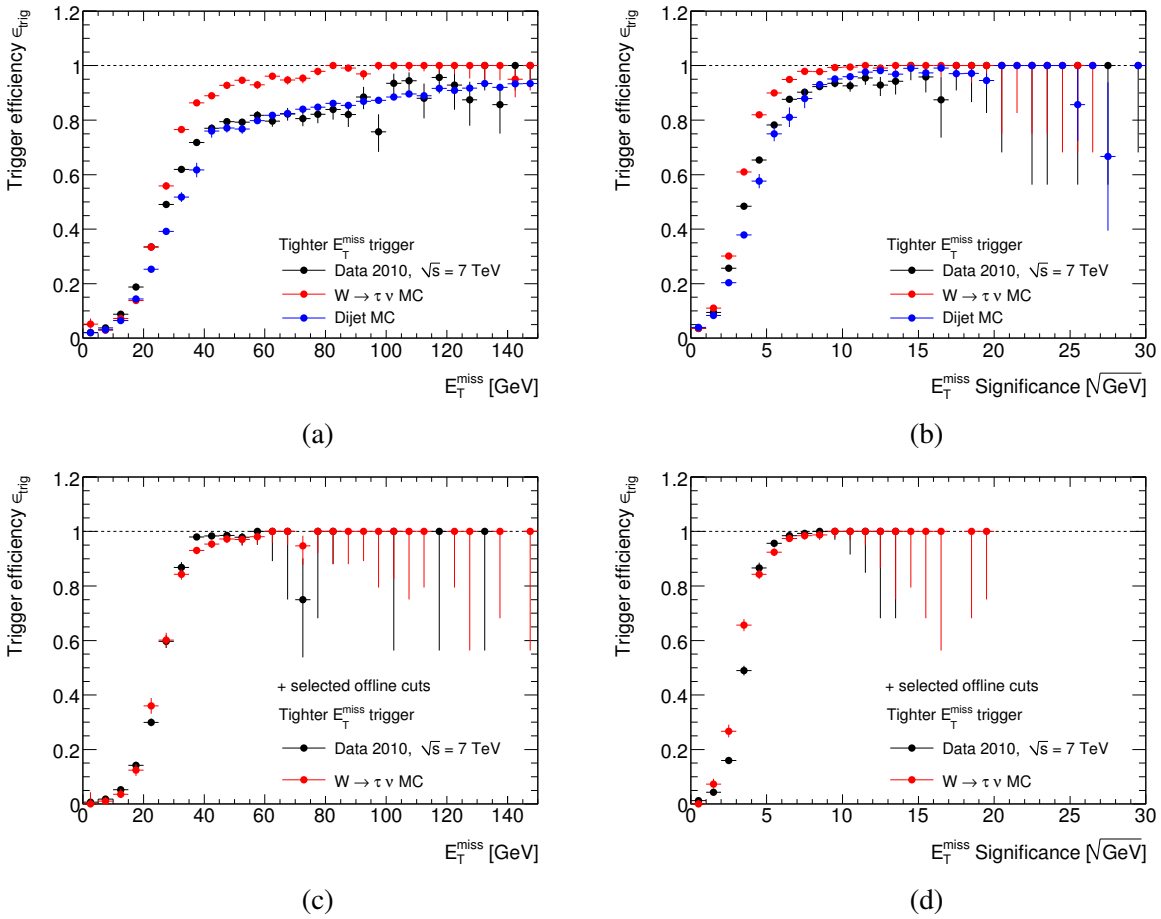

Figure 5.15: Trigger response of EF_xe22_noMu in data compared to signal and QCD background Monte Carlo with respect to EF_tau38_loose as a function of $E_{\mathrm{T}}^{\mathrm{miss}}$ (a) and $S_{E_{\mathrm{T}}^{\mathrm{miss}}}$ (b) without further selection cuts; (c) and (d) show the same distributions after applying the τ_{h}-ID and the $\Delta\phi$ cut.

correction. The trigger efficiencies determined from Monte Carlo for the two different triggers used are summarized in table 5.10.

In order to evaluate a systematic uncertainty arising due to a residual imperfect modeling of the trigger response based on data anyhow, the following procedure is applied:

First it is checked, that the correlations between the two parts of the trigger are negligible. Then the efficiency of the $E_{\mathrm{T}}^{\mathrm{miss}}$ part of the trigger is measured with respect to a τ_{h} trigger and vice versa. This procedure can be compared with the tag-and-probe methods described earlier in section 4.1. Eventually, the combination of the two differences between the efficiencies determined from data and Monte Carlo is taken to be the systematic uncertainty.

Correlation between the trigger parts

The turn-on-curves for the two triggers with respect to the reconstructed $E_{\mathrm{T}}^{\mathrm{miss}}$ and τ_{h} E_{T} can be found in figure 5.12 for the signal Monte Carlo sample. The correlation of the τ and $E_{\mathrm{T}}^{\mathrm{miss}}$ part of the two triggers has been studied with the Monte Carlo sample by comparing the performance of the respective combined trigger with the product of the τ and $E_{\mathrm{T}}^{\mathrm{miss}}$ parts. The results of this study are shown in figure

Signature	Efficiency
EF_tau12_loose_xe20_noMu	81.3 ± 0.8%
EF_tau16_medium_xe22_noMu	62.7 ± 0.7%

Table 5.10: Summary of the trigger efficiencies. The efficiencies are computed with respect to all events satisfying the offline selection for $W \to \tau_h \nu_\tau$ decays (see section 4.3). The quoted uncertainties are statistical only.

5.13. The correlation of the two trigger parts has been evaluated to have an effect less than 5% and thus has a negligible impact on the systematic uncertainty.

E_T^{miss} trigger part

The efficiency of the E_T^{miss} trigger part with respect to a τ_h trigger is calculated as

$$\epsilon_{trig} = \frac{\text{number of events passing the } E_T^{miss} \text{ trigger}}{\text{number of events passing the } \tau_h \text{ trigger}} \tag{5.13}$$

where the E_T^{miss} trigger signatures are EF_xe20_noMu and EF_xe22_noMu, respectively and the τ_h signature is EF_tau38_loose, which has been the lowest unprescaled trigger available. Figures 5.14 (a) and (b) show the trigger response for the EF_xe20_noMu trigger as a function of E_T^{miss} and $S_{E_T^{miss}}$ for data, Monte Carlo signal and QCD jets, the dominant background. The plot suggests that at this stage the data is clearly dominated by the background. Ideally one would now additionally require all of the other offline cuts of the analysis to further enrich the data sample with $W \to \tau_h \nu_\tau$ events. However, due to limited statistics of both data and simulation samples, not all offline cuts can be applied. It turns out that the τ_h-ID and the $\Delta\phi$ cuts alone already remove most of the background, which can also be seen from figures 5.14 (c) and (d). Only small differences between the data and signal Monte Carlo remain, mostly in the region in the vicinity of the trigger threshold. No differences between data and simulations can be seen in the plateau region for events with $S_{E_T^{miss}} > 6$. The systematic uncertainty on the trigger efficiency is now obtained by integrating over all events with $E_T^{miss} > 30$ GeVand weighting by the E_T^{miss} distribution of the sample. For EF_xe20_noMu this error sums up to 1.0%.

The same is done for the EF_xe22_noMu signature with figure 5.15 showing the corresponding plots. Again, before applying the τ_h-ID and $\Delta\phi$ cuts the data is clearly background dominated and much more signal-enriched afterwards. The differences between data and Monte Carlo, however, are slightly larger than for EF_xe20_noMu. Integrating over all events with $E_T^{miss} > 30$ GeV and weighting by the E_T^{miss} distribution, the systematic error amounts to 3.2%.

Tau trigger part

The method to determine the systematic uncertainty due to the τ_h trigger part is done very similarly to the method outlined above for the E_T^{miss} trigger part. A trigger efficiency is defined as

$$\epsilon_{trig} = \frac{\text{number of events passing the } \tau_h \text{ trigger}}{\text{number of events passing the } E_T^{miss} \text{ trigger}} \tag{5.14}$$

where the τ_h trigger signatures are EF_tau12_loose and EF_tau16_medium, respectively and the E_T^{miss} signature is tauNoCut_hasTrk_xe20. In addition to the τ_h-ID and the $\Delta\phi$ cut, the $S_{E_T^{miss}}$ cut is applied to

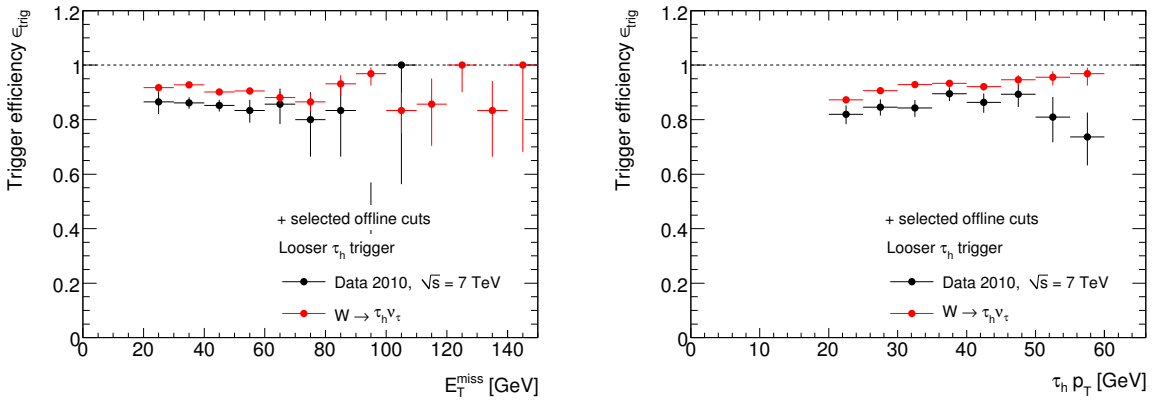

Figure 5.16: Trigger response of EF_tau12_loose with respect to $E_{\mathrm{T}}^{\mathrm{miss}}$ (left) and τ_{h} E_{T} (right) for data and signal Monte Carlo.

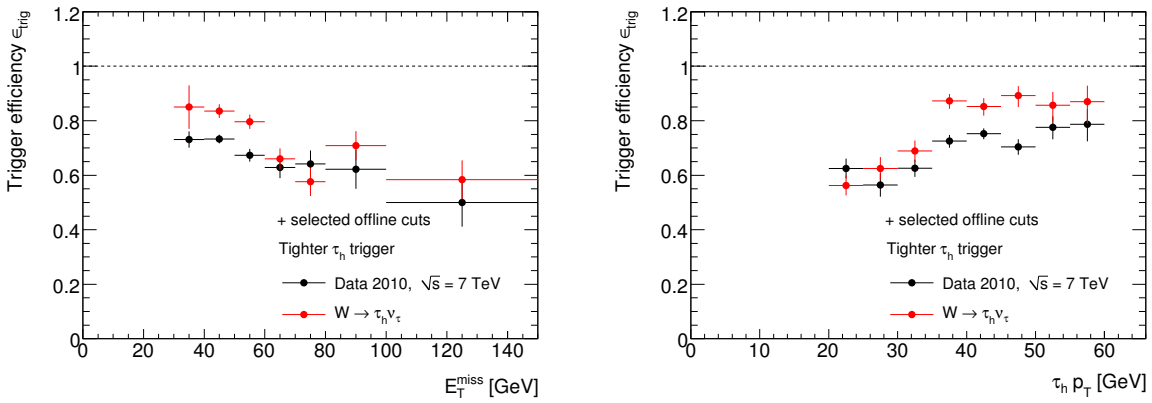

Figure 5.17: Trigger response of EF_tau16_medium with respect to $E_{\mathrm{T}}^{\mathrm{miss}}$ (left) and τ_{h} E_{T} (right) for data and signal Monte Carlo. The events have been tagged by a EF_xe35_noMu trigger.

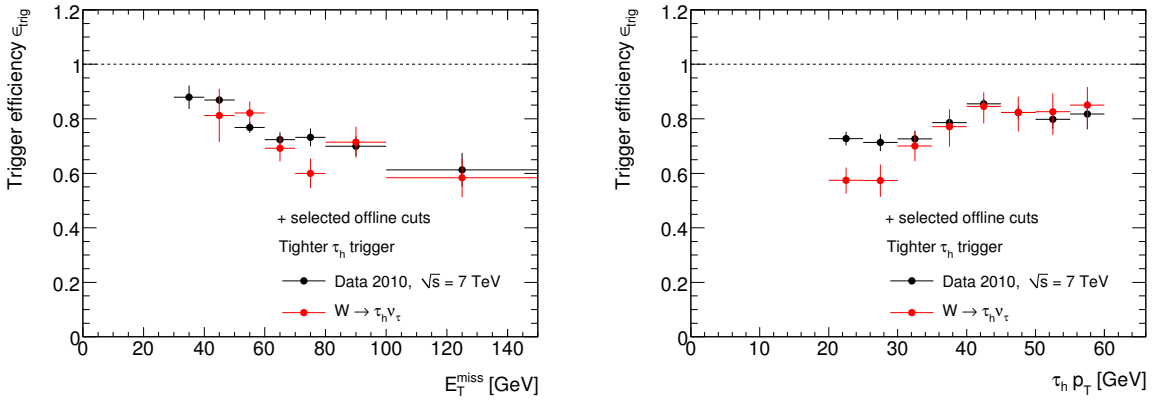

Figure 5.18: Trigger response of EF_tau16_medium with respect to $E_{\mathrm{T}}^{\mathrm{miss}}$ (left) and τ_{h} E_{T} (right) for data and signal Monte Carlo. The events have been tagged by a EF_xe40_noMu trigger.

Signature	Systematic
EF_tau12_loose	6.5%
xe20_noMu	1.0%
EF_tau12_loose_xe20_noMu	6.6%
EF_tau16_medium	5.0%
xe22_noMu	3.2%
EF_tau16_medium_xe22_noMu	5.9%
Combination	6.1%

Table 5.11: Summary of trigger systematics.

reduce background in the data sample. Figure 5.16 shows the τ_h trigger efficiency with respect to the tauNoCut_hasTrk_xe20 signature for data and signal Monte Carlo as a function of missing transverse energy and tau transverse momentum. Reasonable agreement can be observed. As in the case for the E_T^{miss} trigger the systematic uncertainty is obtained by integrating over all events with $E_T^{miss} > 30$ GeVand weighting by the E_T^{miss} distribution, and amounts to 6.5%. Figures 5.17 and 5.18 show the same distributions for EF_tau16_medium. A comparable level of agreement between data and simulations can be observed and the resulting uncertainty is 5.0%.

Summary

The total systematic error is calculated as the quadratic sum of the errors of the two τ_h and E_T^{miss} trigger parts separately for the two different triggers. Finally these errors are combined by weighting them with the respective luminosity fraction. The results are summarized in table 5.11.

The measured trigger efficiency for the combined τ_h-E_T^{miss} trigger is

$$\epsilon_{trigger} = 68.5 \pm 0.8\ (\text{stat}) \pm 6.1\ (\text{sys})\ \%.$$

5.7.5 Jet cleaning

As described in section 5.3, systematic effects from the jet cleaning are negligible.

5.7.6 Energy scale and resolution

The signal acceptance depends likewise on the energy scale of the topological clusters used in the computation of E_T^{miss} and $S_{E_T^{miss}}$ and the E_T^{miss} resolution. The procedure to evaluate the systematic error resulting from the energy scale and resolution uncertainties is the same as in [102]. A brief description of these methods is given below. In addition, the effect from excluding the badly modelled energy depositions in the forward calorimeter (FCal) inner ring cells is discussed.

Topological cluster energy scale

The transverse energy originating from W and Z events is mainly deposited in the central region of the calorimeter ($|\eta| < 3.2$). The uncertainty on the cluster energy scale is derived from E/p studies on single hadrons [103–106] as the differences between data and the Monte Carlo simulation. It is found to be

Systematic		$W \to \tau_h \nu_\tau$	$W \to e\nu_e$	$W \to \mu\nu_\mu$	$W \to \tau_\ell \nu_\tau$	$Z \to \tau\tau$
Energy scale $\lvert\eta\rvert < 3.2$						
a	$N-1$					
0.03	1.20	3.4%	9.1%	4.6%	6.0%	1.4%
-0.03	1.20	-5.6%	-2.1%	-5.0%	-2.6%	-5.3%
Energy scale $\lvert\eta\rvert > 3.2$						
a						
0.10		2.0%	3.9%	2.3%	5.1%	2.3%
-0.10		-2.4%	-4.5%	-1.9%	-1.4%	-1.8%
E_T^{miss} resolution						
α [GeV$^{1/2}$]						
0.50		-0.1%	-3.4%	2.3%	5.5%	-0.5%
0.55		-2.7%	-9.6%	1.1%	-1.3%	-2.6%
Excluding FCAL inner ring		0.6%	-2.8%	0.1%	-0.6%	0.8%
Total uncertainty		6.7%	14.1%	5.8%	9.6%	6.2%

Table 5.12: Relative differences of acceptances after rescaling the cluster energy, after smearing the reconstructed E_T^{miss} and after excluding the energy deposits in the forward calorimeter inner ring cells for the signal and the most important electro-weak background processes. The total systematic uncertainty is obtained by adding the larger of the respective individual contributions quadratically.

at most 10% for an E_T of 500 MeV and within 3% for higher E_T. In order to estimate the systematic uncertainty, the cluster energies have been scaled according to a factor

$$f^{+/-} = 1 \pm a\left(1 + \frac{N-1}{E_T}\right), \tag{5.15}$$

where a indicates the jet energy scale deviation at high transverse energies and N is fixed to give a 10% scale factor at 500 MeV. After the scaling the E_T^{miss} and $\sum E_T$ are recomputed.

The τ_h E_T has also been scaled according to the uncertainties quoted by the Tau Working Group [107]. These uncertainties depend on the number of tracks associated to the tau, the p_T of the candidate and the η region in which the tau was reconstructed. These uncertainties vary from 2.5% to 10%.

In the forward region ($|\eta| > 3.2$) the energy scale uncertainty is estimated from data to be $a = \pm 10\%$ [104] and therefore FCal cluster energies have been scaled by that amount. In this region, taus are not reconstructed.

E_T^{miss} resolution

The E_T^{miss} resolution has been measured to be $0.49\sqrt{\sum E_T}$ in minimum bias events, but is slightly worse when requiring the presence of high-p_T jets [105, 108], ranging from $0.5\sqrt{\sum E_T}$ to $0.55\sqrt{\sum E_T}$. To emulate this worse resolution, the x and y components of E_T^{miss} have been additionally smeared according to a Gaussian before applying the selection cuts. The obtained relative difference compared to the nominal acceptance after cuts has been added to the systematic uncertainty.

τ_h E_T [GeV]			[20,30]		[30,40]		[40,100]	
N_{trk}	τ_h-ID	N_{vtx}	ϵ [%]	sys.[%]	ϵ [%]	sys.[%]	ϵ [%]	sys.[%]
1	BDT medium	≤2	39.8 ± 0.1	(8.7 ± 0.9)	38.3 ± 0.1	(9.5 ± 1.0)	36.7 ± 0.2	(10.8 ± 1.2)
1	BDT medium	≥3	27.7 ± 0.1	(12.9 ± 1.0)	29.2 ± 0.1	(12.6 ± 1.1)	31.6 ± 0.1	(13.2 ± 1.0)
3	BDT tight	≤2	28.9 ± 0.2	(10.3 ± 2.1)	30.0 ± 0.2	(11.7 ± 1.6)	29.2 ± 0.2	(14.6 ± 3.9)
3	BDT tight	≥3	14.2 ± 0.1	(15.8 ± 2.6)	14.7 ± 0.1	(13.8 ± 1.6)	14.5 ± 0.2	(14.4 ± 3.1)

Table 5.13: Tau identification efficiencies ϵ for medium/tight BDT τ_h identification together with the relative systematic uncertainties.

Energy reconstruction in the FCAL inner ring

The energy reconstruction in the FCal inner ring cells ($|\eta| > 4.5$) is poorly reproduced by the simulations. The impact of excluding this region when computing E_T^{miss} and $\sum E_T$ is mainly a reduction of $\sum E_T$ and therefore an increase in the acceptance for the $S_{E_T^{miss}}$ selection.

The effects on the acceptances are summarized in table 5.12 for signal and the main electro-weak background contributions. The total systematic uncertainty is obtained by adding the larger deviation for each of the four contributions in quadrature.

5.7.7 Tau identification efficiency

To identify hadronic tau candidates, the medium BDT identification has been applied for 1-prong taus and the tight BDT selection has been applied for multi-prong taus. The identification efficiency for this analysis' event selection and the different sources of systematic uncertainties have been evaluated based on Monte Carlo studies [109] in bins of p_T and number of vertices. It is found that the efficiency is mainly affected by:

- Detector geometry
- used Monte Carlo generator (implemented underlying event and hadronic shower model)
- Noise thresholds of calorimeter cells used for cluster reconstruction

The resulting efficiencies and systematic uncertainties for 1- and 3-prong taus can be found in table 5.13. The efficiencies hardly vary with p_T since the BDT cuts have been optimized to yield a flat signal efficiency. The largest contribution to the systematic uncertainties results from the noise thresholds applied to the calorimeter cell energies before the clusters are built, especially in the case of a high vertex multiplicity. The smallest contribution comes from the detector geometry.

For τ_h candidates without any track requirement the systematic uncertainty varies between 8% and 13% [107]. Applying these errors yields a systematic uncertainty of 9.6% for $W \to \tau_h\nu_\tau$ events and 9.8% for $Z \to \tau\tau$ events, respectively, which affects the $C_{W\to\tau_h\nu_\tau}$ measurement and the electro-weak background estimation.

5.7.8 Jet fake rates of τ_h candidates

The τ_h fake rate from jets is calculated from a sample of W+jets events on which the standard ATLAS W+jets event selection is applied. The fake rate was measured by dividing the number of identified taus by the number of reconstructed τ_h candidates.

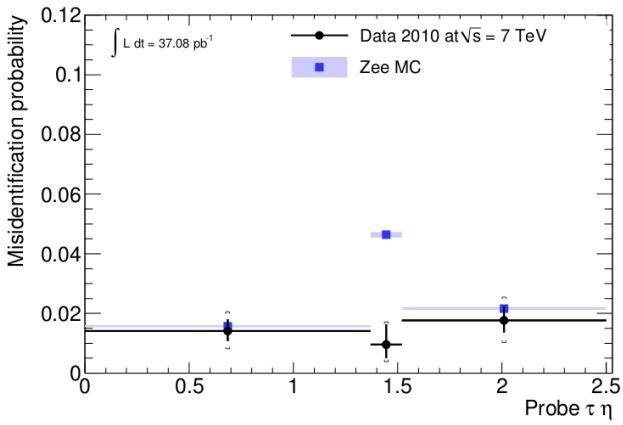

Figure 5.19: Electron-tau mis-identification probability for 1-prong τ_{h} candidates passing the medium BDT τ_{h}-ID with applied tight electron veto shown for $Z \to ee$ Monte Carlo and data. The combined statistical and systematic errors are indicated as well.

The fake rate is measured in both the $W \to e\nu_e$ and $W \to \mu\nu_\mu$ channel, giving consistent results. The uncertainty on this measurement has to be applied to the fraction of background events (considering the channels $W \to e\nu_e$, $W \to \mu\nu_\mu$ and $W \to \tau_\ell\nu_\tau$) where the lepton was not reconstructed and the τ_{h} is reconstructed from a jet in the event.

Using the systematic error from the jet fake rate determination and applying it to the different backgrounds, a systematic uncertainty on $W \to e\nu_e$ of 9%, on $W \to \mu\nu_\mu$ of 13% and of 31% on $W \to \tau_\ell\nu_\tau$, respectively, is obtained. The result is consistent with the fake rate measurement presented in chapter 4 where the tau fake rate due to QCD jets using a BDT tau identification algorithm is determined to be of order $O(5)\%$ for low energetic quark-initiated jets with a systematic uncertainty of order $O(10)\%$.

5.7.9 Lepton fake rates of τ_{h} candidates

Electrons tend to be reconstructed as tau candidates with one track. To suppress this background, a tight cut-based electron veto is applied. The mis-identification probability of electrons being reconstructed as 1-prong hadronic tau candidates after application of this veto and the τ_{h}-ID has been determined with a tag-and-probe method from a sample of $Z \to ee$ events [110]. The tag is chosen to be a tight electron and required to have an invariant mass close to the Z mass together with the probe object. Figure 5.19 shows the mis-identification probability for the BDT medium τ_{h}-ID with applied tight electron veto which is found to be within 1-2%. The amount of 3-prong tau candidates faked by electrons is found to be negligible.

Differences are observed between the fake rate in data and in Monte Carlo. To account for these differences, scale factors are applied to all tau candidates with one track that match a true electron. The difference in the resulting event numbers is taken as the systematic uncertainty. The sample with a non-negligible amount of tau candidates faked by an electron is the $W \to e\nu_e$ sample, the resulting systematic uncertainty amounts to 13.8%.

The mis-identification probability of muons being reconstructed as τ_{h} candidates is negligible.

	$W \to \tau_h \nu_\tau$	$W \to \tau_\ell \nu_\tau$	$Z \to \tau\tau$
Events	232946	126925	34095
GRL	232946	126925	34095
Trigger	19442.4±112.7	7152.4±68.7	2603.9±12.7
Collision cleaning	19433.7±112.6	7151.8±68.7	2603.3±12.7
Jet cleaning	19433.7±112.6	7151.8±68.7	2603.3±12.7
Jet in gap veto	15722.9±102.3	5812.1±62.3	2034.9±11.3
$min(\Delta\Phi(jet, E_T^{miss})) > 0.5$	14760.4±99.3	5478.4±60.5	1621.9±10.2
$E_T^{miss} > 30$GeV	11339.1±88	3423.5±48.3	1108.6±8.5
p_T (τ_h)> 20 GeV	11036.4±86.9	3269.2±47.3	1083.6±8.4
τ_h identification	5233.5±60.8	1077.6±27.3	551.9±6.1
p_T (τ_h)< 60GeV	4489±56.4	726.5±22.5	417±5.3
τ_h-ID ele/mu veto	3773.2±51.8	39.2±5.2	319.2±4.6
Electron veto	3753.3±51.7	29.8±4.5	316.1±4.6
Muon veto	3752.6±51.7	25.1±4.2	241.4±4.1
$S_{E_T^{miss}} > 6$	1787.7±35.8	15.1±3.2	100.9±2.6

Table 5.14: Cut flow for applying the event selection on PYTHIA Monte Carlo samples using the Perugia2010 underlying event and beam remnant. The quoted uncertainties are statistical only.

5.7.10 Electron reconstruction and identification efficiency

Studies of the electron reconstruction efficiency have been performed and a good agreement between data and Monte Carlo has been observed. For the identification efficiency of electrons p_T and η dependent scale factors have been determined using a tag-and-probe method on a simulated $Z \to ee$ sample [111], [112]. These scale factors have been applied to the events with identified electrons which are rejected in the course of the electro-weak background reduction. The relative difference between the number of rejected events before and after scaling is taken as an additional systematic uncertainty. The largest uncertainty is found to be 3.5% for $W \to e\nu_e$ events.

5.7.11 Muon reconstruction and identification efficiency

Studies of the muon reconstruction efficiency have been performed. Scale factors, dependent on the muon η and ϕ have been determined using a tag-and-probe method on a simulated $Z \to \mu\mu$ sample [113], [114]. The efficiency is found to be close to 1 over the entire p_T spectrum except for the barrel-end-cap transition regions where a difference of about 5% is observed. The scale factors are applied to the events with muon candidates that are rejected and the relative difference between the number of events before and after scaling is taken as an additional systematic uncertainty. This uncertainty amounts to 0.8%, similarly for all samples.

5.7.12 Underlying event modeling

The underlying event modeling might affect the distribution of the transverse missing energy. In order to study the effect on the signal and background selections, alternative models have been compared to the default AMBT1 [115] used in this analysis. The resulting cut flows for PYTHIA samples using the Perugia2010 [116] underlying event and beam remnant, which have been modelled based on minimum bias events measured at CDF for $W \to \tau_h\nu_\tau$, $W \to \tau_\ell\nu_\tau$ and $Z \to \tau\tau$, can be seen in table 5.14. Figures 5.20 to 5.21 show the $S_{E_T^{miss}}$ distribution for the different tunes. The deviation after the full cut selection is taken as an additional systematic uncertainty and amounts to 1.1% for $Z \to \tau\tau$ events and 1.3% for

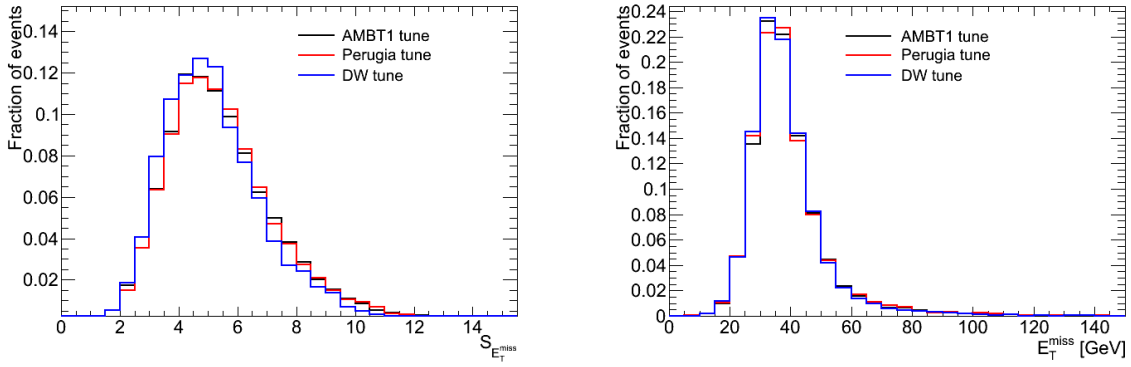

(a) (b)

Figure 5.20: $S_{E_T^{miss}}$ distribution for different underlying event models for the $W \to \tau_h \nu_\tau$ sample after the application of the preselection cuts (a). E_T^{miss} distribution for different underlying event models for the $W \to \tau_h \nu_\tau$ sample after the application of the preselection cuts (b).

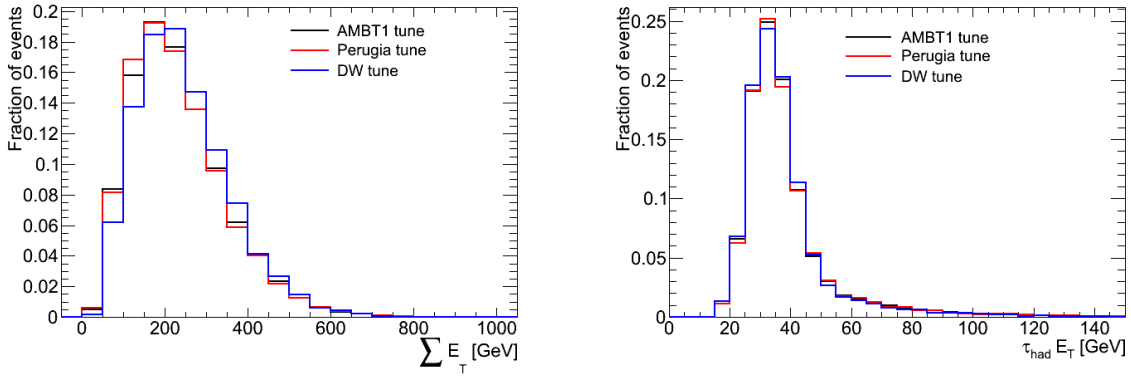

(a) (b)

Figure 5.21: $\sum E_T$ distribution for different underlying event models for the $W \to \tau_h \nu_\tau$ sample after the application of the preselection cuts (a). τ_h E_T distribution for different underlying event models for the $W \to \tau_h \nu_\tau$ sample after the application of the preselection cuts (b).

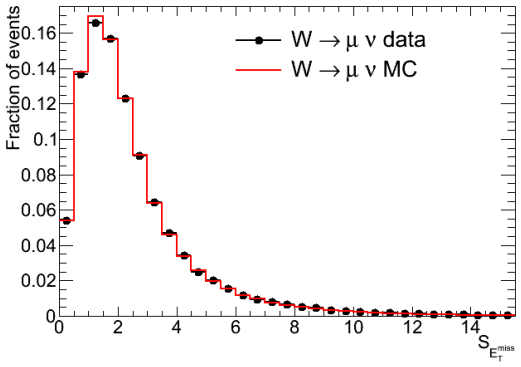

Figure 5.22: $S_{E_T^{miss}}$ distribution in data and Monte Carlo after a $W \to \mu \nu_\mu$ selection has been applied. The good agreement confirms that the underlying event is well modelled in the Monte Carlo and that the corresponding systematic uncertainty is reasonably estimated.

$W \to \tau_h \nu_\tau$ events. This systematic uncertainty is applied to all electro-weak samples.

The reasonability of this systematic uncertainty has been verified by comparisons to the embedding sample as shown in figure 5.7 where the underlying event is taken from data.

In addition, the $S_{E_T^{miss}}$ distribution has been compared for $W \to \mu\nu_\mu$ samples in data and Monte Carlo which are very pure and clean. The comparison of the distributions can be seen in figure 5.22. A very good agreement between the distributions is observed. The difference of the means in Monte Carlo and data lies within 1%. This shows that the underlying event is well modelled in the used Monte Carlo samples and further confirms the estimation of the systematic uncertainty resulting from the underlying event model based on the comparison to the Perugia sample.

5.7.13 Systematic uncertainties on QCD background estimation

Variable correlation

In order to check the stability of the ABCD method and to exclude a possible correlation between the used variables, the $S_{E_T^{miss}}$ threshold is varied between 4 and 6 for the control regions B and D. The largest deviation on the resulting number of background events is 2.7% which is taken as an additional systematic uncertainty.

Signal and electro-weak background contamination

In order to check the effect of the signal and electro-weak background contamination in the control regions, the contamination of the signal and electro-weak background in the four regions can be varied up and down by the combination of their respective systematic errors. The ABCD method is then applied again and the difference between the results is taken as a systematic.

This systematic uncertainty on the QCD background estimation is 2.1%.

5.7.14 Systematic uncertainties on $C_{W\to\tau_h\nu_\tau}$

The systematic uncertainty is mostly composed of the systematic uncertainties on the event selection as already discussed in sections 5.7.1 - 5.7.12. A summary of the systematic uncertainties on $C_{W\to\tau_h\nu_\tau}$ is given in table 5.22.

5.7.15 Systematic uncertainties on $A_{W\to\tau_h\nu_\tau}$

The systematic uncertainty on the geometric and kinematic acceptance factor $A_{W\to\tau_h\nu_\tau}$ defined by equation 5.11 is dominated by the limited knowledge of the proton PDFs and the modeling of the W boson production at the LHC. These uncertainties are assessed by considering three components:

Intrinsic uncertainties of the default PDF set This uncertainty is determined by varying the default sample within the relevant CTEQ6.6 errors [117]. For each error eigenvector i the upper and lower acceptances $A^{i+}_{W\to\tau_h\nu_\tau}$ and $A^{i-}_{W\to\tau_h\nu_\tau}$ are calculated and the uncertainty is derived using the standard prescription

$$\Delta A_{W\to\tau_h\nu_\tau} = \frac{1}{2}\sqrt{\sum_i \left(A^{i+}_{W\to\tau_h\nu_\tau} - A^{i-}_{W\to\tau_h\nu_\tau}\right)^2}. \tag{5.16}$$

The resulting uncertainty is found to be 1.0%.

	$A_{W\to\tau_h\nu_\tau}$
PYTHIA MRSTLO*	0.0975
PYTHIA CTEQ6.6	0.0991
PYTHIA HERAPDF1.0	0.0987
MC@NLO CTEQ6.6	0.1145
MC@NLO spin effect correction	0.0973

Table 5.15: Variation of $A_{W\to\tau_h\nu_\tau}$ values using different Monte Carlo configurations.

Cut	MRSTLO*	CTEQ6.6	HERAPDF1.0
Total	639288.0 ± 799.6	613870.5 ± 783.5	630972.3 ± 794.3
vis. τ p_T	317343.0 ± 563.3	304659.0 ± 552.0	313418.7 ± 559.8
vis τ η	204831.0 ± 452.6	200277.0 ± 447.5	205760.8 ± 453.6
$(\sum p^\nu)_T$	65217.0 ± 255.4	63613.8 ± 252.2	65161.4 ± 255.3
$\Delta\phi$(vis. τ, $\sum \nu$)	62333.0 ± 249.7	60824.1 ± 246.6	62305.3 ± 249.6
Acceptance $A_{W\to\tau_h\nu_\tau}$	0.0975 ± 0.0004	0.0991 ± 0.0004	0.0987 ± 0.0004

Table 5.16: Number of events in the signal Monte Carlo sample for different PDF sets after the acceptance cuts.

	$A_{W\to\tau_h\nu_\tau}$
CTEQ 6.6 eigenvector set	1.0%
Different PDF sets	1.6%
Model dependence	0.2%
Total systematic	1.9%
$A_{W\to\tau_h\nu_\tau}$ value	0.0975
Stat. error	0.0004
Syst. error	0.0019

Table 5.17: Summary table for systematic uncertainties affecting $A_{W\to\tau_h\nu_\tau}$.

	$\frac{\delta C_{W\to\tau_h\nu_\tau}}{C_{W\to\tau_h\nu_\tau}}$	$\frac{\delta N_{EW}}{N_{EW}}$	$\frac{\delta N_{QCD}}{N_{QCD}}$	$\frac{\delta\sigma^{fid}_{W\to\tau_h\nu_\tau}}{\sigma^{fid}_{W\to\tau_h\nu_\tau}}$
Trigger efficiency	6.1%	6.1%	-	7.0%
Energy scale	6.7%	8.7%	-	8.0%
τ_h-ID efficiency	9.6%	4.1%	-	10.3%
Jet τ_h mis-identification	-	7.2%	-	1.1%
Electron τ_h mis-identification	-	4.5%	-	0.7%
Pile-up reweighting	1.4%	1.2%	-	1.6%
Electron reconstruction/identification	-	1.2%	-	0.2%
Muon reconstruction	-	0.3%	-	0.04%
Underlying event modeling	1.3%	1.1%	-	1.5%
Cross section	-	4.5%	-	0.7%
QCD estimation: Stability/correlation	-	-	2.7%	0.2%
QCD estimation: Sig./EW contamination	-	-	2.1%	0.1%
Monte Carlo statistics	1.4%	2.4%	6.0%	1.5%
Total systematic uncertainty	13.4%	15.2%	6.9%	15.1%

Table 5.18: Summary table for systematic uncertainties. Correlations have been taken into account.

Uncertainty due to the used PDF set This uncertainty is evaluated by considering the maximal deviation between the acceptances obtained using the default MRSTLO* PDF set and the values obtained by reweighting the Monte Carlo events to the CTEQ6.6 and HERAPDF1.0 [118] PDF sets. The numbers of accepted events after the fiducial cuts have been applied as defined in section 5.6 are shown in table 5.16. The relative difference is found to be 1.6%.

Uncertainty due to used hadronization model This uncertainty is estimated using simulated events generated with MC@NLO together with the HERWIG hadronization modeling, CTEQ6.6 PDF set and ATLAS MC10 tune. The deviation with respect to the $A_{W\to\tau_h\nu_\tau}$ factor obtained using the default sample reweighted to the CTEQ6.6 PDF set is taken as the uncertainty. It amounts to 0.2%.

Since HERWIG does not handle tau polarizations correctly when combined with external generators, the acceptance obtained is corrected for this effect. The correction factor is derived from dedicated samples by switching on and off the polarization effects. The applied correction factor is 0.8500 ± 0.0002 where the quoted error is statistical only. This correction procedure leads to a more conservative estimate of the systematics.

A summary of the geometric and kinematic acceptance factors obtained from the PDF and hadronization model variations and the corresponding estimated relative uncertainties is given in tables 5.15, 5.16 and 5.17.

5.7.16 Summary on systematic uncertainties

The four tables 5.19, 5.20, 5.21, and 5.22 show summaries of the systematic uncertainties on the individual electro-weak sources, the number of electro-weak background events N_{EW}, the number of QCD background events N_{QCD} and $C_{W\to\tau_h\nu_\tau}$. The systematic uncertainties are not shown for $Z \to ee$, $Z \to \mu\mu$ and the hadronic $t\bar{t}$ decays, since less than 2 events survive the event selection and their contribution to the systematic uncertainty is thus negligible. In table 5.18 the resulting effect of the systematic uncertainties on the fiducial cross section is shown, taking into account the correlation between the different uncertainties.

	$W \to e\nu_e$	$W \to \mu\nu_\mu$	$W \to \tau_\ell\nu_\tau$	$Z \to \tau\tau$	$t\bar{t}$ Lep
Trigger efficiency	6.1%	6.1%	6.1%	6.1%	6.1%
Energy scale	14.1%	5.8%	9.6%	6.2%	-
τ_h identification	-	-	-	9.8%	10.3%
Jet τ_h mis-identification	9%	13%	31%	-	-
Electron τ_h mis-identification	13.8%	-	-	-	-
Pile-up reweighting	0.4%	2.3%	2.6%	1.2%	1.6%
Electron reconstruction/identification	3.5%	-	1.2%	0	0.5%
Muon reconstruction	-	0.8%	0	0.3%	0.4%
Jet cleaning	-	-	-	-	-
Underlying event modeling	1.1%	1.1%	1.1%	1.1%	1.1%
Cross section	3.8%	3.8%	5.0%	5.0%	9.7%

Table 5.19: Summary table for systematic uncertainties affecting the individual electro-weak backgrounds.

	EW Sum
Trigger efficiency	6.1%
Energy scale	8.7%
τ_h identification	4.1%
Jet τ_h mis-identification	7.2%
Electron τ_h mis-identification	4.5%
Pile-up reweighting	1.2%
Electron reconstruction/identification	1.2%
Muon reconstruction	0.3%
Jet cleaning	-
Underlying event modeling	1.1%
Cross section	4.5%
Total systematic	15.0%

Table 5.20: Summary table for systematic uncertainties affecting N_{EW}.

	QCD
QCD estimation: Stability/correlation	2.7%
QCD estimation: Sig./EW contamination	2.1%
Total systematic	3.4%

Table 5.21: Summary table for systematic uncertainties affecting N_{QCD}.

	$C_{W\to\tau_h\nu_\tau}$
Trigger efficiency	6.1%
Energy scale	6.7%
τ_h identification	9.6%
Pile-up reweighting	1.4%
Underlying event modeling	1.3%
Jet cleaning	-
Total systematic	13.3%
$C_{W\to\tau_h\nu_\tau}$ value	0.0799
Stat. error	0.0011
Syst. error	0.0107

Table 5.22: Summary table for systematic uncertainties affecting $C_{W\to\tau_h\nu_\tau}$.

N_{obs}	2335
N_{QCD}	127 ± 8 (stat) ± 4.3 (sys)
N_{EW}	283.6 ± 6.9 (stat) ± 42.6 (sys)
$A_{W\to\tau_h\nu_\tau}$	0.0975 ± 0.0004 (stat) ± 0.0019 (sys)
$C_{W\to\tau_h\nu_\tau}$	0.0799 ± 0.0011 (stat) ± 0.0107 (sys)
BR($\tau \to hadv$)	0.6479 ± 0.0007 [119]

Table 5.23: Summary of all numbers entering the calculation of the cross section together with their statistical and systematic uncertainties.

5.8 Cross section measurement

The quantities that have been measured together with their systematic and statistical uncertainty are summarized in table 5.23.

The measured fiducial cross section of the $W \to \tau_h\nu_\tau$ decay is

$$\sigma^{\text{fid}}_{W\to\tau_h\nu_\tau} = \sigma^{\text{fid}}_{W} \times \text{BR}(W \to \tau\nu) \times \text{BR}(\tau \to \text{hadrons} + \nu) = \left[0.70 \pm 0.02_{(\text{stat})} \pm 0.11_{(\text{sys})} \pm 0.02_{(\text{lumi})}\right] \text{ nb.}$$

After extrapolating the fiducial region, one obtains the total cross section to

$$\sigma^{\text{tot}}_{W\to\tau_h\nu_\tau} = \sigma^{\text{tot}}_{W} \times \text{BR}(W \to \tau\nu) \times \text{BR}(\tau \to \text{hadrons} + \nu) = \left[7.2 \pm 0.2_{(\text{stat})} \pm 1.1_{(\text{sys})} \pm 0.2_{(\text{lumi})}\right] \text{ nb}$$

and the total inclusive cross section to

$$\sigma^{\text{tot}}_{W\to\tau\nu_\tau} = \sigma^{\text{tot}}_{W} \times \text{BR}(W \to \tau\nu) = \left[11.1 \pm 0.3_{(\text{stat})} \pm 1.7_{(\text{sys})} \pm 0.4_{(\text{lumi})}\right] \text{ nb.}$$

The measured cross section is in good agreement with the theoretical NNLO cross section

$$\sigma^{\text{tot, theo}}_{W\to\tau\nu_\tau} = 10.46 \pm 0.52 \text{ [100]}$$

and is consistent with the measurements made at the ATLAS detector of the total cross section

$$\sigma^{\text{tot}}_{W} \times \text{BR}(W \to e\nu) = \left[10.26 \pm 0.03_{(\text{stat})} \pm 0.19_{(\text{sys})} \pm 0.35_{(\text{lumi})} \pm 0.16_{(\text{acc})}\right] \text{ nb [98, 120].}$$

and the total cross section

$$\sigma^{\text{tot}}_{W} \times \text{BR}(W \to \mu\nu) = \left[10.21 \pm 0.03_{(\text{stat})} \pm 0.18_{(\text{sys})} \pm 0.35_{(\text{lumi})} \pm 0.15_{(\text{acc})}\right] \text{ nb [98, 120].}$$

A comparison of the cross section measurements for the different leptonic final states together with the theoretical expectation is shown in figure 5.23.

5.9 Summary

In this chapter a measurement of the total production cross section

$$\sigma^{\text{tot}}_{W\to\tau_h\nu_\tau} \equiv \sigma(pp \to W) \times \text{BR}(W \to \tau\nu) \times \text{BR}(\tau \to \text{hadrons} + \nu)$$

at a center-of-mass energy of $\sqrt{s} = 7$ TeV is described. It is based on the full dataset recorded by the ATLAS experiment in the year 2010 which corresponds to an integrated luminosity of $\int L\,\text{dt} =$

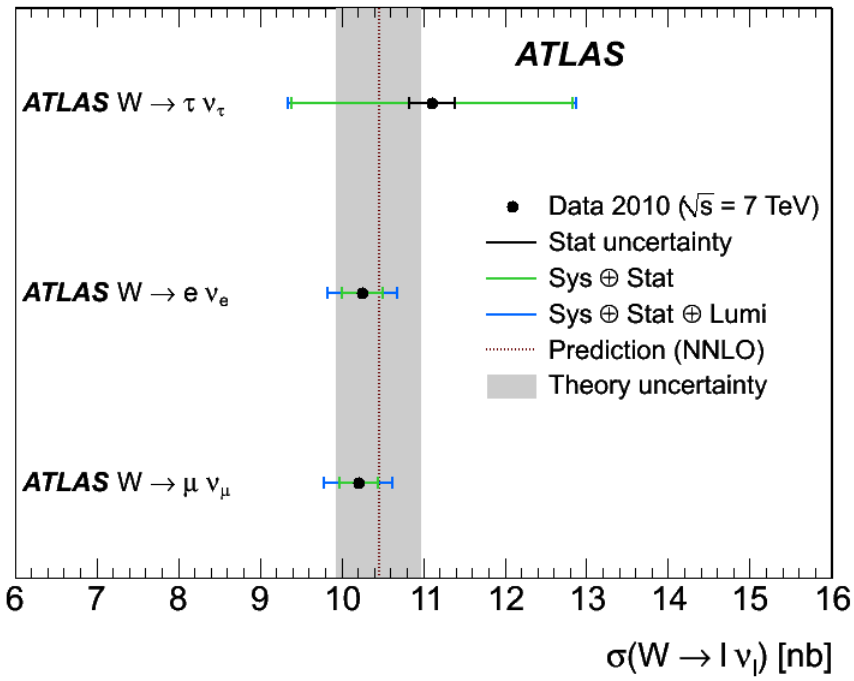

Figure 5.23: Cross sections for the different $W \to \ell\nu$ channels measured in ATLAS with 2010 data. Systematic, luminosity and statistical errors are added in quadrature. The theoretical NNLO expectation is also shown.

34.3 pb^{-1}.

$W \to \tau_h \nu_\tau$ signal events have been selected by using a combined tau-E_T^{miss} trigger and by requiring a well identified tau and a certain amount of well measured missing transverse energy. The majority of the background consists of $Z \to \tau\tau$ events and events with true or mis-measured E_T^{miss} and a jet faking the tau. Thus, it has been further exploited that in signal events the E_T^{miss} and the direction of any jet are unlikely to be aligned and events containing light leptons are vetoed.

After the selection a clear signal is observed. The detector acceptance, the cut efficiency and the remaining electro-weak background is estimated using simulated events which have been checked to give a good description of the data. The QCD background has been directly estimated from data using a sideband method.

Overall good agreement with theory can be stated, although a few more signal events than expected have been found. Sources of systematic errors have been studied. The measurement precision is limited mainly by uncertainties on the trigger and tau identification efficiency, the energy scale and the tau-jet mis-identification probability.

In conclusion, the cross section has been measured to

$$\sigma^{tot}_{W\to\tau\nu_\tau} = \sigma^{tot}_{W} \times \text{BR}(W \to \tau\nu) = \left[11.1 \pm 0.3_{(stat)} \pm 1.7_{(sys)} \pm 0.4_{(lumi)}\right] \text{ nb}.$$

In figure 5.23 a comparison between the measured cross sections for the leptonic W decays and the theoretical prediction can be seen. The cross section $\sigma^{tot}_{W\to\tau\nu_\tau}$ is slightly higher than expected but well within the somewhat large uncertainties. In the next chapter an alternative measurement method is explored which aims for reducing the systematic error.

Chapter 6

A measurement of the ratio of branching fractions $\Gamma(W \to \tau\nu_\tau)/\Gamma(W \to \mu\nu_\mu)$

The result presented in the previous chapter naturally raises the question if one could measure the production cross section $\sigma(pp \to W) \times \mathrm{BR}(W \to \tau\nu_\tau)$ with even higher precision. Given the fact that the delivered total integrated luminosity has ever since increased to 25 fb^{-1} until the end of Run I in the year 2012, one could think of simply adding the additional data to the analysis.

A mere repetition of the measurement with more data, however, proves not to be very promising, because the low-energy-threshold tau and $E_{\mathrm{T}}^{\mathrm{miss}}$ triggers needed for the event signature selection are heavily prescaled during all later runs. Therefore, in this chapter an alternative method is described, which rather aims to measure the ratio of cross sections

$$\frac{\sigma(\mathrm{pp} \to \mathrm{W}) \times \mathrm{BR}(W \to \tau\nu_\tau)}{\sigma(\mathrm{pp} \to \mathrm{W}) \times \mathrm{BR}(W \to \mu\nu_\mu)} = \frac{\mathrm{BR}(W \to \tau\nu_\tau)}{\mathrm{BR}(W \to \mu\nu_\mu)} \equiv \frac{\Gamma(W \to \tau\nu_\tau)}{\Gamma(W \to \mu\nu_\mu)}, \tag{6.1}$$

instead of directly measuring the individual cross sections themselves.

It is organized as follows: in section 6.1 the motivation for this kind of measurement is outlined in more detail, before the analysis method is described briefly in section 6.2. Section 6.3 gives an overview about the used data and simulation samples. An additional section 6.4 summarizes the corrections applied to the Monte Carlo before it can be used for comparisons with the data. The event selection and background estimation are reported in sections 6.5 and 6.6. The chapter concludes with a discussion of the results in section 6.8 and lists various sources of systematic uncertainties in section 6.9.

6.1 Motivation

To reach an accuracy as high as possible for a measurement of the cross section $\sigma(pp \to W) \times \mathrm{BR}(W \to \tau\nu_\tau)$ would be particularly interesting. The most precise measurement so far, which was done at the Large Electron Positron collider (LEP) [32] at CERN, indicates a small excess of the cross section of 2.7 standard deviations towards higher values [15]. Also the result of the last chapter seems to point into the same direction, albeit still with rather large errors. This is even more astounding since the very precise corresponding measurements of the cross sections $\sigma(pp \to W) \times \mathrm{BR}(W \to \mu\nu_\mu)$ and $\sigma(pp \to W) \times \mathrm{BR}(W \to e\nu_e)$ show no such deviations from the expectation. With other words, a real enhancement of the cross section $\sigma(pp \to W) \times \mathrm{BR}(W \to \tau\nu_\tau)$ would violate the so-called Lepton Universality, which predicts within the Standard Model that all leptons behave in many aspects very similarly. In particular, all leptons are expected to couple with the same strength to the W and therefore all weak production cross sections $\sigma(pp \to W) \times \mathrm{BR}(W \to \ell\nu_\ell)$ should be identical (if lepton masses are neglected).

As already mentioned in the introduction, a significantly higher precision cannot be reached by simply adding more data to the analysis, due to the prescaling of the triggers. To probe Lepton Universality,

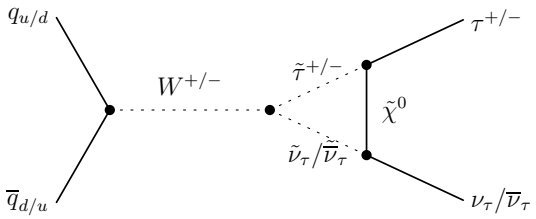

Figure 6.1: Feynman diagram of the decay of a W boson containing a vertex correction. An enhancement of the cross section arises by taking additional particles into account, which are predicted by e.g Supersymmetry.

however, it suffices to measure the various ratios of the cross sections times branching fraction. Consequently, if Lepton Universality applies, these ratios are equal to 1.

What are now possible physics processes that lead to an enhanced cross section $\sigma(pp \to W) \times \mathrm{BR}(W \to \tau\nu_\tau)$ with respect to the Standard Model? A charged Higgs boson $H^\pm$ as it is predicted by some of the most attractive and best motivated extensions of the Standard Model like e.g. Supersymmetry (SUSY) [26] shares the same final state with the W. It is also expected to couple more strongly to the more massive tau than to muons or electrons. This possibility, however, is disfavored by measurements of the angular distributions of the decay products which discriminate between a spin-1 W and a spin-0 $H^\pm$.

A contribution to the cross section can also emerge via higher-order vertex corrections, if additional, yet undetected particles are taken into account. An example of such a process is depicted in figure 6.1. Here, the decay vertex is corrected by an extra loop-term containing a stau, a sneutrino and a neutralino, particles which are also postulated by Supersymmetry.

The next section describes a method which aims to measure the ratio of branching fractions $\Gamma(W \to \tau\nu_\tau)/\Gamma(W \to \mu\nu_\mu)$ and lists reasons why one expects uncertainties to be comparatively small.

6.2 Method

Instead of directly determining the cross section $\sigma(pp \to W) \times \mathrm{BR}(W \to \tau\nu_\tau)$, to probe Lepton Universality the ratio of branching fractions $\Gamma(W \to \tau\nu_\tau)/\Gamma(W \to \mu\nu_\mu)$ shall be measured. For that, $W \to \tau\nu_\tau$ events, where the tau subsequently decays into a muon, and $W \to \mu\nu_\mu$ events are selected simultaneously. From now on, the expression $W \to \tau_\mu\nu_\tau$ should serve as an abbreviation for the decay chain $W \to \tau\nu_\tau \to \mu\nu_\mu\nu_\tau\nu_\tau$, thus the muonic decay channel of $W \to \tau\nu_\tau$. This is possible because both processes are sharing exactly the same visible final state. Now, the differences in suitable variables are exploited to perform a fit of simulated template samples to data in order to obtain the respective fraction with which they contribute to the overall distribution. This procedure is sketched in figure 6.2.
The ratio of branching fractions then computes to

$$\frac{\Gamma(W \to \tau\nu)}{\Gamma(W \to \mu\nu)} = \frac{1}{\mathrm{BR}(\tau \to \mu\nu_\tau\nu_\mu)} \frac{\epsilon_{(\mathrm{W}\to\mu\nu_\mu)}}{\epsilon_{(\mathrm{W}\to\tau_\mu\nu_\tau)}} \frac{f_{(\mathrm{W}\to\tau_\mu\nu_\tau)}}{f_{(\mathrm{W}\to\mu\nu_\mu)}}, \tag{6.2}$$

where $\mathrm{BR}(\tau \to \mu\nu_\tau\nu_\mu)$ is the branching ratio of the tau decaying into a muon, $\epsilon_{(\mathrm{W}\to\mu\nu_\mu)}$ and $\epsilon_{(\mathrm{W}\to\tau_\mu\nu_\tau)}$ are the selection efficiencies estimated from the respective Monte Carlo samples, and $f_{(\mathrm{W}\to\tau_\mu\nu_\tau)}$ and $f_{(\mathrm{W}\to\mu\nu_\mu)}$ are the fractions measured from a fit of the template samples to data.

An analysis using the decay $W \to \tau_\mu\nu_\tau$ has the disadvantage of poorer statistics compared to $W \to \tau_\mathrm{h}\nu_\tau$ due to the lower branching ratio but profits from the fact that muons are experimentally much easier accessible than hadronically decaying taus. Not only do muons have a very clean signature in

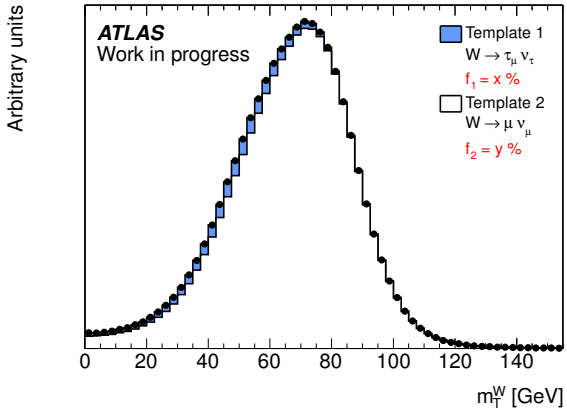

Figure 6.2: Sketch of the measurement method. A clean sample of both $W \to \tau_\mu \nu_\tau$ and $W \to \mu\nu_\mu$ events is selected. From a fit of corresponding simulated template samples to data (black dots), the respective fractions f_i of events are obtained and the ratio of branching fractions can be computed. For that, variables which discriminate between the two processes like e.g. the transverse mass of the W $m_{\mathrm{T}}^{\mathrm{W}}$ are used.

the detector, they also do not suffer that much from systematic uncertainties. Moreover, by measuring the ratio, some systematics even cancel out completely, e.g. the uncertainty on the total integrated luminosity.

It is usually considered difficult to distinguish between the muonic decay channel of $W \to \tau\nu_\tau$ and $W \to \mu\nu_\mu$ events. This statement, however, applies mainly if one seeks for a clean separation between the two processes. For the method described here, it is sufficient to find variables whose shapes differ enough for the fraction fit to converge. In figure 6.3 a selection of such variables is shown. One can see that e.g. the transverse momentum p_{T}^{μ} of the muon peaks at lower values for $W \to \tau_\mu \nu_\tau$ than for $W \to \mu\nu_\mu$ events. This is because in the former case the muon comes from the decay of the light tau instead of the much heavier W. Also, the distribution for the transverse missing energy $E_{\mathrm{T}}^{\mathrm{miss}}$ is shifted towards lower values for $W \to \tau_\mu \nu_\tau$ which can be explained by the neutrinos produced in the tau decay being emitted in the opposite direction of the muons from the W decay, leading to the cancellation of their respective contributions. In addition, the distribution of the angle ϕ between the muon and the missing transverse energy in the azimuthal plane peaks around π for both $W \to \tau_\mu \nu_\tau$ and $W \to \mu\nu_\mu$ events. The peak, however, is smeared out for $W \to \tau_\mu \nu_\tau$ events because of the reduced correlation between the direction of the muon and the direction of the neutrino from the initial W decay. The transverse mass of the W defined as

$$m_{\mathrm{T}}^{\mathrm{W}} = \sqrt{2 p_{\mathrm{T}}^{\mu} E_{\mathrm{T}}^{\mathrm{miss}} \left(1 - \cos\phi\left(p_{\mathrm{T}}^{\mu}, E_{\mathrm{T}}^{\mathrm{miss}}\right)\right)} \tag{6.3}$$

combines the discriminating power of p_{T}^{μ}, $E_{\mathrm{T}}^{\mathrm{miss}}$ and the angle ϕ between the muon and the missing transverse energy. Also, in contrast to $W \to \tau_{\mathrm{h}} \nu_\tau$, the muon in $W \to \tau_\mu \nu_\tau$ events is characterized by a significantly higher transverse impact parameter, since the heavy tau travels quite a distance before it decays.

All these variables are deemed suitable to be used for the measurement method. In principle it is also possible to combine the discriminating power of more than one variable in a multi-dimensional fit.

In the next section the event selection for the analysis is described.

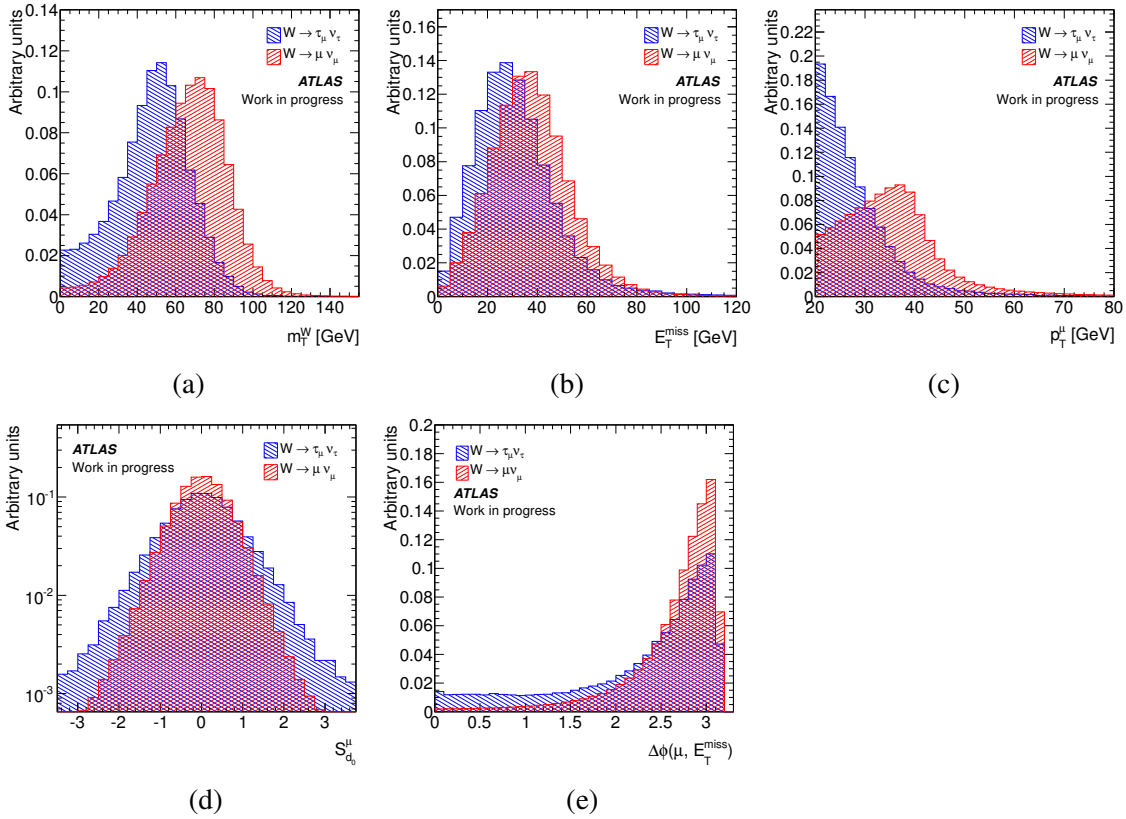

Figure 6.3: Variables discriminating between $W \to \tau_\mu \nu_\tau$ and $W \to \mu\nu_\mu$ decays: transverse mass of the W m_T^W (a), missing transverse energy E_T^{miss} (b), transverse momentum of the muon p_T^μ (c), impact parameter significance $S^\mu_{d_0}$ of the muon (d), angle between the muon and the missing transverse energy $\Delta\phi\left(\mu, E_T^{miss}\right)$ (e).

6.3 Data and simulation samples

The analysis uses data recorded by ATLAS during the run periods D - M in the year 2011. The data taken during periods A and B are not included because of differing run conditions. Overall, the available amount of data corresponds to an integrated luminosity of $\int L\, dt = 4.70\ \text{fb}^{-1}$ using the `OflLumi-7TeV-002` luminosity calibration [90], [91].

6.3.1 Data samples

An overview on the used data samples can be found in table 6.1. Similar to the situation described earlier in section 5.2.1, the data samples have been split into two periods. Again, these two periods correspond to the usage of two different triggers because the looser was prescaled during later runs.

Signal blinding

In order not to bias the measurement results, it is conventional to get an understanding of the relevant backgrounds first. This usually means to choose and tune the analysis cuts on a subset of the available data which is dominated by background events before looking at the regions where a signal is expected.

The design of the measurement method, however, does not allow for such a "signal blinding" in a

Trigger period	Run period	Run subperiods	Run range	Approximate luminosity [fb^{-1}]
First period	D	D1 - D7	179710 - 180481	0.17
	E	E1	180614 - 180776	0.04
	F	F1 - F3	182013 - 182519	0.13
	G	G1 - G6	182726 - 183462	0.51
	H	H1 - H4	183544 - 184169	0.26
Second period	I	I1 - I4	185353 - 186493	0.34
	J	J1 - J2	186516 - 186755	0.23
	K	K1 - K6	186873 - 187815	0.59
	L	L1 - L7	188902 - 190343	1.40
	M	M1 - M10	190503 - 191933	1.03
Total				4.70

Table 6.1: Overview on the ATLAS data samples used in the analysis. For the computation of the quoted integrated luminosities only runs on the list of good quality runs are considered. The total integrated luminosity is $\int L\,\mathrm{d}t = 4.70\ \mathrm{fb}^{-1}$.

strict sense since the signal and background are heavily overlapping in all variables. This also means that it is very difficult to study the validity of the individual template shapes independent from each other. Thus, for the establishment of the cuts, a small fraction (10%) of the total available data has been used (in order to obtain a full representation of the run conditions during the entire 2011 run, every 10th event has been considered). The actual measurement can then be performed on the remaining 90% of the data events.

6.3.2 Simulation samples

The measured data is compared with simulated Monte Carlo events of proton-proton collisions at a center-of-mass energy of $\sqrt{s} = 7$ TeV using various generators. Just as in the analyses described in the previous chapters, the simulation of the detector response is done with the ATLAS simulation framework [80]. Next to the signal processes $W \to \mu\nu_\mu$ and $W \to \tau_\mu\nu_\tau$, the samples incorporate the most important non-QCD background processes such as other W and Z, di-boson and top quark decays. As in the previous analysis, the QCD background is estimated using a data-driven technique which is described in section 6.6. An overview on the used sample types, their corresponding cross sections and the generated statistics can be found in tables 6.2 - 6.6. Wherever necessary, these simulated events have been modified by weight factors in order to match the conditions found in the course of data taking as close as possible and to correct for discrepancies with measurements. A summary and brief description of all weight factors can be found in section 6.4.

As also described in the previous chapter, the $W \to \tau\nu_\tau$ sample comprises all tau decays inclusively. For this analysis, only the taus decaying into muons are considered as signal and the hadronically decaying taus and the taus decaying into electrons are considered as background. Again, the sample has to be split beforehand with the help of the truth information of the simulated events; an event is considered as signal if a true tau produced in a W decay has a final state muon in its list of child particles.

Event generator: POWHEGPYTHIA6					
Channel	Dataset ID	$\sigma \cdot$ BR [nb]	Dataset tag	Number of events	Remarks
$W^+ \to \tau_\mu^+ \nu_\tau$	107390	$5.9822 \cdot 0.176$	p1035	264927	$W \to \tau_\mu \nu_\tau$ Signal
$W^- \to \tau_\mu^- \nu_\tau$	107391	$4.0870 \cdot 0.176$	p1035	264231	
$W \to \tau_\mu \nu_\tau$ (total)	-	$10.0692 \cdot 0.176$	-	539158	
$W^+ \to \mu^+ \nu_\mu$	108298	5.9829	p1035	22996963	$W \to \mu\nu_\mu$ Signal
$W^- \to \mu^- \nu_\mu$	108301	4.0875	p1035	12993984	
$W \to \mu\nu_\mu$ (total)	-	10.0704	-	35990947	
$W^+ \to e^+ \nu_e$	108297	5.9822	p1035	$16 \cdot 10^6$	$W \to e\nu_e$ Background
$W^- \to e^- \nu_e$	108300	4.0870	p1035	$12 \cdot 10^6$	
$W \to e\nu_e$ (total)	-	10.0692	-	$28 \cdot 10^6$	
$W^+ \to \tau^+ \nu_\tau$ other	107390	$5.9822 \cdot 0.824$	p1035	264927	$W \to \tau\nu_\tau$ Background
$W^- \to \tau^- \nu_\tau$ other	107391	$4.0870 \cdot 0.834$	p1035	264231	
$W \to \tau\nu_\tau$ other (total)	-	$10.0692 \cdot 0.834$	-	539158	
$Z/\gamma^* \to ee$ ($m_{\ell\ell} > 53.8$ GeV)	108303	1.006	p1035	$10 \cdot 10^6$	$Z \to ee$ Background
$Z/\gamma^* \to ee$ (38 GeV $< m_{\ell\ell} <$ 53.8 GeV)	129806	0.0878	p1035	$3 \cdot 10^6$	
$Z/\gamma^* \to ee$ (total)	-	1.0948	-	$13 \cdot 10^6$	
$Z/\gamma^* \to \mu\mu$ ($m_{\ell\ell} > 53.8$ GeV)	108304	1.006	p1035	$10 \cdot 10^6$	$Z \to \mu\mu$ Background
$Z/\gamma^* \to \mu\mu$ (38 GeV $< m_{\ell\ell} <$ 53.8 GeV)	129807	0.0878	p1035	$3 \cdot 10^6$	
$Z/\gamma^* \to \mu\mu$ (total)	-	1.0948	-	$13 \cdot 10^6$	
$c\bar{c}$	106059	73.90	p1035	1499697	QCD Background
$b\bar{b}$	108405	28.40	p1035	4494082	

Table 6.2: Overview on the PYTHIA [121–123] Monte Carlo datasets used in the analysis. Next to the signal processes $W \to \tau_\mu \nu_\tau$ and $W \to \mu\nu_\mu$, the list consists of the most important non-QCD background processes such as other W and Z decays. PYTHIA datasets for $Z \to \tau\tau$ are not available at the time thus ALPGEN+HERWIG [124] datasets are used. No additional k-factors are applied to the cross sections. Dedicated heavy-flavor QCD processes are used for coarse checks of the amount of QCD background to be expected. Ultimately, however, the QCD background is estimated from data.

Event generator: ALPGENHERWIG						
Channel	Dataset ID	$\sigma\times$ BR [nb]	k-factor	Dataset tag	Number of events	Remarks
$W \to \tau_\mu \nu_\tau$ + 0 Partons	107700	6.91960×0.176	1.20	p1035	605854	
$W \to \tau_\mu \nu_\tau$ + 1 Parton	107701	1.30420×0.176	1.20	p1035	442830	
$W \to \tau_\mu \nu_\tau$ + 2 Partons	107702	0.37783×0.176	1.20	p1035	665191	$W \to \tau_\mu \nu_\tau$
$W \to \tau_\mu \nu_\tau$ + 3 Partons	107703	0.10188×0.176	1.20	p1035	178813	Signal
$W \to \tau_\mu \nu_\tau$ + 4 Partons	107704	0.02575×0.176	1.20	p1035	44503	Variation 2
$W \to \tau_\mu \nu_\tau$+ $\geq$ 5 Partons	107705	0.00692×0.176	1.20	p1035	11567	
$W \to \tau_\mu \nu_\tau$ (total)	-	8.73618×0.176	1.20	-	1948758	
$W \to \mu \nu_\mu$ + 0 Partons	107690	6.91860	1.20	p1035	6962239	
$W \to \mu \nu_\mu$ + 1 Parton	107691	1.30320	1.20	p1035	4988236	
$W \to \mu \nu_\mu$ + 2 Partons	107692	0.37818	1.20	p1035	3768737	$W \to \mu \nu_\mu$
$W \to \mu \nu_\mu$ + 3 Partons	107693	0.10151	1.20	p1035	1008446	Signal
$W \to \mu \nu_\mu$ + 4 Partons	107694	0.02564	1.20	p1035	254950	Variation 2
$W \to \mu \nu_\mu$+ $\geq$ 5 Partons	107695	0.00704	1.20	p1035	70000	
$W \to \mu \nu_\mu$ (total)	-	8.73417	1.20	-	17052608	
$W \to e \nu_\mathrm{e}$ + 0 Partons	107680	6.9304	1.20	p1035	6952874	
$W \to e \nu_\mathrm{e}$ + 1 Parton	107681	1.3051	1.20	p1035	4998487	
$W \to e \nu_\mathrm{e}$ + 2 Partons	107682	0.37813	1.20	p1035	3768632	
$W \to e \nu_\mathrm{e}$ + 3 Partons	107683	0.10186	1.20	p1035	1008947	$W \to e \nu_\mathrm{e}$
$W \to e \nu_\mathrm{e}$ + 4 Partons	107684	0.02568	1.20	p1035	250000	Background
$W \to e \nu_\mathrm{e}$+ $\geq$ 5 Parton	107685	0.00699	1.20	p1035	69999	
$W \to e \nu_\mathrm{e}$ (total)	-	8.74816	1.20	-	17048939	
$W \to \tau \nu_\tau$ + 0 Partons	107700	6.91960×0.824	1.20	p1035	2812442	
$W \to \tau \nu_\tau$ + 1 Parton	107701	1.30420×0.824	1.20	p1035	2056364	
$W \to \tau \nu_\tau$ + 2 Partons	107702	0.37783×0.824	1.20	p1035	3085795	$W \to \tau_\mathrm{h} \nu_\tau$
$W \to \tau \nu_\tau$ + 3 Partons	107703	0.10188×0.824	1.20	p1035	831133	and
$W \to \tau \nu_\tau$ + 4 Partons	107704	0.02575×0.824	1.20	p1035	205495	$W \to \tau_\mathrm{e} \nu_\tau$
$W \to \tau \nu_\tau$+ $\geq$ 5 Partons	107705	0.00692×0.824	1.20	p1035	53433	Background
$W \to \tau \nu_\tau$ other (total)	-	8.73618×0.824	1.20	-	9044662	
$Z \to ee$ + 0 Partons	107650	0.66832	1.25	p1035	6618284	
$Z \to ee$ + 1 Parton	107651	0.13436	1.25	p1035	1334897	
$Z \to ee$ + 2 Partons	107652	0.04054	1.25	p1035	2004195	
$Z \to ee$ + 3 Partons	107653	0.01116	1.25	p1035	549949	$Z \to ee$
$Z \to ee$ + 4 Partons	107654	0.00288	1.25	p1035	149948	Background
$Z \to ee$ + $\geq$ 5 Partons	107655	0.00083	1.25	p1035	50000	
$Z \to ee$ (total)	-	0.85809	1.25	-	10707273	

Table 6.3: Overview on the ALPGEN+HERWIG [124] Monte Carlo datasets used in the analysis (Part 1). Next to variations of the signal processes $W \to \tau_\mu \nu_\tau$ and $W \to \mu \nu_\mu$, the list consists of the most important non-QCD background processes such as other W and Z decays.

Event generator: ALPGENHERWIG						
Channel	Dataset ID	$\sigma\times$ BR [nb]	k-factor	Dataset tag	Number of events	Remarks
$Z \to \mu\mu$ + 0 Partons	107660	0.66868	1.25	p1035	6615230	$Z \to \mu\mu$ Background
$Z \to \mu\mu$ + 1 Parton	107661	0.13414	1.25	p1035	1334296	
$Z \to \mu\mu$ + 2 Partons	107662	0.04033	1.25	p1035	1999941	
$Z \to \mu\mu$ + 3 Partons	107663	0.01119	1.25	p1035	549896	
$Z \to \mu\mu$ + 4 Partons	107664	0.00275	1.25	p1035	150000	
$Z \to \mu\mu$ + $\geq$ 5 Partons	107665	0.00077	1.25	p1035	50000	
$Z \to \mu\mu$ (total)	-	0.85786	1.25	-	10699363	
$Z \to \tau\tau$ + 0 Partons	107670	0.66840	1.25	p1035	10613179	$Z \to \tau\tau$ Background
$Z \to \tau\tau$ + 1 Parton	107671	0.13481	1.25	p1035	3334137	
$Z \to \tau\tau$ + 2 Partons	107672	0.04036	1.25	p1035	1004847	
$Z \to \tau\tau$ + 3 Partons	107673	0.01125	1.25	p1035	209849	
$Z \to \tau\tau$ + 4 Partons	107674	0.00279	1.25	p1035	144999	
$Z \to \tau\tau$ + $\geq$ 5 Partons	107675	0.00077	1.25	p1035	45000	
$Z \to \tau\tau$ (total)	-	0.85838	1.25	-	15352011	

Table 6.4: Overview on the ALPGEN+HERWIG [124] Monte Carlo datasets used in the analysis (Part 2). Next to variations of the signal processes $W \to \tau_\mu\nu_\tau$ and $W \to \mu\nu_\mu$, the list consists of the most important non-QCD background processes such as other W and Z decays.

Event generator: MC@NLO					
Channel	Dataset ID	$\sigma\times$ BR [nb]	Dataset tag	Number of events	Remarks
$W^+ \to \tau_\mu\nu_\tau$	108328	5.9422×0.176	p1035	176339	$W \to \tau_\mu\nu_\tau$
$W^- \to \tau_\mu\nu_\tau$	108329	4.0595×0.176	p1035	177052	Signal
$W \to \tau_\mu\nu_\tau$ (total)	-	1.7602992	-	353391	Variation 1
$W^+ \to \mu\nu_\mu$	106083	5.9439	p1035	7988774	$W \to \mu\nu_\mu$
$W^- \to \mu\nu_\mu$	106084	4.0637	p1035	5997284	Signal
$W \to \mu\nu_\mu$ (total)	-	10.0076	-	13986058	Variation 1
Single Top (t channel, electrons)	108340	0.00712	p1035	$0.3 \cdot 10^6$	Single Top Background
Single Top (t channel, muons)	108341	0.00712	p1035	$0.3 \cdot 10^6$	
Single Top (t channel, total)	-	0.01424	-	$0.6 \cdot 10^6$	
Single Top (s channel, electrons)	108343	0.00047	p1035	$0.3 \cdot 10^6$	Single Top Background
Single Top (s channel, muons)	108344	0.00047	p1035	$0.3 \cdot 10^6$	
Single Top (s channel, total)	-	0.00094	-	$0.6 \cdot 10^6$	
Single Top (Wt channel)	108346	0.01459	p1035	$0.9 \cdot 10^6$	Single Top Background
$t\bar{t}$	105200	0.1668	p1035	14983835	$t\bar{t}$

Table 6.5: Overview on the MC@NLO [125] Monte Carlo datasets used in the analysis. Next to simulations of the single top and $t\bar{t}$ background, alternative datasets for the signal processes $W \to \tau_\mu\nu_\tau$ and $W \to \mu\nu_\mu$ are provided. No additional k-factors are applied to the cross sections.

Event generator: HERWIG						
Channel	Dataset ID	$\sigma \cdot \mathrm{BR} \cdot \epsilon_{\mathrm{filter}}$ [nb]	k-factor	Dataset tag	Number of events	Remarks
WW	105985	$44.9 \cdot 0.389 \cdot 10^{-3}$	-	p1035	$1.5 \cdot 10^6$	Di-boson Background
WZ	105987	$18.5 \cdot 0.310 \cdot 10^{-3}$	-	p1035	$1.0 \cdot 10^6$	
ZZ	105986	$6.02 \cdot 0.212 \cdot 10^{-3}$	-	p1035	$0.25 \cdot 10^6$	

Table 6.6: Overview on the HERWIG Monte Carlo datasets used in the analysis. The list adds di-boson processes to the list of the overall background.

6.4 Corrections to the Monte Carlo

In order to match the conditions found in the course of data taking as close as possible and to correct for discrepancies with measurements a number of modifications have been applied to the Monte Carlo events. These modifications usually come in the form of weight factors by which (subsets of) the simulated events are multiplied. In this section the various weight factors applied in this analysis are summarized and briefly described. Errors on the weight factors contribute to the error on the number of events via error propagation in the usual way.

6.4.1 Monte Carlo weight

The simulated events generated by MC@NLO have been reweighted in order to correct the transition from leading order to next-to-leading order cross sections.

6.4.2 Pile-up

The simulated events have to be modified in order to match the actual pile-up conditions present in the considered data. For that the Monte Carlo events are reweighted according to the distribution found in data based on the average number of interactions per bunch crossing using the `PileupReweightingTool` [126].

6.4.3 Vertex position weight

The spread of the positions of the reconstructed primary vertices along the beam axis z^{PV} is narrower in data than in the produced Monte Carlo simulations, as shown in figure 6.4. According to the recommendations of the WZSignatures subgroup, this has been corrected for by reweighting the simulated events based on the generated (true) vertex position according to the distribution in data using the `VertexPositionReweightTool` from `egammaAnalysisUtils`. The result of the reweighting procedure can be seen in figure 6.4 (b). The obtained level of agreement between data and Monte Carlo after the reweighting is compatible with the findings of other groups [127]. The effect of the reweighting on the shape of the muon distributions has been found to be negligible.

6.4.4 Boson p_{T} weight

The simulated events have been reweighted according to the measured transverse momentum spectra of the W and Z bosons [128].

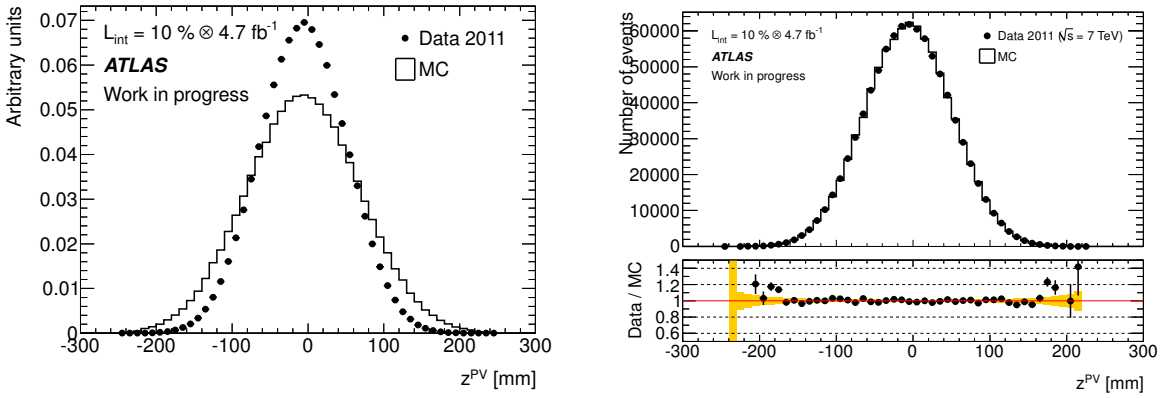

(a) (b)

Figure 6.4: Spread of the reconstructed positions of the primary vertices along the beam axis z^{PV} in simulations before (a) and after reweighting (b) compared to the distribution found in data.

6.4.5 Boson rapidity weight

The boson rapidity distribution for the ALPGEN+HERWIG $W \to \tau\nu_\tau$ and $Z/\gamma^* \to \tau\tau$ samples is known to be wrong at the $\pm(5 \ldots 10)\%$ level, which is fixed by applying a reweight.

6.4.6 Muon reconstruction efficiency weight

The muon reconstruction efficiencies have been measured in data and compared with the ones expected from the Monte Carlo simulations. Small discrepancies have been corrected for by reweighting the Monte Carlo events using the `MuonEfficiencyCorrections` tool provided by the ATLAS muon group. The statistical error on the efficiency measurements however contributes to the uncertainty on the shapes of the muon distributions and has been taken into account as a systematic error on the measurement of the ratio of branching fractions (see also section 6.9.1).

6.5 Event selection

In the following section the event selection for the analysis will be described. It fully implements the recommendations of the WZSignatures subgroup of the ATLAS Standard Model working group for W boson related analyses unless noted otherwise. Similar to the procedure described in the previous chapters a number of cleaning steps are performed in advance in order to ensure good quality of the data.

- The event must be present in the Good Runs List (GRL). The GRL file used is data11_7TeV.periodAllYear_-DetStatus-v36-pro10_CoolRunQuery-00-04-08_WZjets_allchannels_DtoM.xml
- In the course of 2011 data taking, parts of the liquid argon calorimeter were not fully operational. This resulted in corrupted energy measurements of objects hitting the respective areas of the detector and is commonly referred to as the liquid argon calorimeter hole (LAr hole). For the purpose of this analysis, an event is removed if at least one jet with $p_T \geq 20$ GeV is reconstructed within the questionable area

- As also described in sections 4.3 and 5.3, events are checked for bad jets in order to get an accurate $E_{\mathrm{T}}^{\mathrm{miss}}$ measurement. Here, an event is rejected if a jet within $\Delta R < 0.3$ of a selected lepton and $p_{\mathrm{T}} \geq 20$ GeV is flagged as 'looser bad', according to the definition reported in figure A.3 in appendix A. In contrast to the situation given in the previous analyses, this cut is applied to both data and Monte Carlo events
- Events affected by noise bursts in the liquid argon calorimeter are removed. This cut is applied only to data. The total integrated luminosity has been corrected accordingly
- The event must contain at least one reconstructed vertex, with 3 or more associated tracks

6.5.1 Event signature selection

The characterizing feature of both $W \rightarrow \tau_{\mu}\nu_{\tau}$ and $W \rightarrow \mu\nu_{\mu}$ events is to contain exactly one muon and therefore it is the most important task of the event signature selection to look for events with one well reconstructed candidate of these kind of particles. Also, a certain amount of $E_{\mathrm{T}}^{\mathrm{miss}}$ is produced by the escaping neutrinos. However, since this amount turns out to be rather small, especially in $W \rightarrow \tau_{\mu}\nu_{\tau}$ events, $E_{\mathrm{T}}^{\mathrm{miss}}$ is not exploited in the process of the event selection. Therefore, a single muon trigger based on the muGirl (MG) algorithm [129] with a low energy threshold was chosen.

- Each event has to be selected by the following trigger signatures:
  First period: EF_mu18_MG
  Second period: EF_mu18_MG_medium

On reconstruction level the event is required to contain exactly one muon:

- Events with more than one muon are rejected

The muon has to fulfill the following object definition criteria:

- The muon is a combined muon reconstructed by the STACO algorithm [129]
- The longitudinal impact parameter of the muon with respect to the primary vertex has to be within $|z_0| \leq 10$ mm
- The muon has to have a transverse momentum $p_{\mathrm{T}} \geq 20$ GeV
- The muon has to be reconstructed within the pseudorapidity range $|\eta| \leq 2.4$. As in the previous analyses, the reason for this cut is the limited coverage of the tracking system

The muon track has to fulfill the following quality criteria

- If hits in the b-layer are geometrically expected, then the muon track must have at least one b-layer hit
- The number of pixel hits N_{pixel} and the number of dead pixel sensors $N_{\mathrm{dead\ pixel}}$ combined must be $N_{\mathrm{pixel}} + N_{\mathrm{dead\ pixel}} > 1$
- The number of SCT hits N_{SCT} and the number of dead SCT sensors $N_{\mathrm{dead\ SCT}}$ combined must be $N_{\mathrm{SCT}} + N_{\mathrm{dead\ SCT}} \geq 6$
- The number of dead pixel sensors and the number of dead SCT sensors combined must be $N_{\mathrm{dead\ pixel}} + N_{\mathrm{dead\ SCT}} < 2$

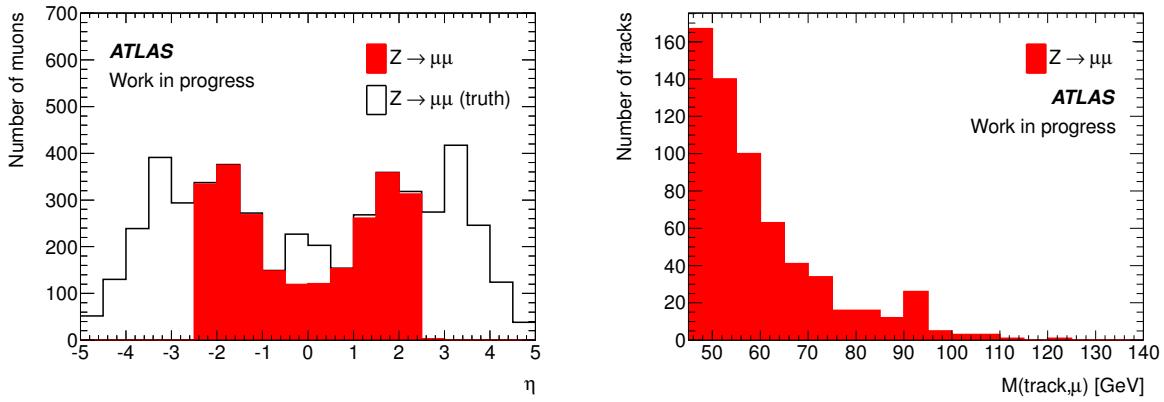

(a) (b)

Figure 6.5: Distributions of the pseudorapidity η of true and reconstructed muons in simulated $Z \to \mu\mu$ events after requiring exactly one muon (a). Invariant mass distribution of the isolated track-muon system (b) also after the one muon cut. The remaining background contribution from $Z \to \mu\mu$ comes from events where one muon escapes detection.

- A successful extension into the TRT is required within the η-acceptance of the TRT. If $N_{\text{TRT hits}}$ denotes the number of TRT hits on the muon track, $N_{\text{TRT outliers}}$ denotes the number of TRT outliers on the muon track and $N_{\text{TRT}} = N_{\text{TRT hits}} + N_{\text{TRT outliers}}$, the following must apply:
  – $N_{\text{TRT}} > 5$ and $N_{\text{TRT outliers}}/N_{\text{TRT}} < 0.9$ for $|\eta| < 1.9$
  – If $N_{\text{TRT}} > 5$, then $N_{\text{TRT outliers}}/N_{\text{TRT}} < 0.9$ is required, otherwise the muon is always accepted for $|\eta| \geq 1.9$

6.5.2 Electro-weak background rejection

Electro-weak background comprises the remaining decay of the W into an electron, the remaining decay channels of $W \to \tau\nu_\tau$ and the leptonic decays of the Z. The only process which shares part of its signature with the signal processes is $Z \to \tau\tau$, in the case that one of the taus decays into a muon. The other processes are efficiently rejected by the trigger requirement but may survive the signature selection mostly because muons are also produced in the course of quark hadronization which accompanies the weak decays. These kind of events can be removed by requiring the muon to be high-energetic and by applying an isolation criterion on the muon, as described in more detail in the next section, where the QCD background is discussed.

In addition, it turned out that a significant fraction of $Z \to \mu\mu$ events survives even the one-muon-requirement, which may be a bit surprising at first glance (see e.g. tables 6.10 and 6.11). This can be understood, however, by having a look at the pseudorapidity distribution of the true muons produced on a small sample of simulated $Z \to \mu\mu$ events after the one muon cut, as shown in figure 6.5 (a). If one makes the comparison with the distribution of muons which are actually reconstructed, shown in red, one can see that in the region $|\eta| \geq 2.5$ and to a somewhat smaller extend in the central region around $|\eta| \approx 0$. almost no reconstructed muons can be found. The reason for this is the limited coverage of the tracking system for large $|\eta|$ and a reduced tracking efficiency in the central region due to assemblies of instrumentation. The plot also shows the fraction of muons reconstructed by the muon spectrometer system only (stand-alone muons) which is represented by the tiny amount of events beyond $|\eta| = 2.5$. Consequently, the inclusion of such muons to the analysis would not help much to reduce this back-

ground.

A second cause for finding only one muon in $Z \to \mu\mu$ events could naturally also be a failing reconstruction of the second muon. To estimate the amount of these kind of events, the invariant mass of the highest-energetic medium isolated track and the reconstructed muon is calculated for each event, which can be seen in figure 6.5 (b). The distribution of the invariant masses should peak at the Z mass for tracks which are in fact mis-reconstructed muons. The figure shows that this is the case only for a small fraction of the considered events and the effect on the cut efficiency is therefore deemed negligible.

To conclude, apart from $Z \to \mu\mu$, which is treated as an extra item, the bulk of the electro-weak background consists of $Z \to \tau\tau$ with one tau decaying into a muon. Overall it can be stated that the total amount of electro-weak background is below 4%.

6.5.3 QCD background rejection

Muons appear in QCD multi-jet events in the course of the decay of heavy quarks. In this case, the muons are mostly found within a cone around and flying along the direction of a jet. Also, the muons are usually rather low-energetic. The key to discriminate between such muons and muons from the signal processes is therefore to demand a certain momentum threshold (20 GeV, see also 6.5.1) and in addition to require the muons to be isolated. Here, isolation is defined as an upper limit on the total energy and/or momentum measured in a cone around the muon. This energy can be determined by summing up the energy deposited in calorimeter cells and the momentum is obtained by adding the momenta of tracks within the cone. A combination of both criteria can also be used.

In this analysis, the default isolation criterion is to require the sum of track transverse momenta within a cone of $\Delta R = 0.4$ to be not greater than 5% of the muon momentum:

- In order to be considered, each event has to satisfy $\frac{\sum^{\Delta R \leq 0.4} p_{\mathrm{T}}^{\mathrm{tracks}}}{p_{\mathrm{T}}^{\mu}} \leq 0.05$

Various isolation criteria have been studied. Next to the isolation requirement specified above, from now on referred to as medium isolation, the following isolation criteria are defined:

- Loose isolation requirement: $\frac{\sum^{\Delta R \leq 0.4} p_{\mathrm{T}}^{\mathrm{tracks}}}{p_{\mathrm{T}}^{\mu}} \leq 0.1$
- Tight isolation requirement: $\max\left(\frac{\sum^{\Delta R \leq 0.4} p_{\mathrm{T}}^{\mathrm{tracks}}}{p_{\mathrm{T}}^{\mu}}, \frac{\sum^{\Delta R \leq 0.4} E_{\mathrm{T}}^{\mathrm{cells}}}{p_{\mathrm{T}}^{\mu}}\right) \leq 0.1$

The tighter the isolation criterion the more QCD background is rejected. However, as described in more detail in section 6.6, it turned out that with a tighter isolation it becomes more and more difficult to estimate the shape of the QCD multijet background distributions from an isolation sideband. Since a reliable knowledge of this shape is crucial to the analysis the medium isolation has been used as a compromise.

6.6 QCD background estimation

For reasons similar to the ones already outlined in section 5.4.2, namely the usually small statistical significance of the QCD Monte Carlo simulations, the number and distribution of the QCD background events is estimated directly from data.

The shape of the QCD background distribution is estimated using a control region which is obtained by loosening the muon isolation criterion. This approach is based on the assumption that the isolation of a muon is to a large extend independent of e.g. the variables determining the muon's kinematics. The

Method	Isolation criterion	Sideband definition
Loose	$\frac{\sum^{\Delta R\leq 0.4} p_{\mathrm{T}}^{\mathrm{tracks}}}{p_{\mathrm{T}}^{\mu}} \leq 0.1$	$0.1 \leq \frac{\sum^{\Delta R\leq 0.4} p_{\mathrm{T}}^{\mathrm{tracks}}}{p_{\mathrm{T}}^{\mu}} \leq 0.2$
Medium	$\frac{\sum^{\Delta R\leq 0.4} p_{\mathrm{T}}^{\mathrm{tracks}}}{p_{\mathrm{T}}^{\mu}} \leq 0.05$	$0.05 \leq \frac{\sum^{\Delta R\leq 0.4} p_{\mathrm{T}}^{\mathrm{tracks}}}{p_{\mathrm{T}}^{\mu}} \leq 0.1$
Tight	$\max\left(\frac{\sum^{\Delta R\leq 0.4} p_{\mathrm{T}}^{\mathrm{tracks}}}{p_{\mathrm{T}}^{\mu}}, \frac{\sum^{\Delta R\leq 0.4} E_{\mathrm{T}}^{\mathrm{cells}}}{p_{\mathrm{T}}^{\mu}}\right) \leq 0.1$	$0.1 \leq \max\left(\frac{\sum^{\Delta R\leq 0.4} p_{\mathrm{T}}^{\mathrm{tracks}}}{p_{\mathrm{T}}^{\mu}}, \frac{\sum^{\Delta R\leq 0.4} E_{\mathrm{T}}^{\mathrm{cells}}}{p_{\mathrm{T}}^{\mu}}\right) \leq 0.2$

Table 6.7: Definitions of the signal and control regions used to determine the shape of the QCD background distribution. The tighter the muon isolation, the more QCD background is rejected. However, the reliability of the shape prediction is better for looser isolation. As a compromise, the medium isolation has been chosen to be the default.

control region is chosen such that it is dominated by QCD events and contains sufficient statistics. It is defined as the set of events, where the summed track momenta in a $\Delta R = 0.4$ cone around the muon are between 5 and 10% of the muon momentum:

- Isolation sideband definition: $0.05 \leq \frac{\sum^{\Delta R\leq 0.4} p_{\mathrm{T}}^{\mathrm{tracks}}}{p_{\mathrm{T}}^{\mu}} \leq 0.1$

The assumption that this region is dominated by QCD has been checked using Monte Carlo simulations. Subsequently, the obtained set of data events has been corrected for pollution by subtracting the Monte Carlo predictions of the other processes.

The requirement, however, of the muon isolation to be independent of other variables is not entirely fulfilled which limits the applicability of this method. This has been studied by varying the sideband definitions based on the loose and tight isolation criteria specified above. The corresponding loose and tight sideband definitions are as follows:

- Loose isolation sideband: $0.1 \leq \frac{\sum^{\Delta R\leq 0.4} p_{\mathrm{T}}^{\mathrm{tracks}}}{p_{\mathrm{T}}^{\mu}} \leq 0.2$
- Tight isolation sideband: $0.1 \leq \max\left(\frac{\sum^{\Delta R\leq 0.4} p_{\mathrm{T}}^{\mathrm{tracks}}}{p_{\mathrm{T}}^{\mu}}, \frac{\sum^{\Delta R\leq 0.4} E_{\mathrm{T}}^{\mathrm{cells}}}{p_{\mathrm{T}}^{\mu}}\right) \leq 0.2$

All sideband definitions are again summarized in table 6.7.

In figure 6.6 one can see a comparison between the different shape predictions from the various isolation sideband definitions. The plots show lines for the predictions of the shape from the corrected data in red (Δ(Data, Non-QCD MC) = # data events - # non-QCD Monte Carlo events) and the expected nominal shape in the signal region in black (Δ(Data, Non-QCD MC) (Signal Region)). As a cross-check, the respective QCD Monte Carlo predictions are also shown. Two things can now be observed. For once the data-driven prediction of the QCD shape in the signal region is always better than the predictions from the simulations, justifying the method. Secondly, one can see that the tighter the muon isolation criterion the poorer is the agreement of the shapes. Consequently, the medium isolation has been chosen to be the default in order to profit from both high background rejection and reliability of the shape prediction. The remaining differences between the estimated shape and the expected shape where taken into account as a systematic uncertainty, which is admittedly maximally conservative.

The total number of QCD background events is obtained by a fit of the normalization of the estimated QCD shape to data. A scaling factor is obtained from the fit by which the predicted number of events has to be multiplied in order to get an estimation on the true total number of events. For the nominal fit the $E_{\mathrm{T}}^{\mathrm{miss}}$ distribution is used, as shown in figure 6.7. The distribution is fitted in the region between 0 and 60 GeV, where most of the QCD background is expected and the obtained scaling factor is 1.37. As

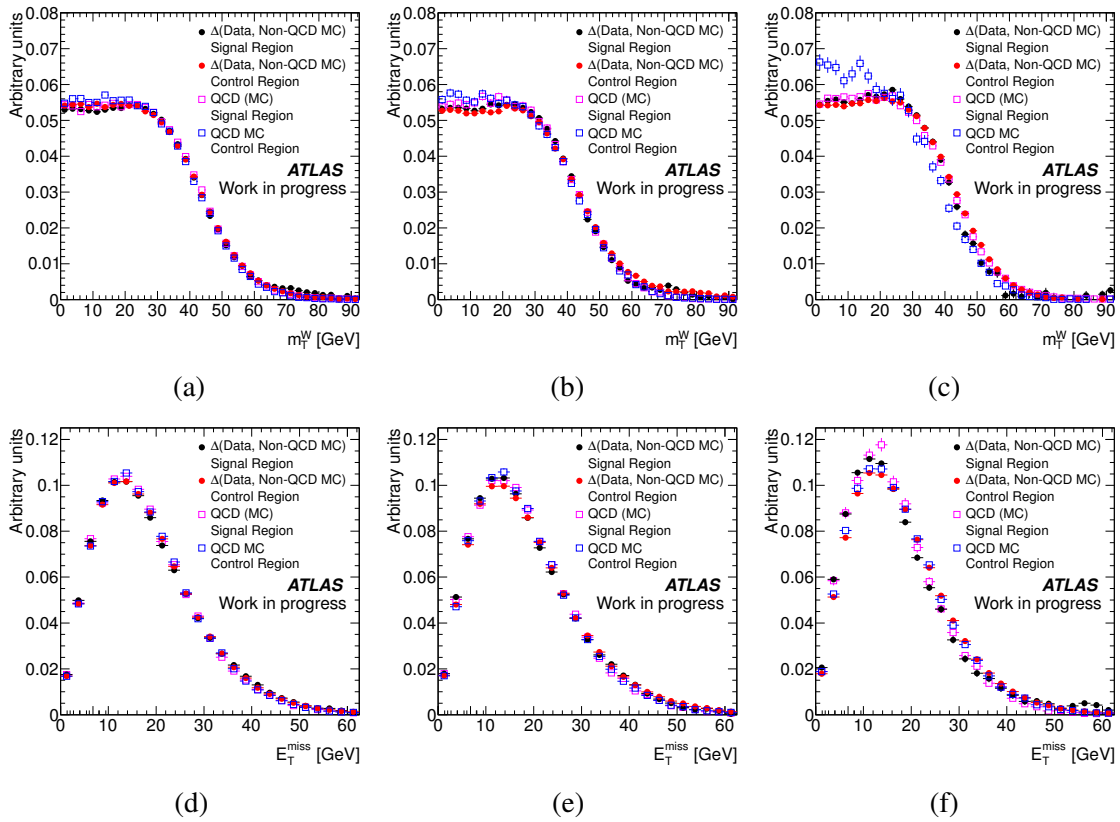

Figure 6.6: From left to right: Muon transverse mass QCD shapes for loose (a), medium (b) and tight (c) isolation. Missing transverse energy QCD shapes for loose (d), medium (e) and tight (f) isolation. The expected QCD shape in the signal region is drawn in black and the QCD shape prediction from the respective sideband is drawn in red. For comparison, the respective predictions from Monte Carlo simulations are also shown (open squares).

a cross-check, the same procedure was repeated for the transverse mass distribution with a compatible result. In both cases the fit quality is barely acceptable. However, both the numerical value of the scaling factor and the reached fit quality is compatible to the results reported by others [127]. The fit quality can be improved by additionally cutting on the transverse mass, in this way reducing the overall QCD background, which can be seen in figures 6.7 (c) and (d). On the other hand, figures 6.7 (e) and (f) show, that the shape estimation using the tight isolation cut and sideband leads to unsatisfying results.

It should be noted, that the knowledge of the total amount of QCD events is not crucial to the measurement method, since it is determined anyways in the final fraction fit. The number obtained here rather serves as a cross check and can be used as the fit's starting value.

6.7 Estimation of the fraction fit precision

Before discussing the actual measurement and the list of systematic uncertainties, this section summarizes a quick study which aims to estimate the expected fraction fit precision. A reduced set of cuts has been applied to simulated events of $W \to \tau_\mu \nu_\tau$, $W \to \mu\nu_\mu$ and $Z \to \mu\mu$ and the resulting distributions have been fitted to a set of toy data:

- An event has to pass the EF_mu18_MG trigger decision

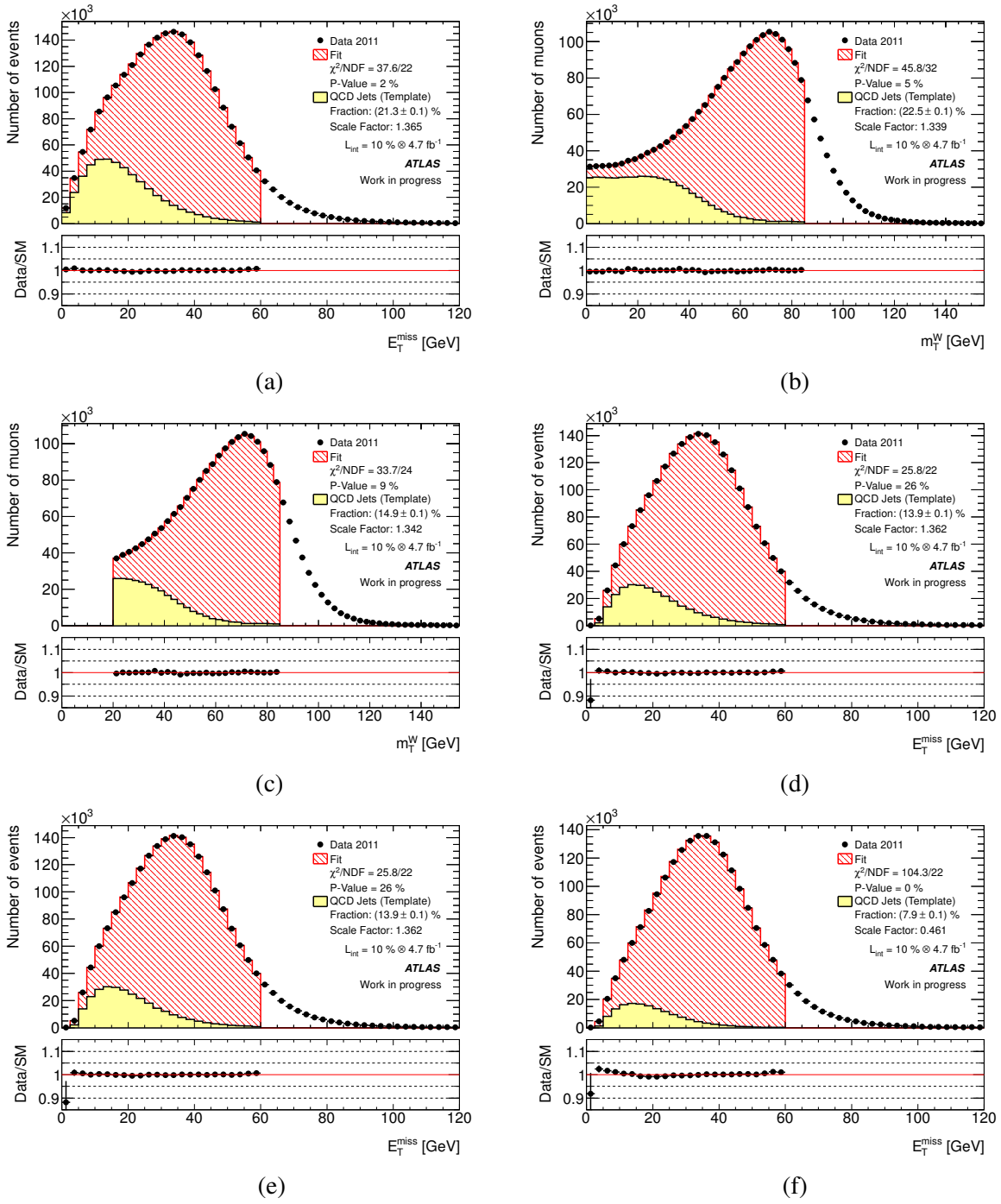

Figure 6.7: Determination of the normalization of the QCD background: The shape of the missing transverse energy E_T^{miss} obtained from the QCD control region is fitted to data to obtain a scale factor (a). As a cross-check, the shape of the transverse mass m_T^W obtained from the same control region is also fitted (b). The obtained scale factors agree reasonably and the fit quality is barely acceptable. Improvement of the fit quality can be seen after an additional cut on the transverse mass of the muon (c), (d). Fit of the shape of the missing transverse energy E_T^{miss} obtained from the medium (e) and tight (f) QCD control regions to data. The decline of the fit quality due to a transition to the tighter muon isolation requirement is clearly visible.

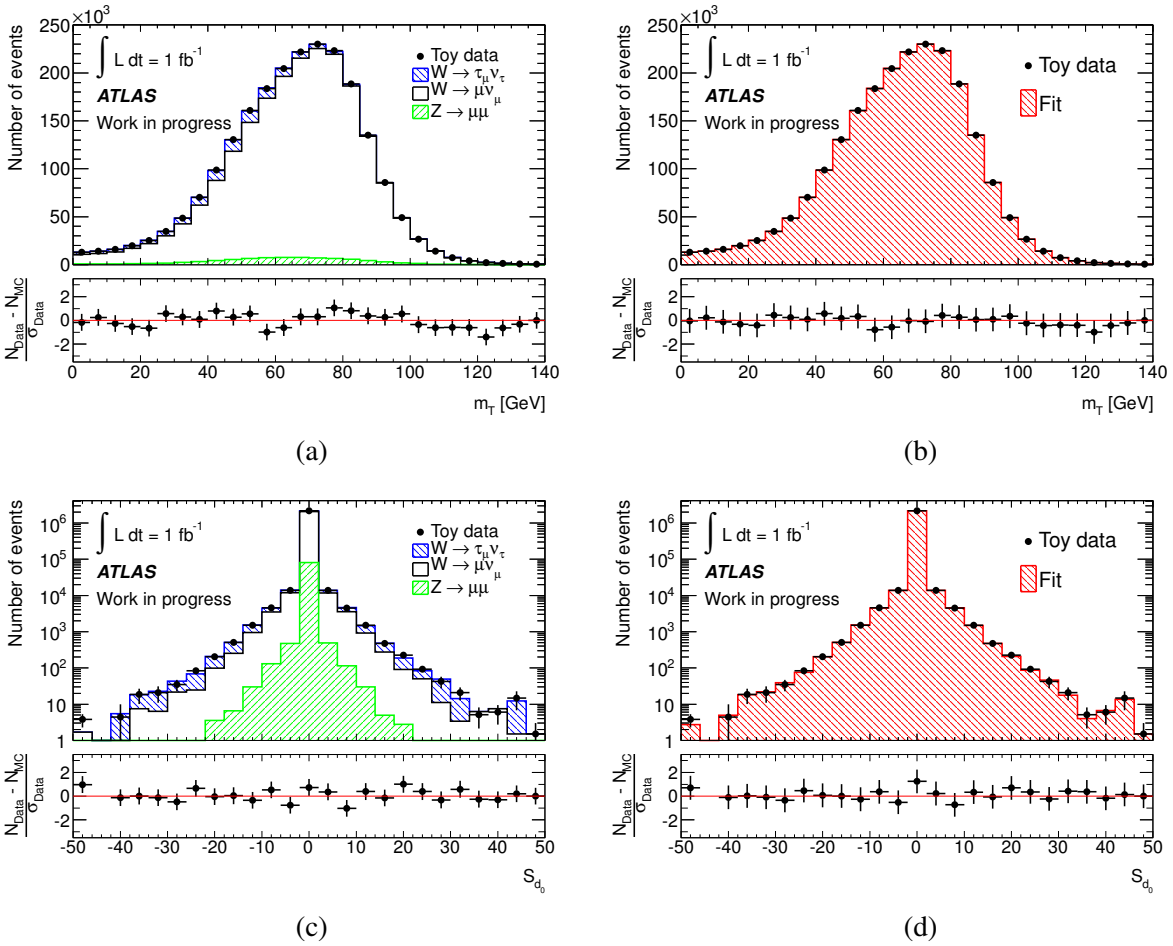

Figure 6.8: Estimation of the fraction fit precision. Distributions of the muon transverse mass and the transverse muon impact parameter significance for Monte Carlo and toy data events after a reduced set of selection cuts and scaling to an integrated luminosity of 1 fb^{-1} (a) and (c). The result of a 2D fraction fit is also shown (b) and (d).

- An event is required to have exactly one muon reconstructed by the STACO algorithm
- The muon has to be isolated according to the medium isolation criterion
- The muon has to have a transverse momentum of at least 20 GeV

The obtained distributions are shown for the transverse mass of the W and the transverse impact parameter significance of the muon in figure 6.8. A set of toy data is generated by Gaussian smearing of the the combined distribution with a standard deviation equal to the statistical error on the number of events one would expect for an integrated luminosity of 1 fb^{-1}. Subsequently, a fit of the combined 2D distribution to the toy data has been performed using the `TFractionFitter` class which is part of the `ROOT` analysis framework [130]. The expected fractions of the contributing samples are well reconstructed, as shown in table 6.8. According to the `TFractionFitter` output, the relative fit precision is better than 1.6%.

This number has been verified with the help of Monte Carlo techniques. For that purpose a new set of toy data is produced and the fit is repeated 1000 times. The distributions of the fitted fractions f_i normalized to the nominal fractions f_0 can be seen in figure 6.9. The fractions are centered around zero

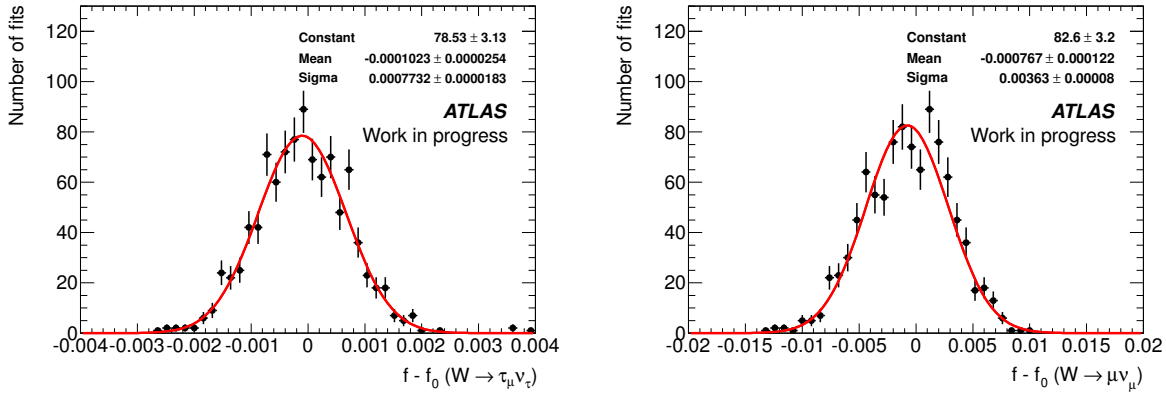

(a) (b)

Figure 6.9: Pull distributions obtained from repeating the fit 1000 times on toy data. The fitted fractions f are normalized to the expected fraction f_0. The true fraction is well reproduced. The estimated relative precision is of order 1.6%.

Sample	True fraction	Fitted fraction	Relative fit error
$W \to \tau_\mu\nu_\tau$	4.68%	4.66%	1.6%
$W \to \mu\nu_\mu$	91.6%	91.7%	0.4%

Table 6.8: Estimation of the fraction fit precision. The expected, true fractions are well reconstructed. The relative fit uncertainty is not greater than 1.6%.

and are Gaussian distributed. The standard deviation of a fitted Gaussian function to these distributions can be used as an estimate on the uncertainty of the fitted fractions. One can see that this uncertainty is nowhere greater than 1.6% in agreement with the previous result.

It is noted explicitly in the documentation of the `TFractionFitter` class that for the fit not only the values of the template fractions are varied. In order to take the systematic uncertainty due to the imperfect knowledge of the template shapes into account, the number of entries in each bin is also varied within its uncertainty (which is the statistical uncertainty on the number of generated Monte Carlo events). This means that the fit precision cited above is strictly speaking a combination of the statistical error (due to limited data) and a systematic error due to the limited Monte Carlo statistics.

6.8 Results

The number of events remaining after cuts for the various combined data samples are listed in table 6.10 and the relative cut efficiencies in table 6.11. A more detailed collection of tables can be found in appendix B.

The number of QCD events has been estimated using a data-driven approach. Overall, the number of data is compatible with the total number of Monte Carlo events after all cuts are applied. Figure 6.10 shows comparisons between data and simulations for selected distributions. Reasonable agreement is found. Additional cuts with the purpose of further reducing the QCD background and their applicability in the context of the measurement method are discussed in section 6.8.1.

The transverse mass of the W $m_{\mathrm{T}}^{\mathrm{W}}$ is tentatively chosen to be the only fit quantity because it shows good agreement over a wide range. This is necessary because it turns out that the fit does not converge

Sample	Expected fraction	Fitted fraction	Standard deviation	Relative fit error
$W \to \tau_\mu \nu_\tau$	3.55%	3.15%	-2.3	5%
$Z \to \mu\mu$	2.65%	2.65%	0.0	fixed
$W \to \mu\nu_\mu$	71.3%	71.6%	1.9	0.2%
QCD	22.5%	22.6%	1.3	0.4%

Table 6.9: Result from the fit over the full range of $m_{\mathrm{T}}^{\mathrm{W}}$. The expected fractions have been obtained by inserting the nominal values of the respective cross sections. The fit error corresponds to 10% of the available data from 2011 and is expected to scale down by accordingly if the full dataset is taken into account.

dependably if the differences between data and Monte Carlo predictions are too large, i.e which cannot be compensated by a reweighting of the fractions of the contributing templates alone. A poorer agreement of the transverse impact parameter significance S_{d_0}, especially in the tails, is the reason why a two-dimensional fit is not attempted. Other variables have less discrimination power or are correlated to a certain degree to the transverse mass.

The fit is performed over the transverse mass range of 0 - 90 GeV. Bins at higher transverse masses are excluded because here the agreement between data and Monte Carlo is poor. On the other hand, the discrimination power of the templates is small in this region, hence the effect on the fit result is expected to be limited. Also, the fraction of the $Z \to \mu\mu$ template is fixed to its predicted value, which is considered necessary since the discrimination power w.r.t the $W \to \tau_\mu \nu_\tau$ sample is too small. It is expected, however, that the modelling of this theoretically well understood process is sufficiently under control. The minuscule contribution of the electro-weak background has also been fixed.

The fit result can be inspected by taking a look at figure 6.11 (b). The obtained fitted distribution shows better agreement with the data and the fit quality is still acceptable. The effect of varying the fit range can also be seen: figure 6.11 (c) shows the numerical results for the ratio of branching fractions obtained by using formula 6.2 for various additional cuts on the transverse mass. A dot representing the fit result is drawn at the lowest bin included in the fit. The indicated error is statistical only and is calculated as

$$
\begin{aligned}
\Delta\left(\Gamma(W \to \tau\nu)/\Gamma(W \to \mu\nu)\right) = \Bigg[& \left(\frac{\partial \Gamma(W \to \tau\nu)/\Gamma(W \to \mu\nu)}{\partial \mathrm{BR}(\tau \to \mu\nu_\tau\nu_\mu)} \cdot \Delta \mathrm{BR}(\tau \to \mu\nu_\tau\nu_\mu) \right)^2 \\
& + \left(\frac{\partial \Gamma(W \to \tau\nu)/\Gamma(W \to \mu\nu)}{\partial \epsilon_{(W \to \mu\nu_\mu)}} \cdot \Delta \epsilon_{(W \to \mu\nu_\mu)} \right)^2 \\
& + \left(\frac{\partial \Gamma(W \to \tau\nu)/\Gamma(W \to \mu\nu)}{\partial \epsilon_{(W \to \tau_\mu\nu_\tau)}} \cdot \Delta \epsilon_{(W \to \tau_\mu\nu_\tau)} \right)^2 \\
& + \left(\frac{\partial \Gamma(W \to \tau\nu)/\Gamma(W \to \mu\nu)}{\partial f_{W \to \mu\nu_\mu)}} \cdot \Delta f_{(W \to \mu\nu_\mu)} \right)^2 \\
& + \left(\frac{\partial \Gamma(W \to \tau\nu)/\Gamma(W \to \mu\nu)}{\partial f_{(W \to \tau_\mu\nu_\tau)}} \cdot \Delta f_{(W \to \tau_\mu\nu_\tau)} \right)^2 \Bigg]^{\frac{1}{2}},
\end{aligned}
$$

Cut	Data	MC (total)
Before cuts	45597336 ± 6753	121964548 ± 43627
GRL	40482200 ± 6363	121964548 ± 43627
Noise bursts	40369248 ± 6354	121964548 ± 43627
Collision cleaning	40083996 ± 6331	121810595 ± 43615
Trigger	19022070 ± 4361	45976403 ± 27743
Muon quality	16733911 ± 4091	43795495 ± 27077
Muon p_{T}	8810537 ± 2968	21264169 ± 18313
Muon η	8679580 ± 2946	21030393 ± 18231
One muon	8459150 ± 2908	20790797 ± 18205
$E_{\mathrm{T}}^{\mathrm{miss}}$ cleaning	8448811 ± 2907	20773935 ± 18197
LAr hole	8403600 ± 2899	20636640 ± 18121
Muon isolation	2247115 ± 1499	2206111 ± 2284

Cut	$W \to \tau_\mu\nu_\tau$	$W \to \mu\nu_\mu$	$Z \to \mu\mu$	QCD background	EW background	$\mathrm{t\bar{t}}$
Before cuts	833167 ± 1171	4734468 ± 797	504140 ± 169	105809033 ± 43531	10005321 ± 2511	78419 ± 26
GRL	833167 ± 1171	4734468 ± 797	504140 ± 169	105809033 ± 43531	10005321 ± 2511	78419 ± 26
Noise bursts	833167 ± 1171	4734468 ± 797	504140 ± 169	105809033 ± 43531	10005321 ± 2511	78419 ± 26
Collision cleaning	829263 ± 1168	4699035 ± 794	499663 ± 169	105753060 ± 43520	9951184 ± 2504	78389 ± 26
Trigger	131034 ± 463	2323711 ± 556	351386 ± 141	43120893 ± 27733	27203 ± 35	22177 ± 14
Muon quality	124597 ± 452	2221110 ± 544	345125 ± 139	41057052 ± 27068	25955 ± 34	21656 ± 14
Muon p_{T}	90726 ± 385	1985466 ± 514	286663 ± 127	18870916 ± 18302	17330 ± 27	13068 ± 11
Muon η	89062 ± 381	1949462 ± 509	257134 ± 120	18704814 ± 18220	16964 ± 26	12957 ± 11
One muon	89031 ± 381	1949165 ± 509	75872 ± 66	18648744 ± 18193	16491 ± 26	11494 ± 10
$E_{\mathrm{T}}^{\mathrm{miss}}$ cleaning	88986 ± 381	1947916 ± 509	75628 ± 66	18633484 ± 18186	16442 ± 26	11478 ± 10
LAr hole	88888 ± 381	1946150 ± 509	75559 ± 66	18498407 ± 18110	16372 ± 26	11264 ± 10
Muon isolation	77277 ± 355	1764856 ± 485	67886 ± 63	273845 ± 2202	13754 ± 23	8493 ± 9

Table 6.10: Number of events after cuts for data and simulations. The quoted errors are statistical only. The total number of QCD events is ultimately estimated from data, leading to a better agreement between expectation and measurement.

Cut	Data	MC (total)				
Before cuts						
GRL		100.00%				
Noise bursts		100.00%				
Collision cleaning		99.87%				
Trigger		37.74%				
Muon quality		95.26%				
Muon p_{T}		48.55%				
Muon η		98.90%				
One muon		98.86%				
$E_{\mathrm{T}}^{\mathrm{miss}}$ cleaning		99.92%				
LAr hole		99.34%				
Muon isolation		10.69%				
Cut	$W \to \tau_\mu \nu_\tau$	$W \to \mu \nu_\mu$	$Z \to \mu\mu$	QCD background	EW background	$\mathrm{t\bar{t}}$
Before cuts						
GRL	100.00%	100.00%	100.00%	100.00%	100.00%	100.00%
Noise bursts	100.00%	100.00%	100.00%	100.00%	100.00%	100.00%
Collision cleaning	99.53%	99.25%	99.11%	99.95%	99.46%	99.96%
Trigger	15.80%	49.45%	70.32%	40.78%	0.27%	28.29%
Muon quality	95.09%	95.59%	98.22%	95.21%	95.41%	97.65%
Muon p_{T}	72.82%	89.40%	83.06%	45.96%	66.77%	60.34%
Muon η	98.17%	98.18%	89.70%	99.12%	97.89%	99.15%
One muon	99.97%	99.98%	29.51%	99.70%	97.21%	88.71%
$E_{\mathrm{T}}^{\mathrm{miss}}$ cleaning	99.95%	99.94%	99.68%	99.92%	99.70%	99.86%
LAr hole	99.89%	99.91%	99.91%	99.28%	99.58%	98.14%
Muon isolation	86.94%	90.69%	89.85%	1.48%	84.01%	75.40%

Table 6.11: Relative number of events after cuts for data and simulations.

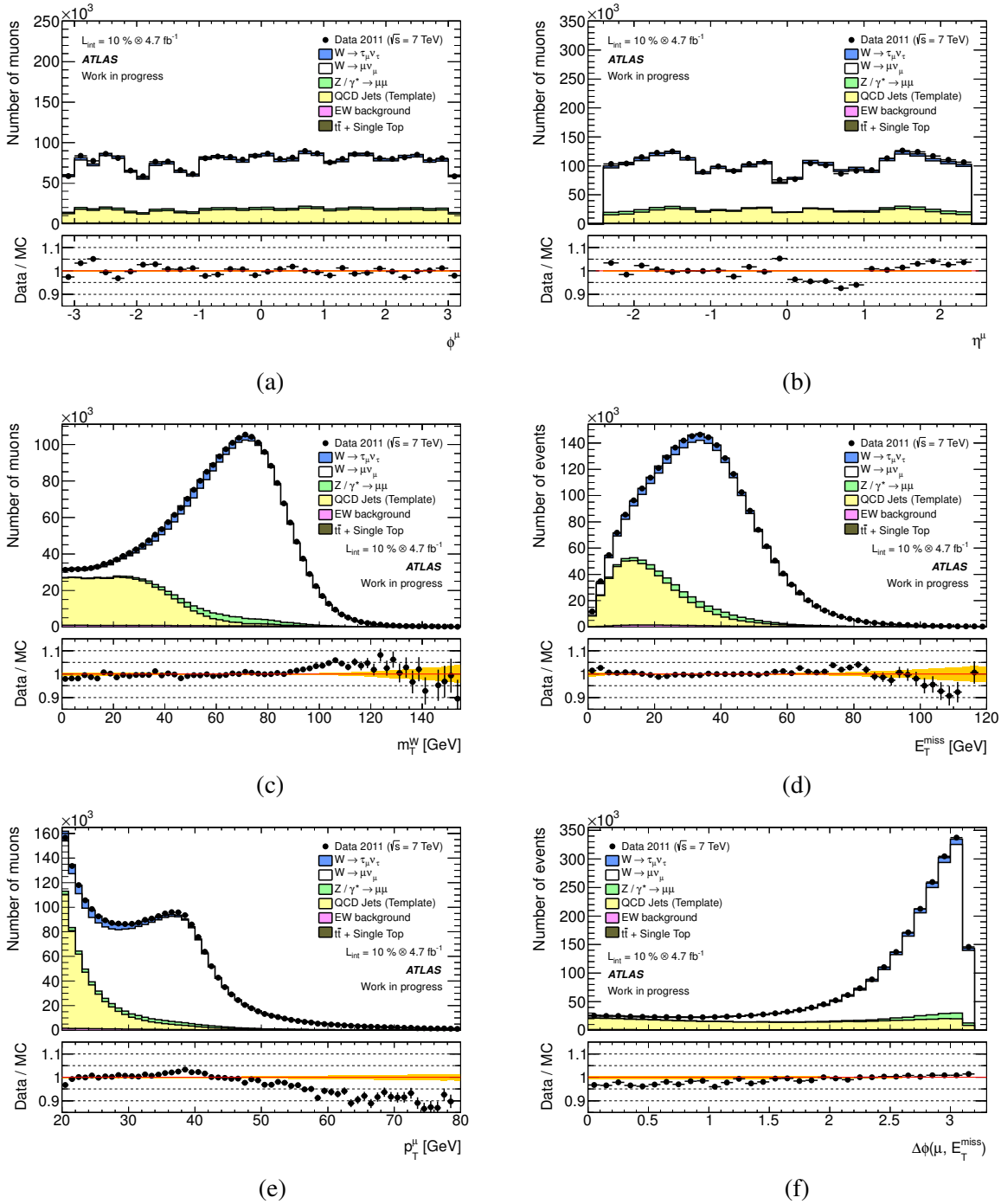

Figure 6.10: Comparison between data and Monte Carlo simulations after the full event selection. Azimuthal angle of the muons ϕ (a), pseudorapidity of the muons η (b), transverse mass of the W $m_{\mathrm{T}}^{\mathrm{W}}$ (c), missing transverse energy $E_{\mathrm{T}}^{\mathrm{miss}}$ (d), transverse momentum p_{T} of the muons (e), angle between the muon and the missing transverse energy $\Delta\phi\left(\mu, E_{\mathrm{T}}^{\mathrm{miss}}\right)$ (f).

where

$$\begin{aligned}
\frac{\partial\Gamma(W\to\tau\nu)/\Gamma(W\to\mu\nu)}{\partial \mathrm{BR}(\tau\to\mu\nu_\tau\nu_\mu)} &= -\frac{1}{\mathrm{BR}(\tau\to\mu\nu_\tau\nu_\mu)^2}\frac{\epsilon_{(W\to\mu\nu_\mu)}}{\epsilon_{(W\to\tau_\mu\nu_\tau)}}\frac{f_{(W\to\tau_\mu\nu_\tau)}}{f_{(W\to\mu\nu_\mu)}}\\
\frac{\partial\Gamma(W\to\tau\nu)/\Gamma(W\to\mu\nu)}{\partial \epsilon_{(W\to\mu\nu_\mu)}} &= \frac{1}{\mathrm{BR}(\tau\to\mu\nu_\tau\nu_\mu)}\frac{1}{\epsilon_{(W\to\tau_\mu\nu_\tau)}}\frac{f_{(W\to\tau_\mu\nu_\tau)}}{f_{(W\to\mu\nu_\mu)}}\\
\frac{\partial\Gamma(W\to\tau\nu)/\Gamma(W\to\mu\nu)}{\partial \epsilon_{(W\to\tau_\mu\nu_\tau)}} &= -\frac{1}{\mathrm{BR}(\tau\to\mu\nu_\tau\nu_\mu)}\frac{\epsilon_{(W\to\mu\nu_\mu)}}{\epsilon^2_{(W\to\tau_\mu\nu_\tau)}}\frac{f_{(W\to\tau_\mu\nu_\tau)}}{f_{(W\to\mu\nu_\mu)}}\\
\frac{\partial\Gamma(W\to\tau\nu)/\Gamma(W\to\mu\nu)}{\partial f_{(W\to\mu\nu_\mu)}} &= \frac{1}{\mathrm{BR}(\tau\to\mu\nu_\tau\nu_\mu)}\frac{\epsilon_{(W\to\mu\nu_\mu)}}{\epsilon_{(W\to\tau_\mu\nu_\tau)}}\frac{1}{f_{(W\to\mu\nu_\mu)}}\\
\frac{\partial\Gamma(W\to\tau\nu)/\Gamma(W\to\mu\nu)}{\partial f_{(W\to\tau_\mu\nu_\tau)}} &= -\frac{1}{\mathrm{BR}(\tau\to\mu\nu_\tau\nu_\mu)}\frac{\epsilon_{(W\to\mu\nu_\mu)}}{\epsilon_{(W\to\tau_\mu\nu_\tau)}}\frac{f_{(W\to\tau_\mu\nu_\tau)}}{f^2_{(W\to\mu\nu_\mu)}}.
\end{aligned}$$

The cut efficiencies are defined as

$$\epsilon_{(W\to\mu\nu_\mu)} = \frac{N^{\mathrm{cuts}}_{(W\to\mu\nu_\mu)}}{N^{\mathrm{all}}_{(W\to\mu\nu_\mu)}} \quad \text{and} \quad \epsilon_{(W\to\tau_\mu\nu_\tau)} = \frac{N^{\mathrm{cuts}}_{(W\to\tau_\mu\nu_\tau)}}{N^{\mathrm{all}}_{(W\to\tau_\mu\nu_\tau)}}, \tag{6.4}$$

where N^{cuts} is the number of events after cuts and N^{all} is the number of all events (before cuts) for the respective sample. The corresponding uncertainties are

$$\Delta\epsilon = \sqrt{\left(\frac{1}{N^{\mathrm{all}}}\cdot\Delta N^{\mathrm{cuts}}\right)^2 + \left(-\frac{N^{\mathrm{cuts}}}{(N^{\mathrm{all}})^2}\cdot\Delta N^{\mathrm{all}}\right)^2}. \tag{6.5}$$

Here, ΔN^{cuts} and ΔN^{all} are the luminosity weighted statistical errors on the number of events. The statistical errors on the fitted fractions $\Delta f_{(W\to\mu\nu_\mu)}$ and $\Delta f_{(W\to\tau_\mu\nu_\tau)}$ are reported by the `TFractionFitter` analysis tool and, as described in section 6.7, have been verified with the help of Monte Carlo techniques. The numerical values for the various factors entering the equation are summarized in table 6.9. For the branching fraction of the muonic decay channel of the tau the measurement $\mathrm{BR}(\tau\to\mu\nu_\tau\nu_\mu) = 0.1734 \pm 0.0005$ is used [15]. It can be observed, that the fit results vary around a central value of roughly 0.8. A treatment of the systematic uncertainties can be found in section 6.9.

6.8.1 Further reduction of the QCD background

The overall number of QCD events after the cut selection is still rather large. Therefore additional cuts with aim to further reduce the QCD background are investigated.

Figure 6.12 shows the distribution of the azimuthal angle between the direction of the muon and the missing transverse energy. One can see that the signal distributions peak at $\Delta\phi \approx 3$ which corresponds to the muon and the $E_{\mathrm{T}}^{\mathrm{miss}}$ being back-to-back, whereas the distribution of QCD is mostly flat. This is explainable since in the rest frames of the W or the tau the neutrinos are emitted into the opposite direction of the muon. For QCD events no such correlation exists, because the $E_{\mathrm{T}}^{\mathrm{miss}}$ arises from mis-measured jet energies with no preferred direction w.r.t. the muon. An additional tentative cut of $\Delta\phi$ is applied:

- In each event, the azimuthal angle between the direction of the muon and the missing transverse energy has to be $\Delta\phi\left(\mu, E_{\mathrm{T}}^{\mathrm{miss}}\right) \geq 2.2$

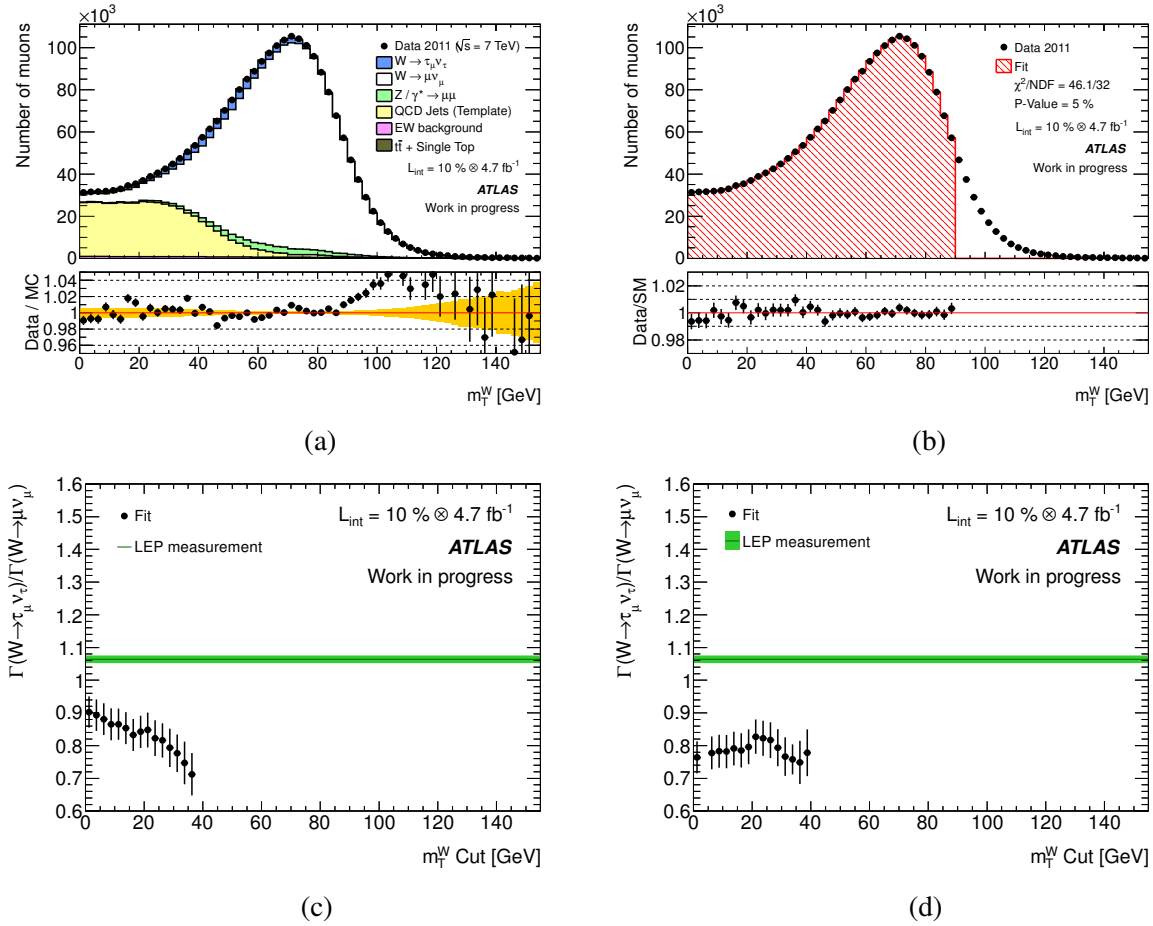

Figure 6.11: Template fit of the transverse mass of the W $m_{\mathrm{T}}^{\mathrm{W}}$ to data. Comparison of data and Monte Carlo simulations after the full event selection (a). Result of the fit of $W \to \tau_\mu\nu_\tau$, $W \to \mu\nu_\mu$ and QCD templates to data. The fit is performed over the range of 0 - 90 GeV and the fractions of the $Z \to \mu\mu$ and electro-weak background templates are fixed to the predicted value (b). Fit results for various cuts on the transverse mass. Each point represents the result of a fit including the statistical error ranging from the bin where it is drawn up to 90 GeV . The LEP measurement and uncertainties are indicated as a green band (c). Fit results after additionally cutting on the angle between the muon and the leading jet (d).

The overall agreement between data and the Monte Carlo simulation is reasonable before and after the cut and the relative reduction of the QCD background is significant. However, this cut leads also to a reduction of the discriminating power between the templates which can be seen from figure 6.12 (c) and (d). Especially the distribution of the QCD template looks more similar to the $W \to \tau_\mu\nu_\tau$ distributions after the cut. Due to the reduction of the discriminating power, the statistical error is increased by roughly one third.

Figure 6.12 shows the distribution of the azimuthal angle between the direction of the muon and the leading jet in the event. A jet is defined, according to the recommendations of the WZSignatures group

- Jet candidates are built from topoclusters by an anti-k_{T}-algorithm
- The candidate has to have $p_{\mathrm{T}} \geq 30$ GeV
- The rapidity of each candidate has to be within $|y| < 2.1$

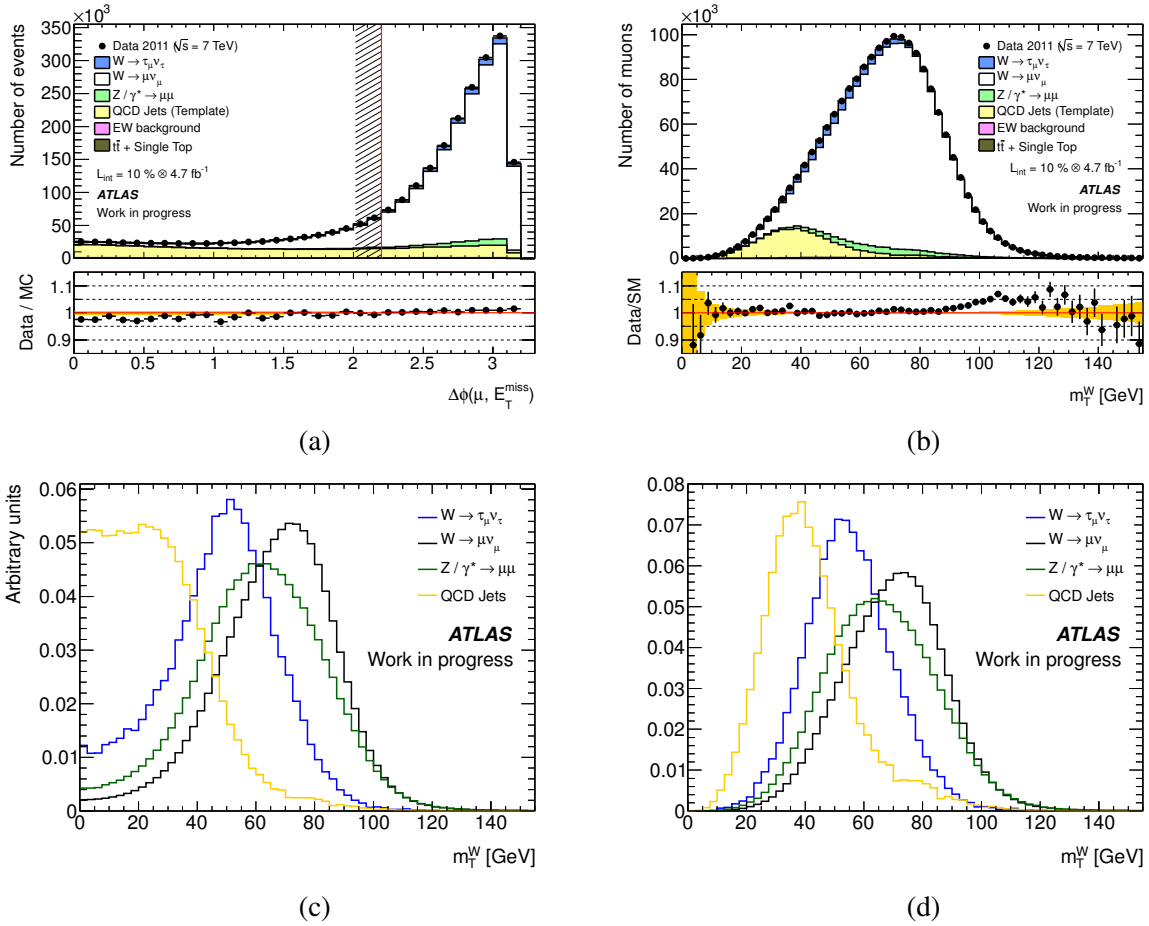

Figure 6.12: Distribution of the azimuthal angle $\Delta\phi\left(\mu, E_{\mathrm{T}}^{\mathrm{miss}}\right)$ between the muon and the missing transverse energy after the full event selection (a). Distribution of the transverse mass of the W $m_{\mathrm{T}}^{\mathrm{W}}$ after a tentative cut on $\Delta\phi$ (b). Comparison of the shapes of the most relevant templates before (c) and after the cut (d).

- The pseudorapidity of each candidate has to be within $|\eta| < 2.4$
- The jet vertex fraction JVF has to be $|\mathrm{JVF}| > 0.75$
- The jet has to fulfill the looser requirement for good reconstructed jets according to appendix A

In the plot, the bin corresponding to negative angles contains the events where no jet fulfills the above criteria. One can see that the leading jet points mostly into or into the opposite direction of the muon for QCD events, which can be explained by the fact that jets are produced back-to-back and the muon is found within the cone of one jet here. No such correlation exists for the signal processes and therefore this quantity can also be used to further discriminate between signal and QCD background events. The agreement between data and Monte Carlo is reasonable albeit not as good as for $\Delta\phi\left(\mu, E_{\mathrm{T}}^{\mathrm{miss}}\right)$. However, the discrepancies are found mostly in the QCD dominated region which can be cut away:

- In each event, the azimuthal angle between the direction of the muon and the leading jet has to be $\Delta\phi\left(\mu, \mathrm{jet}_1\right) \leq 1.5$

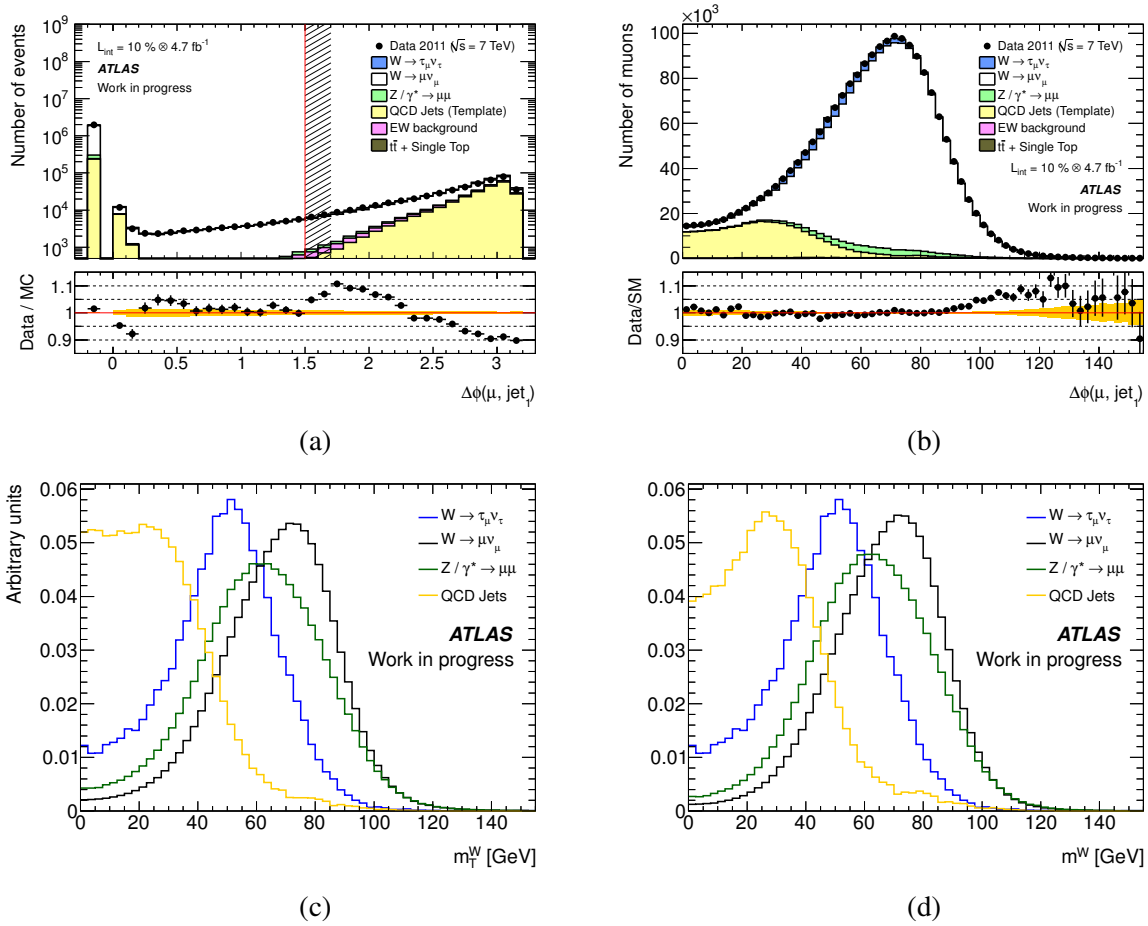

Figure 6.13: Distribution of the azimuthal angle $\Delta\phi(\mu, \text{jet}_1)$ between the muon and the leading jet in the event after the full event selection (a). Distribution of the transverse mass of the W m_{T}^{W} after a tentative cut on $\Delta\phi$ (b). Comparison of the shapes of the most relevant templates before (c) and after the cut (d).

After the cut the agreement between data and Monte Carlo still looks reasonable and the QCD background is decently reduced. The discriminating power between the templates turns out to be unchanged by this cut. As expected, the fit result is very similar to the one obtained before (see figure 6.11 (d)).

6.9 Systematics

In the following section a number of systematic uncertainties are discussed which possibly affect the shapes of the template distributions. These include systematic uncertainties on the measurements of the muons as well as uncertainties on the missing transverse energy.

6.9.1 Muon reconstruction efficiency

The muon reconstruction efficiencies of the ATLAS detector have been measured. In order to accommodate differences between the efficiencies found in data and the simulations, scale factors are applied on the Monte Carlo events which are summarized in table 6.12 for the various detector regions. The error on the scale factors can be separated into a statistical and a systematical part. The systematic error

Detector region	ID	Scale factor	Statistical error	Systematic error
BARRELLG A	1	0.996796	0.000792498	0.00274189
BARRELSM A	2	1.00453	0.00115731	0.00302882
BARREL A	3	0.993528	0.0010427	0.00254301
FEET A	4	0.99447	0.000694275	0.0023006
TRANSITION A	5	0.993478	0.000668932	0.00242063
ENDCAPLG A	6	0.915895	0.00141446	0.00224271
ENDCAPSM A	7	0.986278	0.00137725	0.00223515
BEE A	8	0.991769	0.000931795	0.00226603
FORWARDLG A	9	0.988871	0.000832275	0.00240533
FORWARDSM A	10	0.989635	0.000826387	0.00228868
	11			
FORWARDSM B	12	0.991423	0.000780756	0.00225123
FORWARDLG B	13	0.972367	0.000870821	0.00223014
BEE B	14	0.984505	0.000895112	0.00226544
ENDCAPSM B	15	0.978153	0.00140995	0.00227475
ENDCAPLG B	16	0.929488	0.00135751	0.00237546
TRANSITION B	17	0.990189	0.000695482	0.00238742
FEET B	18	0.990461	0.000703475	0.00239808
BARREL B	19	0.992658	0.00098307	0.00247905
BARRELSM B	20	1.00283	0.00120905	0.00274818
BARRELLG B	21	0.996429	0.000831641	0.00274636

Table 6.12: Muon reconstruction efficiency scale factors including statistical and systematic errors for the various detector regions. The numbers shown are the luminosity weighted scale factors.

on the efficiency corresponds to a global rescaling of the distributions and hence does not affect the template shape. The statistical part, however, is uncorrelated in the bins of the transverse masses.

In order to estimate how the statistical error on the scale factor translates into a systematic error on the measurement of the ratio of branching fractions, the scale factors are randomly varied within their uncertainties and the ratio of branching fractions is recalculated.

Since this study has been performed after the event processing, a mapping between the detector regions and the measured transverse masses has to be created beforehand which is shown in figure 6.14 (a). Now the scaling factors are varied for each detector region according to a Gaussian with a standard deviation equal to the corresponding statistical error and the modified distribution is fitted to data. This procedure is repeated 10000 times. The standard deviation of the Gaussian-distributed fit results is taken to be the systematic error. From figure 6.14 (b) one can see that this uncertainty amounts to 0.2%.

6.9.2 Muon momentum scale

In order to estimate how the application of the muon momentum scale correction affects the measurement, the results with and without the correction are compared. The total difference is taken as an additional systematic uncertainty [131, 132].

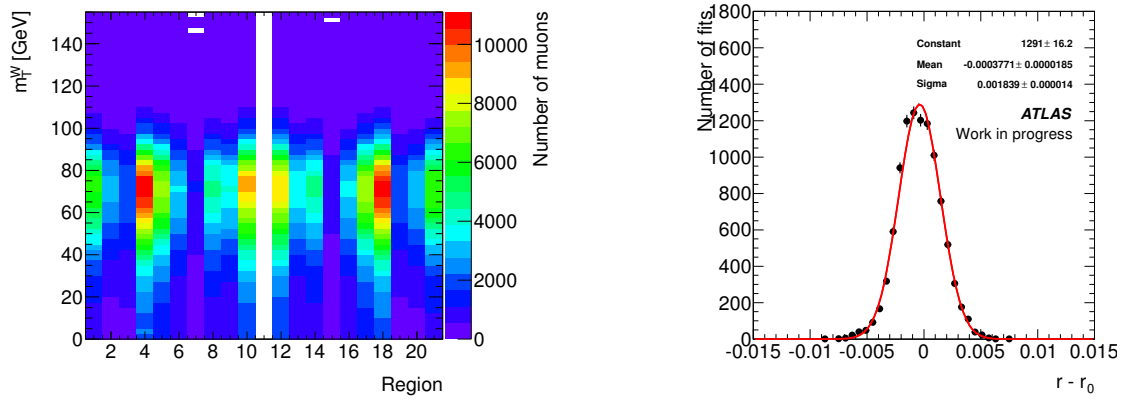

(a) (b)

Figure 6.14: Determination of the systematic uncertainty due to the statistical error on the muon efficiency scaling factors. A mapping between the measured transverse masses and the detector regions where the muons are reconstructed is created (a). The scaling factors are varied within their uncertainties and the fraction fit is repeated. The standard deviation of the Gaussian-distributed fit results $r = \Gamma(W \to \tau\nu_\tau)/\Gamma(W \to \mu\nu_\mu)$ normalized to the central value r_0 is taken to be the systematic error (b).

6.9.3 Muon momentum resolution

The muon momentum resolution measured in data is also worse than the one assumed in the Monte Carlo simulations. In order to estimate the systematic uncertainty on the measurement due to this error on the muon momentum resolution, the simulated muon momenta are smeared according to a Gaussian with a standard deviation equal to this error. The measurement procedure is then repeated with the smeared distributions and the differences between the results are taken to be the systematic uncertainty. Since the uncertainty on the resolution is different between the muon system (MS) and the inner detector, two independent systematic errors are determined corresponding to the different parts and eventually added in quadrature [131, 132].

6.9.4 Missing transverse energy scale

In order to estimate how the application of the $E_{\mathrm{T}}^{\mathrm{miss}}$ scale correction affects the measurement, the results with and without the correction are compared. The total difference is taken as an additional systematic uncertainty.

6.9.5 Missing transverse energy resolution

The $E_{\mathrm{T}}^{\mathrm{miss}}$ resolution measured in data is worse than the one assumed in the Monte Carlo simulations. In order to estimate the systematic uncertainty on the measurement due to this error on the $E_{\mathrm{T}}^{\mathrm{miss}}$ resolution, the simulated missing transverse energies are smeared according to a Gaussian with a standard deviation equal to this error. The measurement procedure is then repeated with the smeared distributions and the differences between the results are taken to be the systematic uncertainty. Since the uncertainty on the resolution is different for various sources of missing energy independent systematic errors are determined corresponding to the different parts and eventually added in quadrature.

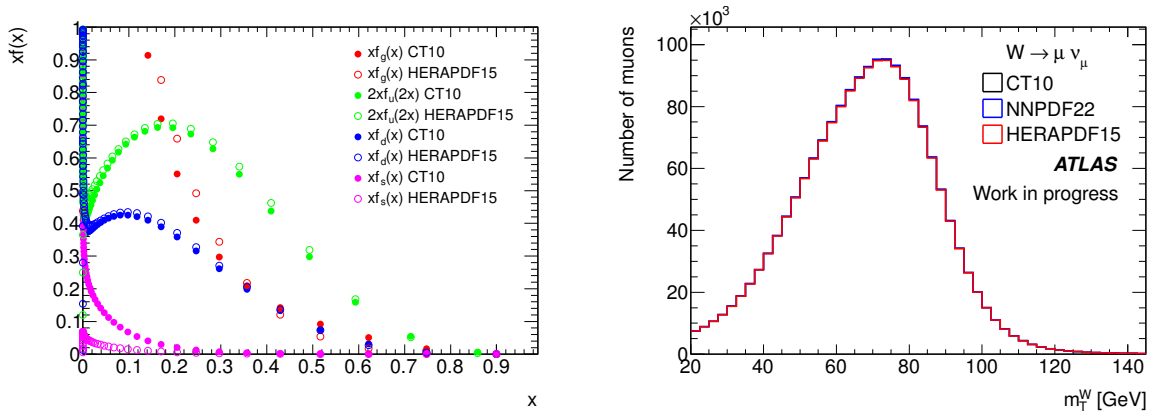

(a) (b)

Figure 6.15: Comparison of the parton density functions from CT10 and HERAPDF15, shown for gluons, up-, down- and strange quarks (a). The differences in the underlying algorithms translate into a varied shape of the transverse mass of the W (b). The differences in the fit of the various shapes from HERAPDF15 and NNPDF10 are taken as the systematic uncertainty.

6.9.6 Jet energy scale

A systematic error on the jet energies affect the result of the $E_{\mathrm{T}}^{\mathrm{miss}}$ calculation. In order to estimate how the application of the jet scale correction affects the ratio measurement, the jet energies and the $E_{\mathrm{T}}^{\mathrm{miss}}$ are recalculated and the fit results with and without the correction are compared. The total difference is taken as an additional systematic uncertainty.

6.9.7 Jet energy resolution

The jet resolution measured in data is worse than the one assumed in the Monte Carlo simulations. In order to estimate the systematic uncertainty on the measurement due to this error on the jet resolution, the simulated jet energies are smeared according to a Gaussian with a standard deviation equal to this error. Subsequently, the $E_{\mathrm{T}}^{\mathrm{miss}}$ is recalculated using the altered jet energies. The measurement procedure is then repeated and the differences between the results are taken to be the systematic uncertainty.

6.9.8 PDF uncertainties

For the estimation of the systematic uncertainty due to the limited knowledge of the true parton densities within the proton (parametrized as parton density functions, PDFs), the simulated events are reweighted according to different assumptions of the underlying PDF algorithms. In the nominal templates the so-called CT10 parametrization is used and compared to the HERAPDF15 and NNPDF10 parametrizations. The error is then obtained by fitting the reweighted templates separately to data and taking the difference.

One can see the effect on the shape of the distribution of the transverse mass of the W in figure 6.15. An interface to the different PDF sets is available via the C++ library LHAPDF [133]. The weighting factor is obtained as

$$w = \frac{\mathrm{pdf}_1^{\mathrm{target}} \cdot \mathrm{pdf}_2^{\mathrm{target}}}{\mathrm{pdf}_1^{\mathrm{default}} \cdot \mathrm{pdf}_2^{\mathrm{default}}},$$

where pdf_i is the density function of the ith parton.

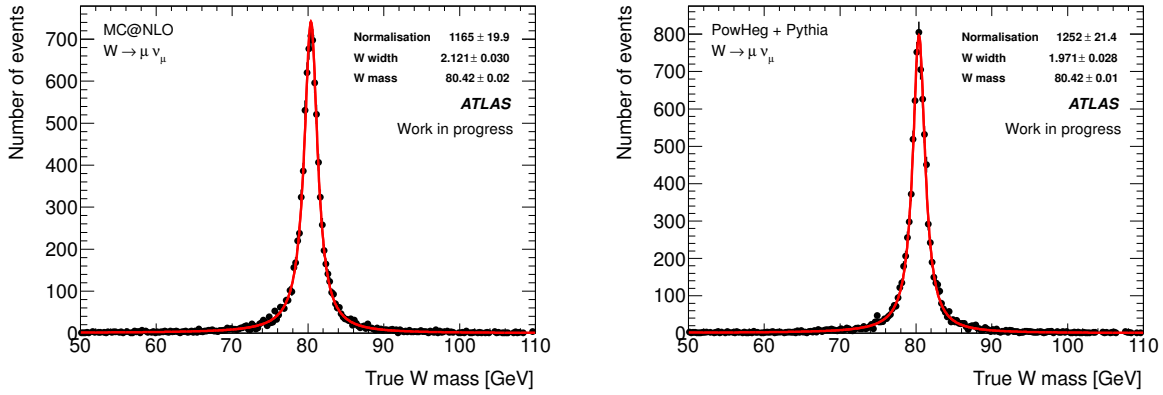

(a) (b)

Figure 6.16: Distribution of the true W mass before cuts. The measured W mass and width are $M_W = (80.385 \pm 0.015)$ GeV and $\Gamma_W = (2.085 \pm 0.042)$ GeV, respectively [15]. A fit of a Breit-Wigner function is also shown.

6.9.9 W mass and width reweighting

The distributions of the true W masses generated by the PowHeg and MCNLO event generators are shown in figure 6.16. In order to check the influence of the mean and width of these distributions on the transverse mass, events have been reweighted within 2 standard deviations of the measured precision. The effect on the fit is found to be marginal and has therefore not been added to the systematic uncertainties.

6.9.10 Generator / Matrix element

The systematic uncertainty due to different implementations of the matrix element calculations done in the available Monte Carlo generators have been estimated. For that, the default signal Monte Carlo generator PowHeg+Herwig+Jimmy is replaced by MC@NLO+Herwig+Jimmy and the analysis is repeated. An impression of the differences between the predictions made by the two event generators can be obtained from figure 6.17.

6.9.11 Combining the systematic errors

A complete list of the studied systematic uncertainties can be found in table 6.13. The quoted numbers are evaluated for the configuration with the lowest total systematic uncertainty which is obtained by adding the individual errors quadratically, separated according to positive and negative contributions.

By simply adding the systematic error contributions, however, the total amount of systematic uncertainty might be over-estimated. It is assumed in the following that the maximally allowed systematic variation of the templates still have to result in a fit with good quality. For an estimation, the templates are gradually morphed from the nominal distribution up to the full systematic deviation. The maximally allowed systematic uncertainty is then obtained by requiring the overall fit to have a p-value of at least 5%.

In figure 6.18 (a) the fit results are presented again, together with the naively combined statistical and total systematic error. Figure 6.18 (b) shows the difference if the maximally allowed systematic uncertainty is restricted by requiring a still good fit quality. Figure 6.18 (c) eventually shows the total

Systematic	Relative uncertainty [%] (morphed)	Relative uncertainty [%] (not morphed)
Muon efficiency scale		
statistical part up	0.22	0.22
statistical part down	-0.22	-0.22
systematical part	cancels out	cancels out
Muon momentum scale		
Muon momentum scale up	$< \pm$ 0.01	-21.0
Muon momentum scale down	8.1	20.1
Muon momentum resolution		
Muon momentum resolution MS up	$< \pm$ 0.01	-0.55
Muon momentum resolution MS down	0.33	0.33
Muon momentum resolution ID up	-0.22	-0.22
Muon momentum resolution ID down	0.11	0.11
Electron systematics		
Electron energy scale up	0.11	0.11
Electron energy scale down	$< \pm$ 0.01	$< \pm$ 0.01
Electron energy resolution up	$< \pm$ 0.01	$< \pm$ 0.01
Electron energy resolution down	$< \pm$ 0.01	$< \pm$ 0.01
Jet systematics		
Jet energy resolution	-1.7	-5.9
Jet energy scale up	2.3	7.9
Jet energy scale down	-8.9	-8.9
E_T^{miss} systematics		
E_T^{miss} Soft terms scale up	-7.3	-9.2
E_T^{miss} Soft terms scale down	$< \pm$ 0.01	9.1
E_T^{miss} Soft terms resolution up	$< \pm$ 0.01	-0.77
E_T^{miss} Soft terms resolution down	0.11	0.11
E_T^{miss} Soft terms pt_hard scale up	-1.4	-1.4
E_T^{miss} Soft terms pt_hard scale down	0.22	1.5
E_T^{miss} Soft terms pt_hard resolution up	-3.1	-3.8
E_T^{miss} Soft terms pt_hard resolution down	$< \pm$ 0.01	4.1
E_T^{miss} Soft terms pt_hard resolution downup	$< \pm$ 0.01	2.0
E_T^{miss} Soft terms pt_hard resolution updown	$< \pm$ 0.01	-1.9
PDF 1 (HERAPDF15)	$< \pm$ 0.01	1.4
PDF 2 (NNPDF10)	-1.1	-0.33
Generator / matrix element	$< \pm$ 0.01	4
QCD shape estimation	13.5	
Total	+15.9 -12.1	+27.8 -26.1

Table 6.13: Overview on the various systematic uncertainties.

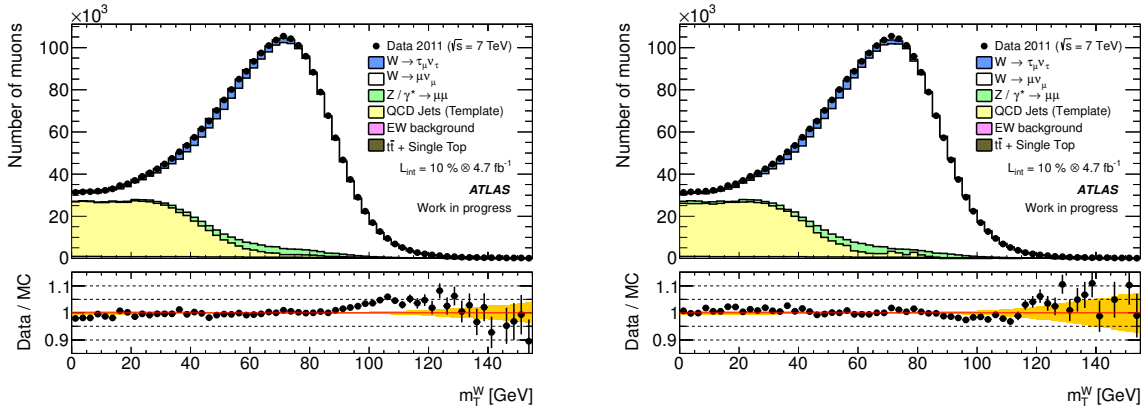

(a) (b)

Figure 6.17: Determination of the systematic uncertainty due to different implementations of the matrix element calculations. The Monte Carlo predictions obtained by PowHeg+Herwig+Jimmy (a) is compared with MC@NLO+Herwig+Jimmy (b).

systematic error including the error on the muon momentum scale, likewise requiring a good fit quality. In all of these figures the QCD shape and generator uncertainties are not yet included.

6.10 Summary

To conclude, the feasibility of a measurement of the ratio of cross sections

$$\frac{\sigma(\mathrm{pp} \to \mathrm{W}) \times \mathrm{BR}(W \to \tau\nu_\tau)}{\sigma(\mathrm{pp} \to \mathrm{W}) \times \mathrm{BR}(W \to \mu\nu_\mu)} = \frac{\mathrm{BR}(W \to \tau\nu_\tau)}{\mathrm{BR}(W \to \mu\nu_\mu)} \equiv \frac{\Gamma(W \to \tau\nu_\tau)}{\Gamma(W \to \mu\nu_\mu)}$$

has been investigated. For that, $W \to \mu\nu_\mu$ and $W \to \tau_\mu\nu_\tau$ events have been selected simultaneously. Simulated template distributions of the transverse mass of the W, the variable which discriminates best between the two processes, have been fitted to data.

The events have been selected by requiring a muon trigger and to contain exactly one muon of good quality. In order to reduce QCD background the muon additionally has to be isolated from other activity in the detector.

It has been found that the remaining background mainly consists of QCD events where a muon is produced in the course of the decay of a heavy quark and $Z \to \mu\mu$ events where one muon escapes detection. The background has been estimated with the help of Monte Carlo events with the exception of QCD which has been estimated using a data-driven approach.

A number of systematic uncertainties have been studied. Despite the fact that some common systematic uncertainties cancel out in the ratio, the measurement is found to be still dominated by systematics. The largest contributions come from the estimation of the shape of the QCD background and the energy scales of muons, missing transverse energy and jets. Overall, the total systematic uncertainty is estimated to be of order 15%. Under the assumption, however, that the template shapes are allowed to vary within their systematics only as long as a good fit quality can be obtained, this error is expected to scale down when more data is taken into account. In figure 6.18 (d) the analysis result including all errors is compared with the result obtained from the direct measurement of the $W \to \tau_\mathrm{h}\nu_\tau$ cross section.

In order to reduce the overall systematic uncertainty, obviously the shapes of the contributing template

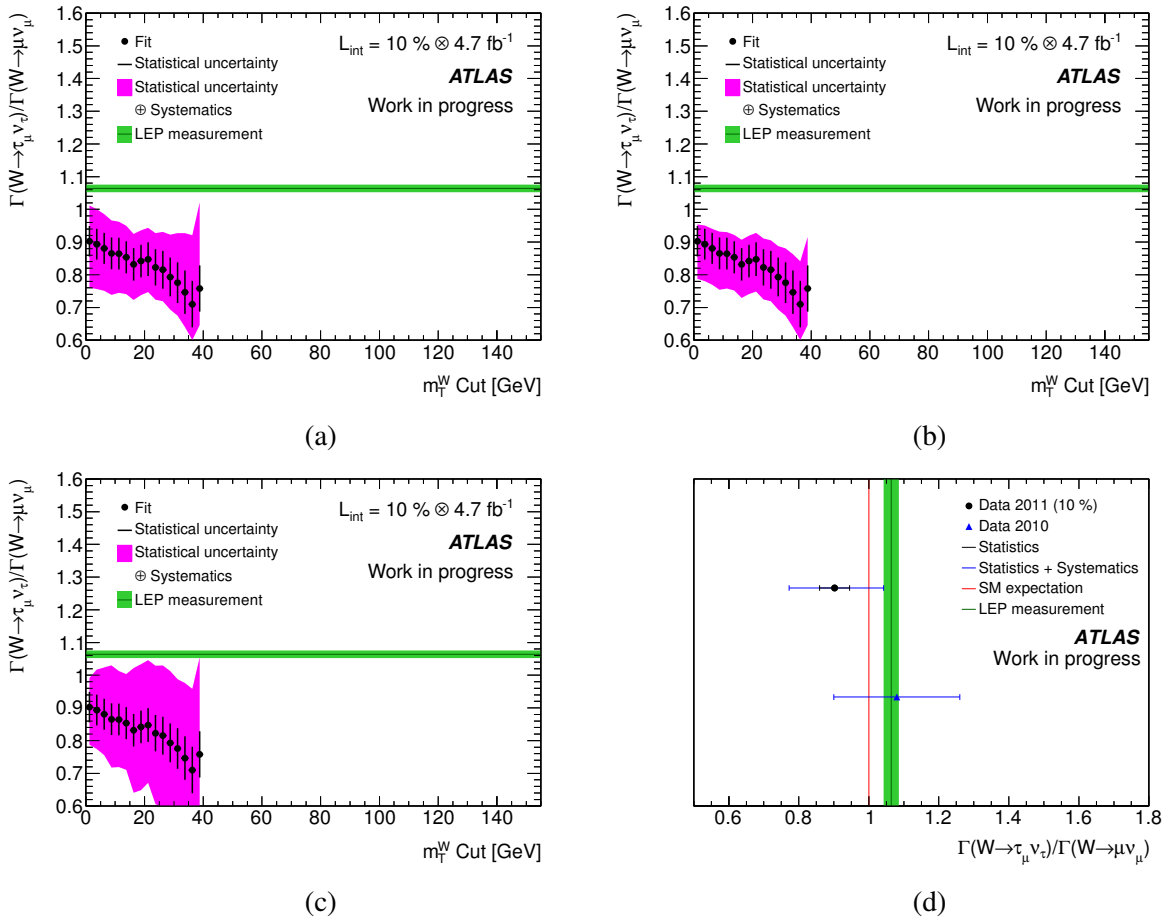

Figure 6.18: Fit results for various cuts on the transverse mass together with the combined statistical and systematic errors (area colored in magenta, a). Systematic uncertainty after the removal of bad fits (b). Total systematic uncertainty including the contribution from the muon momentum scale and also after the removal of bad fits (without QCD shape and generator systematics) (c). Comparison between the results of this analysis (with full systematics) and the direct measurement of the $W \to \tau_{\mathrm{h}}\nu_{\tau}$ cross section (d).

distributions have to be known to a higher degree. Therefore, a measurement of the ratio of branching fractions has not yet been attempted. Propositions for further studies are provided in the following.

6.10.1 Determination of the $Z \to \mu\mu$ background

So far it has been assumed that the $Z \to \mu\mu$ background is sufficiently understood and well modelled in the Monte Carlo. However, since only $Z \to \mu\mu$ events where one muon escapes detection contributes to the background, further studies should investigate if this statement still holds for this particular subset.

6.10.2 QCD background

Alternative approaches to estimate the shape of the QCD background distributions can be applied to reduce the overall systematic error. A relatively clean sample of QCD events can be obtained by making use of a tag-and-probe method. Events with two muons can be selected where the tag muon is required

to be badly isolated. The distribution of the isolated probe muons can then be used to estimate the shape of the QCD background distribution. However, the sample selected by this method might suffer from pollution of $Z \to \mu\mu$ events. Corrections can be provided by subtracting the distribution of the usually well modelled $Z \to \mu\mu$ simulation or by cutting away the Z-peak. Pollution from $W \to \tau_\mu\nu_\tau$ is expected to play a minor role since the QCD background is of interest mostly in a kinematically separated region (e.g. for $m_{\mathrm{T}}^{\mathrm{W}} \leq 40$ GeV).

Chapter 7

Summary

Since the start of data taking in the year 2009 the Large Hadron Collider has been operated very successfully. This work contributes to the task of obtaining a good understanding of the detectors and the performance of the experimental techniques with a measurement of the jet-tau mis-identification probability using ATLAS data recorded in 2010. For that, a tag-and-probe method has been applied on di-jet events, in order to obtain a clean selection of QCD jets from data, which has the advantage to be largely independent of Monte Carlo simulations. The events are triggered by a combination of Level-1 and event filter triggers since single jet triggers are usually heavily prescaled, hereby removing trigger effects at the transition between trigger eras. The probe jets have been subjected to tau reconstruction and identification algorithms and the fraction of mis-identified objects has been extracted.

Fake rates from 0.1%-10% have been obtained with errors dominated by systematics. Through binning these fake rates in appropriate variables, they offer a useful input into various analyses where the identification of taus is required. Multivariate discrimination techniques are found to usually outperform the simple cut based tau identification. No attempt has currently been made to address potential differences between the quark-gluon ratio of the probe jet samples and the expected jet composition of the samples they will be applied to. However, the di-jet fake rates can nevertheless be used where a significant gluon jet contribution is expected.

In a subsequent section of this work a measurement of the total cross section $\sigma(pp \to W) \times \mathrm{BR}(W \to \tau\nu_\tau)$ at a center-of-mass energy of $\sqrt{s} = 7$ TeV with the ATLAS detector is presented. This Standard Model process is an important background to the decays of the Higgs boson and in searches for New Physics such as Supersymmetry. The measurement is also based on 2010 ATLAS data.

$W \to \tau_\mathrm{h}\nu_\tau$ signal events have been selected by using a combined tau-$E_\mathrm{T}^\mathrm{miss}$ trigger and by requiring a well identified tau and a certain amount of well measured missing transverse energy. The majority of the background consists of $Z \to \tau\tau$ events and events with true or mis-measured $E_\mathrm{T}^\mathrm{miss}$ and a jet faking the tau. Thus, it has been further exploited that in signal events the $E_\mathrm{T}^\mathrm{miss}$ and the direction of any jet are unlikely to be aligned and events containing light leptons are vetoed.

After the selection a clear signal is observed. The detector acceptance, the cut efficiency and the remaining electro-weak background is estimated using simulated events which have been checked to give a good description of the data. The QCD background has been directly estimated from data using a sideband method.

Overall good agreement with theory can be stated, although a few more signal events than expected have been found. Sources of systematic errors have been studied. The measurement precision is limited mainly by uncertainties on the trigger and tau identification efficiency, the energy scale and the tau-jet mis-identification probability.

In conclusion, the cross section has been measured to

$$\sigma^\mathrm{tot}_{W\to\tau\nu_\tau} = \sigma^\mathrm{tot}_W \times \mathrm{BR}(W \to \tau\nu) = \left[11.1 \pm 0.3_\mathrm{(stat)} \pm 1.7_\mathrm{(sys)} \pm 0.4_\mathrm{(lumi)}\right] \text{ nb.}$$

A mere repetition of the measurement with more data in order to increase precision, however, proves not to be very promising, because the low-energy-threshold tau and $E_{\mathrm{T}}^{\mathrm{miss}}$ triggers needed for the event signature selection are heavily prescaled during all later runs.

Therefore, an alternative method is developed, which rather aims to measure the ratio of cross sections

$$\frac{\sigma(\mathrm{pp} \to \mathrm{W}) \times \mathrm{BR}(W \to \tau\nu_\tau)}{\sigma(\mathrm{pp} \to \mathrm{W}) \times \mathrm{BR}(W \to \mu\nu_\mu)} = \frac{\mathrm{BR}(W \to \tau\nu_\tau)}{\mathrm{BR}(W \to \mu\nu_\mu)} \equiv \frac{\Gamma(W \to \tau\nu_\tau)}{\Gamma(W \to \mu\nu_\mu)}.$$

For that, $W \to \mu\nu_\mu$ and $W \to \tau_\mu\nu_\tau$ events have been selected simultaneously on a representative data sample corresponding to 10% of the available integrated luminosity recorded by ATLAS in the year 2011. This test sample is used to establish the selection cuts without biasing an actual measurement which then has to be performed on the remaining 90% of data.

The events have been selected by requiring a muon trigger and to contain exactly one muon of good quality. In order to reduce QCD background, the muon additionally has to be isolated from other activity in the detector. Subsequently, simulated template distributions of the transverse mass of the W, the variable which discriminates best between the two processes, have been fitted to data.

It has been found that the remaining background mainly consists of QCD events where a muon is produced in the course of the decay of a heavy quark and $Z \to \mu\mu$ events where one muon escapes detection. The background has been estimated with the help of Monte Carlo events with the exception of QCD which has been estimated using a data-driven approach.

A number of systematic uncertainties have been studied. Despite the fact that some common systematic uncertainties cancel out in the ratio, the measurement is found to be still dominated by systematics. The largest contributions come from the estimation of the shape of the QCD background and the energy scales of muons, missing transverse energy and jets. Overall, the total systematic uncertainty is estimated to be of order 15%. Under the assumption, however, that the template shapes are allowed to vary within their systematics only as long as a good fit quality can be obtained, this error is expected to scale down when more data is taken into account.

In order to reduce the overall systematic uncertainty, obviously the shapes of the contributing template distributions have to be known to a higher degree than available at the time of this study. Therefore, a measurement of the ratio of branching fractions has not yet been attempted.

Appendix A

Jet cleaning

This appendix summarizes the jet cleaning recommendations of the ATLAS JetMET group for 2010 [82], [134], [135] and 2011 [136] data.

Jet candidates happen to be reconstructed from energy deposits in the calorimeters, which do not originate from proton-proton collisions. These so-called bad jets may have properties which are not reproduced by the Monte Carlo simulations but first of all affect the accuracy of an event's (missing) energy determination. Hence events containing at least one of these jets are usually removed.

Bad jets mainly arise from three different sources: coherent noise in the electromagnetic calorimeter (EMC), noise spikes in the hadronic calorimeter (HEC) and cosmic rays or beam background.

Jets reconstructed from coherent noise in the EMC are characterized by unusual large fractions of deposited energy in this part of the detector. Jets from noise spikes on the other hand deposit almost all of their energy into a small number of cells in the HEC. Eventually, jets reconstructed from cosmic rays or beam background deposit all energy mostly in one calorimeter layer, are out-of-time and are often tilted w.r.t the beam axis. In addition, all bad jets show pulse shape discrepancies when compared to expectations for good jets.

In ATLAS, a cut-based method is used to discriminate between good and bad jets. Usually, a jet has to have a calibrated transverse momentum of at least 20 GeV in order to be considered for cleaning. In the following, the discriminating variables are listed and briefly explained

- Emf or EMf: fraction of a jet's energy deposited in the electromagnetic calorimeter
- Hecf or HECf: fraction of a jet's energy deposited in the hadronic calorimeter
- Fmax or FMax: maximum energy fraction deposited in one calorimeter layer
- Q or LArQ: jet quality. This is the fraction of energy corresponding to LAr cells, which show differences between expected and measured pulse shapes above a certain level
- HECQ: defined as LArQ but calculated from HEC cells only
- AverageLArQF: the energy squared cells mean quality of a jet
- LArQmean: AverageLArQF/65335
- n90: minimum number of cells containing at least 90% of a jet's energy
- t: jet time computed as the energy squared cells mean time
- η: pseudorapidity of a jet at the electromagnetic scale
- neg.E: negative energy in a jet

- chf or Chf: charged fraction of a jet. This is the ratio of the summed transverse momenta of tracks associated to a jet divided by the calibrated transverse momentum of the jet

Various cleaning levels exist ranging from loose cleaning, which usually requires no further modifications of the Monte Carlo simulations but already removes the bulk of events with bad jets, to almost perfect tight cleaning. In the case of the latter, however, additional corrections to the Monte Carlo are mandatory in order to compensate for the (in-)efficiencies of the cleaning. An overview on the existing bad jet definitions can be found in figures A.1 and A.2 which apply to the analyses with 2010 data and in figure A.3 for the 2011 data, respectively.

	Bad jet definition (for rel15 data)			
	Loose	**Loose+ = Loose or**	**Tight = Loose or**	**Tight+ = Tight or**
EM coherent noise	**Emf>0.95 and |Q|>0.8 or**		**Emf>0.90 and |Q|>0.6 or**	
HEC spike	**Hecf>0.8 and n90<=5 or Hecf>0.5 and |Q|>0.5 or**		**Hecf>0.3 and |Q|>0.3 or Hecf>1-|Q|**	
Cosmics - Beam background	**|t|>25 ns or Emf<0.05 or Fmax>0.99 and |η|<2**	**Emf>0.98 and chf<0.02 and |eta|<2**	**Emf<0.10 or Fmax>0.95 and |η|<2**	**Emf>0.95 and chf<0.05 and |eta|<2**

Figure A.1: Bad jet definitions for 2010 ATLAS data (data processing release 15).

	Loose	**Medium = Loose OR**	***under discussion*** **Tight = Medium OR**
HEC spikes	HECf>0.5 && |HECQ|>0.5 or |neg. E|>60GeV	HECf>1-|HECQ|	
EM coherent noise	EMf>0.95 &&|LArQ|>0.8 && |eta|<2.8	EMf>0.9 && |LArQ|>0.8 && |eta|<2.8	|LArQ|>0.95 or EMf>0.98 && |LArQ|>0.05
Non-collision background & Cosmics	|t|>25ns or EMf<0.05 && Chf<0.05 && |eta|<2 or EMf<0.05 && |eta|>=2 or FMax>0.99 && |eta|<2	|t|>10ns or EMf<0.05 && Chf<0.1 && |eta|<2 or EMf>0.95 && Chf<0.05 && |eta|<2	EMf<0.1 && Chf<0.2 && |eta|<2 or EMf<0.1 && |eta|>=2 or EMf>0.9 && Chf<0.02 && |eta|<2

Figure A.2: Bad jet definitions for 2010 ATLAS data (data processing release 16).

Name	Looser	Loose	Medium	Tight
		Looser or	loose or	medium or
HEC spikes	HECf>0.5 && |HECQ|>0.5 &&LArQmean>0.8, or |neg. E| >60 GeV	HECf>0.5 && |HECQ|>0.5	HECf>1-|HECQ|	
EM coherent noise	EMf>0.95 &&|LArQ|>0.8 &&LArQmean>0.8 && |eta|<2.8	EMf>0.95 &&|LArQ|>0.8&& |eta|<2.8	EMf>0.9 && |LArQ|>0.8 && |eta|<2.8	LArQ > 0.95 or EMf > 0.98 && |LArQ| > 0.05
Non-collision bkg & cosmics	EMf<0.05 && Chf <0.05&& |eta| < 2 or EMf<0.05 && |eta| >= 2 or FMax > 0.99 && |eta|<2	|t|>25 ns	|t|>10 ns or EMf<0.05 && Chf < 0.1 && |eta| < 2 or EMf>0.95 && Chf < 0.05 && |eta| < 2	Emf<0.1&&Chf < 0.2 && |eta| < 2.5 or EMf>0.9 && Chf<0.1 && |eta| <2.5 Or Chf < 0.01 && |eta| < 2.5 or EMf<0.1 && |eta| > 2.5

Figure A.3: Bad jet definitions for 2011 ATLAS data (data processing release 17).

Appendix B

Cut flows

This appendix lists the cut flows for the analysis presented in chapter 6, separated according to the used data and Monte Carlo samples.

Cut	Data	MC (total)
Before cuts	45597336 ± 6753	121964548 ± 43627
GRL	40482200 ± 6363	121964548 ± 43627
Noise bursts	40369248 ± 6354	121964548 ± 43627
Collision cleaning	40083996 ± 6331	121810595 ± 43615
Trigger	19022070 ± 4361	45976403 ± 27743
Muon quality	16733911 ± 4091	43795495 ± 27077
Muon p_{T}	8810537 ± 2968	21264169 ± 18313
Muon η	8679580 ± 2946	21030393 ± 18231
One muon	8459150 ± 2908	20790797 ± 18205
$E_{\mathrm{T}}^{\mathrm{miss}}$ cleaning	8448811 ± 2907	20773935 ± 18197
LAr hole	8403600 ± 2899	20636640 ± 18121
Muon isolation	2247115 ± 1499	2206111 ± 2284

Cut	$\mathrm{W} \to \tau_\mu \nu_\tau$	$\mathrm{W} \to \mu \nu_\mu$	$\mathrm{Z} \to \mu\mu$	QCD background	EW background	$\mathrm{t\bar{t}}$
Before cuts	833167 ± 1171	4734468 ± 797	504140 ± 169	105809033 ± 43531	10005321 ± 2511	78419 ± 26
GRL	833167 ± 1171	4734468 ± 797	504140 ± 169	105809033 ± 43531	10005321 ± 2511	78419 ± 26
Noise bursts	833167 ± 1171	4734468 ± 797	504140 ± 169	105809033 ± 43531	10005321 ± 2511	78419 ± 26
Collision cleaning	829263 ± 1168	4699035 ± 794	499663 ± 169	105753060 ± 43520	9951184 ± 2504	78389 ± 26
Trigger	131034 ± 463	2323711 ± 556	351386 ± 141	43120893 ± 27733	27203 ± 35	22177 ± 14
Muon quality	124597 ± 452	2221110 ± 544	345125 ± 139	41057052 ± 27068	25955 ± 34	21656 ± 14
Muon p_{T}	90726 ± 385	1985466 ± 514	286663 ± 127	18870916 ± 18302	17330 ± 27	13068 ± 11
Muon η	89062 ± 381	1949462 ± 509	257134 ± 120	18704814 ± 18220	16964 ± 26	12957 ± 11
One muon	89031 ± 381	1949165 ± 509	75872 ± 66	18648744 ± 18193	16491 ± 26	11494 ± 10
$E_{\mathrm{T}}^{\mathrm{miss}}$ cleaning	88986 ± 381	1947916 ± 509	75628 ± 66	18633484 ± 18186	16442 ± 26	11478 ± 10
LAr hole	88888 ± 381	1946150 ± 509	75559 ± 66	18498407 ± 18110	16372 ± 26	11264 ± 10
Muon isolation	77277 ± 355	1764856 ± 485	67886 ± 63	273845 ± 2202	13754 ± 23	8493 ± 9

Cut	$W^+ \to \tau_\mu \nu_\tau$	$W^- \to \tau_\mu \nu_\tau$	$W^+ \to \tau_\mu \nu_\tau$ (Var. 1)	$W^- \to \tau_\mu \nu_\tau$ (Var. 1)		
Before cuts	494992 ± 967	338175 ± 661	491682 ± 1388	335900 ± 952		
GRL	494992 ± 967	338175 ± 661	491682 ± 1388	335900 ± 952		
Noise bursts	494992 ± 967	338175 ± 661	491682 ± 1388	335900 ± 952		
Collision cleaning	492571 ± 964	336692 ± 660	488677 ± 1384	334132 ± 949		
Trigger	78850 ± 384	52184 ± 259	76750 ± 545	52416 ± 371		
Muon quality	74940 ± 375	49657 ± 253	72914 ± 531	49697 ± 361		
Muon p_{T}	54089 ± 318	36637 ± 217	52251 ± 449	36690 ± 309		
Muon η	53058 ± 315	36004 ± 215	51301 ± 445	35994 ± 306		
One muon	53043 ± 315	35988 ± 215	51295 ± 445	35981 ± 306		
$E_{\mathrm{T}}^{\mathrm{miss}}$ cleaning	53019 ± 315	35967 ± 215	51255 ± 445	35936 ± 306		
LAr hole	52959 ± 315	35929 ± 215	51222 ± 444	35895 ± 306		
Muon isolation	45919 ± 293	31358 ± 201	43818 ± 412	30865 ± 284		
Cut	$W \to \tau_\mu \nu_\tau$ + 0 Partons	+1 Parton	+2 Partons	+3 Partons	+4 Partons	+ ≥ 5 Partons
Before cuts	687067 ± 887	129498 ± 196	37516 ± 46	10116 ± 24	2557 ± 12	687 ± 6
GRL	687067 ± 887	129498 ± 196	37516 ± 46	10116 ± 24	2557 ± 12	687 ± 6
Noise bursts	687067 ± 887	129498 ± 196	37516 ± 46	10116 ± 24	2557 ± 12	687 ± 6
Collision cleaning	682199 ± 884	129299 ± 195	37501 ± 46	10114 ± 24	2557 ± 12	687 ± 6
Trigger	97785 ± 334	25110 ± 86	8147 ± 21	2407 ± 12	648 ± 6	187 ± 3
Muon quality	92101 ± 324	24191 ± 84	7879 ± 21	2330 ± 12	627 ± 6	181 ± 3
Muon p_{T}	65774 ± 273	18317 ± 73	6004 ± 18	1759 ± 10	466 ± 5	131 ± 3
Muon η	64433 ± 270	18027 ± 73	5913 ± 18	1733 ± 10	459 ± 5	129 ± 3
One muon	64430 ± 270	18016 ± 73	5905 ± 18	1728 ± 10	458 ± 5	129 ± 3
$E_{\mathrm{T}}^{\mathrm{miss}}$ cleaning	64391 ± 270	18002 ± 73	5898 ± 18	1726 ± 10	457 ± 5	128 ± 3
LAr hole	64379 ± 270	17950 ± 72	5859 ± 18	1710 ± 10	452 ± 5	126 ± 3
Muon isolation	55262 ± 251	15678 ± 68	5017 ± 17	1436 ± 9	373 ± 5	98 ± 2

Cut	$W^+ \to \mu\nu_\mu$	$W^- \to \mu\nu_\mu$	$W^+ \to \mu\nu_\mu$ (Var. 1)	$W^- \to \mu\nu_\mu$ (Var. 1)		
Before cuts	2812783 ± 590	1921685 ± 536	2794447 ± 1171	1910496 ± 927		
GRL	2812783 ± 590	1921685 ± 536	2794447 ± 1171	1910496 ± 927		
Noise bursts	2812783 ± 590	1921685 ± 536	2794447 ± 1171	1910496 ± 927		
Collision cleaning	2790243 ± 587	1908792 ± 534	2769472 ± 1165	1895187 ± 923		
Trigger	1442874 ± 422	880837 ± 362	1433610 ± 835	878843 ± 624		
Muon quality	1378778 ± 412	842332 ± 354	1366475 ± 814	837805 ± 608		
Muon p_{T}	1225536 ± 389	759929 ± 336	1216439 ± 768	758872 ± 579		
Muon η	1202926 ± 385	746536 ± 333	1194221 ± 761	745266 ± 573		
One muon	1202769 ± 385	746397 ± 333	1194103 ± 761	745174 ± 573		
$E_{\mathrm{T}}^{\mathrm{miss}}$ cleaning	1202002 ± 385	745915 ± 333	1193268 ± 760	744645 ± 573		
LAr hole	1200968 ± 385	745182 ± 333	1192330 ± 760	744088 ± 573		
Muon isolation	1086136 ± 366	678720 ± 318	1072640 ± 722	675289 ± 546		
Cut	$W \to \mu\nu_\mu$ + 0 Partons	+1 Parton	+2 Partons	+3 Partons	+4 Partons	+ ≥ 5 Partons
Before cuts	3903228 ± 1487	735219 ± 331	213356 ± 110	57268 ± 57	14465 ± 29	3972 ± 15
GRL	3903228 ± 1487	735219 ± 331	213356 ± 110	57268 ± 57	14465 ± 29	3972 ± 15
Noise bursts	3903228 ± 1487	735219 ± 331	213356 ± 110	57268 ± 57	14465 ± 29	3972 ± 15
Collision cleaning	3861320 ± 1479	733700 ± 331	213242 ± 110	57260 ± 57	14465 ± 29	3972 ± 15
Trigger	1836579 ± 1018	385809 ± 239	114653 ± 81	31405 ± 42	8037 ± 21	2223 ± 11
Muon quality	1742542 ± 992	372746 ± 235	111021 ± 80	30412 ± 42	7785 ± 21	2154 ± 11
Muon p_{T}	1563595 ± 940	331028 ± 222	96638 ± 74	25924 ± 39	6465 ± 19	1741 ± 10
Muon η	1532545 ± 930	325311 ± 220	95036 ± 74	25505 ± 38	6361 ± 19	1715 ± 10
One muon	1532487 ± 930	325197 ± 220	94942 ± 74	25457 ± 38	6342 ± 19	1709 ± 10
$E_{\mathrm{T}}^{\mathrm{miss}}$ cleaning	1531467 ± 930	324895 ± 220	94828 ± 74	25423 ± 38	6332 ± 19	1706 ± 10
LAr hole	1531076 ± 930	323935 ± 219	94255 ± 73	25186 ± 38	6251 ± 19	1678 ± 10
Muon isolation	1383305 ± 884	291636 ± 208	83340 ± 69	21871 ± 35	5339 ± 17	1394 ± 9

Cut	$W \to e\nu_e$ + 0 Partons	+1 Parton	+2 Partons	+3 Partons	+4 Partons	+ ≥ 5 Partons
Before cuts	3909885 ± 1490	736291 ± 331	213327 ± 111	57466 ± 57	14488 ± 29	3944 ± 15
GRL	3909885 ± 1490	736291 ± 331	213327 ± 111	57466 ± 57	14488 ± 29	3944 ± 15
Noise bursts	3909885 ± 1490	736291 ± 331	213327 ± 111	57466 ± 57	14488 ± 29	3944 ± 15
Collision cleaning	3877648 ± 1484	735041 ± 331	213229 ± 111	57457 ± 57	14486 ± 29	3943 ± 15
Trigger	33 ± 4	175 ± 5	149 ± 3	77 ± 2	30 ± 1	12 ± 1
Muon quality	23 ± 4	147 ± 5	127 ± 3	66 ± 2	25 ± 1	10 ± 1
Muon p_{T}	8 ± 2	88 ± 4	79 ± 2	42 ± 2	15 ± 1	6 ± 1
Muon η	8 ± 2	88 ± 4	78 ± 2	42 ± 2	15 ± 1	6 ± 1
One muon	8 ± 2	88 ± 4	78 ± 2	42 ± 2	15 ± 1	6 ± 1
$E_{\mathrm{T}}^{\mathrm{miss}}$ cleaning	8 ± 2	88 ± 4	78 ± 2	42 ± 2	14 ± 1	6 ± 1
LAr hole	8 ± 2	87 ± 4	77 ± 2	41 ± 2	14 ± 1	6 ± 1
Muon isolation	0 ± 0	4 ± 1	1 ± 0	0 ± 0	0 ± 0	0 ± 0
Cut	$W \to \tau_\mu\nu_\tau$ + 0 Partons (other)	+1 Parton	+2 Partons	+3 Partons	+4 Partons	+ ≥ 5 Partons
Before cuts	3216725 ± 1928	606285 ± 425	175642 ± 101	47361 ± 52	11970 ± 27	3217 ± 14
GRL	3216725 ± 1928	606285 ± 425	175642 ± 101	47361 ± 52	11970 ± 27	3217 ± 14
Noise bursts	3216725 ± 1928	606285 ± 425	175642 ± 101	47361 ± 52	11970 ± 27	3217 ± 14
Collision cleaning	3202349 ± 1924	605630 ± 425	175578 ± 100	47353 ± 52	11969 ± 27	3217 ± 14
Trigger	175 ± 14	193 ± 8	143 ± 3	72 ± 2	27 ± 1	11 ± 1
Muon quality	125 ± 12	153 ± 7	118 ± 3	60 ± 2	23 ± 1	9 ± 1
Muon p_{T}	52 ± 8	98 ± 5	72 ± 2	37 ± 1	13 ± 1	5 ± 1
Muon η	52 ± 8	97 ± 5	72 ± 2	37 ± 1	13 ± 1	5 ± 1
One muon	52 ± 8	96 ± 5	72 ± 2	37 ± 1	13 ± 1	5 ± 1
$E_{\mathrm{T}}^{\mathrm{miss}}$ cleaning	52 ± 8	96 ± 5	72 ± 2	36 ± 1	13 ± 1	5 ± 1
LAr hole	52 ± 8	94 ± 5	71 ± 2	36 ± 1	13 ± 1	5 ± 1
Muon isolation	22 ± 5	8 ± 2	4 ± 0	1 ± 0	0 ± 0	0 ± 0

Cut	$Z \to ee$ + 0 Partons	+1 Parton	+2 Partons	+3 Partons	+4 Partons	+ ≥ 5 Partons
Before cuts	392752 ± 153	78960 ± 69	23824 ± 17	6558 ± 9	1692 ± 4	488 ± 2
GRL	392752 ± 153	78960 ± 69	23824 ± 17	6558 ± 9	1692 ± 4	488 ± 2
Noise bursts	392752 ± 153	78960 ± 69	23824 ± 17	6558 ± 9	1692 ± 4	488 ± 2
Collision cleaning	389438 ± 153	78836 ± 69	23813 ± 17	6557 ± 9	1692 ± 4	488 ± 2
Trigger	3 ± 0	12 ± 1	13 ± 0	8 ± 0	3 ± 0	1 ± 0
Muon quality	2 ± 0	10 ± 1	11 ± 0	7 ± 0	3 ± 0	1 ± 0
Muon p_{T}	1 ± 0	5 ± 1	6 ± 0	4 ± 0	2 ± 0	1 ± 0
Muon η	1 ± 0	5 ± 1	6 ± 0	4 ± 0	2 ± 0	1 ± 0
One muon	1 ± 0	5 ± 1	6 ± 0	4 ± 0	2 ± 0	1 ± 0
$E_{\mathrm{T}}^{\mathrm{miss}}$ cleaning	1 ± 0	5 ± 1	6 ± 0	4 ± 0	2 ± 0	0 ± 0
LAr hole	1 ± 0	5 ± 1	6 ± 0	4 ± 0	2 ± 0	0 ± 0
Muon isolation	0 ± 0	0 ± 0	0 ± 0	0 ± 0	0 ± 0	0 ± 0
Cut	$Z \to \mu\mu$ + 0 Partons	+1 Parton	+2 Partons	+3 Partons	+4 Partons	+ ≥ 5 Partons
Before cuts	392964 ± 154	78830 ± 69	23701 ± 17	6576 ± 9	1616 ± 4	453 ± 2
GRL	392964 ± 154	78830 ± 69	23701 ± 17	6576 ± 9	1616 ± 4	453 ± 2
Noise bursts	392964 ± 154	78830 ± 69	23701 ± 17	6576 ± 9	1616 ± 4	453 ± 2
Collision cleaning	388648 ± 153	78683 ± 69	23689 ± 17	6575 ± 9	1616 ± 4	453 ± 2
Trigger	265940 ± 126	60069 ± 60	18478 ± 15	5232 ± 8	1298 ± 4	368 ± 2
Muon quality	260653 ± 125	59354 ± 59	18286 ± 15	5181 ± 8	1286 ± 4	365 ± 2
Muon p_{T}	220335 ± 115	47089 ± 53	14145 ± 13	3896 ± 7	939 ± 3	259 ± 2
Muon η	197205 ± 108	42543 ± 50	12781 ± 12	3524 ± 7	849 ± 3	233 ± 1
One muon	59599 ± 60	11862 ± 27	3300 ± 6	860 ± 3	199 ± 1	52 ± 1
$E_{\mathrm{T}}^{\mathrm{miss}}$ cleaning	59408 ± 60	11824 ± 27	3288 ± 6	857 ± 3	199 ± 1	52 ± 1
LAr hole	59392 ± 60	11798 ± 27	3271 ± 6	850 ± 3	196 ± 1	51 ± 1
Muon isolation	53337 ± 57	10689 ± 25	2907 ± 6	743 ± 3	168 ± 1	43 ± 1

Cut	$Z \to \tau\tau$ + 0 Partons	+1 Parton	+2 Partons	+3 Partons	+4 Partons	+ ≥ 5 Partons
Before cuts	392799 ± 121	79224 ± 52	23718 ± 24	6611 ± 9	1640 ± 4	453 ± 2
GRL	392799 ± 121	79224 ± 52	23718 ± 24	6611 ± 9	1640 ± 4	453 ± 2
Noise bursts	392799 ± 121	79224 ± 52	23718 ± 24	6611 ± 9	1640 ± 4	453 ± 2
Collision cleaning	390906 ± 121	79142 ± 52	23709 ± 24	6610 ± 9	1639 ± 4	452 ± 2
Trigger	18478 ± 26	5137 ± 13	1732 ± 6	531 ± 3	144 ± 1	42 ± 1
Muon quality	17692 ± 26	4970 ± 13	1679 ± 6	514 ± 3	139 ± 1	41 ± 1
Muon p_{T}	11724 ± 21	3433 ± 11	1164 ± 5	355 ± 2	95 ± 1	27 ± 1
Muon η	11453 ± 21	3369 ± 11	1144 ± 5	349 ± 2	93 ± 1	27 ± 1
One muon	11109 ± 20	3285 ± 11	1113 ± 5	339 ± 2	90 ± 1	26 ± 1
$E_{\mathrm{T}}^{\mathrm{miss}}$ cleaning	11074 ± 20	3276 ± 11	1110 ± 5	338 ± 2	90 ± 1	25 ± 1
LAr hole	11047 ± 20	3255 ± 10	1101 ± 5	334 ± 2	89 ± 1	25 ± 1
Muon isolation	9529 ± 19	2875 ± 10	939 ± 5	278 ± 2	71 ± 1	20 ± 0

Cut	$c\bar{c}$	$b\bar{b}$	$t\bar{t}$
Before cuts	76434873 ± 36243	29374160 ± 24112	78419 ± 26
GRL	76434873 ± 36243	29374160 ± 24112	78419 ± 26
Noise bursts	76434873 ± 36243	29374160 ± 24112	78419 ± 26
Collision cleaning	76389830 ± 36232	29363231 ± 24108	78389 ± 26
Trigger	31668609 ± 23303	11452284 ± 15037	22177 ± 14
Muon quality	30078022 ± 22713	10979030 ± 14724	21656 ± 14
Muon p_{T}	13742195 ± 15307	5128722 ± 10032	13068 ± 11
Muon η	13619559 ± 15238	5085254 ± 9989	12957 ± 11
One muon	13574063 ± 15213	5074680 ± 9979	11494 ± 10
$E_{\mathrm{T}}^{\mathrm{miss}}$ cleaning	13563076 ± 15207	5070408 ± 9974	11478 ± 10
LAr hole	13472394 ± 15148	5026013 ± 9924	11264 ± 10
Muon isolation	216711 ± 1928	57134 ± 1063	8493 ± 9

Bibliography

[1] S. L. Glashow, “Partial-symmetries of weak interactions”, *Nuclear Physics* 22(4) (1961) 579–588.

[2] S. Weinberg, “Elementary particle theory of composite particles”, *Phys. Rev.* 130 (1963) 776–783.

[3] S. Weinberg, “A model of leptons”, *Phys. Rev. Lett.* 19 (1967) 1264–1266.

[4] M. Uhlenbrock, “Studie zur Rekonstruktion der mSUGRA-Parameter aus LHC-Observablen mit Fittino”, *Diploma thesis, University of Bonn* (2008).

[5] P. W. Higgs, “Broken symmetries, massless particles and gauge fields”, *Phys. Lett.* 12 (1964) 132–133.

[6] P. W. Higgs, “Broken symmetries and the masses of gauge bosons”, *Phys. Rev. Lett.* 13 (1964) 508–509.

[7] F. Englert and R. Brout, “Broken symmetry and the mass of gauge vector mesons”, *Phys. Rev. Lett.* 13 (1964) 321–323.

[8] G. S. Guralnik, C. R. Hagen and T. W. B. Kibble, “Global conservation laws and massless particles”, *Phys. Rev. Lett.* 13 (1964) 585–587.

[9] The ATLAS Collaboration, “Observation of a new particle in the search for the Standard Model Higgs boson with the ATLAS detector at the LHC”, *Phys. Lett. B 716* (2012) 1–29.

[10] M. E. Peskin and D. V. Schroeder, *An Introduction to Quantum Field Theory*, Addison-Wesley, 1995.

[11] J. Schwinger, “On Quantum-Electrodynamics and the Magnetic Moment of the Electron”, *Phys. Rev.* 73 (1948) 416.

[12] R. P. Feynman, “Mathematical Formulation of the Quantum Theory of Electromagnetic Interaction”, *Phys. Rev.* 80 (1950) 440.

[13] A. Salam and J. Ward, “Weak and electromagnetic interactions”, *Il Nuovo Cimento* 11 (1959) 568–577.

[14] H. Fritzsch, M. Gell-Mann and H. Leutwyler, “Advantages of the color octet gluon picture”, *Phys. Lett. B* 47(4) (1973) 365–368.

[15] W.-M. et al. (Particle Data Group), “The Review of Particle Physics”, *J. Phys. G 33, 1 (2006) and 2007 partial update for the 2008 edition* (200r78).

[16] K. Adel and F. J. Yndurain, “Production of heavy quarks close to threshold”, *Phys. Rev. D* 52 (1995) 6577–6594.

[17] G. ’t Hooft and M. Veltman, “Regularization and renormalization of gauge fields”, *Nuclear Physics B* 44(1) (1972) 189–213.

[18] N. Cabibbo, "Unitary symmetry and leptonic decays", *Phys. Rev. Lett.* 10 (1963) 531–533.

[19] M. Kobayashi and T. Maskawa,
"CP-violation in the renormalizable theory of weak interaction",
Progress of Theoretical Physics 49(2) (1973) 652–657.

[20] S. Collaboration, "Direct evidence for neutrino flavor transformation from neutral-current interactions in the Sudbury neutrino observatory", *Phys. Rev. Lett.* 89 (2002).

[21] Z. Maki et al., "A unified model for elementary particles",
Prog. Theor. Phys. 23 (1960) 1174–1180.

[22] M. L. Perl et al., "Evidence for anomalous lepton production in e^+e^- annihilation",
Physical Review Letters 35 (Dec. 1975) 1489–1492.

[23] D. Zeppenfeld, "Event generation and parton shower", *PiTP lecture* (2005).

[24] M. E. Peskin and D. V. Schroeder, "Introduction to Quantum Field Theory",
Westview Press, Boulder, Colorado (2005).

[25] P. Schmüser, *Feynman-Graphen und Eichtheorien für Experimentalphysiker*, Springer, 1995.

[26] I. J. R. Aitchison, "Supersymmetry and the MSSM: An Elementary Introduction"
(2005), arXiv:hep-ph/05055105v1.

[27] U. Amaldi, W. de Boer and H. Fuerstenau, "Comparison of grand unified theories with electroweak and strong coupling constants measured at LEP",
Physics Letters B, 260/3,4 (1991).

[28] D. Clowe et al., "A direct empirical proof of the existence of dark matter",
Astrophys. J. 648 (2006) L109–L113, arXiv:astro-ph/0608407.

[29] C. L. Bennett et al., "First Year Wilkinson Microwave Anisotropy Probe (WMAP) Observations: Preliminary Maps and Basic Results", *Astrophys. J. Suppl.* 148 (2003) 1.

[30] Detailed information from the design report to present status may be found at
http://lhc.web.cern.ch/lhc/.

[31] L. Evans and P. Bryant, "LHC Machine", *JINST 3* S08001 (2008).

[32] R. A. et al., *Nucl. Phys. B, Proc. Suppl.* 9 (2002) 17-31.

[33] H. Edwards, "The Tevatron Energy Doubler: A Superconducting Accelerator",
Ann. Rev. Nucl. Part. Sci. 35 (1985) 605.

[34] M. Benedikt, P. Collier, V. Mertens et al., "LHC Design Report" (2008).

[35] The ATLAS Collaboration, "Luminosity public results" (2011),
eprint: https://twiki.cern.ch/twiki/bin/view/AtlasPublic/LuminosityPublicResults#Luminosity_versus_day.

[36] S. Chatrchyan et al., "The CMS experiment at the LHC",
Journal of Instrumentation 3(08) (2008).

[37] K. Aamodt et al., "The ALICE experiment at the LHC",
Journal of Instrumentation 3(08) (2008).

[38] A. Augusto Alves Jr. et al., "The LHCb experiment at the LHC",
Journal of Instrumentation 3(08) (2008).

[39] The ATLAS Collaboration, "The ATLAS Experiment at the CERN Large Hadron Collider", *JINST 3* S08003 (2008).

[40] The ATLAS Collaboration, "ATLAS inner detector: Technical Design Report", *Technical Design Report ATLAS* (1997).

[41] G. Aad et al., "The ATLAS Inner Detector commissioning and calibration", *European Physical Journal C* 70 (Dec. 2010) 787–821, arXiv:1004.5293 [physics.ins-det].

[42] Wermes, N. and Hallewel, G., "ATLAS pixel detector: Technical Design Report", *Technical Design Report ATLAS* (1997).

[43] A. Ahmad, Z. Albrechtskirchinger et al., "The silicon microstrip sensors of the ATLAS semiconductor tracker", *Nuclear Instruments and Methods in Physics Research Section A: Accelerators, Spectrometers, Detectors and Associated Equipment* 578(1) (2007) 98–118.

[44] E. Abat, T. N. Add et al., "ATLAS transition radiation tracker (TRT) proportional drift tube: design and performance", *Journal of Instrumentation* 3(2) (2008).

[45] The ATLAS Collaboration, "ATLAS end-cap toroids: Technical Design Report", *Technical Design Report ATLAS* (1997).

[46] The ATLAS Collaboration, "ATLAS liquid-argon calorimeter: Technical Design Report", *Technical Design Report ATLAS* (1996).

[47] The ATLAS Collaboration, "ATLAS tile calorimeter: Technical Design Report", *Technical Design Report ATLAS* (1996).

[48] The ATLAS Collaboration, "ATLAS muon spectrometer: Technical Design Report", *Technical Design Report ATLAS* (1997).

[49] The ATLAS Collaboration, "ATLAS magnet system: Technical Design Report", *Technical Design Report ATLAS* (1997).

[50] The ATLAS Collaboration, "ATLAS central solenoid: Technical Design Report", *Technical Design Report ATLAS* (1997).

[51] The ATLAS Collaboration, "ATLAS barrel toroid: Technical Design Report", *Technical Design Report ATLAS* (1997).

[52] The ATLAS Collaboration, "ATLAS Level-1 Trigger: Technical Design Report", *Technical Design Report ATLAS* (1998).

[53] P. Jenni et al., "ATLAS high-level trigger, data acquisition and controls: Technical Design Report", *Technical Design Report ATLAS* (2003).

[54] M. Dam and the Atlas Tdaq Collaboration, "The ATLAS tau trigger", *Journal of Physics: Conference Series* 219.3 (2010).

[55] G. Duckeck et al., "ATLAS computing: Technical design report" (2005), ed. by G. Duckeck.

[56] S. Agostinelli et al., "GEANT4: A Simulation toolkit" (2003).

[57] W. Lukas, "Fast Simulation for ATLAS: Atlfast-II and ISF", *Journal of Physics: Conference Series* 396.2 (2012).

[58] W. Lampl, D. Laplace S. Lelas et al.,
"Calorimeter clustering algorithms. Description and performance. Technical Report",
ATL-LARG-PUB-2008-002, ATL-COM-LARG-2008-003 (2008).

[59] G. Aad et al.,
"Expected performance of the ATLAS experiment - detector, trigger and physics" (2008).

[60] G. Aad et al., "Measurement of inclusive jet and dijet production in pp collisions at $\sqrt{s} = 7$ TeV using the ATLAS detector", *Phys.Rev.* D86 (2012) 014022, arXiv:1112.6297 [hep-ex].

[61] P. Adragana, C. Alexa, K. Anderson et al.,
"Measurement of pion and proton response and longitudinal shower profiles up to 20 nuclear interaction lengths with the ATLAS tile calorimeter. Technical Report",
CERN-PH-EP-2009-019, ATL-TILECAL-PUB-2009-009 (2009).

[62] E. Abat, J. M. Abdallah, T. N. Addy et al., "Response and shower topology of 2 to 180 GeV pions measured with the ATLAS barrel calorimeter at the CERN test-beam and comparison to Monte Carlo simulations. Technical Report", ATL-CAL-PUB-2010-001 (2010).

[63] E. Abat, J. M. Abdallah, T. N. Addy et al., "Study of energy response and resolution of the ATLAS central calorimeter to pions of energies from 20 to 350 GeV",
Nucl. Instrum. Methods Phys. Res., A 621:134-150 (2010).

[64] E. Abat, J. M. Abdallah, T. N. Addy et al., "Study of the response of the ATLAS central calorimeter to pions of energies from 3 to 9 GeV",
Nucl. Instrum. Methods Phys. Res., A 607(2):372-386 (2009).

[65] C. Cojocaru, L. Pinfold, J. Soukup et al., "Hadronic calibration of the ATLAS liquid argon endcap calorimeter in the pseudorapidity region $1.6 < |\eta| < 1.8$ in beam tests",
Nucl. Instrum. Methods Phys. Res., A 531:481-514 (2004).

[66] G. Aad et al., "Jet energy scale and its systematic uncertainty in proton-proton collisions at $\sqrt{s} = 7$ TeV in ATLAS 2010 data. Technical Report", ATLAS-CONF-2011-032 (2011).

[67] S. Lai and A. Kaczmarska,
"Reconstruction and Identification of Hadronic Tau Decays with ATLAS" (2008),
arXiv:0809.5144 [hep-ex].

[68] The ATLAS Collaboration,
"Performance of the Reconstruction and Identification of Hadronic Tau Decays with ATLAS",
ATLAS-CONF-2011-152, ATLAS-COM-CONF-2011-179 (2011).

[69] The ATLAS Collaboration, "Cut based identification of hadronic tau decays",
ATL-PHYS-PUB-2010-001, ATL-COM-PHYS-2009-583 (2010).

[70] The ATLAS Collaboration, "Reconstruction, Energy Calibration, and Identification of Hadronically Decaying Tau Leptons",
ATLAS-CONF-2011-077, ATLAS-COM-CONF-2011-057 (2011).

[71] G. Aad et al., "Muon reconstruction efficiency and momentum resolution of the ATLAS experiment in proton-proton collisions at $\sqrt{s}$=7 TeV in 2010", *Eur.Phys.J.* C74 (2014) 3034, arXiv:1404.4562 [hep-ex].

[72] G. Aad et al., "Performance of Missing Transverse Momentum Reconstruction in Proton-Proton Collisions at 7 TeV with ATLAS", *Eur.Phys.J.* C72 (2012) 1844, arXiv:1108.5602 [hep-ex].

[73] The ATLAS Collaboration, "Measurement of the Mis-identification Probability of τ Leptons from Hadronic Jets and from Electrons", ATLAS-CONF-2011-113 (2011).

[74] Bechtle, P. and others, "Studying Tau Reconstruction and Identification Performance in Di-Jet, Three-Jet and Photon-Jet Events with the ATLAS Experiment", ATLAS internal note (2011).

[75] The ATLAS Collaboration, *Expected electron performance in the ATLAS experiment*, ATL-PHYS-PUB-2011-006.

[76] "https://atlas-datasummary.cern.ch/lumicalc".

[77] "Updated Luminosity Determination in pp Collisions at root(s)=7 TeV using the ATLAS Detector", tech. rep. ATLAS-CONF-2011-011, Geneva: CERN, 2011.

[78] T. e. a. Sjostrand, "High-energy-physics event generation with PYTHIA 6.1", *Comput. Phys. Commun.* 135 (2001) 238–259, eprint: hep-ph/0010017.

[79] G. Aad et al., "Charged-particle multiplicities in pp interactions measured with the ATLAS detector at the LHC", *New J. Phys.* 13 (2011) 053033.

[80] The ATLAS Collaboration, "The ATLAS Simulation Infrastructure", *Eur. Phys. J.* C70 (2010) 823–874.

[81] "Measurement of the Mis-identification Probability of τ Leptons from Hadronic Jets and from Electrons", tech. rep. ATLAS-CONF-2011-113, Geneva: CERN, 2011.

[82] M Baak, M Petteni and N Makovec, "Data-Quality Requirements and Event Cleaning for Jets and Missing Transverse Energy Reconstruction with the ATLAS Detector in Proton-Proton Collisions at a Center-of-Mass Energy of *sqrts* = 7 TeV", tech. rep. ATLAS-COM-CONF-2010-038, (Was originally 'ATL-COM-PHYS-2010-247'), Geneva: CERN, 2010.

[83] G. P. S. M. Cacciari and G. Soyez, "Dispelling the N^3 myth for the Kt jet-finder", *Phys. Lett.* B641 (2006) 57.

[84] The ATLAS Collaboration, *Calorimeter clustering algorithms: Description and performance*, ATL-LARG-PUB-2008-002.

[85] The ATLAS Collaboration, *Tau Reconstruction and Identification Performance in ATLAS*, ATLAS-CONF-2010-086.

[86] *Studies of Diffractive Enhanced Minimum Bias Events in ATLAS*, ATLAS-COM-CONF-2010-050.

[87] The ATLAS Collaboration, "New ATLAS event generator tunes to 2010 data", ATL-PHYS-PUB-2011-008, ATL-COM-PHYS-2011-329 (2011).

[88] E. Coniavitis and M. Flechl, *ATLAS Tau Identification in Early Data using a Robust Logarithmic Likelihood*, ATLAS note.

[89] D. O. E.N. Dawe and S. Protopopescu, *Using Boosted Decision Trees for Hadronic Tau Identification*, ATLAS note.

[90] G. Aad et al., "Luminosity Determination in pp Collisions at $\sqrt{s}$ = 7 TeV Using the ATLAS Detector at the LHC", *Eur.Phys.J.* C71 (2011) 1630, arXiv:1101.2185 [hep-ex].

[91] G. Aad et al., "Improved luminosity determination in pp collisions at $\sqrt{s}$ = 7 TeV using the ATLAS detector at the LHC", *Eur.Phys.J.* C73 (2013) 2518, arXiv:1302.4393 [hep-ex].

[92] S. Frixione and B. R. Webber,
"Matching NLO QCD computations and parton shower simulations",
Journal of High Energy Physics 2002.06 (2002) 029.

[93] S. Jadach et al., "The τ decay library TAUOLA, version 2.4",
Computer Physics Communications 76.3 (1993) 361 –380.

[94] P. Golonka and Z. Was,
"PHOTOS Monte Carlo: a precision tool for QED corrections in Z and W decays",
The European Physical Journal C - Particles and Fields 45 (1 2006) 97–107.

[95] A. Andreazza et al., "Measurement of the $W \to \tau\nu$ Cross section in pp Collisions at $\sqrt{s}$ = 7 TeV with the ATLAS Experiment", ATL-PHYS-INT-2012-041 (2012).

[96] A. Sherstnev and R. Thorne, "Parton distributions for LO generators",
The European Physical Journal C - Particles and Fields 55 (4 2008) 553–575.

[97] "Charged particle multiplicities in p p interactions at $\sqrt{s}$ = 0.9 and 7 TeV in a diffractive limited phase-space measured with the ATLAS detector at the LHC and new PYTHIA6 tune", tech. rep. ATLAS-CONF-2010-031, Geneva: CERN, 2010.

[98] "A measurement of the total $W^{\pm}$ and $Z/\gamma*$ cross sections in the e and μ decay channels and of their ratios in pp collisions at $\sqrt{s}$ = 7 TeV with the ATLAS detector",
tech. rep. ATLAS-CONF-2011-041, Geneva: CERN, 2011.

[99] "A combined measurement of the top quark pair production cross-section using dilepton and single-lepton final states", tech. rep. ATLAS-CONF-2011-040, Geneva: CERN, 2011.

[100] M. Schott et al., "Supporting Document: Total inclusive W and Z boson cross-section measurements, cross-section ratios and combinations in the electron and muon decay channels at 7TeV based on 300nb-1", tech. rep. ATL-PHYS-INT-2010-125, Geneva: CERN, 2010.

[101] "Updated Luminosity Determination in pp Collisions at $\sqrt{s}$ = 7 TeV using the ATLAS Detector", tech. rep. ATLAS-CONF-2011-011, Geneva: CERN, 2011.

[102] A Ahmed et al., "Supporting Document: Measurement of the W cross section and asymmetry in the electron and muon decay channels at *sqrts*=7 TeV",
tech. rep. ATL-PHYS-INT-2010-116, Geneva: CERN, 2010.

[103] "Jet energy scale and its systematic uncertainty for jets produced in proton-proton collisions at sqrt(s) = 7 TeV and measured with the ATLAS detector", tech. rep. ATLAS-CONF-2010-056, Geneva: CERN, 2010.

[104] "In-situ pseudo-rapidity inter-calibration to evaluate jet energy scale uncertainty and calorimeter performance in the forward region", tech. rep. ATLAS-CONF-2010-055, Geneva: CERN, 2010.

[105] "ATLAS Calorimeter Response to Single Isolated Hadrons and Estimation of the Calorimeter Jet Scale Uncertainty", tech. rep. ATLAS-CONF-2011-028, Geneva: CERN, 2011.

[106] "Reconstruction and Calibration of Missing Transverse Energy and Performance in Z and W events in ATLAS Proton-Proton Collisions at 7 TeV", tech. rep. ATLAS-CONF-2011-080, Geneva: CERN, 2011.

[107] TauWG, *https://twiki.cern.ch/twiki/bin/view/AtlasProtected/TauSystematicsWinterConf2011*.

[108] "Performance of the Missing Transverse Energy Reconstruction and Calibration in Proton-Proton Collisions at a Center-of-Mass Energy of 7 TeV with the ATLAS Detector", tech. rep. ATLAS-CONF-2010-057, Geneva: CERN, 2010.

[109] E Coniavitis et al., "Reconstruction, Energy Calibration, and Identification of Hadronically Decaying Tau Leptons", tech. rep. ATLAS-COM-CONF-2011-057, Geneva: CERN, 2011.

[110] P Bechtle et al., "Measurement of the Mis-identification Probability of tau Leptons from QCD Jets and from Electrons", tech. rep. ATLAS-COM-CONF-2011-067, Geneva: CERN, 2011.

[111] ATLAS Egamma Combined performance group, *https://twiki.cern.ch/twiki/bin/view/AtlasProtected/EfficiencyMeasurements*.

[112] O Arnaez and D Froidevaux, "Electron efficiency measurements using ATLAS 2010 data at sqrt(s) = 7 TeV: Supporting note for the 2010 egamma paper", tech. rep. ATL-COM-PHYS-2011-322, Geneva: CERN, 2011.

[113] ATLAS Muon Combined performance group, *https://twiki.cern.ch/twiki/bin/view/AtlasProtected/MCPAnalysisGuidelinesRel16*.

[114] "Determination of the muon reconstruction efficiency in ATLAS at the Z resonance in proton-proton collisons at sqrt(s)=7 TeV", tech. rep. ATLAS-CONF-2011-008, Geneva: CERN, 2011.

[115] "Charged particle multiplicities in p p interactions at phase-space measured with the ATLAS detector at the LHC and sqrts = 0.9 and 7 TeV in a diffractive limited new PYTHIA6 tune", tech. rep. ATLAS-CONF-2010-031, Geneva: CERN, 2010.

[116] P. Skands, "Tuning Monte Carlo Generators: The Perugia Tunes", tech. rep. MCNET-10-08, CERN-PH-TH-2010-113, 2010.

[117] P. M. Nadolsky et al., "Implications of CTEQ global analysis for collider observables", *Phys. Rev. D* 78.1 (2008) 013004.

[118] "Combined measurement and QCD analysis of the inclusive ep scattering cross sections at HERA", *Journal of High Energy Physics* 2010 (1 2010) 1–63.

[119] K. Nakamura et al., "Review of particle physics", *J. Phys. G* 37 (2010).

[120] M. Bellomo, "http://cdsweb.cern.ch/record/1367129", to be published in proceedings of Europhysics Conference On High Energy Physics, Grenoble, 2011.

[121] S. Frixione, P. Nason and C. Oleari, "Matching NLO QCD computations with Parton Shower simulations: the POWHEG method", *JHEP, 11:070* (2007).

[122] S. Alioli et al., "NLO vector-boson production matched with shower in POWHEG", *JHEP, 07:060* (2008).

[123] S. Alioli et al., "A general framework for implementing NLO calculations in shower Monte Carlo programs: the POWHEG BOX", *JHEP, 06:043* (2010).

[124] G. Corcella et al., "HERWIG 6.5: an event generator for Hadron Emission Reactions With Interfering Gluons (including supersymmetric processes)", *JHEP, 01:010* (2001).

[125] S. Frixione and W. B. R., "Matching NLO QCD computations and parton shower simulations", *JHEP, 06:029* (2002).

[126] W. Buttinger, "ExtendedPileupReweighting" (2011), CERN twiki: https://twiki.cern.ch/twiki/bin/viewauth/AtlasProtected/ExtendedPileupReweighting.

[127] K Bachas et al., "Measurement and QCD Analysis of Differential Inclusive W+- -> lnu and Z/gamma* -> ll Production and Leptonic Decay Cross Sections with ATLAS: Analysis STDM-2012-20: W and Z inclusive cross section with 2011 data", tech. rep. ATL-COM-PHYS-2013-217, Geneva: CERN, 2012.

[128] A. Belloni et al., "Measurement of the W Boson Transverse Momentum using Muons and Electrons in proton-proton collisions at sqrt(s) = 7 TeV with the ATLAS detector", *Technical Report* ATL-COM-DAQ-2011-008 (2011).

[129] The ATLAS Collaboration, "Expected Performance of the ATLAS Experiment" (2008).

[130] R. Brun and F. Rademakers, "ROOT - An Object Oriented Data Analysis Framework", *Nucl. Inst. & Meth. in Phys. Res. A* 389 (1997) 81–89.

[131] F. Cerutti et al., "Muon momentum resolution in first pass reconstruction of pp collision data recorded by atlas in 2010", *Technical Report* ATLAS-COM-CONF-2011-003 (2011).

[132] A. Kapliy, P. Onyisi and M. Shochet, "Muon momentum scale from Z bosons", *Technical Report* ATL-COM-MUON-2011-015 (2011).

[133] M. Whalley, D. Bourilkov and R. Group, "The Les Houches accord PDFs (LHAPDF) and LHAGLUE" (2005), arXiv:hep-ph/0508110 [hep-ph].

[134] JetMETGroup, "HowToCleanJets" (2010), CERN twiki: https://twiki.cern.ch/twiki/bin/view/AtlasProtected/HowToCleanJets.

[135] T Carli and A Schwarzman, "Jet energy measurement with the ATLAS detector in proton-proton collisions at sqrt(s)=7 TeV taken in 2010", tech. rep. ATL-COM-PHYS-2011-978, Geneva: CERN, 2011.

[136] JetMETGroup, "HowToCleanJets2011" (2011), CERN twiki: https://twiki.cern.ch/twiki/bin/view/AtlasProtected/HowToCleanJets2011.

List of Figures

List of Tables